Proceedings of the Eighth Workshop on Digital Fluid Power (DFP16)

DFP 16

Proceedings of THE EIGHTH WORKSHOP ON DIGITAL FLUID POWER

May 24-25, 2016, Tampere, Finland

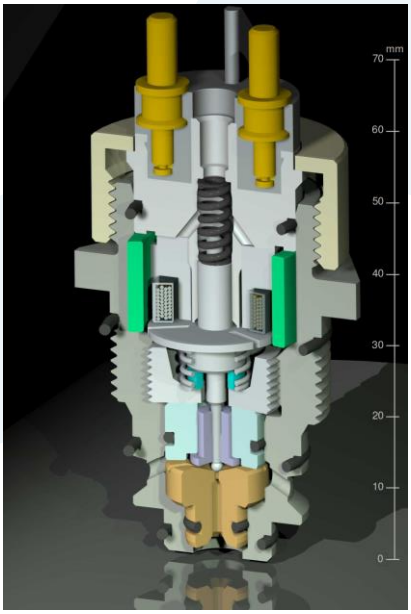

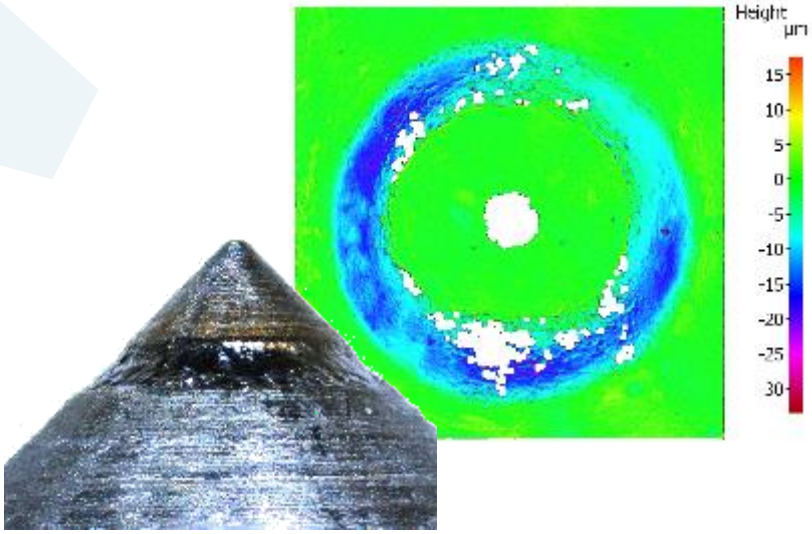

TAMPERE UNIVERSITY OF TECHNOLOGY

ACCM
AUSTRIAN CENTER OF COMPETENCE IN MECHATRONICS

Rexroth
Bosch Group

Tampereen teknillinen yliopisto - Tampere University of Technology

Janne Uusi-Heikkilä & Matti Linjama

Proceedings of the Eighth Workshop on Digital Fluid Power (DFP16)

May 24-25 2016, Tampere, Finland

Tampere University of Technology
Department of Intelligent Hydraulics and Automation
Tampere 2016

ISBN 978-952-15-3755-4 (printed)
ISBN 978-952-15-3756-1 (USB)
ISBN 978-952-15-3757-8 (PDF)

PREFACE

It is my pleasure to welcome you to the Eighth Workshop on Digital Fluid Power – DFP16. This time we have very international workshop and we have participants from 10 countries. The number of research units is also big; Digital Fluid Power is studied widely around the world.

Two main themes of this DFP workshop are valves and control. We still have lack of perfect switching valve – small size, big flow capacity, fast response, good durability and low cost – and this motivates the valve research. The utilization of automotive design is one interesting option. Good valve is nothing without good controller. The computational power is increasing, which allows new control solutions and moves the area of focus from components and implementation to clever control code. Digital pumps/motors and switching technologies are also important research areas. The digital pumping has potential for very good efficiency but the pulsating flow is a problem. The same problem troubles the switching systems. Maybe bigger computational power and clever control helps also here. I feel that digital pneumatics should have more important status in DFP. There should be lot of applications for leak free, high performance and more efficient digital pneumatic solutions.

My sincere thanks to Mrs. Virpi Multanen and M.Sc. Janne Uusi-Heikkilä for their help in organizing this workshop. I hope that you all enjoy the DFP16!

Tampere, May 2016

Adj. Prof. Matti Linjama

CONTENT

Switching Systems

Valves II

Control II

DEVELOPMENT AND EXPERIMENTAL RESULTS OF A SMALL FAST SWITCHING VALVE DERIVED FROM FUEL INJECTION TECHNOLOGY

DI Florian Messner, Prof Dr Rudolf Scheidl
Institute of Machine Design and Hydraulic Drives
Johannes Kepler University Linz
4040 Linz, Austria
E-mail: florian.messner@jku.at

ABSTRACT

This paper discusses the development of a valve as an experimental platform for the testing of hydraulic switching control in the low power, fast response and high precision domain. An exemplary application for such systems could be the actuation of automotive wet clutches, in particular of dual clutch systems. The nominal flow rates are in the tenth of litres per minute at 5 bar pressure loss range, pressures might typically go up to two hundred bars.

The valve development is based upon an electromagnetic actuation system derived from common rail injection technology. Samples of such magnetic actuation systems, originally developed and used in common rail systems for truck engines, have been granted to the authors. Those samples were integrated into an appropriate valve design, incorporating ball type seat valves. The valve design was modified to fit the requirements for the envisaged application domains. A housing was designed to encapsulate two valves, for in- and outflow respectively. Furthermore, an appropriate system for generating the required valve current feed had to be set up.

The valves have been tested to evaluate their performance. Sufficient flow rate could be achieved with a valve stroke of only 50 µm, allowing for a valve operation up to frequencies of 1 kHz, not permanently, but for a period of some seconds. With such high frequencies a very fast but still reasonably accurate control of low power drives can be accomplished. This is demonstrated for the pressure control of a small cylinder.

KEYWORDS: fast switching valve; frequencies up to 1 kHz

1. INTRODUCTION

Within the last two decades the term “Digital Hydraulics” has gained some popularity in hydraulics, mostly accompanied by keywords like *energy efficiency*, *cost savings* and improved *contamination sensitivity*.

In general, digital hydraulics may be separated up into three different classes ([1]). The first class consists of simple on/off type hydraulics, where actuators or drives are only operated in two different modes (i.e. pressure at high or low level, a pump spinning or not). The second class utilizes parallel connection of on/off type actuators (mostly of different size) in order to realize an output separated into multiple levels, with the number of these levels depending on the number of actuators. This principle somewhat resembles an electronic h-bridge multilevel inverter and has proved its usability in the last years by several commercial applications. The last class consists of switching techniques, imitating a continuous output behavior by switching an on/off type actuator at high frequencies similar to electronic switching converters. This technology has established in some niche markets like automotive anti-lock braking systems (ABS), hydraulic buck converters ([2]) and others. However, the most limiting parameter for this class of digital hydraulics is the switching frequency which currently is in the range of 100 to 200 Hz. Nevertheless, for a lot of applications higher switching frequencies might be beneficial. As an example the actuation of an automotive wet clutch is given. For such systems, the full range of transmission torque has to be accessible within 100 to 150 ms at an accuracy of approximately one percent full range ([3], [4]). If using hydraulic actuation, these requirements are scalable to a control pressure range of 30 to 150 bar adjustable within the mentioned time range, at a supply pressure of 200 bar and a required flow rate of approximately 0.2 liters/minute. But up to now, the required combination of dynamic and precision is not accomplishable with existing switching technology.

Therefore, the main objective of the paper at hands is the development of a rather small but very fast switching valve as an experimental prototype to clarify whether an increased switching frequency can meet the requirements stated in the example above or not. The entire setup is based on an electromagnetic actuation system derived from 3rd generation common rail injection technology. Section 2 is giving a summary of the manufacturer’s data and requirements for this actuation system. Afterwards section 3 and 4 deal with the mechanical and electrical design in order to meet those requirements. Finally, section 5 presents some results obtained with the developed switching valve.

2. THE ELECTROMAGNETIC VALVE ACTUATION SYSTEM

As mentioned above the electromagnetic actuation system was donated from a renowned automotive supply industry manufacturer. A schematic illustration of the 3rd generation actuation system is given in Figure 1.

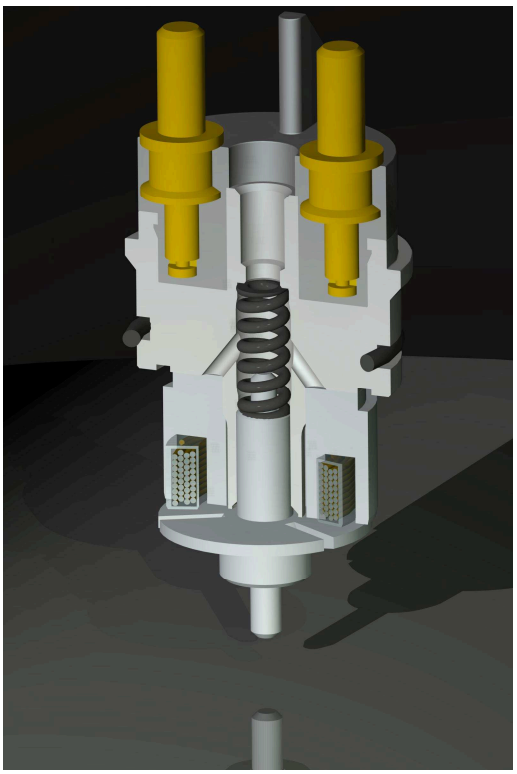

Figure 1: Solenoid actuation system

The pot core type solenoid with flat armature is acting against a return spring. Depending on the preload of this spring as well as the actual air gap, opening times between 200 and 300 µs are specified by the manufacturer. Spring preload is adjusted using shims, inducing a closing force which has to exceed the desired maximum operating pressure.

In order to realize such fast responses, a magnet force well beyond 100 N is stated, depending on valve current and air gap. Typical armature strokes are in the range of $s_V = 50$ µm, which is quite small but sufficient for the intended valve size of approximately 0.2 l/min at 5 bar pressure loss. As the armature features a minimum air gap of 50 µm in the upper position, the overall air gap remains between 50 and 100 µm.

The opening times listed above, are only achievable using a valve current boost method as shown in Figure 2. Valve activation is started with the boost sequence. Boosting in this context means, that the solenoid remains connected ($u_{Sw} = 1$) to the supply voltage until a desired boost current i_{boost} is met. Therefore the current gradient and, subsequently, the build-up of the magnetic field are maximized. After the corresponding boost duration t_{boost} the solenoid is disconnected ($u_{Sw} = 0$) for $t_{b,br}$ and the next sequence is started.

During the following sequence the armature has to be lifted to the upper position (raise sequence). This is achieved by keeping the solenoid current at an elevated level i_{raise}, resulting in a force imbalance on the armature and, consequently, an acceleration upwards. Once the upper position is reached, any further current feed at i_{raise} is unreasonable. Thus a current i_{hold}, which is sufficient to hold the armature at its upper position, has to be adjusted (hold sequence). The duration of the holding sequence can be chosen freely, as long as no thermal limits are violated, and is subject to the control concept.

Keeping the valve current at a constant level, for both, raise and hold sequence, turns out to be a simple matter of choosing an appropriate on/off-ratio. In general, higher frequencies result in shorter on/off times and therefore in a reduced peak-to-peak ripple of the current feed.

Manufacturer's recommendations for a proper valve operation, including sequence durations, currents and breaks, are listed in Table 1.

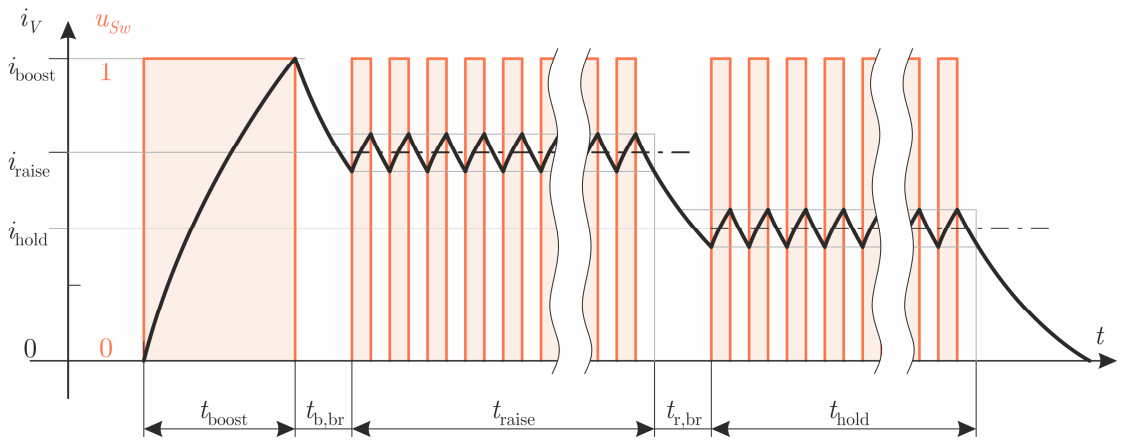

Figure 2: Idealized boost-, raise and hold sequence for valve current feed

Table 1: Manufacturer's recommendations for valve currents and timing

Timing	***Current***	***Break***
$t_{boost} \approx 110\ \mu s$ (@ 48 V)	$i_{boost} \approx 25\ A$	$t_{b,br} \approx 15\ \mu s$
$t_{raise} \approx 50 \ldots 350\ \mu s$	$i_{raise} \approx 15\ A$	$t_{r,br} \approx 40\ \mu s$
$t_{hold} \approx 0 \ldots 6000\ \mu s$	$i_{hold} \approx 11\ A$	

3. MECHANICAL DESIGN

The actuation system described in section 2 had to be complemented by a proper mechanical valve design. This design was subject to several requirements:

- Incorporate a leakage free valve seat, i.e. a ball type seat;
- Provide a volumetric flow rate of approximately 0.2 l/min at 5 bar pressure loss and 50 µm valve stroke;
- Act as receiver for the actuation system;
- Separate actuation system from regions of high pressure;
- Connect valve seat with supply and load;
- Proper sealing between supply, load and tank connections;
- Easy and cheap production of subcomponents;
- Design as cartridge-type valve to increase compactness and ease maintenance

3.1. Valve seat

Proven solutions for a leakage-free valve are either a taper or a ball type seat. Typically both seat types would be made of hardened and precision-grinded steel. As these processes are rather expensive, the valve seat was produced by impressing a hardened

chrome steel ball into a turned steel cone (see Figure 4).The estimated flow rate Q is calculated from the orifice equation ([5])

$$Q = \alpha_D \, A \sqrt{\frac{2}{\rho}} \sqrt{\Delta p} \quad , \tag{3.1}$$

where α_D denotes the flow coefficient for the flow area A, ρ the fluid density and Δp the corresponding pressure drop. With a ball diameter $d_b = 1.588$ mm (=1/16”), a hole diameter $d_h = 0.8$ mm and a flow coefficient of $\alpha_D \approx 0.8$ the nominal flow rate at 5 bar pressure drop calculates to $Q_N = 0.203 \; {}^{\mathrm{l}}/_{\mathrm{min}}$ for a nominal valve stroke of $s_V = 50$ µm.

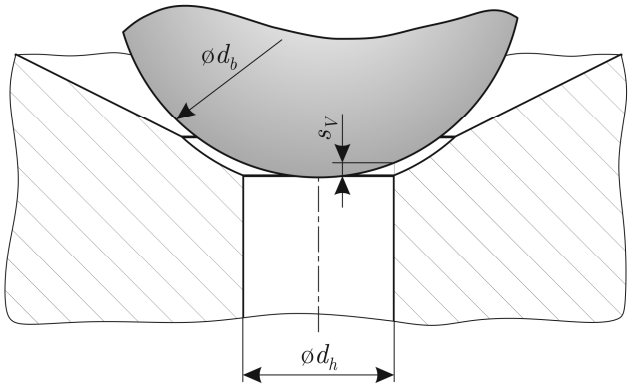

Figure 3: Valve seat and flow area

Thus the demanded valve flow rate as well as the requirement for a leakage free and easy to produce valve can be met by the use of a ball type valve seat.

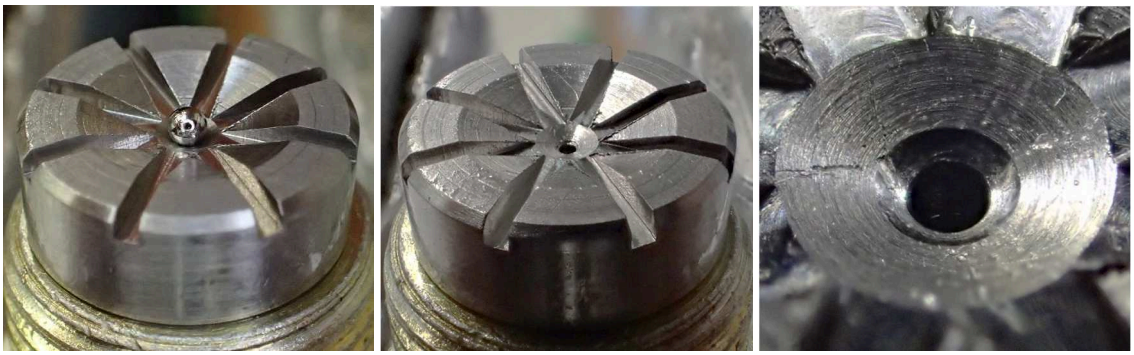

Figure 4: Impressing the valve seat

3.2. Separation between valve seat and actuation system

As mentioned previously the actuation system has to be separated from regions of higher pressure. This is due to the housing of the solenoid being made of some low-strength synthetic material. However, as the armature stroke needs to be transferred to the valve seat, an appropriate sealing system between these two regions is necessary. For cost reasons and due to poor documentation of the sealing performance of elastomer materials at high frequencies, this separation was accomplished with a gap sealing. The first version consisted of a precision rod and a reamed bore, both with a nominal diameter of 1.5 mm. Unfortunately, reaming did not allow for the required gap precision causing unacceptably high leakage flow. Therefore, a high precision sleeve was used, reducing gap tolerances to less than 5 µm and subsequently the leakage flow to a minimum. The final design of the sealing gap is illustrated in Figure 5.

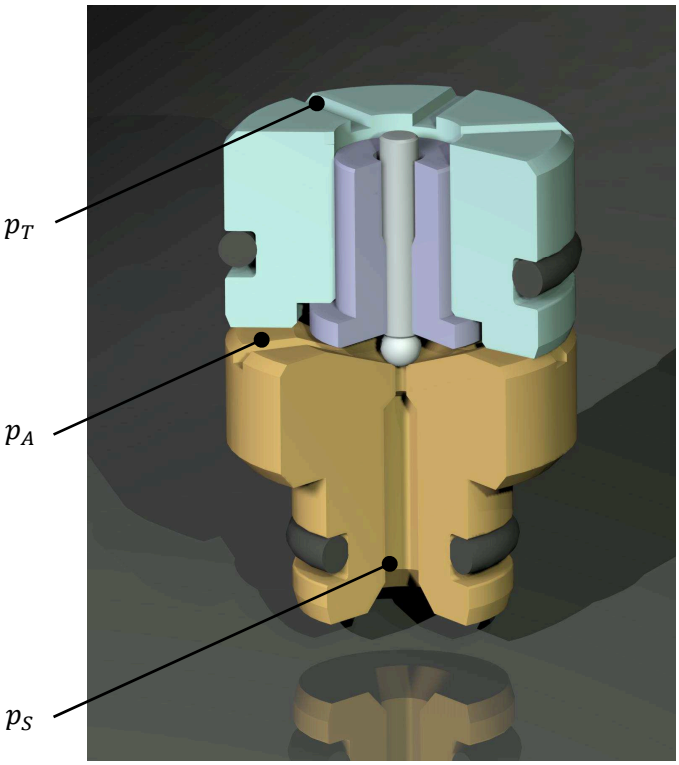

Figure 5: Separation between valve seat and actuation system

3.3. Valve housing

The valve housing and the final valve design are illustrated in Figure 6. The bottom area contains the valve seat as already depicted in Figure 5. The valve is mounted inside the housing with a metric fine thread. The top area mainly consists of the actuation system and is fixed with a cap nut on the outside of the housing. Accurate positioning of the actuation system inside the housing is achieved with a precision grinded spacing ring.

Sealing between regions with different pressure levels inside the valve housing (see Figure 5) is done with O-rings. These different levels are:

- Supply pressure p_S at the bottom of the valve seat;
- Load pressure p_A between valve seat and the guiding piece for the precision rod. The load flow rate is conducted outwards by flow channels on the top of the valve seat and drill holes in the housing.
- Tank pressure p_T for all parts above, especially the actuation system due to reasons of low strength. Connection to tank is achieved with holes in the valve housing placed beyond the mounting thread on the outside (not visible in Figure 6).

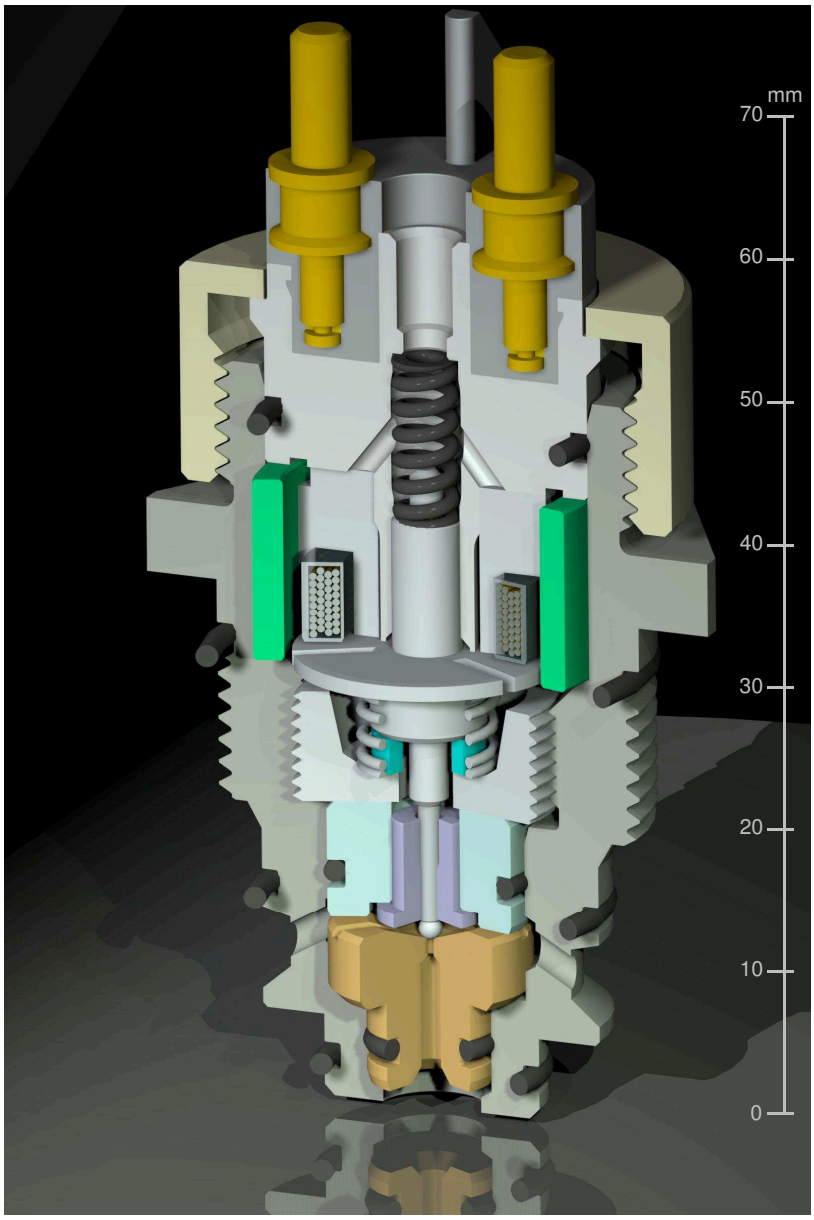

Figure 6: Intersection of final valve design

The bore on top of the actuation system is usually sealed. It may be utilized to verify top and bottom armature position throughout production using a dial gauge or similar devices. Unfortunately this kind of measurement can't be performed during operation as it influences the system's dynamic behaviour (increased moved mass). An appropriate measurement system oppressing any interactions with the armature – e.g. eddy current sensors – couldn't be purchased due to space limitations. Consequently, for the paper at hands, the *dynamic valve stroke is not measured*.

Furthermore, a mounting plate was developed, acting as a receiver for two valves, and allowing for a connection to one combined load.

4. SOLENOID CURRENT FEED

As already mentioned in section 2, the proposed valve response time can only be reached with a proper valve current feed. Figure 2 illustrates an idealized valve current progression, consisting of three different subsequences: boost, raise and hold. The corresponding parameters and thresholds are listed in Table 1. Electronics realizing such a valve current feed are commercially available, but cannot hold for the demanded switching times and the maximum peak currents [6]. Therefore, an appropriate setup providing the desired current feed had to be developed. This setup was subject to several requirements:

- An H- or full bridge capable of providing currents up to approximately 30 amps;
- Additionally, this bridge needs to be fast enough to keep up with the demanded switching frequencies in the range of some hundred kilohertz up to one megahertz;
- A programmable signal source providing the input signal u_{Sw} for the bridge at the specified frequency;
- A possibility to interfere with the signal source, such that the real-time operating system can change specific current feed parameters during runtime, i.e. in every sampling interval;

The requirements listed above could be met using the setup depicted in Figure 7. This setup consists of a real time operating system running on a standard desktop PC with a fixed sample rate of 1 kHz. The PC is equipped with a National Instruments PCI-card NI-6259 (for further information see [7]). Using the internal PCI-bus, data can be transferred between the real time system and the PCI-card. In addition, the PCI-card offers a digital output method using FIFO's (First In First Out), known as CDO (Correlated Digital Output). This method allows for the data samples inside the FIFO to be output in *correlation* to an adjustable internal clock generator. Finally, the output of the PCI-card drives an H-bridge connecting the valve solenoid to a supply voltage in forward or backward direction.

In summary, the signal flow for the valve current feed is realized in the following manner: First of all, within the current sampling interval, an appropriate control strategy determines whether the valve has to be activated or not. If actuation is required, an adequate digital switching sequence is calculated, if possible with respect to the current control error. Afterwards the entire switching sequence is downloaded to the PCI-card FIFO using a polling method. Therefore the real-time CPU remains occupied until the download is completed. The last step for the real-time CPU consists of starting the CDO,

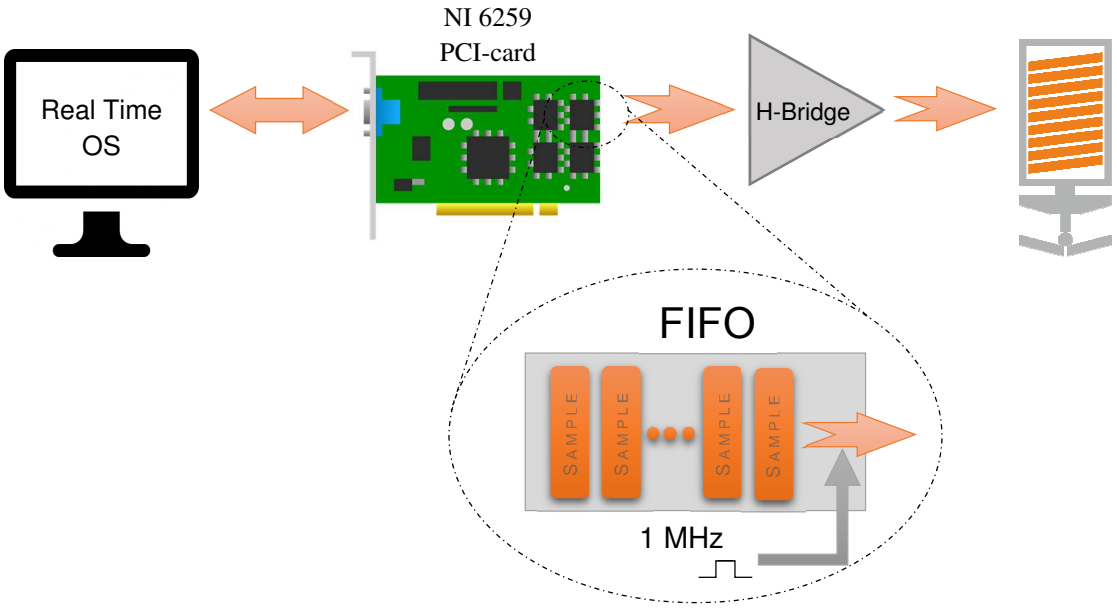

Figure 7: Schematic signal flow for valve actuation

which is a simple register entry. When done, the CPU is released and the subsequent operations are executed *independently* from the real time system. As shown in Figure 7, CDO is timed using an internal clock generator which is fixed at 1MHz for this particular setup. This means that the samples inside the FIFO are written to the output in equidistant steps of 1 µs, allowing for a timing accuracy in the same order of magnitude. At last, the digital PCI-card output is passed to the H-bridge connecting the solenoid in forward or backward direction to a supply voltage of 35 V.

In order to realize the data transfer between the real-time system and the PCI-card an appropriate driver had to be developed using the C programming language. During this development it was decided to separate both, raise and hold sequence, into repeated on and off cycles with n_i repetitions. Therefore the sequence durations calculate to

$$\begin{aligned} t_{raise} &= \left(t_{r,on} + t_{r,off}\right) \cdot n_{raise} \quad , \quad n_{raise} \in \mathbb{N} \\ t_{hold} &= \left(t_{h,on} + t_{h,off}\right) \cdot n_{hold} \quad , \quad n_{hold} \in \mathbb{N} \quad . \end{aligned} \tag{4.1}$$

Due to the choice of 1MHz for the internal clock generator, the on and off times $t_{i,on}$ and $t_{i,off}$ are not arbitrary numbers, but integer multiples of 1 µs.

As a consequence to the modifiable valve actuation time (see Equation (4.1)) and the possibility to choose whether the valve is actuated at all within each real-time step (1 kHz means 1ms), the resulting actuation method is a mixture of PWM and PFM, a so called Variable-Frequency-Pulse-Width-Modulation (VF-PWM). Hereafter the terms *actuation time* and *actuation frequency* are distinguished accordingly.

5. MEASUREMENTS, EXPERIMENTS AND FINDINGS

This section deals with the measurements and the corresponding findings. In subsection 5.1 the performance of the developed valve current feed method is presented, followed by the valve characteristics for a given test rig setup in subsection 5.2. Finally subsection 5.3 deals with a simple control strategy and corresponding results for different trajectories.

5.1. Measured valve current feed

Figure 8 is depicting a measurement of the valve current feed generated with the method described in section 4, the corresponding timing parameters are listed in Table 2. Boost, raise and hold sequences are highlighted using coloured areas. The hold sequence is plotted for different values of the previously mentioned hold parameter n_{hold}, implying a valve actuation with varying actuation time. The top row of Figure 8 presents the digital output u_{Sw} of the PCI-card (5 V TTL) and the measured valve solenoid voltage u_V for a h-bridge supply voltage of 35 V. The bottom row illustrates the corresponding valve current feed i_V, measured with two different current sensors: an internal current transducer (i_{int}) and an external current probe (i_{ext}) attached immediately at the solenoid.

Taking a closer look at the depicted current feed reveals, that the desired boost current $i_{boost} \approx 25$ A can't be reached within time. This is due to a limited supply voltage of 35 V compared to the manufacturer's original suggestion of 48 V. Furthermore, the internal current sensor exhibits strong peaks on i_{int} when switching. These may be due to a supply voltage drop caused by an improper switching inside the H-bridge. However, the external sensor indicates a satisfying current feed with the expected ripples described in section 2. The peak-to-peak value of those ripples heavily depends upon the switching times $t_{i.on}$ and $t_{i.off}$, but just as well upon the supply voltage used during raise and hold sequence.

Summing up, the developed valve actuation method reveals a very satisfying overall behaviour. Even though the manufacturer's specifications couldn't be met perfectly, the valve current feed performs as expected.

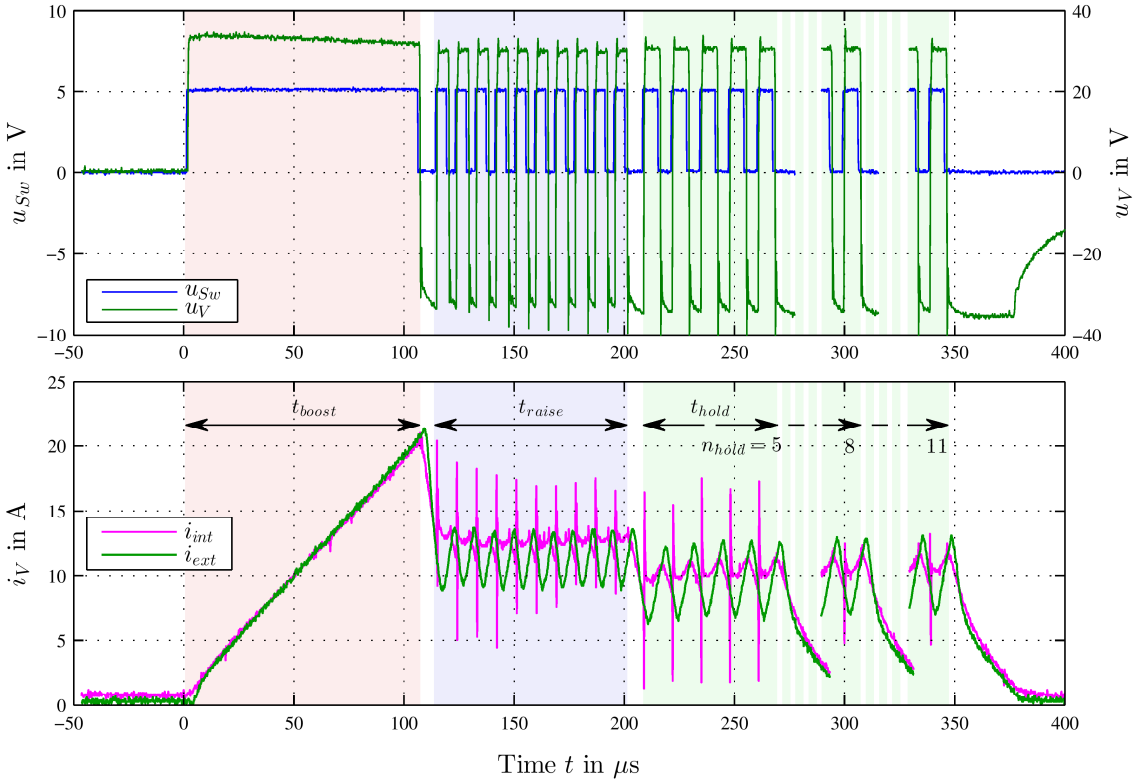

Figure 8: Measured valve current feed for different holding times

Table 2: Parameters for measured valve current feed in Figure 8

Sequence	***Parameters***			
Boost	$t_{boost} = 105$ µs	⋯	⋯	$t_{b,br} = 8$ µs
Raise	$t_{r,on} = 5$ µs	$t_{r,off} = 4$ µs	$n_{raise} = 10$	$t_{r,br} = 4$ µs
Hold	$t_{h,on} = 7$ µs	$t_{h,off} = 6$ µs	$n_{hold} = 5$	⋯
	$t_{h,on} = 7$ µs	$t_{h,off} = 6$ µs	$n_{hold} = 8$	⋯
	$t_{h,on} = 7$ µs	$t_{h,off} = 6$ µs	$n_{hold} = 11$	⋯

5.2. Measured System Response

In order to evaluate the influence of the developed valve on low power systems or systems with low actuation volume the test rig setup in Figure 9 was implemented. This setup consists of a hydraulic plunger cylinder acting against a very stiff spring, limiting the overall cylinder stroke to less than 3 mm for a maximum supply pressure p_S of 200 bar. Choosing such a stiff behaviour was due to ease comparison with commercial systems, for example wet clutches. The test rig setup features two valves for controlling in- and outflow.

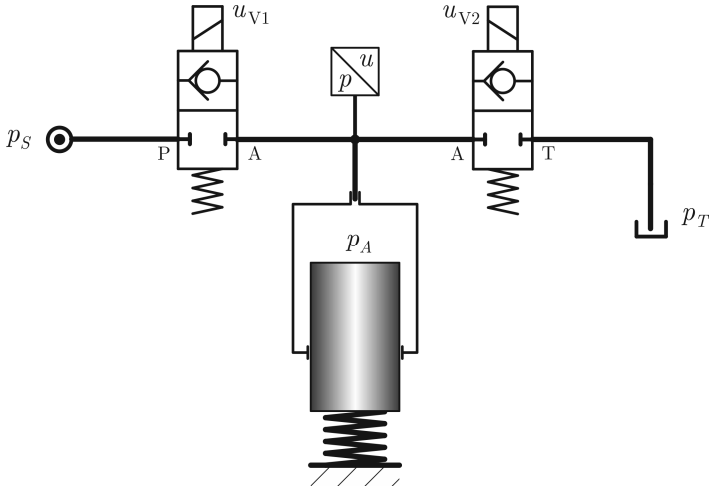

Figure 9: Schematic of the implemented test rig setup

The results presented below deal with the response of the system as described in Figure 9 due to a specific valve actuation. As already stated in section 4, the developed valve allows for a mixed operation of PWM and PFM. In order to identify the system response distinct to a variation in valve actuation time, i.e. hold sequence parameter n_{hold}, the actuation frequency has been fixed to 100 Hz. This setting is used for both, Figure 10 and Figure 11, respectively. The corresponding actuation parameters are listed in Table 3.

Figure 10 illustrates the measured pressure development p_A for actuating the inflow valve using different values of the hold sequence parameter n_{hold}. Each measurements is conducted for a fixed value of $n_{hold} \in [0, \dots, 20]$ and a starting pressure of approximately 50 bar. While testing, the inflow valve is actuated every 10 ms according to the selected actuation frequency of 100 Hz. The resulting chart reveals a very distinct dependency on the parameter n_{hold}. Furthermore, the measurements exhibit an unexpected linear behaviour contrary to the hypothetical square-root-characteristic. This may be due to the load pressure p_A acting on the precision rod, causing a variation in the force equilibrium of the entire armature. Consequently, the valve opens faster and closes slower at higher pressures, increasing the entire period of valve actuation.

In contrast to the inflow valve the outflow valve (see Figure 11) reveals the mentioned square-root-behaviour as the pressure acting on the precision rod is fixed to tank pressure p_T. At this point it has to be mentioned, that the outflow valve stroke was increased to 80 µm, in order to achieve higher effluent flow rates.

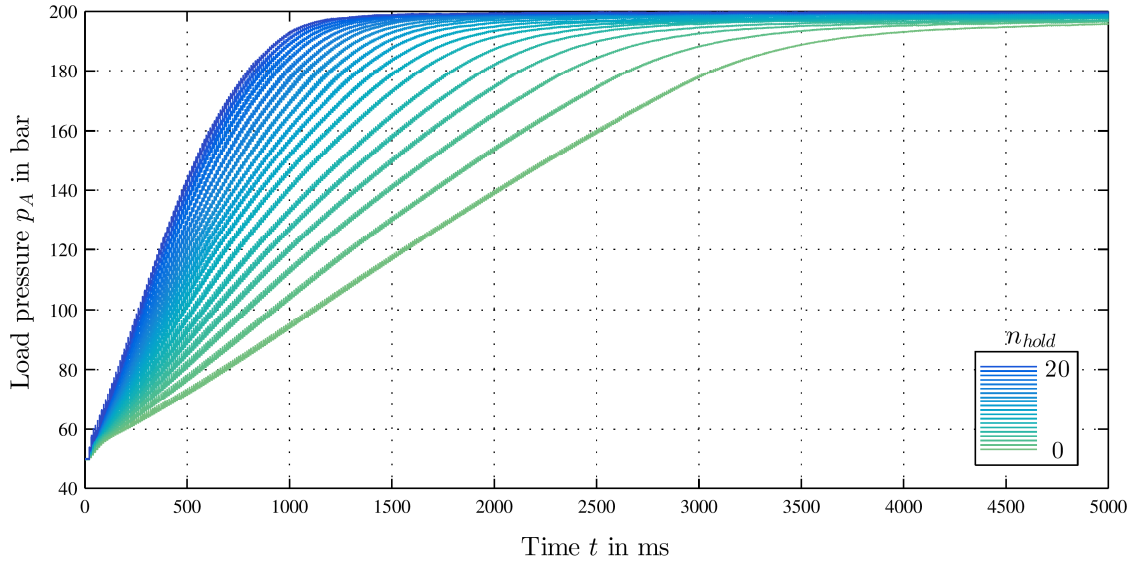

Figure 10: Measured pressure development for fixed frequency and varying valve actuation time of inflow valve

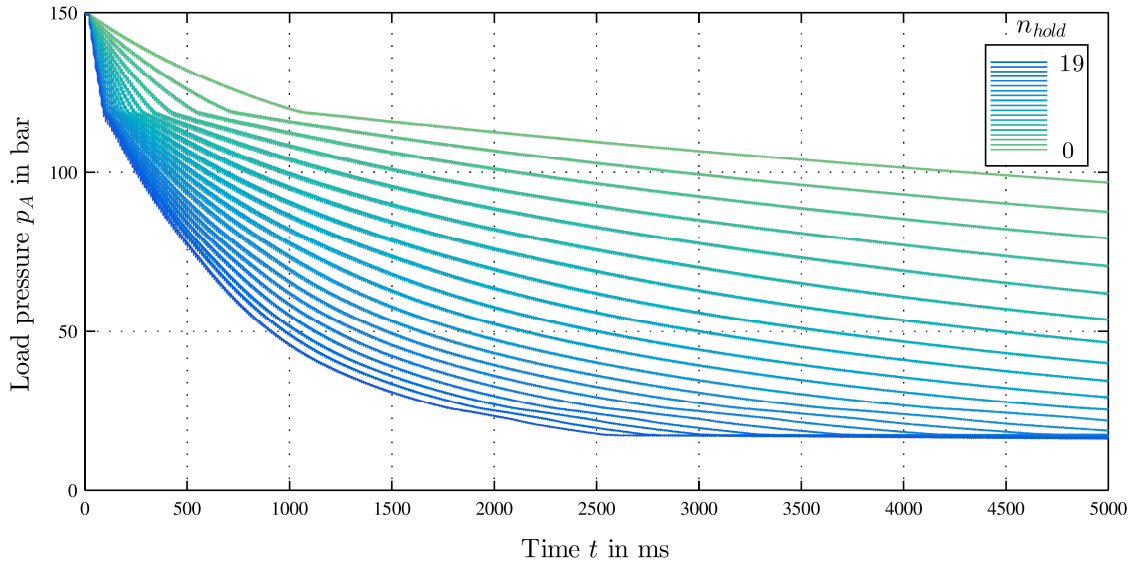

Figure 11: Measured pressure development for fixed frequency and varying valve actuation time of outflow valve

Table 3: Valve parameters used in Figure 10 and Figure 11

	Max. Stroke	***Actuation Parameters***		
Inflow Valve	45 µm	$t_{boost} = 120$ µs $t_{b,br} = 8$ µs	$t_{r,on} = 5$ µs $n_{raise} = 6$ $t_{r,off} = 4$ µs $t_{r,br} = 5$ µs	$t_{h,on} = 7$ µs $t_{h,off} = 6$ µs
Outflow Valve	80 µm	$t_{boost} = 120$ µs $t_{b,br} = 8$ µs	$t_{r,on} = 5$ µs $n_{raise} = 12$ $t_{r,off} = 4$ µs $t_{r,br} = 5$ µs	$t_{h,on} = 7$ µs $t_{h,off} = 6$ µs

5.3. Results for a simple pressure control strategy

The results presented in this subsection are derived for a very simple pressure control strategy. The hold parameter n_{hold} is calculated proportional to the current pressure error. Relating to Figure this seems reasonable for the inflow valve, according to Figure the outflow valve is extended by a function compensating for the square-root-characteristic

$$\begin{aligned} n_{hold}^{Vin} &= \left\lfloor P_{hold}^{Vin} \cdot \left(p_A^d - p_A^m\right) \right\rfloor \quad , \ \in [0 \dots 19] \\ n_{hold}^{Vout} &= \left\lfloor P_{hold}^{Vout} \cdot \left(p_A^d - p_A^m\right) \right\rfloor + \left\lfloor K_{comp}^{Vout} \cdot (p_{lim} - p_A^m)^2 \right\rfloor \quad , \ \in [0 \dots 19] \quad . \end{aligned} \tag{5.1}$$

Here p_A^d represents the desired pressure trajectory, p_A^m the measured load pressure, $P_{hold}^{Vin/out}$ the proportionality constants of both valves, K_{comp}^{Vout} the compensation constant for the outflow valve and p_{lim} the maximum pressure for which the outflow valve is compensated. Furthermore, the gauss brackets $\lfloor \cdot \rfloor$ indicate rounding down to the nearest integer. The decision whether a valve has to be activated or not is calculated proportional to the pressure error

$$\begin{aligned} \bar{S}_{in} &= \begin{cases} \bar{r}_{in} & , \ \left(p_A^d - p_A^m\right) > p_{th,in} \\ 0 & , \ \text{else} \end{cases} \\ &\text{with} \quad \bar{r}_{in} = \begin{cases} 1 & , \ \Sigma \left[P_{freq}^{\text{Vin}} \cdot \left(p_A^d - p_A^m\right)\right] > 10 \\ 0 & , \ \text{else} \end{cases} \\ \bar{S}_{out} &= \begin{cases} \bar{r}_{out} & , \ \left(p_A^d - p_A^m\right) \leq p_{th,out} \\ 0 & , \ \text{else} \end{cases} \\ &\text{with} \quad \bar{r}_{out} = \begin{cases} 1 & , \ \Sigma \left[P_{freq}^{\text{Vout}} \cdot \left(p_A^d - p_A^m\right)\right] > 10 \\ 0 & , \ \text{else} \end{cases} , \end{aligned} \tag{5.2}$$

where $p_{th,in/out}$ denote switching thresholds and $P_{freq}^{Vin/out}$ the proportionality constants. Σ represents a simple summation over time, similar to an integration, but is reset every time when a switching process is triggered. The variables $\bar{S}_{in}$ and $\bar{S}_{out}$ are Boolean expressions. If they equal 1, the actuation data is downloaded to the PCI-card and the corresponding valve is actuated, otherwise not. As shown in Equation (5.2), these expressions are calculated proportional to the pressure error summed over time. This simply means, that for small pressure errors obtaining $\bar{S}_{in/out} = 1$ will take longer than for bigger pressure errors. Consequently the actuation frequency for small pressure errors is less than for big pressure errors.

As the decision variables $\bar{S}_{in}$ and $\bar{S}_{out}$ in Equation (5.2) are calculated every sampling interval T_S, the actuation period is restricted as an integer-multiple of T_S. Consequently, the actuation frequency results as a discrete variable.

Figure 12 illustrates the results for applying the control strategy described in Equation (5.1) and (5.2) to the test rig setup shown in Figure 9. On the left hand side measurements for a rectangular pressure trajectory with a pressure step of 100 bar and frequencies of

0.5, 2 and 5 Hz are listed. The right hand side shows measurements for a sinusoidal pressure trajectory with a similar parameter set.

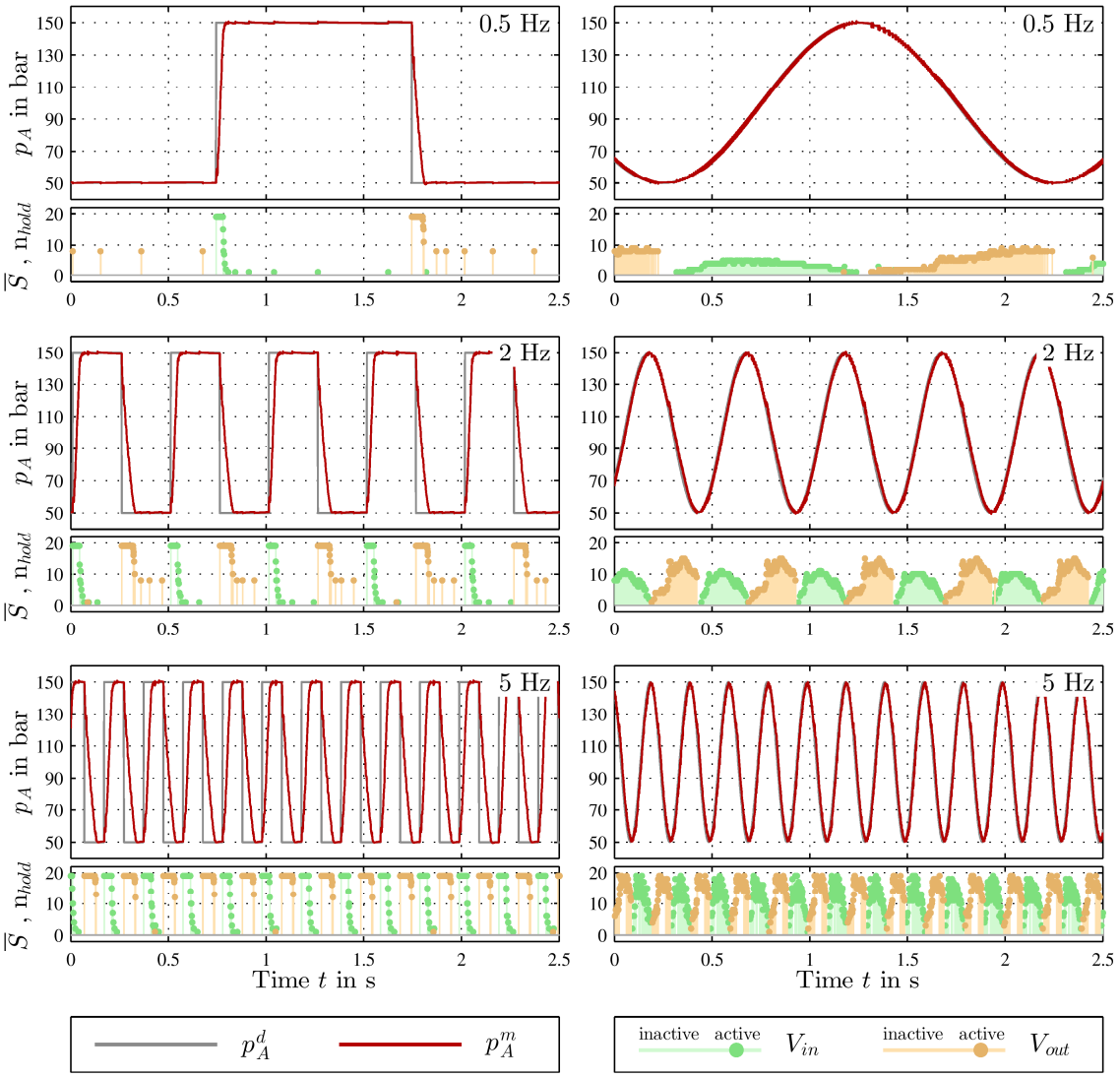

Figure 12: Results for different pressure trajectories

The top left image in Figure 12 identifies the maximum dynamics of the setup. The desired pressure step from 50 to 150 bar can be followed in approximately 40 to 50 ms. Within this period the inflow valve is driven at its maximum performance. Actuation time parameter n_{hold}^{Vin} is set to the maximum value of 19 and the valve is actuated every time step which is equivalent to the maximum actuation frequency of 1000 Hz. When approaching the target pressure of 150 bar, both actuation frequency and actuation time parameter n_{hold}^{Vin} are decreased, allowing for a smooth settling without overshoot. This decrease is also visible in the development of the control variables $\bar{S}_{in}$ and n_{hold}^{Vin} in the subsequent plot. The behaviour for decreasing the pressure from 150 bar to 50 bar is very similar. Values of n_{hold}^{Vout} at 50 bar are due to the compensation function. Results for a pressure trajectory with 2 and 5 Hz, respectively, are given in the subsequent plots on the left hand side. They are quite similar to the one already described.

The right hand side of Figure 12 is showing the results for a sinusoidal pressure trajectory at different frequencies. Apparently, the desired trajectory can be followed sufficiently accurate for all frequencies. A major difference compared to the scenario on the left hand side becomes obvious when looking at the control variables. In case of a sinusoidal trajectory the valve is getting activated much more often, which is due to the trajectory being a time-dependent function.

Table 4: Control parameters

	Actuation Time	***Actuation Frequency***
Inflow Valve	$P_{hold}^{Vin} = 2$	$p_{th,in} = 0.5\ \text{bar}$ $P_{freq}^{\text{Vin}} = 1.8$
Outflow Valve	$P_{hold}^{Vout} = -2$ $K_{comp}^{Vout} = 0.0016$ $p_{lim} = 120\ \text{bar}$	$p_{th,out} = -0.5\ \text{bar}$ $P_{freq}^{\text{Vout}} = -2$

6. CONCLUSION AND RECOMMENDATIONS FOR FUTURE WORK

The conducted measurements in section 5 reveal a very satisfying overall behaviour. The developed valve and actuation method are capable of combining an impressing dynamic response with very good accuracy. Therefore, the application of the valve to commercial systems as already described in section 1 seems to be very promising.

Despite the very convincing results there are still a lot of things that are worth improving:

Valve Design:

- Separation of the valve seat from the solenoid with a gap sealing is just a temporary solution. Leakage at this point has to be avoided completely. Either isolate those two regions completely or redesign the solenoid to become pressure resistant.
- Investigation of piezoelectric actuation and corresponding advantages/disadvantages in timing and actuation.
- Find an appropriate position measurement system for measuring the valve stroke dynamically. Challenging due to space limitations inside solenoid.
- Perform endurance tests for life-cycle determination.
- Investigate different designs in order to reduce production costs.

Valve Current Feed:

- Development of a proper circuit board with different voltage levels for boost, raise and hold sequence in order to reduce peak-to-peak ripple in current feed and improve boost dynamic; investigate reasons for faulty current measurement of the existing current sensor (see i_{int} in Figure 8).
- Enable DMA (Direct Memory Access) on PCI-card for faster data transfer and much more autonomic PCI-card behaviour; This might only be possible in combination with interrupt request.
- Setting up an AI-FIFO (Analogue Input-FIFO) in order to measure the valve current parallel to setting the valve actuation output.

Control Concept:

- Development of an ILC (Iterative Learning Control) for the valve current. This is only possible with a proper working AI-FIFO for measuring the valve current.
- Improve control concepts with model based approaches.

REFERENCES

[1] Linjama M., Digitalna Hidravlika, 2008; Digital Hydraulics – Towards Perfect Valve Technology;

[2] Kogler H., Trauner Verlag, 2012; The Hydraulic Buck Converter – Conceptual Study and Experiments;

[3] Goetz M., Thesis, University of Leeds, February 2005; Integrated Powertrain Control for Twin Clutch Transmissions;

[4] Buchanan M., Nienstedt J., BorgWarner, 2013; Control of Dual Clutch Transmissions with One Way Clutch; VDI Getriebetagung 2013; June 2013;

[5] Murrenhoff H., Aachen, Shaker Verlag, 2007; Grundlagen der Fluidtechnik,

[6] Bosch Rexroth, Retrieved from: http://www.boschrexroth.com/ics/Vornavigation/Vornavi.cfm?Language=EN&DisplayType=tile&Region=none&VHist=Start,p537409,p537410,p537722&PageID=p563945; 2016, February 8;

[7] National Instruments, Austin, Texas, July 2008; DAQ M Series User Manual;

PERFORMANCE OF HIGH-SPEED ON/OFF VALVE WITH INTELLIGENT THREE POWER SOURCE EXCITATION

Bin Zhang, Qi Zhong, Haocen Hong, Huayong Yang
Zhejiang University
The State Key Lab of Fluid Power Transmission and Control
Hangzhou 310027, China

ABSTRACT

Frequency response is an important index of high-speed on/off valves. In this paper, an intelligent three power source excitation method is proposed by the authors. A high excitation voltage engages an electromagnet quickly, shutting a valve. A lower voltage is used to keep the electromagnet engaged and a negative voltage is used to unload the current to disengage the electromagnet quickly. Adaptive switching of the power supply is realized by using a current feedback control method. A series of simulation are carried out and the results show that this control strategy could effectively reduce the switching time of high-speed on/off valves. Duration of electromagnet engagement (and thus valve closure) is shortened from 3.63ms to 2.10ms and duration of electromagnet disengagement is shortened from 5.63ms to 2.31ms. Benefiting from the adaptive switching of power sources, the high-speed on/off valve retains dynamic performance as coil resistance increases under higher temperatures.

KEYWORDS: High-speed on/off Valve, Intelligent, Three Power Source Excitation, Current Feedback, Changing Resistance, Dynamic Performance

1. INTRODUCTION

High-speed on/off valve (HSV) is a typical digital valve which is widely used in hydraulic and pneumatic systems because of its advantages such as excellent switching performance, compact structure, anti- pollution and low cost. Recently, digital hydraulic systems have placed higher demands on the dynamic performance and energy consumption of HSVs, which act as key components of flow and pressure control in such systems. There are two operation states of HSV, on and off. Because of this working characteristic, fluid through HSV is always discrete, but when the operating frequency gets high enough, the discrete liquid can be considered as continuous liquid. The higher the operating frequency of HSV, the more accurate the control of flow and pressure, to the point that they can through discrete flow width modulation approach the function of proportional valves. A three power source driving circuit to improve the dynamic performance of HSV is presented in [1]. A new scheme of parallel coils is introduced in [2], this scheme can greatly decrease the delay time. In [3] an intelligent “bit-split” control

approach in switching technologies is presented, which can expand the real application range of digital hydraulics. In [4] the effect of armature mass on dynamic performance of high-speed on/off valve is studied and its optimal range is also discussed. In [5] the influence of electromagnet dimensions and the turn number of coils on the electromagnet is studied. A new type high-speed on/off valve with giant magnetostrictive material(GMM) is shown in [6], which has an excellent force performance of 1500N with an air gap of 0.15mm, and a dynamic performance of 0.45ms switching time.

In this research, A 2/2 way high-speed on/off valve and the parameters of its electromagnet are presented. A series of simulations are carried out to verify the improvements in switching time by the intelligent three power source excitation (I3PSE).

2. PRINCIPLE OF HSV

Based on an existing structure of 2/2 way, an improved structure with larger flow is put forward, which is shown in Figure 1. Port P is oil inlet and port T is oil outlet. When the coil is de-energized, the steel ball will be moved to the right by the pressure of the supply port P. As a result, the port P will be connected to the port T. When the coil is energized, the steel ball will be moved to the left by the electromagnetic force. As a result, a seal will be created between port P and port T. The structure's main parameters are shown in Table 1. Simulation results show that the rate of flow reaches 14.3L/min at the supply pressure of 15Mpa.

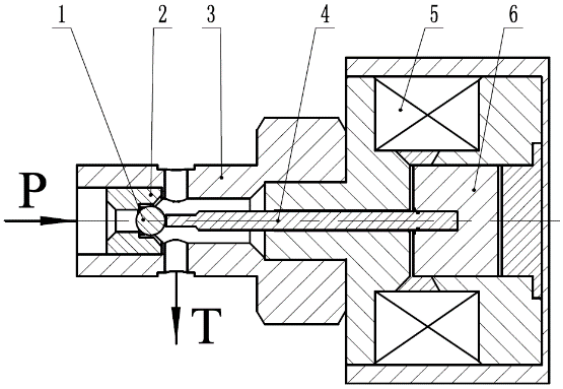

1. Steel ball, 2. Ball seat, 3. Valve housing, 4. Push rod, 5. Coil, 6. Armature
Figure 1. Schematic of high-speed on/off valve

Table 1. Structure parameters

Parameters	value
Steel ball diameter (mm)	3
Seat diameter (mm)	2
Maximum displacement (mm)	0.45
Volume at port P (cm^3)	0.8
Volume at port T (cm^3)	1.2

3. ELECTROMAGNET MODELING AND SIMULATION

The high-speed electromagnet is the key part of HSV and has a great deal of influence on

the dynamic characteristics of HSV. The most important characteristics of such electromagnets are large electromagnetic force and low inductance. This section presents the results of an electromagnet simulation model built using an Ansoft finite element method stationary solver, covering the range of 0-1500A of current with an interval of 100A and the range of 0-0.8mm of displacement with an interval of 0.05mm. The main magnetic part of the solenoid is defined as DT4, its bulk conductivity is $1.03 \times 10^7 \mathrm{s/m}$, and its B-H curve is shown in Figure 2.

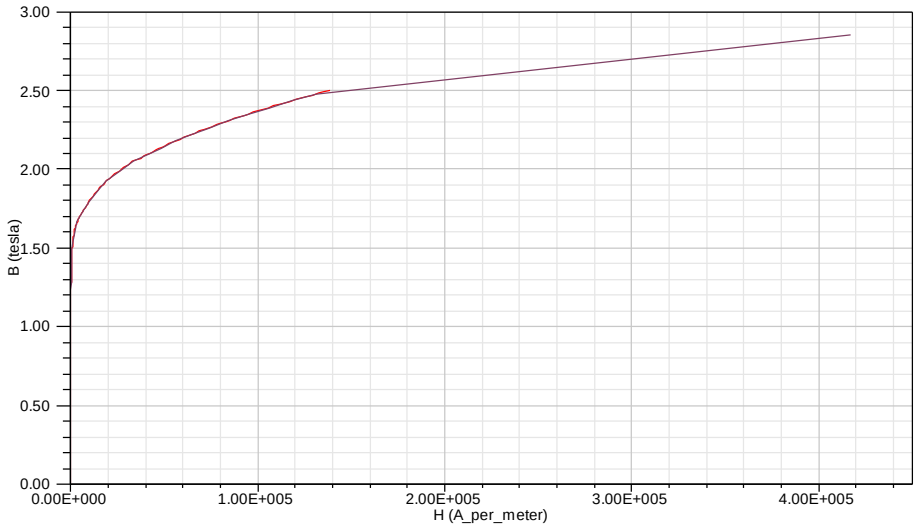

Figure 2. B-H curve of DT4

The resulting electromagnetic force over that range is shown in Figure 3, and the resulting inductance is shown in Figure 4.The electromagnetic force increases with the ampere-turns but decreases with the air gap, with the peak force approaching 350N, which perfectly meets the requirements of the valve. Because the flux linkage changes rapidly in the area of 0-200 ampere-turns and 0-150μm air gap, so the inductance in this area is extremely high, which will increase the delay time, so this paper selects 0.15 mm to 0.6 mm as the operation air gap.

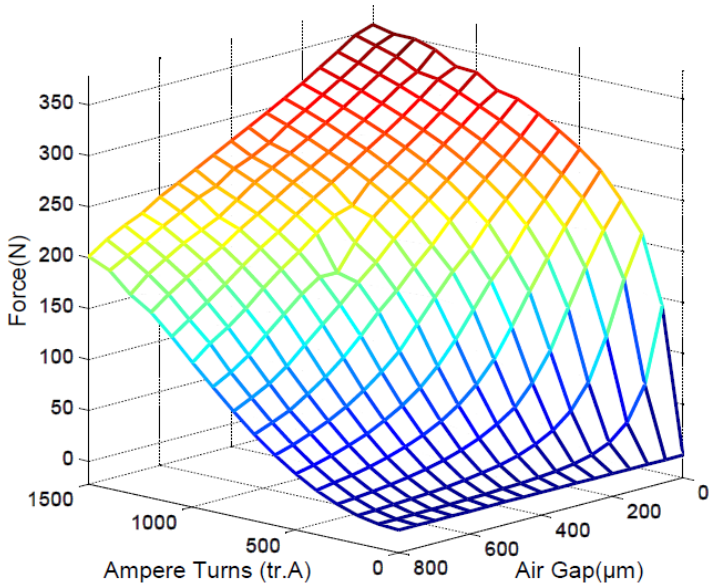

Figure 3. Electromagnetic force characteristic

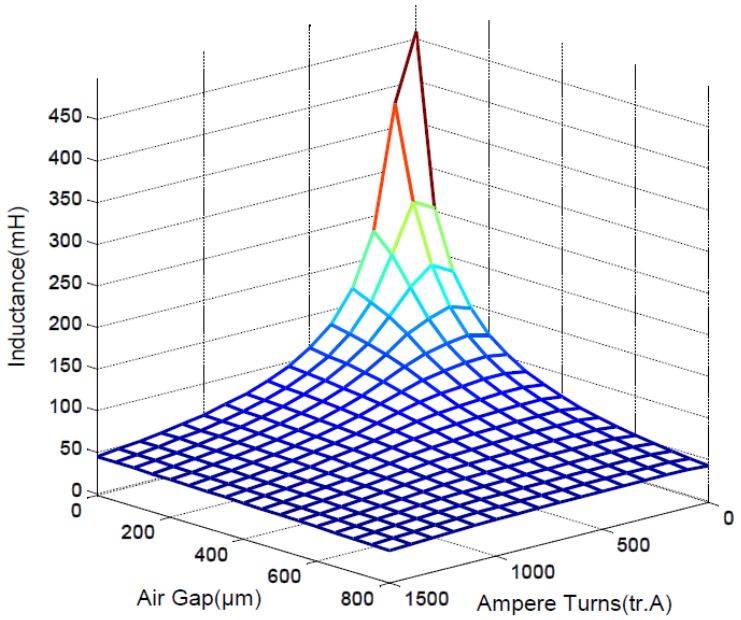

Figure 4. Inductance characteristics

The performance of the electromagnet is a function of its force and inductance, so its electromagnet sub-model is able to be created according to the two characteristics. The sub-model will be used in subsequent HSV dynamic simulation.

4. THEORETICAL ANALYSIS

Under fixed operating conditions, the electromagnetic forces needed in the engaged moment(engaged critical states) and disengaged moment(disengaged critical states) are constant. The corresponding engaged current (I_{on}) and disengaged current (I_{off}) are also constant. When the electromagnet is in engaged critical state, there is a maximum initial air gap, so more ampere-turns will be needed to overcome returning force, which will result in a higher I_{on}. When the electromagnet is in disengaged critical state, there is a minimum initial air gap, so fewer ampere-turns will be needed to overcome returning force, which will result in a lower I_{off}.

Due to the influence of coil inductance, there will be a delay time before current increase to I_{on} when the coil is energized, and there will also be a delay time before current decrease to I_{off} when the coil is de-energized.

The electrical circuit model can be written as:

$$U = RI + L\frac{\mathrm{dI}}{\mathrm{dt}} \qquad (1)$$

Where U is the driving voltage, R is the equivalent resistance, I is the current of coil and L is the equivalent inductance.

The current transient process of coil can be written as:

$$I = I_{\mathrm{i}} + \left(\frac{U}{R} - I_{\mathrm{i}}\right)\left(1 - e^{-t\frac{R}{L}}\right) \tag{2}$$

Where I_{i} is the initial current of coil, so the delay time can be written as:

$$t_d = \frac{L}{R}\ln\frac{U - I_{\mathrm{i}}R}{U - IR} \tag{3}$$

Where t_d is the delay time. Hence the delay times of the engaging process and disengaging process, respectively, can be written as:

$$t_{d\mathrm{on}} = \frac{L_{\mathrm{on}}}{R}\ln\frac{U - I_{\mathrm{i}}R}{U - I_{\mathrm{on}}R} \tag{4}$$

$$t_{d\mathrm{off}} = \frac{L_{\mathrm{off}}}{R}\ln\frac{U - I_{\mathrm{i}}R}{U - I_{\mathrm{off}}R} \tag{5}$$

Where $t_{d\mathrm{on}}$ is the engaged delay time, L_{on} is the equivalent inductance in the engaged initial position, $t_{d\mathrm{off}}$ is the disengaged delay time and L_{off} is the equivalent inductance in the disengaged initial position.

It can be seen from Eqs. (4) and (5) that a larger initial current and excitation voltage are helpful to reduce $t_{d\mathrm{on}}$ and a smaller initial current and excitation voltage are helpful to reduce $t_{d\mathrm{off}}$. Of course, a negative voltage is better to accelerate the decrease of current in the disengaging process.

5. INTELLIGENT THREE POWER SOURCE EXCITATION

This section presents an intelligent three power source excitation (I3PSE) method, which consists of a high voltage source, a low voltage source, a negative voltage source, a current detector and a controller. Hardware connection is shown in Figure 5.The voltage level of the low voltage source is slightly higher than the product of the equivalent resistance R and I_{off}. The voltages are used to drive the HSV and the current detector is used to detect real-time current and provide that as feedback to the controller, which controls the status of each voltage source according to the control signal and the feedback value of current.

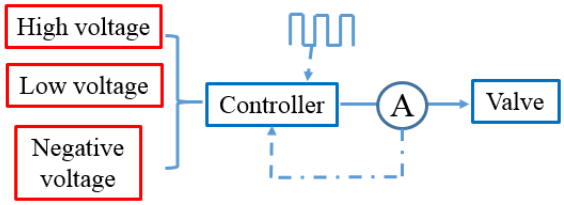

Figure 5. Hardware connection

The operation principle is shown in Figure 6. The control signal is used to control the operation frequency and duty ratio of HSV. Once the system starts, the high voltage source powers the circuit during the rising edge of the control signal, while the low voltage source and negative voltage source remain disconnected. Under the excitation of

high voltage, current raises to I_{on} rapidly, the electromagnet is engaged and the valve is closed. Next, the high voltage source is disconnected and the low voltage source is connected. Under low voltage, the current decreases slowly and stabilizes on a value slightly larger than I_{off} to maintain electromagnet engagement. The low voltage remains connected until the falling edge of the control signal is reached. At this time, the negative voltage source replaces the low voltage source, which results in a rapid decrease in current because of the unloading function of negative voltage. When the current reduces to I_{off}, all voltage sources are disconnected and the current drops slowly until the next rising edge of the control signal, at which point the system will repeat the above-mentioned process.

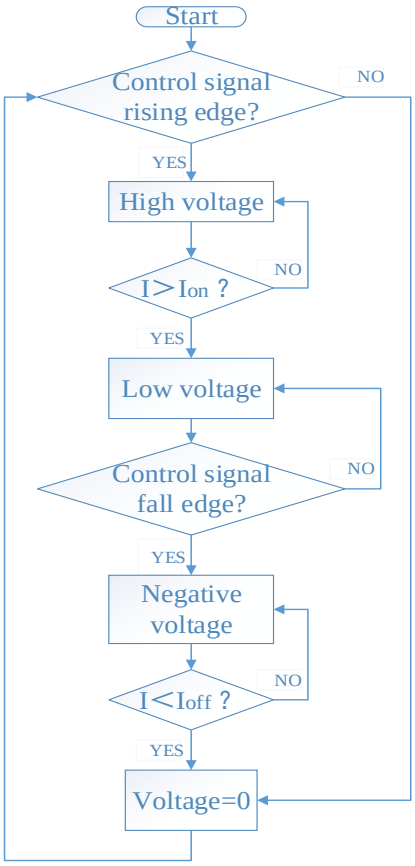

Figure 6. Control flow chart

Under this method of control, current begins to drop automatically once it reaches I_{on}, which will make the initial current lower at the moment of disengagement and decrease $t_{d\text{off}}$. Once current drops below I_{off}, the negative voltage source will be disconnected and current will decrease slowly. This will provide a larger initial current at the next moment of electromagnet engagement and decrease $t_{d\text{on}}$. The current is always in the optimal state during the whole process, as shown in Figure 7.

This method uses current feedback to realize the adaptive switching of voltage sources. Even under the influence of varying coil resistance caused by temperature increases, the switching time of each voltage source can be adjusted adaptively. Therefore this method not only can effectively improve the working frequency of HSVs, but also can reduce the current in the coil, so that temperature increases can be decreased greatly, which will help to extend the service life of HSVs.

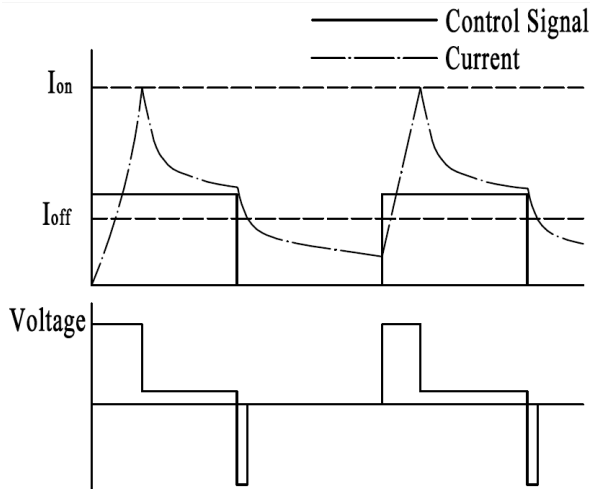

Figure 7. Current characteristics under I3PSE

6. SIMULATIONS AND RESULTS

This section presents a simulated model of the new HSV proposed. Parameters used in the simulation are shown in Table 2. The control circuits of I3PSE and conventional two power source excitation (C2PSE) are also simulated, and the parameters used are shown in Table 3.

Table 2. *HSV simulation parameters*

Parameters	value
Total coil turns (tr)	450
Coil resistance (Ω)	4.5
Electromagnet initial air gap (mm)	0.6
Moving mass (g)	19
Flow coeficient	0.55
Supply pressure (MPa)	15
Electromagnet force characteristics	Figure 3
Electromagnet inductance characteristics	Figure 4

Table 3. *Control circuit parameters*

I3PSE circuit	
High voltage (V)	48
Low voltage (V)	2
Negative voltage (V)	-48
C2PSE circuit	
High voltage (V)	24
Negative voltage (V)	-24

6.1. Simulations and results of C2PSE

The excitation voltage can't be too high in a C2PSE circuit, because the continuous increase of the current will result in a higher temperature rise and a larger t_{doff}, so the

high voltage is determined as 24V and the negative voltage is determined as -24V. The results are shown in Figure 8.

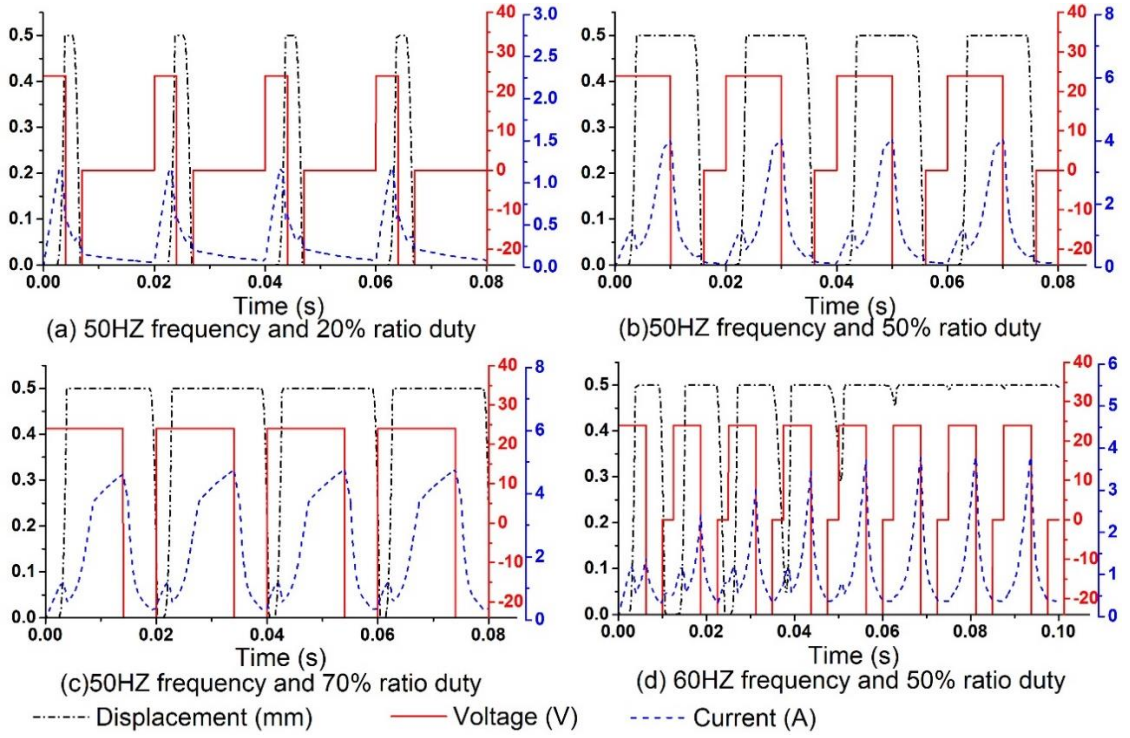

Figure 8. Dynamic performance of C2PSE method

The electromagnet totally engaged time (t_{on}) is 3.63ms, and totally disengaged time (t_{off}) is 5.63ms when the HSV operates at 50HZ frequency and 50% duty ratio. Adjusting the duty ratio of high voltage to 20% and 70%, we can see the HSV can work normally, but is close to the critical state. The electromagnet will probably not be engaged if the duty ratio is less than 20% and also will probably not be disengaged if the duty ratio is greater than 70%. When the driving frequency is increased to 60HZ, the HSV has been unable to switch successfully. Thus it may be known, the maximum controllable frequency of C2PSE method is 50HZ and adjusting duty cycle ranges of 20-70%.

From the curve shown in Figure 8, it can be seen that due to the continuous supply of high voltage in C2PSE circuits, the current continually increases after the electromagnet is engaged, which will lead to a large initial current at the moment of disengagement and a larger t_{doff}, as well as a higher temperature in the system which will have a negative influence on the service life of the HSV. Another issue is the difficulty of determining the optimal duration for the application of the negative voltage. Negative voltage is used to achieve fast unloading of the positive current. However, too short a duration will not disengage the electromagnet successfully, and too long a duration will cause a negative current. A large enough negative current will engage the electromagnet again and destroy the operational stability of the HSV.

6.2. Simulations and results of I3PSE

Figure 8 illustrates that the engaged current of the C2PSE electromagnet is 1.3A, and the disengaged current of electromagnet is 0.32A. In order to ensure the HSV is fully

switched, I_{on} is set as 1.5A, and I_{off} is set as 0.1A.

Figure 9 shows the dynamic performance of the C3PSE HSV in various conditions. Graph (a) of Figure 9 shows the performance with a control signal of 50HZ frequency and 50% duty ratio. In this situation, T_{on} reduces to 2.10ms and T_{off} reduces to 2.31ms, which is shortened by 42% and 59% respectively when compared to C2PSE. Pictures (b), (c), and (d) of Figure 9 show that the HSV can operate perfectly with control signals of 100HZ,150HZ and 200HZ. Pictures (e) and (f) of Figure 9 show that the critical duty ratio under a control signal of 100HZ are 20% and 80%.

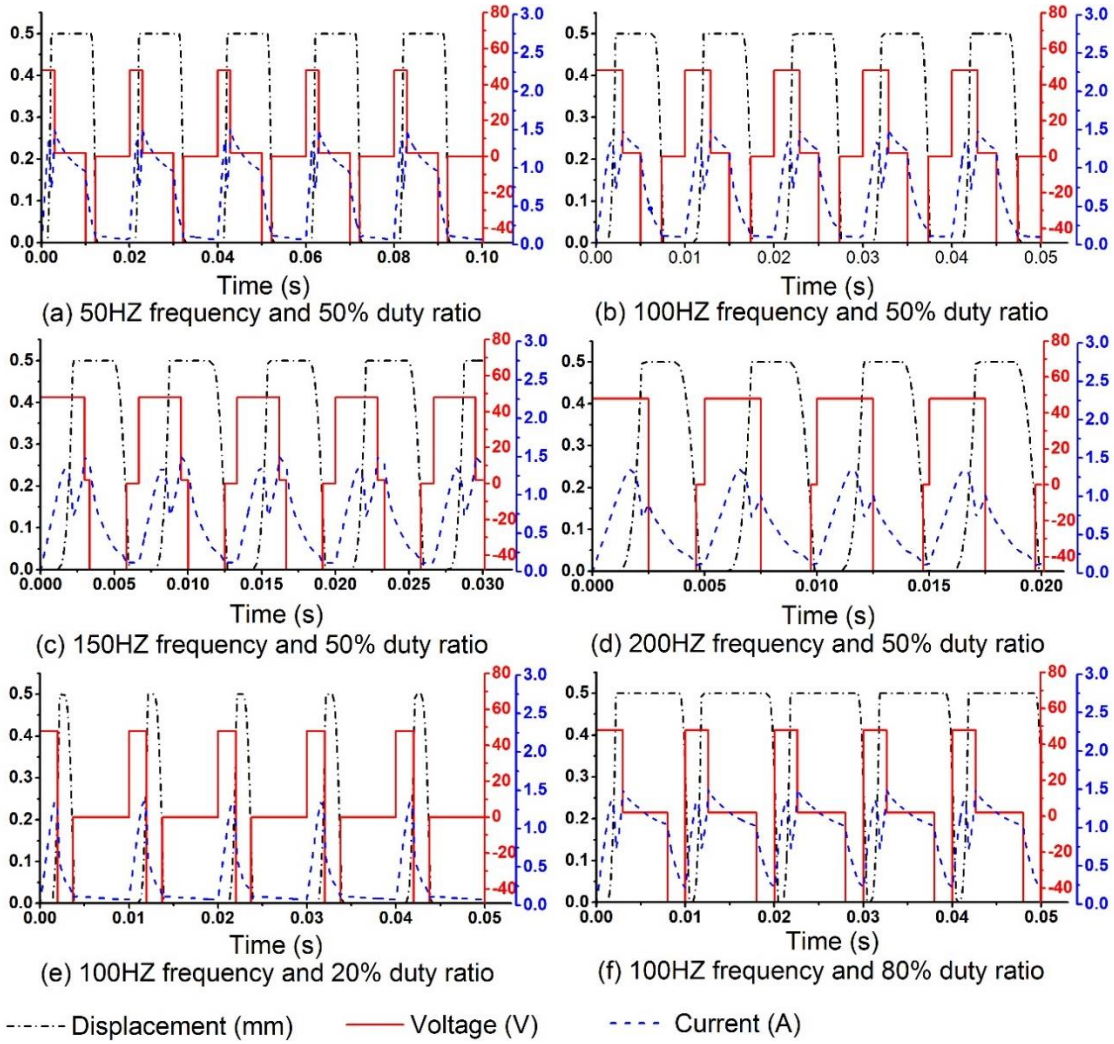

Figure 9. Dynamic performance of I3PSE

Altogether, Figure 9 shows that, with the control of I3PSE, electromagnet is completely engaged after the current reaches 1.5A. At this point, the high voltage source is disconnected and the current begins to decline. When current reduces to 0.1A, the electromagnet is fully disengaged and the negative voltage source is disconnected. Hence, this working mechanism effectively ensures that the HSV is fully switched, and at the same time, that the current is kept in an optimal state.

6.3. Simulations and results of I3PSE with changing resistance

It is easily understood that a lot of heat will be generated during valve operation. This will

have a great influence on coil resistance, and the changing coil resistance will affect the dynamic performance of the HSV. The dynamic performance of the HSV with changing coil resistance and I3PSE is discussed here. Simulation results are shown in Figure 10.

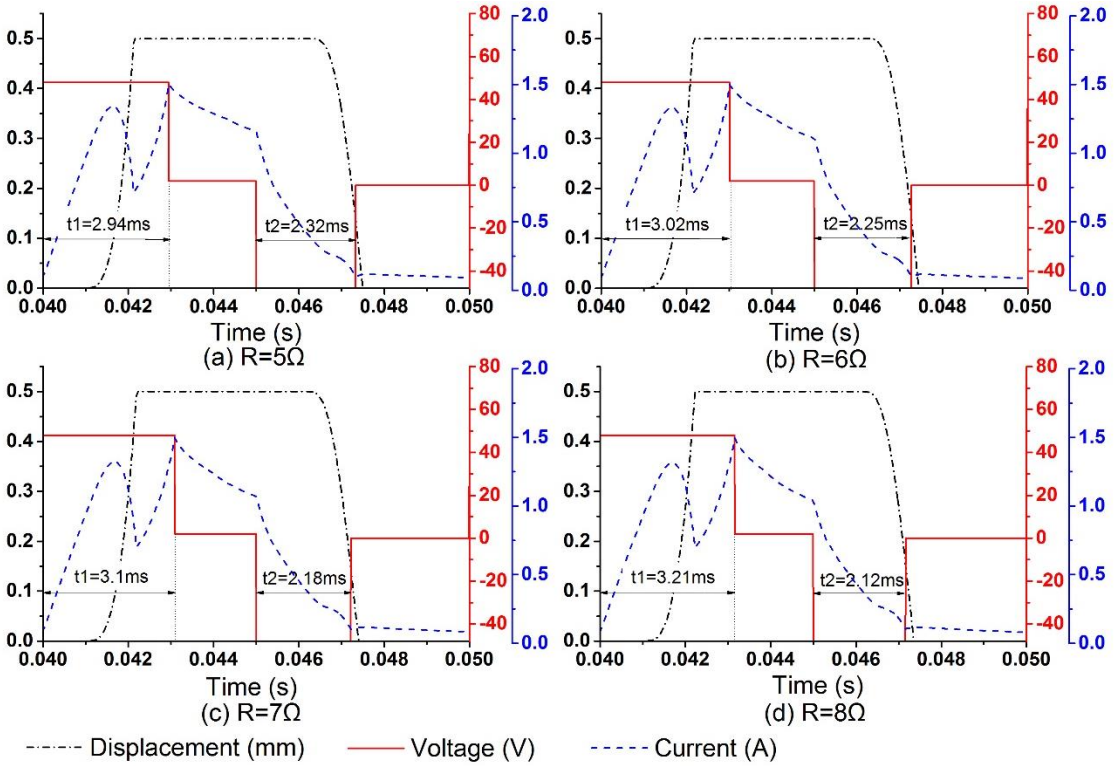

Figure 10. Dynamic performance with changing resistance

When the control signal is 50HZ and the duty ratio 50%, a resistance of 6, 7, and 8 Ohms causes the high voltage excitation time to increase from 2.94ms with 5 Ohms to 3.02ms, 3.10ms, and 3.21ms respectively. Likewise, the negative voltage excitation time decreases from 2.32ms for 5 Ohms to 2.25ms, 2.18ms, and 2.12ms respectively. However, even with the changing of voltage excitation time, T_{on} and T_{off} still remain as before: 2.10ms and 2.31ms respectively. This means that the dynamic characteristics of the HSV are not influenced by the changing resistance. The I3PSE will automatically adjust to changes in resistance so as to ensure the high performance of the HSV.

7. CONCLUSION

An intelligent three power source excitation method is put forward in this paper and its superiority to existing conventional two power source excitation methods is investigated by theoretical analysis and simulation analysis. The following conclusions are reached:

- Large initial current and higher voltage excitation are helpful to engage the electromagnet quickly.
- Small initial current and negative voltage excitation with reasonable duration are helpful to disengage the electromagnet quickly.
- The intelligent three power source excitation method can effectively improve the dynamic performance of high-speed on/off valves.
- The intelligent three power source excitation method functions irrespective of

changes of resistance and maintains the dynamic characteristics of the high-speed on/off valve.

REFERENCES

[1] Lee III, Y. 2006. Switching response improvement of a high speed On/Off solenoid valve by using a 3 power source type valve driving circuit. The Industrial Technology, ICIT, IEEE International Conference, December 2006, pp. 1823-1828

[2] Kong, X., & Li, S. 2014. Dynamic performance of high speed solenoid valve with parallel coils. Chinese Journal of Mechanical Engineering, 27(4), 816-821.

[3] Flor, M., Scheller, S., Heidenfelder, R., & AG, B. 2012. DIGITAL HYDRAULICS AT BOSCH REXROTH–A TREND EVOLVES TO REAL APPLICATIONS. The Fifth Workshop on Digital Fluid Power, October 24-25, Tampere, Finland, pp. 5-13.

[4] Passarini, L. C., & Nakajima, P. R. 2003. Development of a high-speed solenoid valve: an investigation of the importance of the armature mass on the dynamic response. Journal of the Brazilian Society of Mechanical Sciences and Engineering, 25(4), 329-335.

[5] Kajima, T., & Kawamura, Y. 1995. Development of a high-speed solenoid valve: investigation of solenoids. Industrial Electronics, IEEE Transactions on, 42(1), 1-8.

[6] Lv,F., Xiang,Z., Qi,Z. &. Cheng,Y. 2001. The development and dynamic response characteristics of high-speed and powerful micro displacement mechanism with giant magnetostrictive material. Mechanical Science and Technology, 20(2), 198-199.(in Chinese)

[7] Linjama, M., Laamanen, A. & Vilenius, M. 2003. Is it time for digital hydraulics? The Eighth Scandinavian International Conference on Fluid Power, May 7–9, Tampere, Finland, pp. 347–366.

OPTIMIZATION OF MOVING COIL ACTUATORS FOR DIGITAL DISPLACEMENT MACHINES

Christian Noergaard, Michael M. Bech, Daniel B. Roemer, Henrik C. Pedersen
Department of Energy Technology
Aalborg University
Pontoppidanstraede 111, 9220 Aalborg East, Denmark
E-mail: {chn,mmb,dbr,hcp}@et.aau.dk

ABSTRACT

This paper focuses on deriving an optimal moving coil actuator design, used as force producing element in hydraulic on/off valves for Digital Displacement machines. Different moving coil actuator geometry topologies (permanent magnet placement and magnetization direction) are optimized for actuating annular seat valves in a digital displacement machine. The optimization objectives are to the minimize the actuator power, the valve flow losses and the height of the actuator. Evaluation of the objective function involves static finite element simulation and simulation of an entire operation cycle using a single chamber Digital Displacement lumped parameter model. The optimization results shows that efficient operation is achievable using all of the proposed moving coil geometries, however some geometries require more space and actuator power. The most appealing of the optimized actuator designs requires approximately 20 W on average and may be realized in 20 mm $\times$ Ø 22.5 mm (height $\times$ diameter) for a 20 kW pressure chamber. The optimization is carried out using the multi-objective Generalized Differential Evolution optimization algorithm GDE3 which successfully handles constrained multi-objective non-smooth optimization problems.

KEYWORDS: Moving Coil Actuator, Digital Fluid Power, Digital Displacement Machines, Multi-Objective Optimization, Digital Hydraulic Valves

1 INTRODUCTION

Digital Displacement Machines (DDM's) are a promising new topology which relies on several pressure chambers being connected to a high- and low-pressure manifold through two on/off valves, controlled on a stroke-by-stroke basis. For the machine operation to be efficient, the valves must be fast switching, leakage free, induce a low pressure drop and the actuators must be efficient. To this end, direct electro-magnetic actuators are typically used in combination with an annular seat valve [1] in an integrated and compact mechatronic valve design. Annular seat valves features a large discharge area relative to the stroke length which, facilitates both fast switching and lower pressure losses during valve

flow (compared against spool valves). The most widespread electro-magnetic actuators in fluid power are solenoids, as they feature a simple and robust design. However, the transient performance suffers from an inherent magnetic diffusion delay and are non-linear in nature making them complicated to control. MC actuators possess some desirable features and characteristics e.g. rapid fast force response, typically they have linear current to force characteristics and they facilitate bi-directional force capability [2]. Still, MC actuators are not widespread in hydraulics, and the research published on their performance is limited. The nature of the DDM operation make great demands to the robustness of the actuators and valves, as they must be durable for large number cycles, and furthermore, the moving member is exposed to high and fluctuating pressure levels. To verify the simulation models used in the optimization and to test the mechanical robustness, a valve and actuator prototype has been produced based on the optimization results presented in this paper. The valve and actuator prototype are shown in Fig. 1. In the near future the valve prototype is to be installed in a hydraulic radial piston machine which has been modified to accommodate DDM operation.

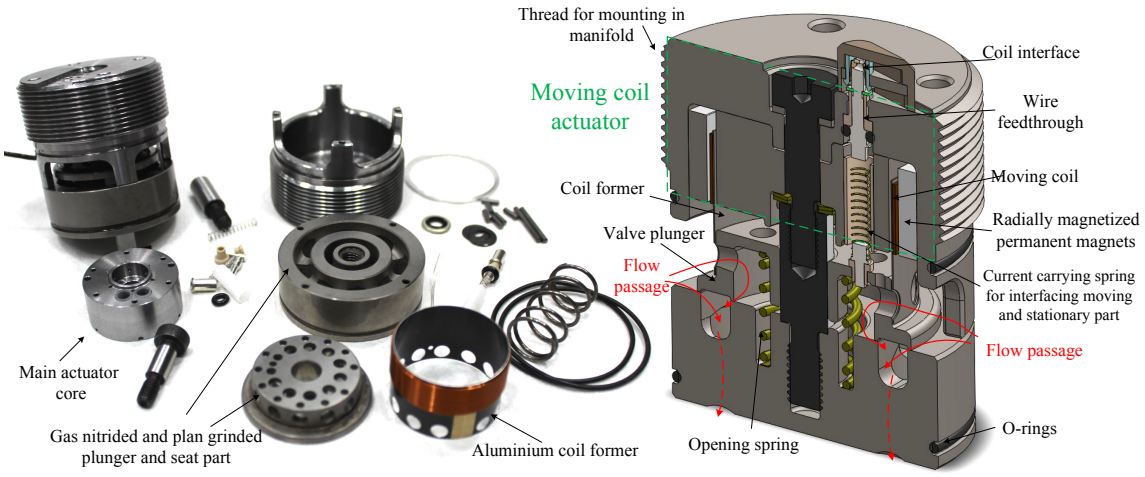

Figure 1: Illustrations of the valve and the actuator prototype.

To evaluate the performance of a MC actuator design, a number of simulation models are used, incl. static electro-magnetic finite-element analysis (FEA) and lumped parameter time dependent simulation, which facilitates simulation of entire DDM operation cycles. The FEA enables accurate estimates of important actuator parameters while the lumped model enables simulation of the machines performance when imposing different operating conditions.

The paper is organized as follows: Section 2 provides some background information on DDM's, electro-magnetic actuators, and the GDE3 optimization algorithm. Section 3 explains the mathematical models used to evaluate the optimization objectives. Section 4 presents how the optimization problem is formulated and Section 5 presents and discusses the optimization results. Finally, some conclusions are drawn based on the optimization results in Section 6.

2 BACKGROUND

The Digital Displacement technology was invented at the University of Edinburgh, and later spun off in the company Artemis Intelligent Power Ltd. The first patent for the Digital Displacement pump was filed in 1989 [3], followed by the Digital Displacement motor in 1990 [4]. In 2011 Mitsubishi Heavy Industries announced plans for testing a wind turbine in the 7 MW class where the drivetrain is based on the Artemis technology, but detailed information is still not published [5]. Although no detailed information is available regarding valve performance or design specifications, the valves installed in the machine appear to be direct actuated seat valves, with a variable reluctance actuator (solenoid) as the force producing element, based on graphics included in the patent applications [6, 7, 8].

Several different electro-magnetic actuator topologies exist which may be utilized as the force producing element in the fast switching valves of DDM's. Feasible topologies include variable reluctance actuators (solenoids) [9], polarized variable reluctance actuators [10], moving magnet actuators [11], and MC actuators (voice coils) [12]. However, since all of these electro-magnetic actuator topologies are feasible for use as DDM valve actuator, it is not apparent which topology is the most suited for the application. In [2] the suitability of different actuator topologies applied in DDM's is analysed revealing the moving magnet actuator to exhibit superior performance characteristics.

Differential Evolution (DE) algorithms are a relatively new class of Evolutionary Algorithms. It has gained popularity since it has proven to be capable of solving difficult multi-objective optimization problems successfully. The DE algorithm, which GDE is an extension of, was introduced by Storn and Price in 1995 [13]. The key benefits of the DE algorithm, when first introduced, were its simplicity, efficiency and a low number of optimization control variables. The algorithm used to carry out the optimization is referred to as Generalized Differential Evolution 3 (GDE3). GDE3 improves earlier GDE versions in the case of multiple objectives by giving a better distributed solution [14]. The GDE3 uses Pareto optimization i.e. the algorithm returns a set of solutions which are non-dominated by any other solution. The GDE3 algorithm uses weak-constraint domination which means the degree of constraint violation should be expressed in the constraint functions. This accelerates the convergence of the algorithm since designs with a high degree of constraint violation is opted out through comparison and pruning schemes [15].

3 MODEL FRAMEWORK

The model framework comprises two distinct models which are executed sequentially. Firstly, a static electro-magnetic FEA is carried out based on a specified actuator geometry, and secondly a lumped parameter DDM simulation model is executed. The FEA enables calculation of important actuator parameters based on the solution of the initial magnetic field induced by the permanent magnets of the MC actuator. The lumped parameter DDM model simulates the entire operation cycle using the parameters obtained from the FEA, some DDM parameters and some predetermined DDM operating conditions. The following sub-sections describe the main details of both simulation models.

3.1 Static Electro-Magnetic Finite-Element-Analysis

The problem is modelled as an axi-symmetric problem since the actuator geometry primary is primarily rotation-symmetric. The model is simulated using the open-source software FEMM v.4.2 scripted through Matlab. The software returns a solution to the initial magnetic field generated by the permanent magnets which satisfies both expressions of Eq. 1 via a magnetic vector potential approach [16].

$$\nabla \cdot \overrightarrow{B} = 0 \qquad \nabla \times \overrightarrow{H} = \overrightarrow{J} \tag{1}$$

where $\overrightarrow{H}$ is the field intensity and $\overrightarrow{B}$ is the flux density. The field intensity and flux density are related through the permeability μ. The advantage of solving for the magnetic vector potential is that all the conditions to be satisfied can be combined into a single equation. By rewriting the flux density as $\overrightarrow{B} = \nabla \times \overrightarrow{A}$, where $\overrightarrow{A}$ is the magnetic vector potential, both expressions in Eq. 1 can be combined to Eq. 2. For the general 3-D case $\overrightarrow{A}$ is a vector with three components. However, in the axi-symmetric case two of these components are zero which reduces the computational effort needed to solve the model significantly.

$$\nabla \times \left(\frac{1}{\mu\left(\overrightarrow{B}\right)} \nabla \times \overrightarrow{A} \right) = \overrightarrow{J} \tag{2}$$

To solve Eq. 2 magnetic and electrical properties must be specified for all materials used in the model. The materials properties used in the model are given in Tab. 1. Fig. 2 shows measured hysteresis loops for low carbon steel used as core material.

Table 1: Magnetic and electrical properties of materials used in static electro-magnetic FEA.

Material	**BH-relation [A/m,T]**	**Conductivity [S/m]**
Air	$\mu_r = 1$	0
Copper (@100°C)	$\mu_r = 1$	$4.55 \cdot 10^7$
Magnet (NeFeB 35MGOe)	$\mu_r = 1.045$, $H_c = 9.15 \cdot 10^5$	0 (shell magnets)
Low carbon steel (11SMnPb30)	see Fig. 2	$5.8 \cdot 10^6$
Cast steel	Selected points:*(H,B)*={(0,0)(1.15k,1.11), (1.73k,1.27), (4.08k,1.53),(16.93k,1.87)}	$6.20 \cdot 10^6$

Based on the (specified) actuator geometry input, the regions are defined with the appropriate properties. Additional to the regions given by the actuator geometry a surrounding air domain is included with asymptotic boundary conditions to emulate an open space. Each region of the solution domain is meshed using the software's auto-mesh method which typically results in a mesh consisting of 2500 to 5000 triangular elements. The initial magnetic flux distribution, using the geometry of the derived optimal design used for the valve prototype, is shown in Fig. 4 along with the generated mesh.

The average total field intensity at the core steel boundary adjacent to the air gap and the average radial flux density in the air gap, indicated in Fig. 4, are extracted from the FEA results to calculate the MC actuator parameters. These quantities, along with an estimate of static inductance, are used in the dynamic lumped actuator model explained in Section 3.2.

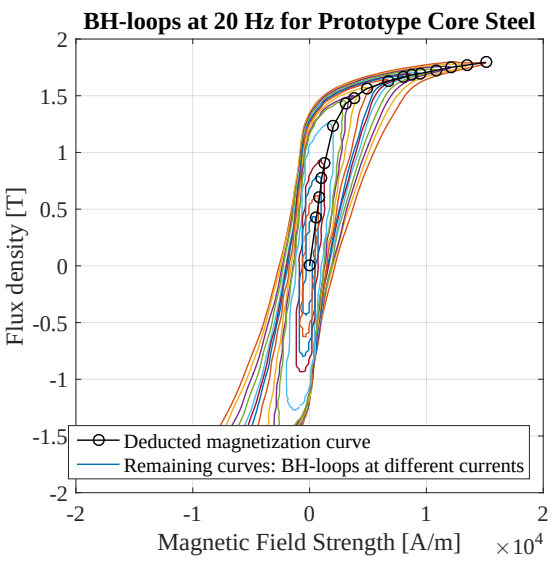

Figure 2: Measured hysteresis BH-curves, using the approach given in [17], for the steel used in the prototype with the deducted BH-curve used in the FEA.

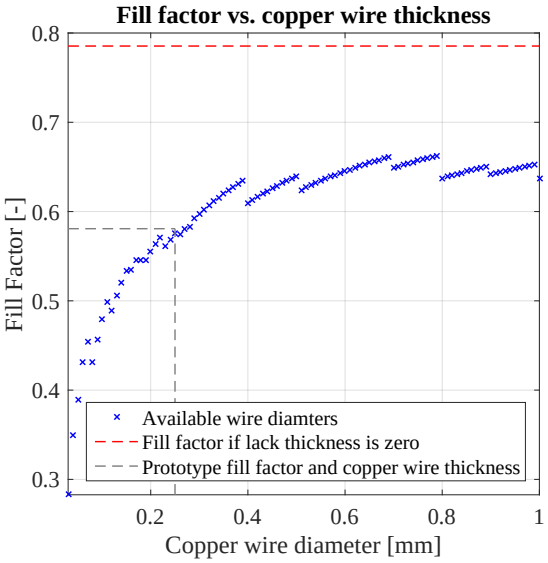

Figure 3: Achievable fill factor as a function of copper wire diameter. Data based on available wires at voice coil manufacturer Nikkei Electric Co., LTD.

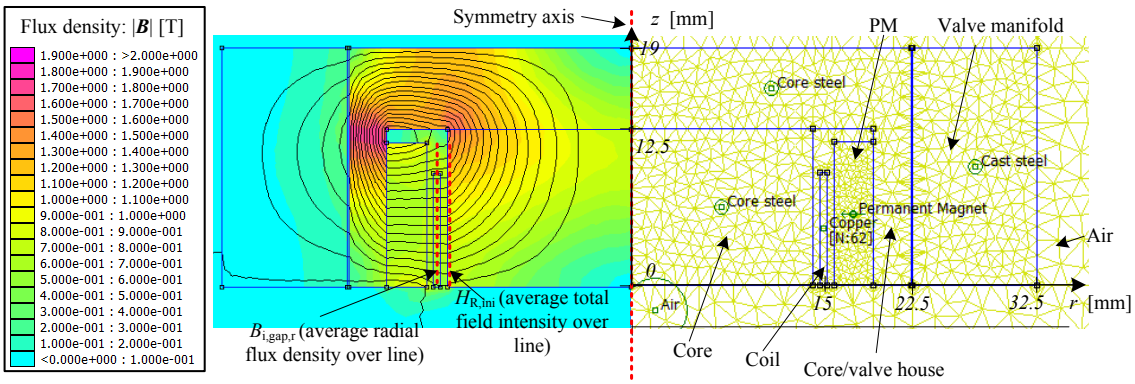

Figure 4: Auto generated mesh consisting of 3238 triangular elements and the initial magnetic flux distribution generated by the permanent magnets for the prototype actuator.

The coil fill factor used in the FEA and optimization is incorporated as a discrete function of the wire thickness as shown in Fig. 3. This is done to account for the poor achievable fill factor when using thin wires. The data is based on the available wire thickness (and resulting insulation lack layer) from the coil manufacturer used for the valve prototype.

3.2 Lumped Parameter Digital Displacement Machine Simulation Model

A lumped parameter model for a single pressure chamber of a DDM has been constructed which facilitates simulation of entire machine cycles under various operating conditions. The model comprises several sub-models, which each seek to describe specific energy exchanges that happen within a DDM. The sub-models of the DDM simulation model interact as shown in Fig. 5. The driving input is the movement of the shaft from which the movement of the piston in the pressure chamber is obtained. By imposing appropriate initial conditions and manipulating the valve control signals at appropriate times, according to the piston position, the model facilitates simulation of all three operation cycles i.e.

motoring, pumping and idling. However for the optimization problem at hand only the motoring cycle is used. During simulation, several internal transient states of the DDM are solved e.g. pressures, flows, plunger dynamics, actuator currents etc. From analysis of the transient states important measures on performance and efficiency can be evaluated.

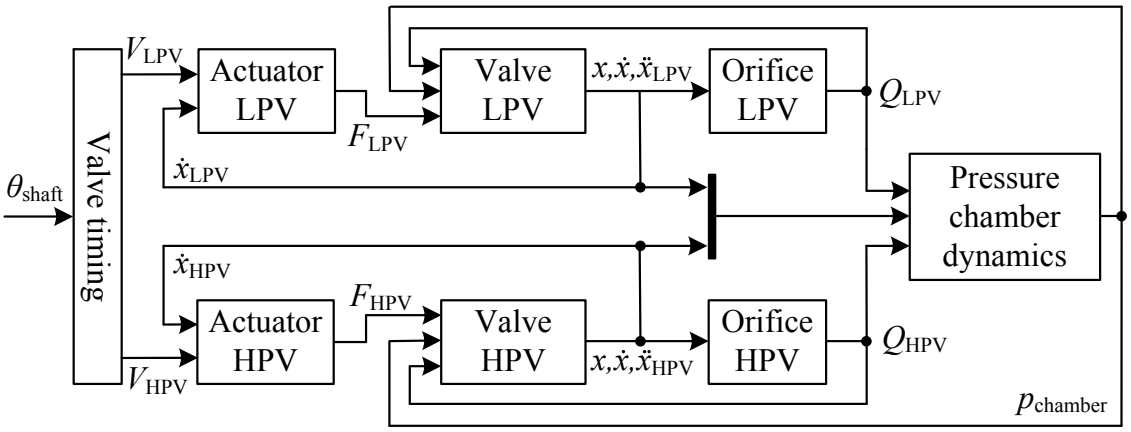

Figure 5: Block diagram showing how the different sub-models of the lumped parameter simulation model interacts.

This section focuses on the sub-models that has dominating influence on the valve and actuator related losses. These sub-models are a lumped MC actuator model, a valve dynamics model, and a flow restriction model (flow vs- pressure characteristics).

Moving Coil Lumped Parameter Actuator Model

The MC electrical dynamics is modelled using an analytical transformer model with an air gap and a primary- and secondary coil, see Fig. 8. The primary coil is the MC of the actuator and the secondary coil is a modelling element which accounts for the eddy currents generated in the core upon a change in flux density. This approach was suggested in [18], and in [19] a method to extend the approach to include non-linear magnetic diffusion effects was presented by the authors. The secondary coil parameters are based on an estimation of the magnetic field depth as a function of time [20]. The diffusion depth is defined as illustrated in Fig. 6 and Eq. 3 gives an expression for the magnetic diffusion depth.

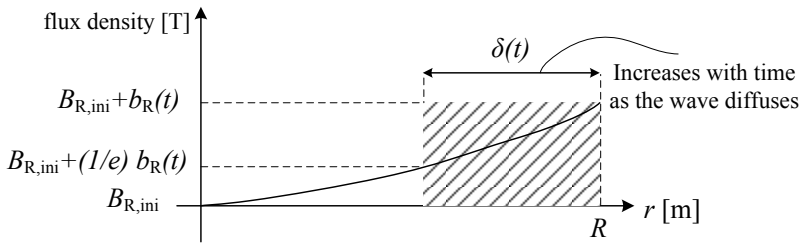

Figure 6: Illustration of the rectangular profile approximation. The radial integral of a diffusing wave is approximated by the flux density $B_{R,ini}$ at the boundary of the inner yoke material and the characteristic penetration depth $\delta(t)$.

$$\delta(t) = \delta^{(0)}(t) + \frac{\left(\delta^{(0)}(t)\right)^2}{6R} \text{ where : } \delta^{(0)}(t) = \sqrt{\frac{2\int_0^t h_{\mathrm{R}}(t)dt}{\sigma b_{\mathrm{R}}(t)}} \tag{3}$$

R is the inner core radius, h_{R} and b_{R} are the magnetic field strength and flux density change, due to coil current transients, at the boundary of the inner core (see Fig. 4). h_{R} and b_{R} are related through the obtained BH-curve data of Fig. 2, with the offset $H_{\mathrm{R,ini}}$ and $B_{\mathrm{R,ini}}$ respectively. By considering the magnetic path of the flux generated by the current as a number of reluctances connected in series, h_{R} may be calculated as [19].

$$h_{\mathrm{R}} = \frac{Ni_{\mathrm{coil}}}{l_{avg}} - \frac{Ni_{\mathrm{eddy}}}{l_{avg}} - \frac{b_{\mathrm{gap,r}} l_{\mathrm{gap}}}{l_{\mathrm{avg}}}\mu_0 - \frac{b_{\mathrm{PM}} l_{\mathrm{PM}}}{l_{\mathrm{avg}}\mu_0\mu_{\mathrm{r,PM}}} \tag{4}$$

The flux density change $b_{\mathrm{gap,r}}$ and b_{PM}, due to the coil current, is calculated based on an estimate of the flux generated by the coil current. The flux is calculated based on the diffusion depth, and the calculated flux density at the boundary of the inner core as (rectangular profile approximation):

$$\phi_{\mathrm{coil}} = A_{\mathrm{z}}\left(\delta(t)\right) b_{\mathrm{R}} \tag{5}$$

A_{z} ((t)) is the axial cross sectional area the flux passes through which varies with the diffusion depth, see Fig. 7. $b_{\mathrm{gap,r}}$ and b_{PM} are calculated from the coil flux and their cross sectional areas normal to the flux.

$$b_{\mathrm{gap}} = \frac{\phi_{\mathrm{coil}}}{A_{\mathrm{r,gap}}} \qquad b_{\mathrm{PM}} = \frac{\phi_{\mathrm{coil}}}{A_{\mathrm{r,PM}}} \tag{6}$$

$A_{\mathrm{r,gap}}$ and $A_{\mathrm{r,PM}}$ are the radial cross sectional areas which the flux passes through. Based on the diffusion depth, parameters of the two winding transformer model is continuously estimated. The eddy current resistance R_{eddy} and the eddy current paths leakage inductance L_{eddy} are calculated as:

$$R_{\mathrm{eddy}} = \frac{l_{\mathrm{eddy}}}{h_{\mathrm{coil}}\delta(t)\sigma} \qquad L_{\mathrm{eddy}} = N^2 \frac{\mu_0\mu_r A_{\mathrm{z}}\delta(t)}{h_{\mathrm{coil}}} \tag{7}$$

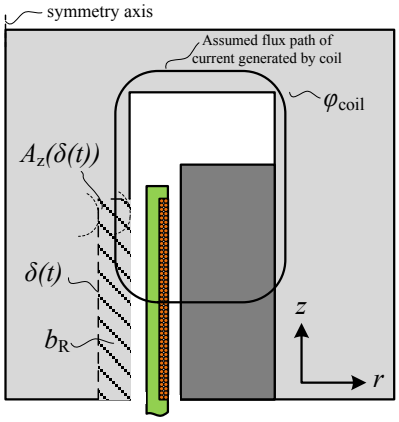

Figure 7: Sketch showing the assumed flux path of the flux generated by the coil current.

Fig. 8 illustrates the transformer model applied to the MC actuator and the equivalent magnetic circuit diagram. The governing equations, derived from the equivalent magnetic

circuit diagram are given in Eq. 8 and 9 where the shorted turn winding parameters have been referred to the coil winding:

$$v_{\text{coil}} = R_{\text{coil}} i_{\text{coil}} + (M + L_{\text{coil}}) \frac{di_{\text{coil}}}{dt} - M \frac{d(i_{\text{eddy}}/N)}{dt} - \underbrace{\dot{x} l_{\text{avg,wire}} N B_{\text{i,gap,r}}}_{\varepsilon} \tag{8}$$

$$0 = N^2 R_{\text{eddy}}(t)(i_{\text{eddy}}/N) - M \frac{di_{\text{coil}}}{dt} + (M + L_{\text{eddy}}(t)) \frac{d(i_{\text{eddy}}/N)}{dt} \tag{9}$$

where v_{coil} is the coil voltage, R_{coil} is the coil resistance (incl. current carrying spring- and wire feedthrough resistance), M is the mutual inductance linking both the main eddy current path and the coil, L_{coil} and L_{coil} is the leakage inductance of the coil and the eddy current path respectively, N is the number of coil turns, $\dot{x}$ is the velocity of the coil, $l_{\text{avg,wire}}$ is the average length of a single wire turn, i_{coil} and i_{eddy} is the coil current and the eddy current magnitude respectively. The generated magnetic Lorentz force is calculated as:

$$F_{\text{act}} = i_{\text{coil}} B_{\text{i,gap,r}} l_{\text{avg,wire}} N \tag{10}$$

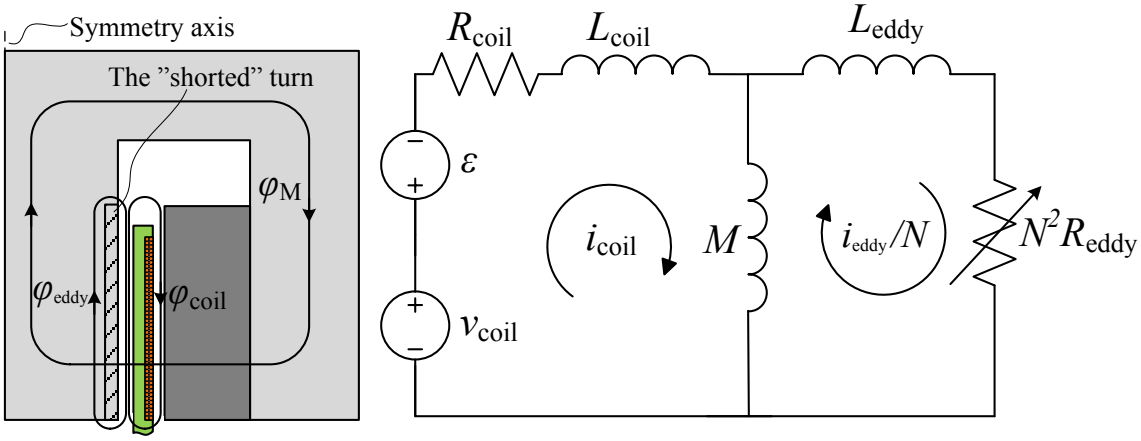

Figure 8: Transformer model applied to MC actuator and equivalent magnetic circuit diagram where the shorted turn parameters are referred to the coil side.

Modelling of Valve Plunger Dynamics

When leading flow through semi-opened valves the flow losses are considerable. In addition, the optimization results reveal the that the actuators should be relatively weak actuators. This establishes demands to the accuracy of the models since the valve movement is likely to be dominated by the flow- and movement induced fluid forces acting on the plunger during switching. While the models must give accurate and reliable characteristics they should still be computational efficient to keep the computational burden at a manageable level.

Since only the actuator of the valve is to be optimized in this design step, the plunger geometry is fixed. The flow and movement dependent parameters are obtained through CFD simulations, in [21] and are used in the lumped parameter model. The force equilibrium may be written as:

$$\ddot{x} = \frac{1}{m_{\text{moving}}} \left(F_{\text{mov}}(x, \dot{x}, \ddot{x}) + F_{\text{fluid}}(x, Q, p_{\text{c}}) + F_{\text{act}}(i_{\text{coil}}) + F_{\text{spring}}(x) \right) \tag{11}$$

Where F_{mov} is the movement-induced fluid force, F_{fluid} is the flow- and pressure-induced fluid force, F_{act} is the electro-magnetic actuator force and $F_{\text{spring}}$is the opening spring force. In addition to the force contributions shown in Eq. 11 a suitable end-stop model have been implemented which limits the plunger position within the confines of the actuator stroke-length and resets the plunger acceleration and velocity accordingly.

Movement-Induced Fluid Force Model

The movement-induced fluid force arises as the valve moving member is forced through the surrounding fluid whereby the surrounding fluid is forced to displace. This force contribution is often neglected in non-CFD models due to the complexity of describing this force for general valve geometries. For fast switching valves with large shadow areas this force contribution may be significant [22, 23].

Generally, the force exerted on a rigid body moving through a fluid domain is governed by the Navier-Stokes equation. Analytical solutions to this problem is limited to simple cases, they may however still be useful for gaining insight to the governing characteristics for more complicated geometries. The model is derived based on an analytic solution to the Navier-Stokes equation for a sphere moving in a linear path through an otherwise stationary fluid [24]. The used model, proposed in [21] is shown in Eq. 12 where the parameters k_{a}, k_{v}, k_{d}, k_{h} are determined using CFD analysis.

$$F_{mov} = \underbrace{k_{\text{a}}(x)\ddot{x}}_{Added\,mass\,term} - \underbrace{k_{\text{v}}(x)\dot{x}}_{Viscous\,term} - \underbrace{k_{\text{d}}|\dot{x}|\dot{x}}_{Drag\,term} - \underbrace{k_{\text{h}}\int_0^t \frac{d\dot{x}}{d\tau}\frac{1}{\sqrt{t-\tau}}d\tau}_{History\,term} \tag{12}$$

In order to simulate the movement-induced fluid forces using Eq. (12), the history term must be -reformulated to a form appropriate for discrete time domain simulation. Assuming piece-wise constant acceleration, the history term may be approximated using:

$$k_{\text{h}}\int_0^t \frac{d\dot{x}}{d\tau}\frac{1}{\sqrt{t-\tau}}d\tau \tag{13}$$
$$= 2k_{\text{h}}\left(\left.\frac{d\dot{x}}{dt}\right|_{T_1}(\sqrt{t}-\sqrt{t-T_1}) + \left.\frac{d\dot{x}}{dt}\right|_{T_2}(\sqrt{t-T_1}-\sqrt{t-T_2}) + \ldots + \left.\frac{d\dot{x}}{dt}\right|_{T_{\text{f}}}(\sqrt{t-T_{\text{f}-1}}-\sqrt{\text{t}-\text{T}_{\text{f}}})\right)$$

Where sampling times are denoted $t = \{T_1, T_2, \ldots, T_{\text{f}}\}$. The above expression increases in size during simulation, and all previous accelerations and the corresponding time stamps must be assessable during simulation. Evaluation of the history term is relatively time consuming, especially after some time as the number of samples increases. To circumvent this and keep the computational burden at a manageable level, the history term is only evaluated during valve movement, and the number of sampling times in the evaluation is kept at a fixed and manageable number. More details on derivation of the movement-induced fluid forces and model verification are presented in [21].

Flow and Pressure Induced Forces

The flow force F_{flow} is modelled as:

$$F_{\text{flow}} = k_{\text{f1}}(x)Q^2 + k_{\text{f2}}(x)Q \tag{14}$$

Where k_{f1} and k_{f2} are functions of the valve plunger position fitted through CFD analysis (details in [21]). When the valve is closed $(x = 0)$, a switched condition is used to account for the force induced by the pressure difference across the valve:

$$F_{\text{fluid}} = \begin{cases} F_{\text{flow}} & x > 0 \\ A_s \Delta p & x = 0 \end{cases} \tag{15}$$

Where A_s is the axial shadow area of the valve plunger and Δp is the pressure difference across the valve.

Flow vs. Pressure Loss Model

The pressure loss during valve flow must be modelled with a relatively large degree of accuracy since the associated energy loss is significant. The used model aims to model the relation between flow and pressure for a wide range of flow rates and for complicated valve geometries. The used model was proposed in [25] and showed good accuracy for a wide range of flow rates:

$$\Delta p = k_{p1}(x)Q^2 + k_{p2}(x)Q \tag{16}$$

where k_{p1} and k_{p2} are functions of the valve position determined through a number of CFD simulations.

3.3 Objective Function Evaluation

All of the objectives used in the optimization are calculated using the described simulation models. Depending on the specified design vector, some constraints could be violated during execution of the static FEA model. In this case, the lumped parameter simulation model is not executed to reduce the computational time. Similarly, execution of the lumped parameter simulation model is omitted if the actuator force at steady current does not exceed the opposing spring force the actuator must overcome to initiate movement. Figure 9 illustrates how the objective function is evaluated. The bold face letters represents the constraint and objective functions, which are additional explained in Section 4.

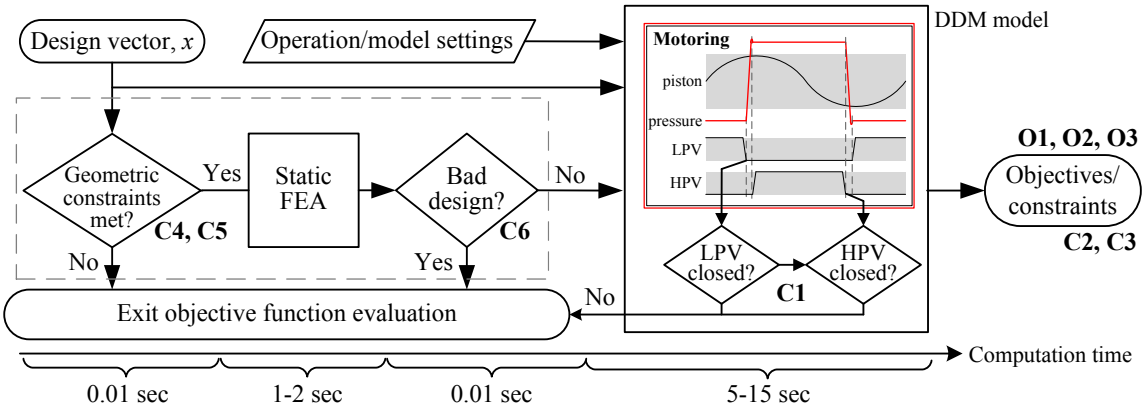

Figure 9: Flow chart illustrating how the objective function is evaluated.

In addition to the efforts made to reduce the computational time several designs are evaluated simultaneously. This is realized by using a workstation PC with 16 GB ram and 8 cores, each optimized for running dual threads, leaving 16 threads at disposal for parallel processing of the objective function.

3.4 Simulation Example of Model

Fig. 10 shows a simulation example of the lumped parameter DDM model, using the optimized prototype design and the operating conditions given in Tab. 2. The valves are actively closed by a rapid response of the MC actuator while the valve opening occurs passively due to pressure and spring forces.

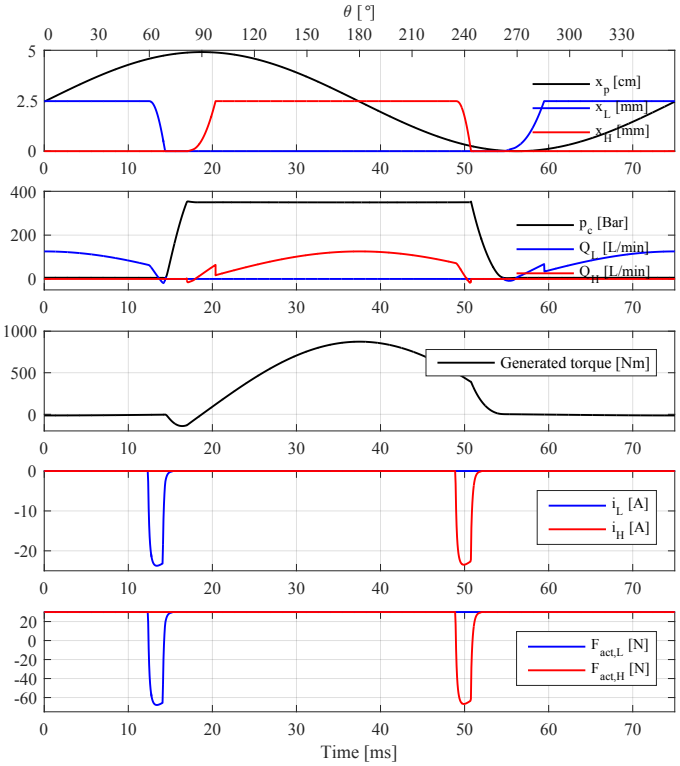

DDM parameters	**Value**
Piston stroke length	49 mm
Piston bore Ø	36mm
Cylinder dead volume	62 CC
Displacement[1]	50 CC/rev
Prototype valve par.	
Stroke length, l_{stroke}	2.5 mm
Shadow area, A_s	4.9 cm^2
spring preload, L/H	(30/30)N
Coil Layers	2
Operating cond.	
Shaft speed	800 RPM
Supply pressure, L/H	(5/350) bar
Supply voltage	80 V
Performance data	
Avg. act. power, L/H	(21/21)W
Avg. flow loss, L/H	(25/25)W
L/H closing time	(2.1/1.9) ms
L/H opening time	(3.1/3.3) ms
Avg. power[1]	22 kW
Cycle efficiency[2]	99.4%

Figure 10 & Table 2: Simulation example using the prototype actuator design and DDM parameters and operation conditions given in the table.

4 FORMULATION OF THE OPTIMIZATION PROBLEM

The valves should be fast switching to minimize the flow when the valves are semi-open. But how much actuator power should be invested to minimize the combined valve and actuator losses? In addition, typically, several valves and actuators are integrated in a compact DDM design. Therefore, size and compactness of the actuators should also be emphasized in the design. To this end, the used objectives to be minimized are:

O1 Avg. actuator power: $P_{\text{act}} = \left(\int_0^{T_{\text{cycle}}} v_{\text{L}}\, i_{\text{L}}\, dt + \int_0^{T_{\text{cycle}}} v_{\text{H}}\, i_{\text{H}}\, dt \right) \Big/ T_{\text{cycle}}$

O2 Core height: h_{core} (see Fig. 12).

O3 Avg. flow losses: $P_{\text{flow}} = \left(\int_0^{T_{\text{cycle}}} \Delta p_{\text{L}}\, Q_{\text{L}}\, dt + \int_0^{T_{\text{cycle}}} \Delta p_{\text{H}}\, Q_{\text{H}}\, dt \right) \Big/ T_{\text{cycle}}$

[2]Only valve losses considered.
[1]Only one chamber considered.

Where T_{cycle} is the cycle duration, v_{L}, v_{H}, i_{L} and i_{H} are the actuator voltages and currents, Δp_{L}, Δp_{H}, Q_{L} and Q_{H} are the valve pressure drops and flows. By minimizing these three objectives an efficient motoring operation is ensured, along with an efficient and compact actuator design.

The permanent magnet (PM) could be placed in several different positions and magnetized in different directions. The different geometries or permanent magnet placements that have been explored are shown in Fig. 11. Each of the four geometries represents an optimized design point (highlighted in Fig. 13). The PM of design **A** and **B** are radially magnetized, whereas for design **C** and **D** the PM is axially magnetized.

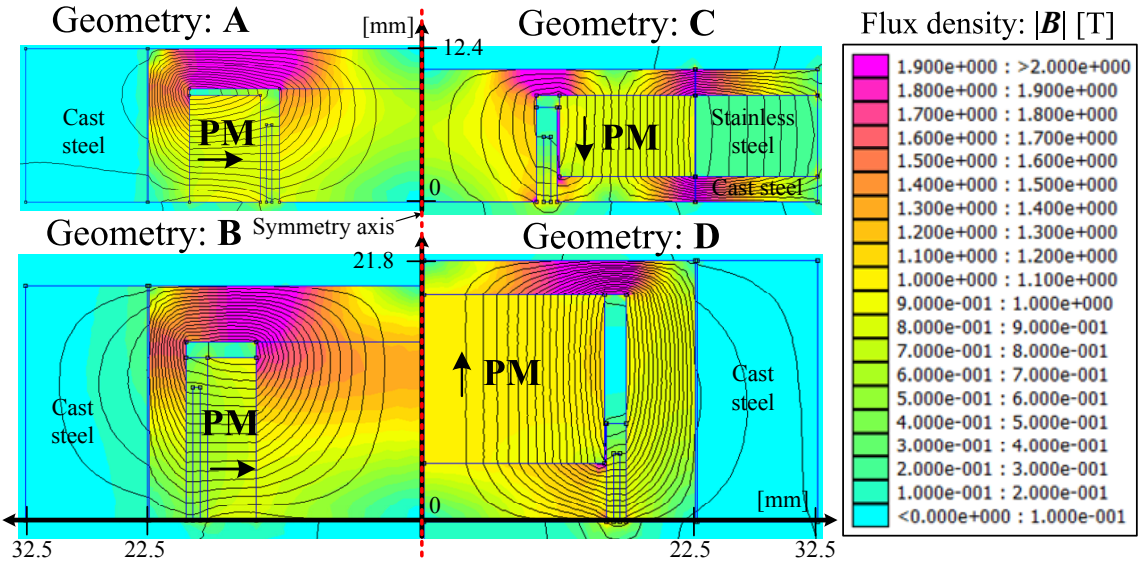

Figure 11: Overview of the different geometries that are explored in the paper. Each design is optimized and represents the highlighted points of Fig. 13.

In connection, not only performance should be considered, the design topology should also be easy to manufacture and assemble. When using axial magnetization the permanent magnet can be realized in a one solid which easily can be incorporated in the design. The radial magnetization is realized by a number of cylinder ring section shaped shell magnets, each individually magnetized (to realize sufficient flux levels during magnetization). Also, geometry **C** has a ring of stainless steel incorporated in the outer cast iron to avoid magnetic short-circuiting in the outer cast. Figure 12 shows the parametrization of geometry **C** (with a two coil layer winding), and Tab. 3 gives the design variables.

In addition to the geometry related design variables, four control related design variables are used for defining a simple modulation. The MC is excited with voltage pulses of constant amplitude. One design variable is used to determine the voltage pulse start shaft angle, and one design variable determines the duration of the corresponding voltage pulse, for each valve (see Tab. 3).

Lastly, constraint functions must be formulated. The constraint functions are formulated to express the violation degree of each constraint function to benefit from the weak constraint domination scheme of GDE3. A number of geometry related constraint functions are formulated for each of the geometries that have been tested. Additionally, constraints are used for designs that are obviously bad or simulation of the lumped parameter model did not finish successfully. The constraints used for geometry A are:

C1 Success indicator: Depending on the design point, the operation cycle may only be

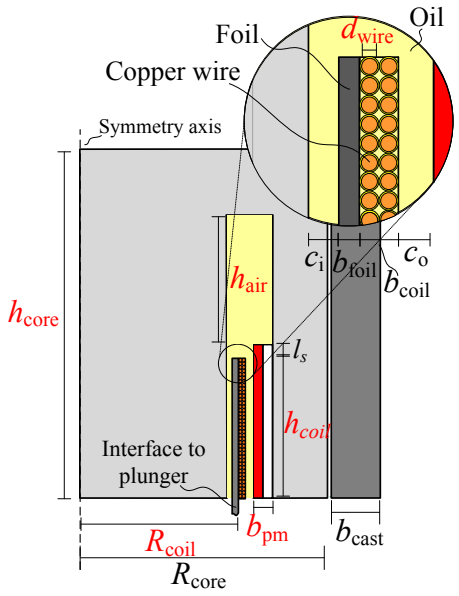

Design var.	Description	Bounds
h_{core}	Height of act. core	[0.1,1] mm
R_{coil}	Radius of coil	[5,20]mm
b_{PM}	Thickness of PM	[0,10]mm
h_{coil}	Height of coil	[3,50]mm
d_{wire}	Copper wire thickness	[0.1,1]mm
h_{air}	Height of gap above PM	[0,10]mm
V_{supply}	Supply voltage for acts.	[5,300]V
θ_L	Voltage step angle	[50,90]rad
θ_H	Voltage step angle	[230,270]rad
$\Delta\theta_L$,$\Delta\theta_H$	Voltage step duration	[1,15]rad
Geo Consts.	**Description**	**Value**
c_i,c_o	Inner and outer clearance	(0.4,0.5)mm
R_{core}	outer core radius	22.5 mm
b_{cast}	outer cast thickness	10 mm
b_{foil}	former thickness	0.2 mm

Figure 12 & Table 3: Parametrization of geometry A. The red parameters are design variables and the black parameters constants. The Table gives all design variables for geometry A along with some geometrical constants.

completed partially (too weak actuators, bad timing, etc). The violation degree is set based on the simulation time at which the operation cycle failed.

C2 Efficiency out of range: an cycle efficiency in the range 75-100 % is expected. The constraint is unsatisfied if the evaluated efficiency lies out of that range.

C3 Energy utilization constraint: the output energy should be at least half of the ideal input energy.

C4 Geometry constraint: coil height must be smaller than actuator core height.

C5 Geometry constraint: outer radius of PM must be smaller than outer core radius.

C6 Bad design indicator: magnetic force in steady state at voltage level V_{supply} must be greater than the opposing spring force.

5 OPTIMIZATION RESULTS

This section shows the optimization results obtained while using the different MC actuator geometry topologies. Fig. 13 shows the achieved Pareto fronts using the four proposed geometries while Tab. 4 gives the problem infos and solution statistics. The geometry and initial flux distribution for the highlighted design points are shown in Fig. 4 and 11. For geometry A, B and C each design point of the population are non-dominated by any other design point i.e. Pareto optimial, whereas only 30 % of the population for geometry D are non-dominated. Common for all the different geometries is the average flow loss which only varies vaguely for the majority of the design points (between 50 W and 55 W), therefore **O3** may be disregarded in the decision making process when selecting a design point. This indicates that a similar actuator response is achievable using each of the four geometries, and therefore only **O1** vs. **O2** is shown separately. A trade off exist between the average actuator power and actuator core height. Naturally, designs with small actuator height demands larger actuator power and vice-versa. The average actuator power varies for most designs in the range 40-500 W while the actuator heights for most design are in the range 8-40 mm. It is worth noticing that, if a too small or inefficient actuator design is

used, the actuator power quickly exceeds the flow losses by several factors. The actuator height using geometry D is generally larger than for the remaining geometries. The results show similar Parato front's for geometry A and B.

The actuator prototype design is given by:

$$\vec{x} = (d_{\text{wire}}, h_{\text{coil}}, R, b_{\text{pm}}, h_{\text{core}}, h_{\text{air}}, V_{\text{supply}}, \theta_{\text{cl,L}}, \theta_{\text{cl,H}}, \Delta\theta_{\text{cl,L}}, \Delta\theta_{\text{cl,H}})$$

is

$$\vec{x} = (0.25\text{ mm}, 9.0\text{ mm}, 15.0\text{ mm}, 3.1\text{ mm}, 1\text{ mm}, 19.0\text{ mm}, 85\text{ V}, 59.2\text{ deg}, 234.8\text{deg}, 8.4\text{ deg}, 8.7\text{ deg})$$

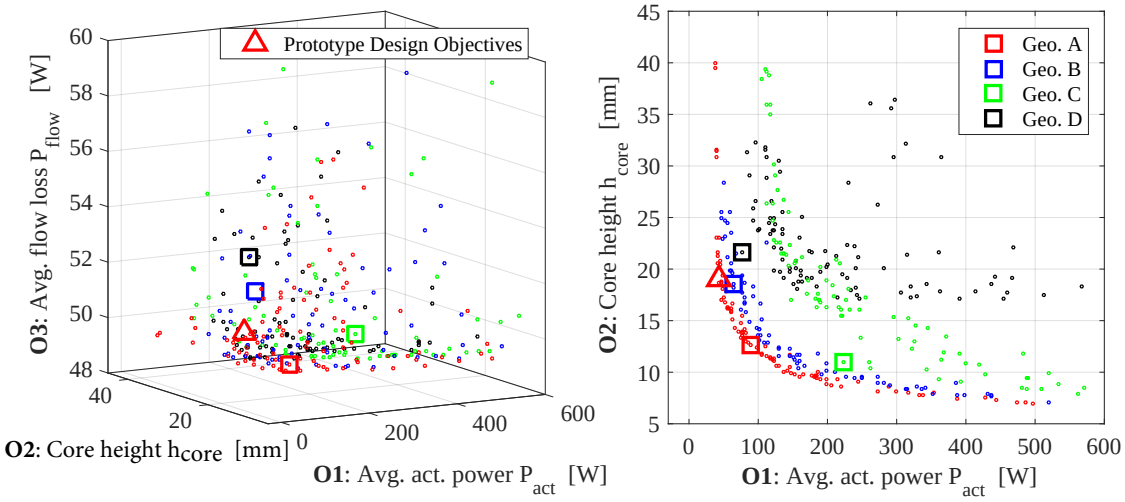

Figure 13: Optimization results using the four different actuator geometries. The minimum objective points for each design objective have been highlighted along with the design point of the actuator prototype.

Table 4: Magnetic and electrical properties of materials used in static electro-magnetic FEA.

Description	**Geo. A**	**Geo. B**	**Geo. C**	**Geo. D**
No. of objectives	3	3	3	3
No. of design variables	11	11	11	12
No. of constraints	6	7	7	9
Population size	100	100	100	100
No. generations	250	250	250	250
No. function evaluations	25k	25k	25k	25k
GDE3 control settings: CR,F	0.75,0.25	0.75,0.25	0.75,0.25	0.75,0.25
No. fronts in final generation	1	1	1	3
% of gen. in first front	100	100	100	30

6 CONCLUSIONS AND FUTURE WORK

Different moving coil actuator geometry topologies, for DDM's, have been explored through optimization. In total, four different permanent magnet placement have been tested to find the most suited topology. The objectives are to minimize the actuator height and actuator power and flow loss. Evaluation of the objectives include static-electro magnetic FEA and

lumped parameter models enabling simulation of entire DDM cycles. The optimization tool successfully converged towards a set of non-dominated solutions for each optimisation problem. The optimization result showed that the average flow losses only varies vaguely which indicates efficient machine operation is feasible using all of the proposed topologies. However, some geometries generally require more space than others, and some geometries requires larger actuator power. The most suited topologies are geometry A and B which both uses radially magnetized permanent magnets. An actuator and valve prototype has been manufactured based on the optimization results with a core height of 19 mm and an average actuator power 20 W, enabling an efficiency of 99.4 % during motoring operation (only valve related losses are considered). Future work involves experimental testing of the prototype to verify the models used in the optimization.

References

[1] Daniel Beck Roemer. *Design and Optimization of Fast Switching Valves for Large Scale Digital Hydraulic Motors*. PhD thesis, 2014.

[2] Daniel Roemer, Per Johansen, Henrik C. Pedersen, and Torben Ole Andersen. *Topology Selection and Analysis of Actuator for Seat Valves suitable for use in Digital Displacement Pumps/Motors*, pages 418–424. IEEE Press, 2013.

[3] S.H. Salter and W.H.S. Rampen. Pump control method and poppet valve therefor, March 2 1993. US Patent 5,190,446.

[4] S.H. Salter and W.H.S. Rampen. Improved fluid-working machine, July 15 1992. EP Patent App. EP19,900,915,148.

[5] J. Quilter. Mitsubishi to unveil 7MW offshore turbine. Wind Power Monthly, November 2011. Available at www.windpowermonthly.com.

[6] Kazuhisa Tsutsumi, Toshihide Noguchi, Yasuhiro Korematsu, Masayuki Shimizu, Alasdair Robertson, Uwe Stein, and Hauke Karstens. Hydraulic pump structure for wind turbine generator or tidal current generator and method of mounting hydraulic pump, November 28 2012. CN Patent App. CN 201,080,003,097.

[7] T. Kameda, M. Uchida, O. Uehara, H. Dodson, A. Robertson, and W. Rampen. Hydraulic pump, method for maintaining same, and wind power generation device, July 23 2014. EP Patent App. EP20,130,809,430.

[8] Salter Stephen, Stein Uwe, Dodson Henry, Fox Robert, Robertson Alasdair, and Mcgrath Tom. Method and apparatus for performing maintenance on hydraulic pump, and power generating apparatus of renewable energy type, May 8 2013. CN Patent App. CN 201,180,031,163.

[9] I. Haskara., V. V. Kokotovic, and L. A. Mianzo. Control of an electro-mechanical valve actuator for a camless engine. *International Journal of Robust and Nonlinear Control*, 14(6):561–579, 2004.

[10] Static performance of a polarized permanent-magnet reluctance actuator for internal combustion engine valve actuation. *IEEE Transactions on Magnetics*, 42(8):2063–2070, Aug 2006.

[11] B. Lequesne. Fast-acting long-stroke bistable solenoids with moving permanent magnets. *IEEE Transactions on Industry Applications*, 26(3):401–407, May 1990.

[12] Liang Liu and S. Chang. A moving coil electromagnetic valve actuator for camless engines. In *2009 International Conference on Mechatronics and Automation*, pages 176–180, Aug 2009.

[13] R. Storn and K. Price. Differential Evolution - A simple and efficient adaptive scheme for global optimization over continuous spaces. Tech. report TR-95-012, Berkeley, Cambridge, MA, May 1995.

[14] S. Kukkonen and J. Lampinen. Gde3: the third evolution step of generalized differential evolution. In *2005 IEEE Congress on Evolutionary Computation*, volume 1, pages 443–450 Vol.1, Sept 2005.

[15] S. Kukkonen. *Generalized Differential Evolution for Global Multi-Objective Optimization with Constraints*. PhD thesis, Lappeenranta University of Technology, 2012.

[16] D. Meeker. Finite element method magnetics, version 4.2, user's manual, 2015.

[17] W. L. Soong. Bh curve and iron loss measurements for magnetic materials, May 12 2008.

[18] J A Wagner. The shorted turn in the linear actuator of a high performance disk drive. *Magnetics, IEEE Transactions on*, 18(6):1770–1772, 1982.

[19] C. Noergaard, D. B. Roemer, and M. M. Bech. Modelling of moving coil actuators in fast switching valves suitable for digital hydraulic machines. In *Proc. of 2015 ASME Fluid Power and Motion Control*, Chicago, US, October 2015.

[20] Isaak D Mayergoyz. *Nonlinear Diffusion of Electromagnetic Fields*. Academic Press, 1998.

[21] D. B. Roemer, P. Johansen, L. Schmidt, and T. O. Andersen. Modeling of movement-induced and flow-induced fluid forces in fast switching valves. In *Proc. of 2015 International Conference on Fluid Power and Mechatronics*, Harbin, China, August 2015.

[22] S. Salter. Digital hydraulics for renewable energy. In *Proc. of World Renewable Energy Conference Aberdeen 2005*, Aberdeen, UK, 2005.

[23] G.S.Payne. Potential of digital displacement hydraulics for wave energy conversion. In *the 6th European Wave and Tidal Energy Conference*, Glasgow, UK, 2005.

[24] Robert Y. S. Lai and Lyle F. Mockros. The stokes-flow drag on prolate and oblate spheroids during axial translatory accelerations. *Journal of Fluid Mechanics*, 52:1–15, 3 1972.

[25] W. Borutzky, B. Barnard, and J. Thoma. An orifice flow model for laminar and turbulent conditions. *Simulation Modelling Practice and Theory*, 10(34):141 – 152, 2002.

Simulation of Radial Piston Constant Flow Pump with Digital Distribution under Random Low Speed Driving

Shi Guanglin Yu Licheng Qi Lidong
School of Mechanical Engineering of Shanghai Jiao Tong University
Shanghai, China, 200240
shiguanglin@sjtu.edu.cn

ABSTRACT

With the application of hydraulic technique in wind-energy and ocean-energy generation, it's necessary to study the constant output flow of the hydraulic pump under random low speed driving to ensure the stability of the power system input. In this situation, this paper introduces a kind of radial piston constant flow hydraulic pump with digital distribution when it is driven under random low speed. Here, a digital distribution, which is composed of five high speed on/off valves and an absolute encoder to replace the traditional distribution mechanism, is used for flow-distribution of this pump. When the input speed of this pump is low and random, its output flow can be maintained at approximate constant value through a controller to adjust the duty ratio of the valves. Firstly, the principle of this pump with digital distribution is analyzed in this paper. Secondly, the mechanical structure of this pump with digital distribution is designed by 3D software. Thirdly, the mathematic model of this pump with digital distribution is put forward and its simulation model is also established through the MATLAB/Simulink. Lastly, the simulations of dynamic characteristics of the output flow of the pump with digital distribution are carried out when it is driven under different random low speed. The simulations' results show that the output flow of this pump with digital distribution can be kept at approximate constant under low random speed driving when the correct control methods are employed to five high speed on/off valves.

KEYWORDS: random low speed, hydraulic pump, digital distribution, high speed on/off valve, constant flow output, dynamic characteristics

1. INTRODUCTION

At present, with the influence of traditional energy reduction and environmental protection, wind power, ocean power and other sustainable use of new energy and power generation technology have been paid on more and more attention. But wind and wave all have the characteristics of random and variable size, resulting some shortcomings and weakness of the traditional power system.

In recent years, hydraulic technology with high power output, reliable control precision and less space begins to get application in wind power and ocean power generation [1]-

[3]. So, hydraulic pump can be used as the energy collection and conversion component in the power generation situations. Hydraulic power generation technology research mainly uses the structure of constant displacement hydraulic pump with variable displacement hydraulic motor to collect wind or ocean power. But most constant displacement hydraulic pump is designed according to the constant speed driving. So it is difficult to ensure a long period of time to meet the demand of the working condition at random occurrence and variable size of wind and ocean power generation. And constant displacement hydraulic pump is difficult run in the low speed under continuous operation over a long period of time.

Therefore, this paper puts forward a kind of digital distribution radial piston pump which uses high speed on/off valves to replace the traditional mechanical distribution. With the aid of numerical control technology [4]-[8], the pump can be ensured to reliably absorb the wind or ocean energy and transform them into a stable flow output. In this paper, according to the principle of digital distribution, the digital pump structure model is built. With the piston kinematics and dynamic analysis, the mathematical model is set up and the constant flow output method is put forward. Then through the Matlab/Simulink simulation software, the flow output characteristics of the digital distribution pump under the condition of low random speed input are analyzed and the feasibility of the constant flow output control is studied.

2. DIGITAL DISTRIBUTION PRINCIPLE AND MECHANISM

In this paper, the structure of digital distribution pump is based on radial piston pump. Traditional radial piston pump according to the distribution mode is mainly divided into valve distribution, shaft distribution and end plate distribution. The work pressure of valve distribution pump is high and pump displacement is small, and the dynamic response and the volume efficiency are low. Shaft distribution pump mechanical processing is difficult and distribution shaft is easy to wear which affects the pump service life. Relatively, the distribution structure of digital pump is simple to process and it can adapt to the variation of input speed.

The structure principle diagram of the radial 5-piston constant flow pump with digital distribution is shown in Figure 1. The piston number is Ⅰ, Ⅱ, Ⅲ, Ⅳ, Ⅴ clockwise. Distribution mechanism is mainly composed of five high speed on/off valves and one absolute encoder. Connected to the pump shaft, the absolute encoder is used to on-line detect the rotation speed and the spatial relationship among the pistons. In the process of pump rotation, the pump controller changes the corresponding high speed on/off valve switch state and duty cycle according to the volume change characteristics of the piston chamber, so that the digital distribution pump can realize the piston chamber change of oil absorption an expulsion state switch and the adjustment of the pump output flow, which realizes the right sequence of the digital distribution and the constant flow output.

According to Figure 1, each high speed on/off valve separately controls the corresponding piston of the pump ontology structure, connecting the piston chamber with oil tank when the valve is de-energized or connecting the piston chamber with the load when the valve is energized. Pump shaft angle signal collected by the absolute encoder is calculated through pump controller. And then the controller gives the corresponding signal of the valve energized or de-energized to realize each piston

chamber linking with the oil tank or the load in order. The pump shaft angle is set as 0° when piston chamber Ⅰ is at the top dead position, and counter clockwise direction is set as the positive direction. When the angle is less than 36°, high speed on/off valve 4 and 5 are energized and others are de-energized. So piston chamber Ⅳ, Ⅴ absorb the oil from the tank and the piston chambers Ⅰ, Ⅱ, Ⅲ expulse the oil to the load. The state diagram flow distribution of each angel interval when pump shaft rotates counter-clockwise is shown in Table 1.

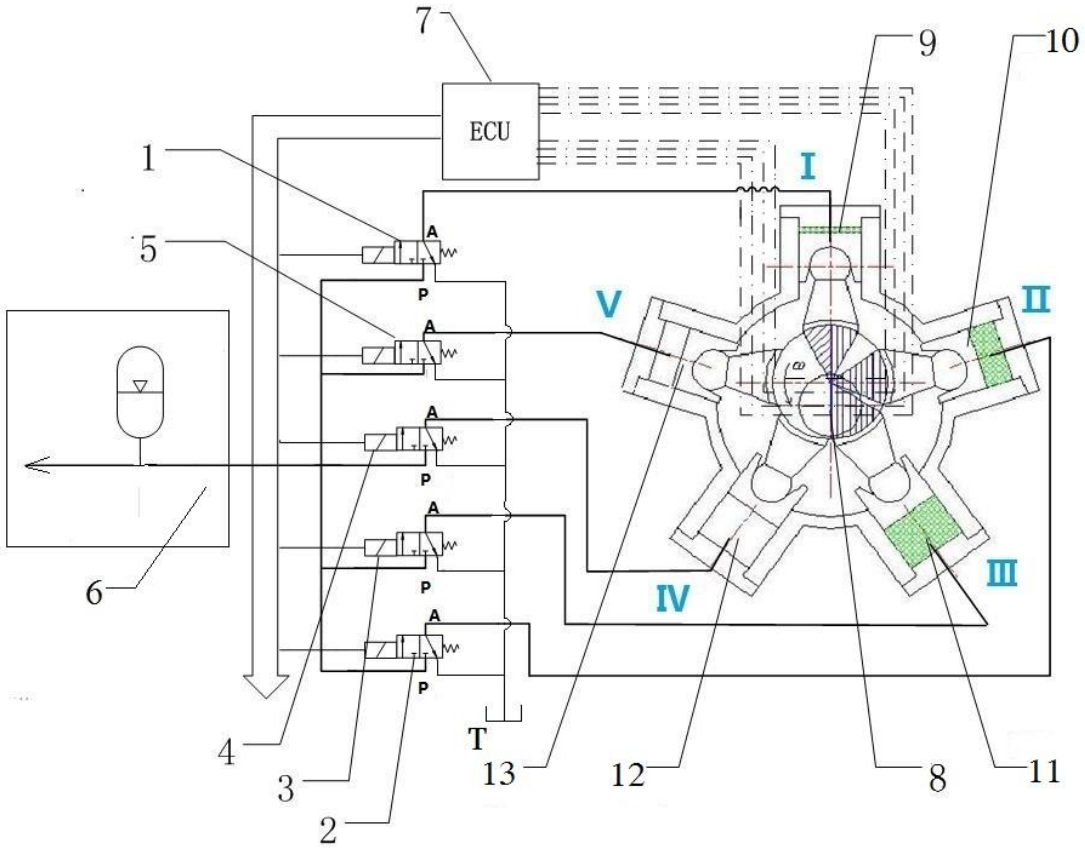

Figure 1. Schematic of the hydraulic pump with digital distribution
(1~5.Two-position three-way high speed on/off valve, 6.Load, 7.Controller, 8.Absolute encoder, 9~13.Plunger chamber)

According to the structure characteristics of the piston pump, the absorption state and the expulsion state change every 36°, and meanwhile the piston number of each state changes between 2 and 3 in cycle. Furthermore, the piston cavity finishes oil absorption and oil expulsion once every cycle. Each piston's oil expulsion interval is shown in Table 2.

Then based on the design requirements, the ontology structure of the digital pump, the absolute encoder type and the high speed on/off valve style are selected. The digital distribution mechanical structure is designed and the 3D model of the whole pump is shown in Figure 2.

Table 1. The state diagram flow distribution when pump shaft rotates counter-clockwise

Pump shaft angle		Shaft rotates CCW		The state of high speed on/off valve		
		Oil-absorption piston chamber	Oil-expulsion piston chamber	Energized	De-energized	Piston chamber state-change
1	0~36 °	Ⅰ, Ⅱ, Ⅲ	Ⅳ, Ⅴ	4, 5	1, 2, 3	Ⅰ oil-expulsion to oil-absorption
	36 ~ 72 °	Ⅰ, Ⅱ	Ⅲ, Ⅳ, Ⅴ	3, 4, 5	1, 2	Ⅲoil-absorption to oil-expulsion
2	72 ~ 108 °	Ⅰ, Ⅱ, Ⅴ	Ⅲ, Ⅳ	3, 4	1, 2, 5	Ⅴ oil- expulsion to oil-absorption
	108 ~ 144 °	Ⅰ, Ⅴ	Ⅱ, Ⅲ, Ⅳ	2, 3, 4	1, 5	Ⅱ oil-absorption to oil- expulsion
3	144 ~ 180 °	Ⅰ, Ⅳ, Ⅴ	Ⅱ, Ⅲ	2, 3	1, 4, 5	Ⅳoil- expulsion to oil-absorption
	180 ~ 216 °	Ⅳ, Ⅴ	Ⅰ, Ⅱ, Ⅲ	1, 2, 3	4, 5	Ⅰ oil-absorption to oil- expulsion
4	216 ~ 252 °	Ⅲ, Ⅳ, Ⅴ	Ⅰ, Ⅱ	1, 2	3, 4, 5	Ⅲoil- expulsion to oil-absorption
	252 ~ 288 °	Ⅲ, Ⅳ	Ⅰ, Ⅱ, Ⅴ	1, 2, 5	3, 4	Ⅴ oil-absorption to oil- expulsion
5	288 ~ 324 °	Ⅱ, Ⅲ, Ⅳ	Ⅰ, Ⅴ	1, 5	2, 3, 4	Ⅱ oil- expulsion to oil-absorption
	324 ~ 360 °	Ⅱ, Ⅲ	Ⅰ, Ⅳ, Ⅴ	1,4,5	2,3	Ⅳoil-absorption to oil- expulsion

Table 2. The oil-expulsion piston chamber angle range for pump shaft CCW rotation

Piston chamber number	Oil expulsion interval
Ⅰ	0 ~180 °
Ⅱ	108 ~288 °
Ⅲ	36 ~216 °
Ⅳ	324 ~360 °, 0 ~144 °
Ⅴ	252 ~360 °, 0 ~72 °

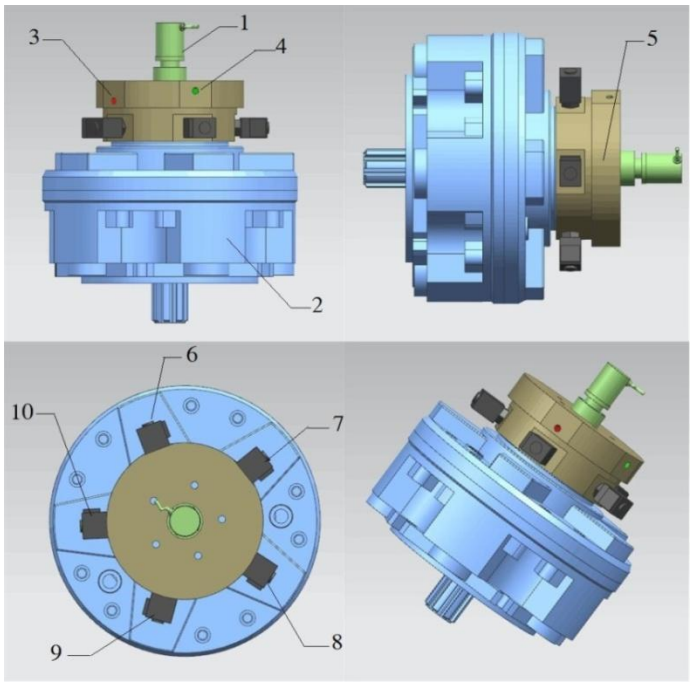

Figure 2. Structure of the digital distribution hydraulic pump
(1.Absolute encoder, 2.Pump ontology structure, 3.Oil-expulsion port, 4.Oil-absorption port, 5.Flow-distribution structure, 6~10.Two-position three-way high speed on/off valve)

3. MATHMETATICAL MODELING

The movement rule of the radial piston pump with digital distribution is equivalent to crank connecting rod mechanism. Isolating a certain piston, its movement principle and the instantaneous flow formula of the pump are carried out. Shown in Figure 3, O_1 is the pump shaft's rotation center, O_2 is pump shaft's eccentric center and O_3 is connection center between the piston and the crank. So the distance of O_1O_3 changes in the piston movement. When the piston moves away from O_1, the piston chamber is on oil-expulsion, otherwise on oil-absorption.

Equations (1) - (6) focus on the kinematic mathematical model of the digital pump.

Piston chamber Ⅰ is supposed at the top dead center position at the beginning, the distance of O_1O_3 is:

$$d_0 = e + R + L \tag{1}$$

Shaft angular velocity is set as ω, when it turns angle φ, the angle of each piston is φ_i. i shows the serial number of each piston. Each piston moving distance is s_i and velocity is v_i. e shows the eccentric distance and R shows the eccentric radius. The distance between the connecting rod ball head center and the surface of the eccentric is L. After simplification, the following formulas can be derived.

$$\varphi_i = \varphi + (i-1)\frac{2\pi}{5} \tag{2}$$

$$s_i = e[(1-\cos\varphi_i)+\frac{K}{4}(1-\cos 2\varphi_i)] \tag{3}$$

$$v_i = e\omega(\sin\varphi_i+\frac{K}{2}\sin 2\varphi_i) \tag{4}$$

Among them, $K=\frac{e}{R+L}$. By the definition of the piston movement, v_i is positive on oil-absorption and negative on oil-expulsion. Thus, the flow rate of the oil-expulsion takes the absolute value.

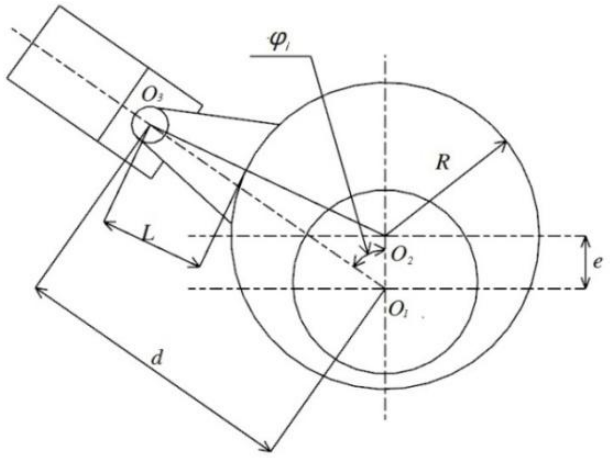

Figure 3. Schematic of signal piston movement

The number of the oil-expulsion piston chamber is *m* and the piston area is A. Then the instantaneous flow of the pump ontology is:

$$q = Ae\omega\sum_{i=1}^{m}\left|(\sin\varphi_i+\frac{K}{2}\sin 2\varphi_i)\right| \tag{5}$$

According to the above position and direction assumptions, $\beta=\pi/5$, when $0\le\varphi<\beta$, $m=2$; when $\beta\le\varphi\le 2\beta$, $m=3$. The duty ratio of the high speed on/off valve is α. After mathematical treatment, the instantaneous flow of the digital pump through the high speed on/off valve is:

$$\begin{cases} 0\le\varphi<\beta & q_{out}=\alpha Ae\omega[\dfrac{\cos(\frac{\beta}{2}-\varphi)}{2\sin\frac{\beta}{2}}+\dfrac{K}{2}\dfrac{\sin(2\varphi-\beta)}{2\cos\beta}] \\ \beta\le\varphi\le 2\beta & q_{out}=\alpha Ae\omega[\dfrac{\cos(\frac{3\beta}{2}-\varphi)}{2\sin\frac{\beta}{2}}+\dfrac{K}{2}\dfrac{\sin(3\beta-2\varphi)}{2\cos\beta}] \end{cases} \tag{6}$$

Because the five pistons are uniform radial distribution, the distribution rule of each piston chamber and flow equation of the pump are the same at $[2\beta,4\beta],[4\beta,6\beta],[6\beta,8\beta],[8\beta,10\beta]$.

The equation (6) ignores some practical factors, such as friction, inertia force and volume leakage. Through adjusting the duty ratio, the instantaneous flow fluctuation and the average flow rate of the digital pump can be controlled.

Equations (7) - (14) focus on the dynamic mathematical model of the digital pump.

In angle range $[0,\beta]$, the flow rate through high speed on-off valve, the flow continuity equation is:

$$q_i = A|v_i| - c_p(p_i - p_L) - \frac{V_{i0} + As_i}{\beta_e}\frac{\mathrm{d}p_i}{\mathrm{d}t}(i = 4,5) \tag{7}$$

In equation (7), V_{i0} shows the initial control volume of piston chamber; p_i shows the pressure of piston chamber; p_L shows the load pressure; c_p shows the leakage coefficient of signal piston.

Hydraulic torque is shown in equation 8. For the oil-expulsion piston chamber, the torque is negative; for the oil-absorption piston chamber, the torque is greater than or equal to zero.

$$M_i = Ap_i e(\sin\varphi_i + \frac{K}{2}\sin 2\varphi_i) \tag{8}$$

For the friction resistance torque, it is mainly produced by the contact force between the eccentric wheel surface and the piston. The friction resistance torque [9] equation is:

$$M_f = \Delta pAe\mu[(\frac{R}{e} - \frac{K}{2})\cdot m + \sum_{i=1}^{m}\cos\varphi_i + \frac{K}{2}\sum_{i=1}^{m}\cos 2\varphi_i] \tag{9}$$

In equation (9), μ shows the friction coefficient; Δp shows the differential pressure of the digital pump.

Then the pump shaft torque balance equation is:

$$T_D + \sum_{i=1}^{5} M_i = J_t\frac{\mathrm{d}^2\varphi}{\mathrm{d}t^2} + B\frac{\mathrm{d}\varphi}{\mathrm{d}t} + M_f \tag{10}$$

In equation (10), T_D shows the input torque; J_t shows the pump shaft equivalent inertia. B shows the total viscous damping coefficient.

Combined with the above formulas, setting $x_1 = \varphi, x_2 = \frac{\mathrm{d}\varphi}{\mathrm{d}t}, x_3 = p_4, x_4 = p_5$, the dynamic mathematical model is got at angle-range $[0,\beta]$ in equation (11).

$$\begin{cases} \dfrac{\mathrm{d}x_1}{\mathrm{d}t} = x_2 \\ \dfrac{\mathrm{d}x_2}{\mathrm{d}t} = \dfrac{1}{J_t}(T_D + Ae[\sum_{i=1}^{3} p_0(\sin\varphi_i + \dfrac{K}{2}\sin 2\varphi_i) + \\ \qquad x_3(\sin\varphi_4 + \dfrac{K}{2}\sin 2\varphi_4) + x_4(\sin\varphi_5 + \dfrac{K}{2}\sin 2\varphi_5)] - Bx_2 - M_f) \\ \dfrac{\mathrm{d}x_3}{\mathrm{d}t} = \dfrac{\beta_e[Aex_2\left|(\sin\varphi_4 + \dfrac{K}{2}\sin 2\varphi_4)\right| - K_1\sqrt{x_3 - p_L} - c_p(x_3 - p_L)]}{V_{40} + Ae[(1-\cos\varphi_4) + \dfrac{K}{4}(1-\cos 2\varphi_4)]} \\ \dfrac{\mathrm{d}x_4}{\mathrm{d}t} = \dfrac{\beta_e[Aex_2\left|(\sin\varphi_5 + \dfrac{K}{2}\sin 2\varphi_5)\right| - K_1\sqrt{x_4 - p_L} - c_p(x_4 - p_L)]}{V_{50} + Ae[(1-\cos\varphi_5) + \dfrac{K}{4}(1-\cos 2\varphi_5)]} \end{cases} \tag{11}$$

And the output flow is equation (12).

$$q_{out} = \alpha(q_4 + q_5) = \alpha K_1(\sqrt{x_3 - p_L} + \sqrt{x_4 - p_L}) \tag{12}$$

In angle range $[\beta, 2\beta]$, the number of oil-expulsion piston chamber changes from 2 to 3, setting $x_1 = \varphi, x_2 = \frac{\mathrm{d}\varphi}{\mathrm{d}t}, x_3 = p_3, x_4 = p_4, x_5 = p_5$, the dynamic mathematical model is got in equation (13).

$$\begin{cases} \dfrac{\mathrm{d}x_1}{\mathrm{d}t} = x_2 \\ \dfrac{\mathrm{d}x_2}{\mathrm{d}t} = \dfrac{1}{J_t}(T_D + Ae[\sum_{i=1}^{2} p_0(\sin\varphi_i + \dfrac{K}{2}\sin 2\varphi_i) + \\ \qquad x_3(\sin\varphi_3 + \dfrac{K}{2}\sin 2\varphi_3) + x_4(\sin\varphi_4 + \dfrac{K}{2}\sin 2\varphi_4) + \\ \qquad x_5(\sin\varphi_5 + \dfrac{K}{2}\sin 2\varphi_5)] - Bx_2 - M_f) \\ \dfrac{\mathrm{d}x_3}{\mathrm{d}t} = \dfrac{\beta_e[Aex_2\left|(\sin\varphi_3 + \dfrac{K}{2}\sin 2\varphi_3)\right| - K_1\sqrt{x_3 - p_L} - c_p(x_3 - p_L)]}{V_{30} + Ae[(1-\cos\varphi_3) + \dfrac{K}{4}(1-\cos 2\varphi_3)]} \\ \dfrac{\mathrm{d}x_4}{\mathrm{d}t} = \dfrac{\beta_e[Aex_2\left|(\sin\varphi_4 + \dfrac{K}{2}\sin 2\varphi_4)\right| - K_1\sqrt{x_4 - p_L} - c_p(x_4 - p_L)]}{V_{40} + Ae[(1-\cos\varphi_4) + \dfrac{K}{4}(1-\cos 2\varphi_4)]} \\ \dfrac{\mathrm{d}x_5}{\mathrm{d}t} = \dfrac{\beta_e[Aex_2\left|(\sin\varphi_5 + \dfrac{K}{2}\sin 2\varphi_5)\right| - \alpha K_1\sqrt{x_5 - p_L} - c_p(x_5 - p_L)]}{V_{50} + Ae[(1-\cos\varphi_5) + \dfrac{K}{4}(1-\cos 2\varphi_5)]} \end{cases} \tag{13}$$

And the output flow is got in equation (14).

$$q_{out} = \alpha(q_3 + q_4 + q_5) = \alpha K_1(\sqrt{x_3 - p_L} + \sqrt{x_4 - p_L} + \sqrt{x_5 - p_L}) \tag{14}$$

Similarly, according to the distribution flow status table 1, the principle of each angle range is derived.

4. SIMULATION AND ANALYSIS

4.1. Ideal model simulation

The target average flow rate is supposed as q_0 and its corresponding angular velocity is ω_0, When the input angular velocity is $\omega \geq \omega_0$ and randomly changes, the pump output flow will no longer be held constant. And then it needs high speed on/off valve to adjust and control the output flow. Duty ratio α is:

$$\alpha = \frac{q_0}{V_\omega \cdot \omega} = \frac{\omega_0}{\omega} \tag{15}$$

In formula (15), $V_\omega = 5Ae/\pi$. The equation is derived in ideal situation and it can be adjusted due to the practical factors.

Given input rotation speed of the digital pump as 10r/min， 15r/min， 20r/min， 25r/min，30r/min，35r/min，40r/min, the output flow is shown in Figure 4. The flow is basically kept steady, but in a cycle it conducts periodical small ripple with angle change, which is caused by the pump's radial piston structure.

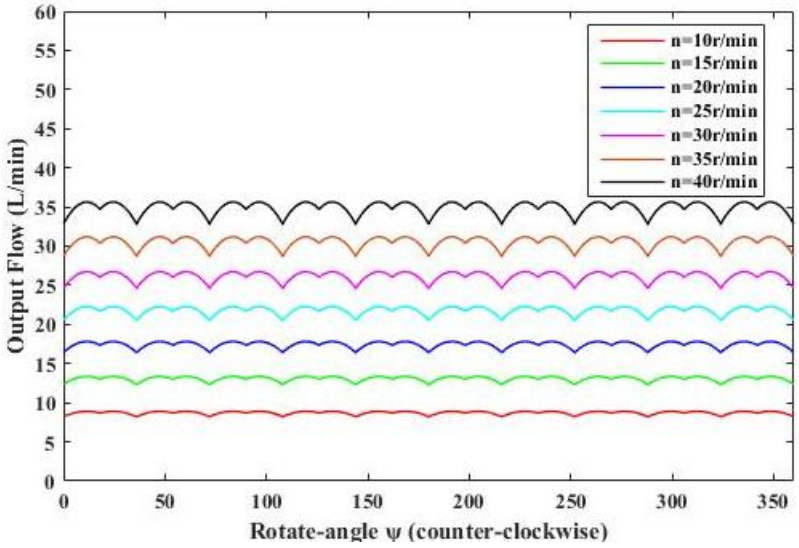

Figure 4. The digital distribution pump's instantaneous output flow under constant rotating speed

According to the kinematic model, when a random input the pump's input rotating speed is random, the pump's output flow is controlled and equal to the target flow rate, shown in Figure 5.

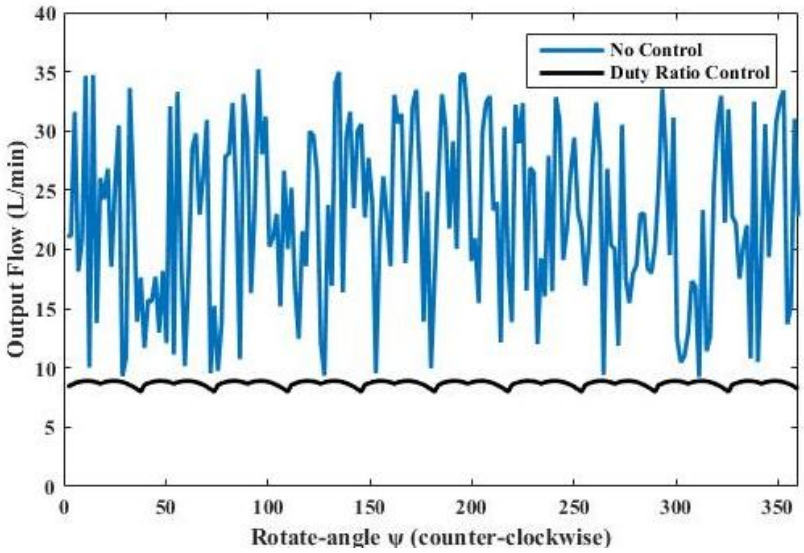

Figure 5. The pump's random input rotating speed and output flow

4.2. Practical model simulation

When taking the friction torque and load torque into consideration, the dynamic model carries out the output flow characteristics. The simulation model in angel-range $[0, \beta]$ is shown in Figure 6. By changing the input torque and load pressure, the digital pump's dynamic characteristics of each angel range is studied. There are altogether 10 angel ranges. Each adjacent angle range needs the initial value such as angle and angle velocity. When the angle value arrives at the ending node of each angle range, the simulation model stops and exports the corresponding results. After finishing all 10 angle range simulation, the results are combined in the whole angle range.

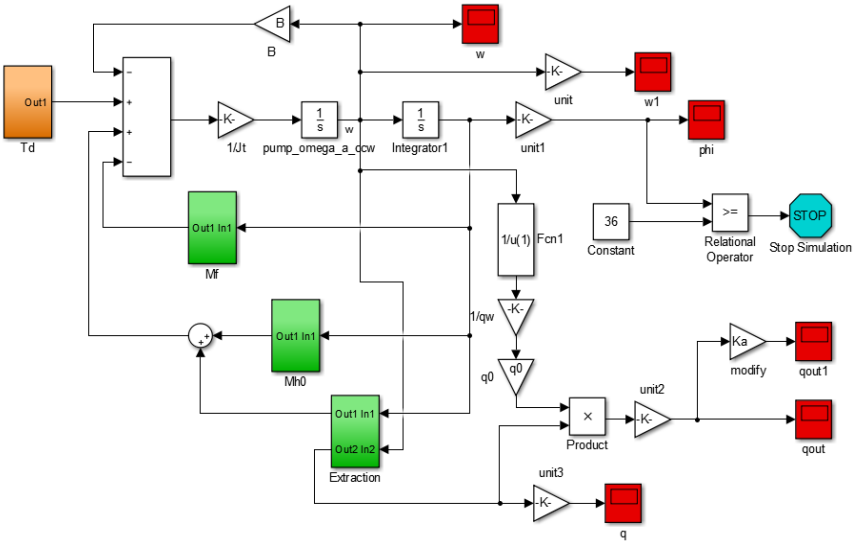

Figure 6. The angle-range dynamic Simulink model ($0 \le \varphi < \pi / 5$)

Given an approximate sinusoidal signal of torque, the difference of the rotation speed response of the pump with and without friction force are shown in Figure 7, which indicate that the friction torque decreased its amplitude and have a time delay.

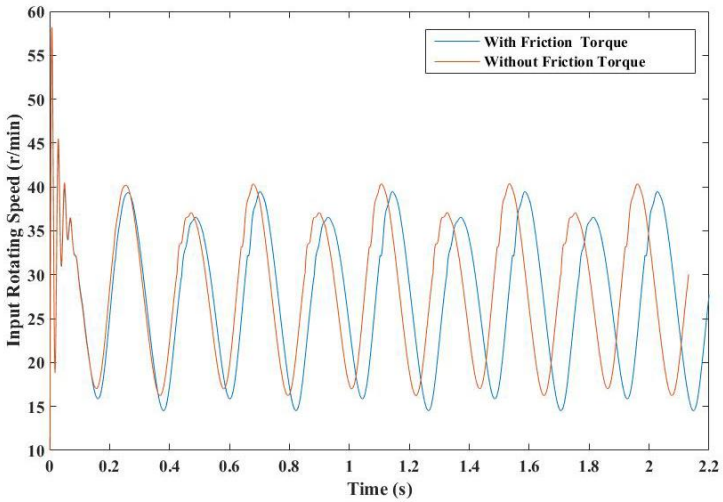

Figure 7. The rotation speed response under same torque with and without friction torque

Given rotation speed randomly at range $20\text{r/min} \sim 35\text{r/min}$, and the load pressure is 0MPa, 5MPa and 10MPa, the pump's output flow is shown in Figure 8 - Figure 10.

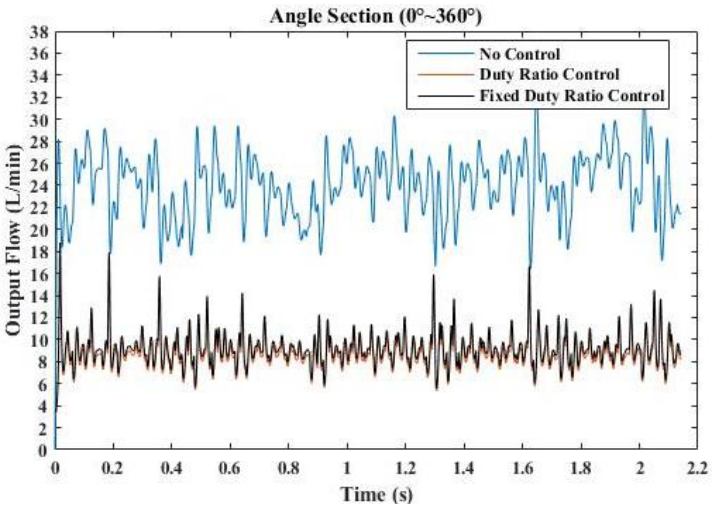

Figure 8. The output flow under random input (0 MPa load)

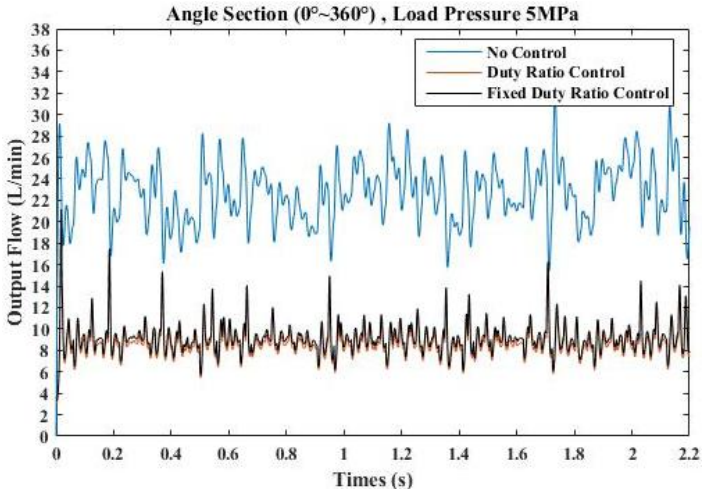

Figure 9. The output flow under random input (5 MPa load)

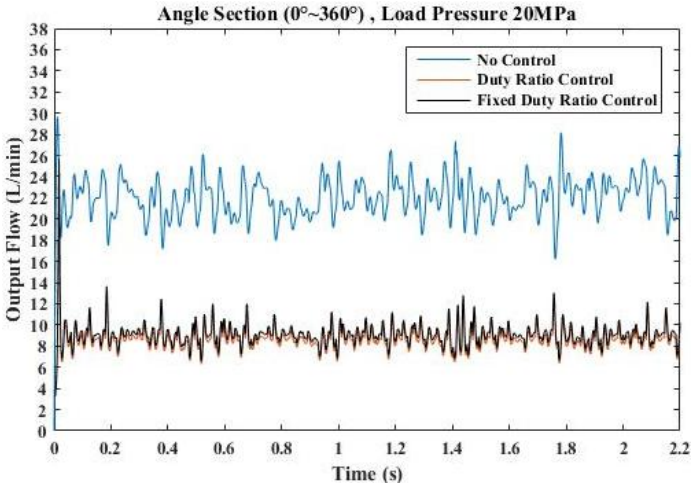

Figure 10. The output flow under random input (10 MPa load)

From Figure 8 and Figure 10, with the increasing of load pressure, pump output flow reduces with the increasing leakage. Through modified duty ratio control, it decreases the difference between the practical output flow and target output flow.

5. CONCLUSION

In this paper, a radial piston constant flow hydraulic pump with digital distribution under random low speed driving is designed. High speed on/off valve group is used to process the flow distribution. The digital distribution principle is introduced and the 3D model of the digital pump is built. Then the static and dynamic mathematical models are established and the constant flow output control method is put forward.

Through establishing Matlab/Simulink simulation model, the kinematic and dynamic performance of the digital pump is carried out by the simulation analysis. Results show that under certain input driving torque, both the rotation speed and the output flow rate have difference because of the friction torque and the load torque. While under certain input driving rotation speed, the output flow rate only has the difference because of the leakage caused by pressure drop. Above all, the duty ratio control method is proved to be effective to maintain the constant flow output under random input.

6. ACKNOWLEDGEMENT

This paper is supported by the National Natural Science Foundation of China (Number: 51475285).

REFERENCES

[1] Peter Chapple, Michael Niss and Knud Erik Thomsen. 2012. Wind Turbines with Variable Hydraulic Transmissions and Electrically Excited Synchronous Generators Directly Connected to the Grid[C]. Proceedings of the ASME/BATH 2012 Symposium on Fluid Power and Motion Control (FPMC 2012), September 12-14, Bath, Great Britain, pp. 579-592.

[2] Henrik C. Pedersen, Anders H. Hansen, Rico H. Hansen, Turban O. Andersen, Michael M. Bech. 2012. Design and Control of Full Scale Wave Energy Simulator System[C]. Proceedings of the ASME/BATH 2012 Symposium on Fluid Power and Motion Control, September 12-14, pp. 551-564.

[3] Mortensen, K. A., & Henriksen, K. H. 2011. Efficiency Analysis of a Radial Piston Pump Applied in a 5MW Wind Turbine with Hydraulic Transmission (Doctoral dissertation, Denmark: Aalborg University).

[4] Heikkilä, M., Tammisto, J., Huova, M., Huhtala, K., & Linjama, M. 2010. Experimental evaluation of a piston-type digital pump-motor-transformer with two independent outlets. Fluid Power and Motion Control, pp. 83-97.

[5] Merrill, K. J., Breidi, F. Y., & Lumkes, J. 2013. Simulation based design and optimization of digital pump/motors. 2013 Symposium on Fluid Power and Motion Control American Society of Mechanical Engineers, October, V001T01A045.

[6] Huang Ruijia, Shi Guanglin. 2013. Research on the Constant Speed Control System of Hydraulic Motor under Variable Flow-rate Input Based on Dual-PID Method[C]. Proceedings of the ASME/BATH 2013 Symposium on Fluid Power & Motion Control, October 6-9, Sarasota, Florida, USA, V001T01A018.

[7] Lei, X., Ni, M., Li, D., & Ma, Y. 2011. Study on simulation of digital pump-control cylinder position control system. Procedia Engineering, 16, pp.729-736.

[8] Holland, M., Wilfong, G., Merrill, K., & Lumkes, J. 2011. Experimental Evaluation of Digital Pump/Motor Operating Strategies with a Single-Piston Pump/Motor. In Proceedings of the 52nd National Conference on Fluid Power pp. 13-20.

[9] Pan, J., & Shi, G. L. 2011. Simulation and implementation of a new crank shaft and connecting rod-type radial-plunger low-speed-high-torque hydraulic motor with digital distributor. Proceedings of the Institution of Mechanic at Engineers, Part C: Journal of Mechanical Engineering Science, February 2012, vol. 226.2, pp. 533-543.

DIGITAL HYDRAULIC POWER MANAGEMENT SYSTEM – MEASURED CHARACTERISTICS OF A SECOND PROTOTYPE

M. Sc. Mikko Heikkilä, M. Sc. Jyrki Tammisto, Adj. Prof. Matti Linjama,
Prof. Kalevi Huhtala
Tampere University of Technology
Department of Intelligent Hydraulics and Automation
P.O. BOX 589
FI-33101 Tampere, Finland

ABSTRACT

The Digital Hydraulic Power Management System (DHPMS) is a multi-outlet alternative for conventional variable displacement pump/motors. Based on the digital pump/motor technology, the DHPMS have the potential for good efficiency; the valve timing can be optimised for each pressure level and displacement is controlled by leaving some of the pumping pistons idle (unpressurised). This paper introduces a second prototype of the piston-type DHPMS. The machine has five independent outlets and it has been put together using commercial components. The pumping and motoring efficiencies are investigated for a single 6-piston unit, but the construction allows doubling the number of pistons for a further study. The results show that using of the commercial control valves and several independent outlets result in large compression volumes for the pumping pistons. Nevertheless, the pumping efficiencies are mostly over 0.7 at displacements greater than 40% of the theoretical maximum. Moreover, the motoring efficiencies are only slightly lower than the pumping efficiencies. The DHPMS is also able to transfer the power between the outlets without impairing the total efficiency; thus, a hybrid system utilizing hydraulic energy storage can be implemented.

KEYWORDS: Displacement control, hybrid system, pump/motor, transformer

1. INTRODUCTION

Digital pump/motors have been proven to have better efficiency than conventional variable displacement pumps [1]. Especially at partial displacement the digital machines benefit from a capability for idling individual pistons. A concept of combining several radial piston units of the digital pump/motors to a common shaft has been presented in [2]. The approach allows isolation between the services while the mechanical torque and power are summed. The digital pump/motors can be applied to hydraulic hybrids [3], tidal current energy converters [4] and wind turbines [5] for example.

The Digital Hydraulic Power Management System (DHPMS) is basically a digital pump/motor with several independent outlets [6]; each piston of the DHPMS can be controlled independently and they can be connected to whichever outlet via actively controlled on/off valves. Hence, the power can also be transferred from one outlet to another regardless of the pressure levels. The hydraulic connectivity of the outlets enables the DHPMS to be sized according to the summed maximum total flow at the outlets, whereas each mechanically connected pump/motor unit has to be sized according to the maximum flow at its outlet. The DHPMS can be applied to a system where the supply line pressures need to be controlled [7] or actuators can be directly controlled by the DHPMS [8].

2. TEST SYSTEM

2.1. Modified Pump Unit

The first prototype DHPMS has been studied in [9]. It was based on a 6-piston pump unit and had geometrical displacement of about 30 cm^3. In addition, two independently controlled outlets were realised. The second prototype (see Figure 1) has the same base but the following improvements are aim at:

1. Increasing the number of independent outlets
2. Increasing the number of pumping pistons
3. Decreasing geometrical displacement of each individual pumping piston
4. Minimising the leakages

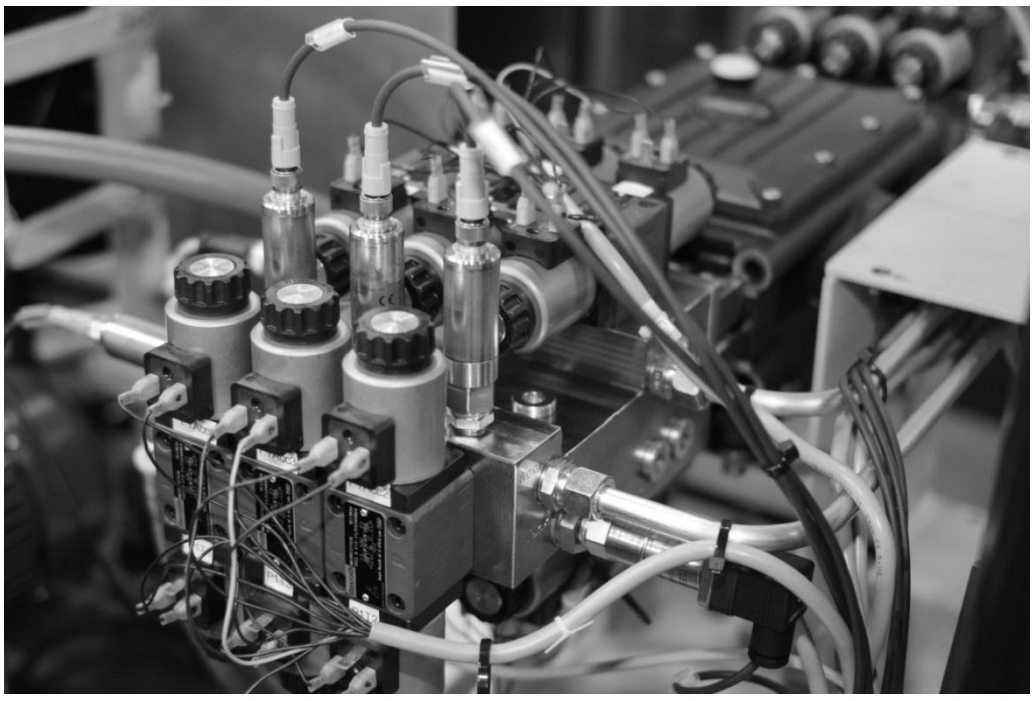

Figure 1. Digital multi-outlet pump-motor unit with commercial control valves.

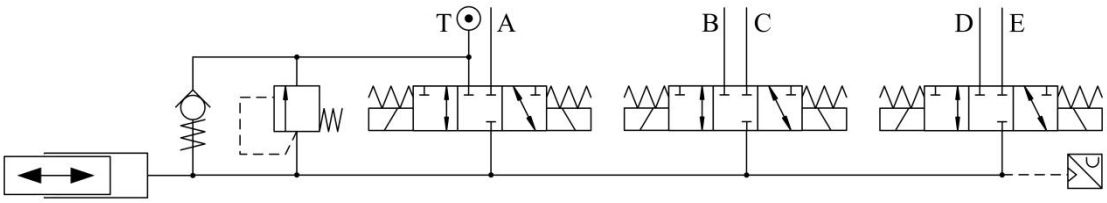

Figure 2. Connectivity of control valves for a pumping piston in the studied DHPMS.

The studied DHPMS has five independent outlets and it has an option to be expanded to a 12-piston machine. However, a single 6-piston unit is studied in this paper. Original geometrical piston displacement of about 5 cm^3 is reduced to 1.8 cm^3 yielding overall geometrical displacement of 10.8 cm^3. Control valves the DHPMS uses, are commercial Bosch Rexroth SEC 3/3 poppet valves witch are directly controlled with solenoid actuation. Figure 2 shows the connection of a cylinder chamber to the inlet and outlet ports through the directional valves; each pumping cylinder requires three valves. In addition, original check valves ease the filling from the tank line. The pressure relief valves prevent the chamber pressures to rise too high in case of an operation failure. The setting for the relief valves is 20 MPa and the pressure of each piston chamber can be monitored as well.

2.2. Measurement setup

The measurement setup is shown in Figure 3. The numbered components 1–10 are detailed in Table 1, whereas the used transducers I–VII are itemised in Table 2. A 300 kW DC motor (1) is used as a prime mover and the motor torque can be measured by a torque measurement flange (I). A flywheel (2) is attached to the motor shaft and it includes a gear ring enabling a magnetic rotation angle measurement (II). The rotational speed is further calculated according to the time between the pulses. Additionally, a non-linear filter algorithm is used to give a better estimate for the rotational speed [9]. A centrifugal pump (3) is used to feed the inlet port of the DHPMS. The inlet pressure is around 0.2 MPa and can be measured from the line (III).

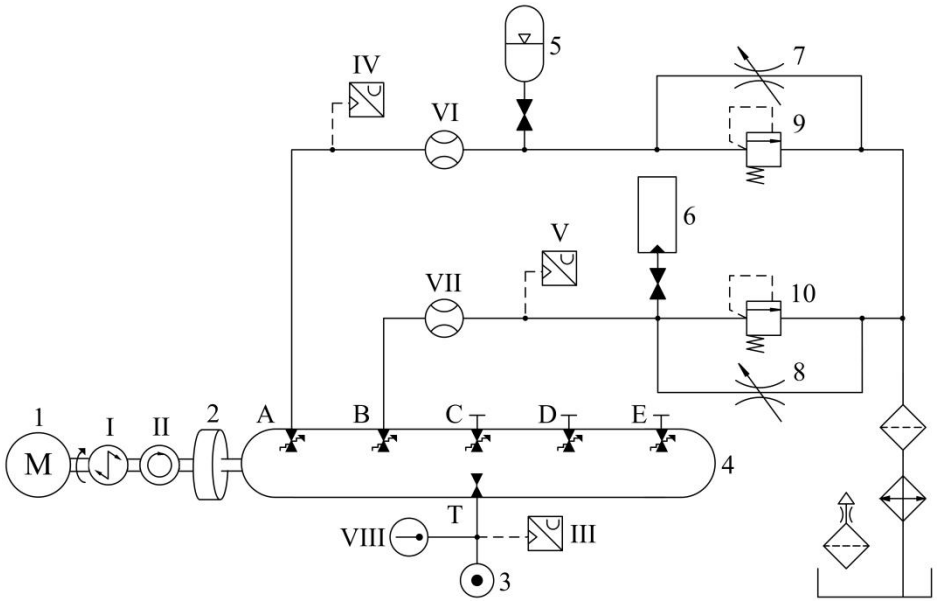

Figure 3. Hydraulic diagram of the measurement system.

Table 1. Numbered components 1–10 in Figure 3.

no.	Component	Details
1	DC Motor	Nominal power: 300 kW
2	Flywheel	Moment of inertia: 0.15 kgm2
3	Centrifugal pump	Max. flow rate: 200 l/min, Max. head: 9 m
4	Six piston pump/motor unit	Geometrical displacement: 10.8 cm3
5	Accumulator	Nominal size: 4 l, Inflation pressure: 5 MPa
6	Rigid wall volume	Fluid volume: 2 l
7	Needle valve A	Adjustable flow rate
8	Needle valve B	Adjustable flow rate
9	Pressure relief valve A	Adjustable opening pressure
10	Pressure relief valve B	Adjustable opening pressure

Table 2. Numbered transducers I–VIII in Figure 3.

no.	Transducer	Range	Accuracy
I	Torque	±200 Nm	0.1%
II	Rotation angle	–	2.5°
III	Inlet pressure	0–2 MPa	0.2%
IV	Outlet pressure A	0–25 MPa	0.2%
V	Outlet pressure B	0–25 MPa	0.2%
VI	Outlet volume A	–	0.1 cm3
VII	Outlet volume B	–	0.1 cm3
VIII	Inlet temperature	-50–150 °C	0.2%

The pump/motor unit has six pistons and five independent outlets but only two of them are used. A hydro-pneumatic accumulator (5) is installed in the outlet A but it can be isolated from the system with a ball valve. The outlet line B has an additional rigid wall volume (6) but it can be also isolated from the system. The outlet lines also have adjustable needle valves (7, 8) and pressure relief valves (9, 10) to realise different loadings. The pressures (IV, V) as well as the volume flows (VI, VII) are measured at each outlet. In addition, the oil temperature can be monitored using a transducer (VIII) mounted to the DHPMS inlet.

2.3. Control Method

Displacement control is used to control the volume flow at a DHPMS outlet. Graph (a) in Figure 4 illustrates the control principle. The cumulative fluid volume reference V_{ref} is a time integral of a volume flow reference set by a user. In the example sequence, the pumping mode (mode decision 1) is decided before the piston reaches the Bottom Dead Centre (BDC). As the difference between the target volume V_{ref} and the estimated fluid volume V_{est} is larger than geometrical piston displacement, it is chosen to pump to the outlet X in order to minimise the fluid volume error at that outlet. Simultaneously, effective piston displacement calculated considering the compressibility is added to the cumulative fluid volume estimate V_{est}. The actual fluid volume at the outlet increases after a delay during the pumping stroke. The motoring mode is decided before the piston reaches the Top Dead Centre (TDC). In order to keep the fluid volume error of the outlet X in its minimum, the controller chooses to motor from the tank line T; hence,

the estimated and actual volumes remain unchangeable. At the next pumping mode decision instant (mode decision 3) it is chosen to increase the fluid volume of the outlet X to minimise the volume error. Correspondingly, an optimal choice for the next motoring mode (mode decision 4) is to motor from the outlet X to decrease the fluid volume closer to the target value.

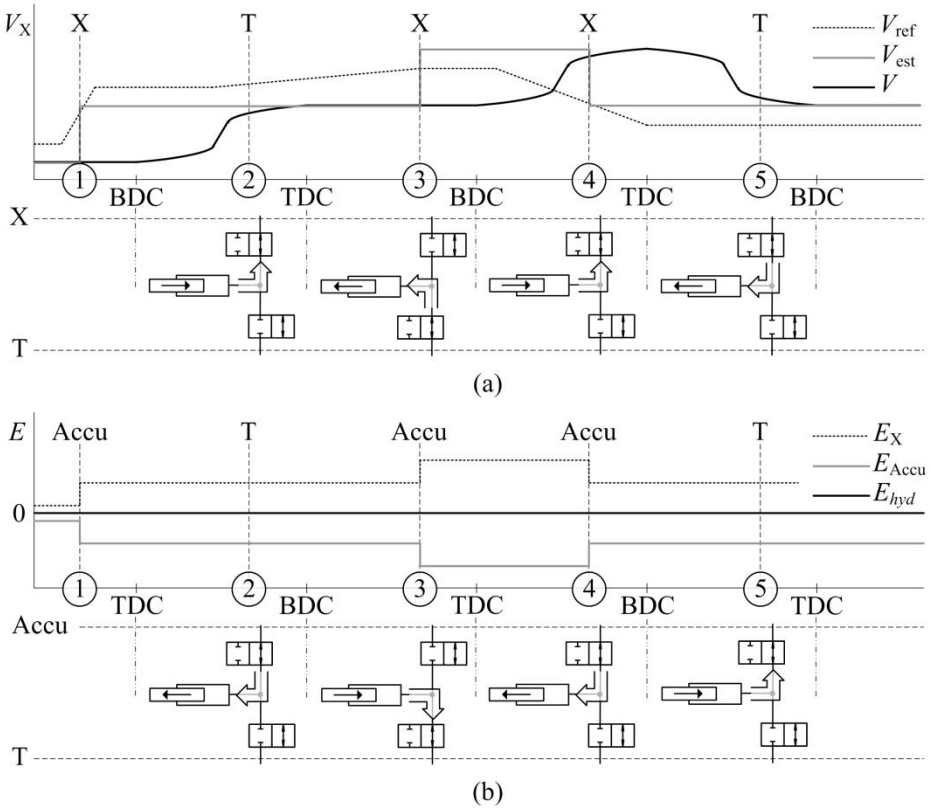

Figure 4. Mode choosing principle for the displacement control (a) and accumulator energy control (b).

The DHPMS is able to use an accumulator as a secondary power source as well. A premise for controlling the accumulator energy is to balance the hydraulic power of the DHPMS which results in the stabilised prime mover power. Graph (b) in Figure 4 shows an example of the mode selection logic for an accumulator line which is selected in tandem with the flow controlled outlet presented in graph (a) in Figure 4. Thus the modes are selected for a piston pair having an opposite phase. The example assumes that the pressure levels at the both outlets are the same. Therefore, each time it has decided to pump to the outlet X, the motoring from the accumulator is selected yielding the balanced total energy for a pair of pistons (mode decisions 1 and 3). Correspondingly, the controller decides to pump to the accumulator line in case the motoring from the outlet X has been decided for another piston (mode decisions 4). The DHPMS can operate also as a transformer; therefore, stabilisation of the prime mover power can be realised independent of the accumulator pressure. For example, if the fluid is pumped to an outlet having three times bigger pressure level than that of the accumulator, the motoring rate from the accumulator need to be three times higher than the pumping rate to the outlet in order to balance the hydraulic power of the DHPMS. Thus, the only restriction is set by the available flow rate at the outlets.

An accurate timing of the DHPMS control valves is important from the smooth operation point of view. In addition, unnecessary pressure losses can be avoided by compensating the compressibility of the fluid during the pumping and motoring processes. Graph (a) Figure 5 shows the valve control principle in case the fluid is pumped to the higher pressure than the piston chamber is filled from (ideal pumping cycle). The low pressure valve is closed at the BDC and chamber pressure is raised to the level of the high pressure before the high pressure valve is opened. The pumping continues until the high pressure valve is closed at the TDC and the pressure is released in the beginning of the return stroke. The low pressure valve is opened at the moment when the pressure difference over the valve is zero. After the chamber is filled the low pressure valve is closed again at the BDC.

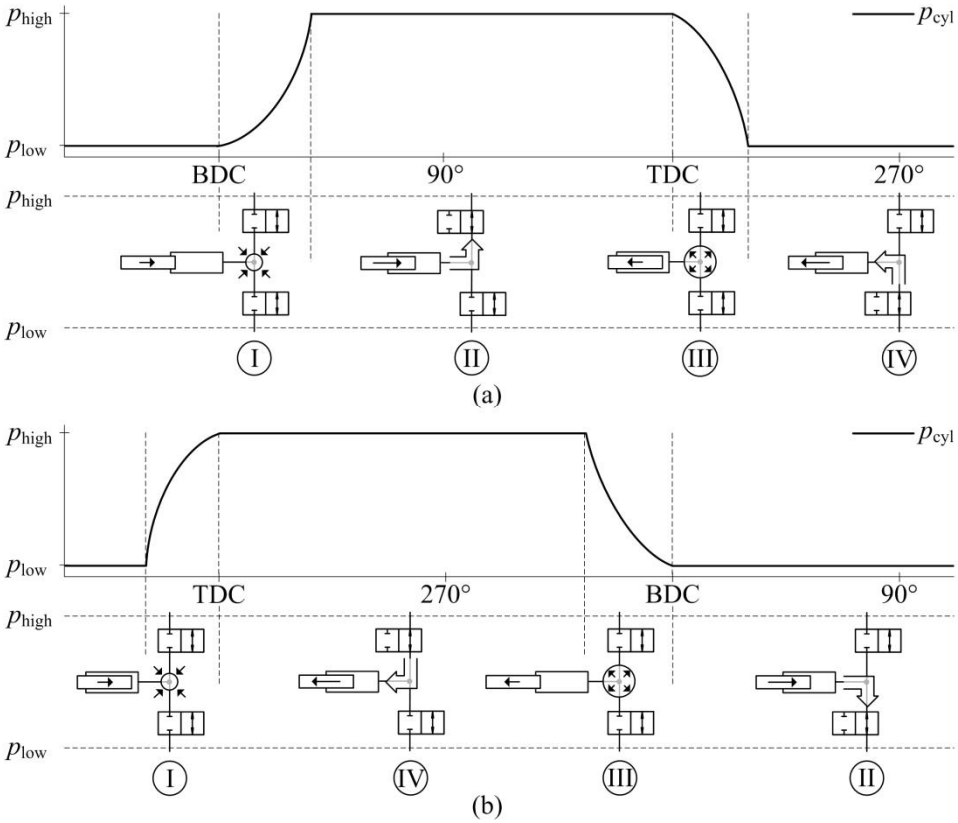

Figure 5. Valve control principle for the pumping (a) and motoring (b) cycles: Pre-compression (I), pumping (II), de-compression (III), motoring (IV).

Graph (b) in Figure 5 presents the valve control principle in case the fluid is motored from the higher pressure and drained to the lower pressure (ideal motoring cycle). The low pressure valve is closed in the end of the pumping stroke before the TDC. The closing is timed such that the chamber pressure rises to the level of the higher pressure before the high pressure valve is opened at the TDC. The chamber fills from the higher pressure until the high pressure valve is closed before the BDC. As the return stroke still continues the chamber pressure decreases to the level of the lower pressure. The low pressure valve is opened at the BDC the pumping to the lower pressure begins again. The valves are controlled according to the estimated rotation angle and the valve delays can be also compensated for by utilizing an estimate of the rotational speed.

2.4. Efficiency Calculation

The studied DHPMS is measured for its pumping and motoring efficiencies. For the full pumping and motoring cycles, the volumetric and hydro-mechanical efficiencies can be analysed in addition to the total efficiency. For partial displacement, only the total efficiency is determined because geometrical displacement is difficult to define as some of the pistons are occasionally disabled. The volumetric efficiency for a pumping cycle is calculated from

$$\eta_{\mathrm{vol}} = \frac{Q}{n\,V_{\mathrm{g}}} \tag{1}$$

where Q is the measured volume flow rate, n the rotational speed, V_{g} geometrical displacement of the DHPMS. In addition, the hydro-mechanical efficiency for a pumping cycle is calculated from

$$\eta_{\mathrm{hm}} = \frac{\Delta p\,V_{\mathrm{g}}}{2\pi\,T} \tag{2}$$

where Δp is the measured pressure difference over the DHPMS and T the measured torque. The total efficiency is a product of the volumetric and hydro-mechanical efficiencies which results in the equation

$$\eta_{\mathrm{tot}} = \frac{Q\,\Delta p}{2\pi\,n\,T} \tag{3}$$

For a motoring cycle the equations are the inverse.

3. EXPERIMENTAL RESULTS

3.1. Idling losses

Figure 6 shows the parasitic losses of the DHPMS during idling; thus, the fluid is received from and pumped to the tank line. The losses mainly consist of the pressure losses in the on/off control valves and mechanical friction losses. Losses are determined for six different rotational speeds between 200–1200 r/min by measuring the mechanical input power from the rotation shaft. The oil temperature throughout the tests is around 39 °C.

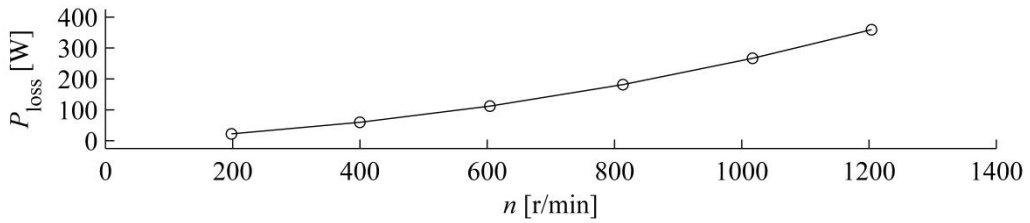

Figure 6. Idling losses with the oil temperature of 39 °C.

The idling losses are around 60 W at the rotational speed of 400 r/min, whereas the number is about 180 W at the rotational speed of 800 r/min yielding that doubling the speed results in three times bigger parasitic losses. At the rotational speed of 1200 rpm, the losses are around 360 W.

3.2. Pumping efficiency

The pumping efficiency of the DHPMS at full displacement is measured for the rotational speeds of 500, 750 and 1000 rpm, and the pressure differences of 4–16 MPa are studied. The outlet A is used with the accumulator disengaged. The different loadings are realised by adjusting the opening pressure of the pressure relief valve to a desired level. The needle valve is kept closed. The oil temperature of about 39 °C is used throughout the tests. Figure 7 show the volume flow loss as a relation of the pumped and theoretical volume flows at the measured rotational speed. Due to the big dead volume at the pumping cylinders, the effective volume flow is considerably smaller than the theoretical one. It can be seen that the compressibility is somewhat linear in relation to the pressure difference over the DHPMS. The volume flow loss is around 23% at the highest studied working pressure.

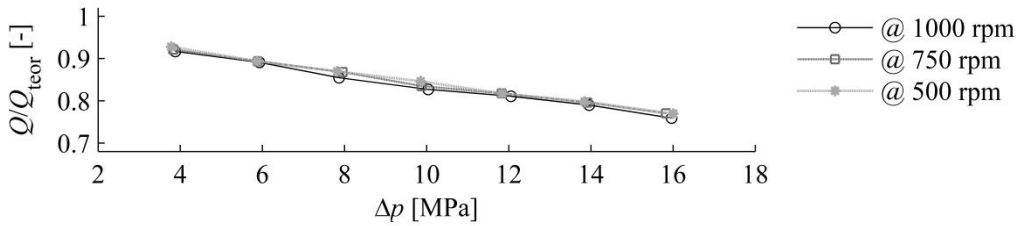

Figure 7. Relation of the pumped and theoretical volume flow with the oil temperature of 39 °C.

Graph (a) in Figure 8 shows the total, volumetric and hydro-mechanical pumping efficiencies at full displacement when the rotational speed of 1000 r/min is used. The volumetric efficiency varies between 0.76–0.92 which corresponds to the volumetric flow loss due to the compressibility of the fluid; the volumetric efficiency decreases as the pressure difference increases. The hydro-mechanical efficiency varies from 0.71 to 1.1 such that the lowest value is present at the smallest pressure difference and the highest value at the biggest pressure difference respectively. Due to the drastic compression of the fluid, the hydro-mechanical efficiency can be over one. The total efficiency is about 0.65 at lowest but stays above 0.8 at the pressure differences over 10 MPa.

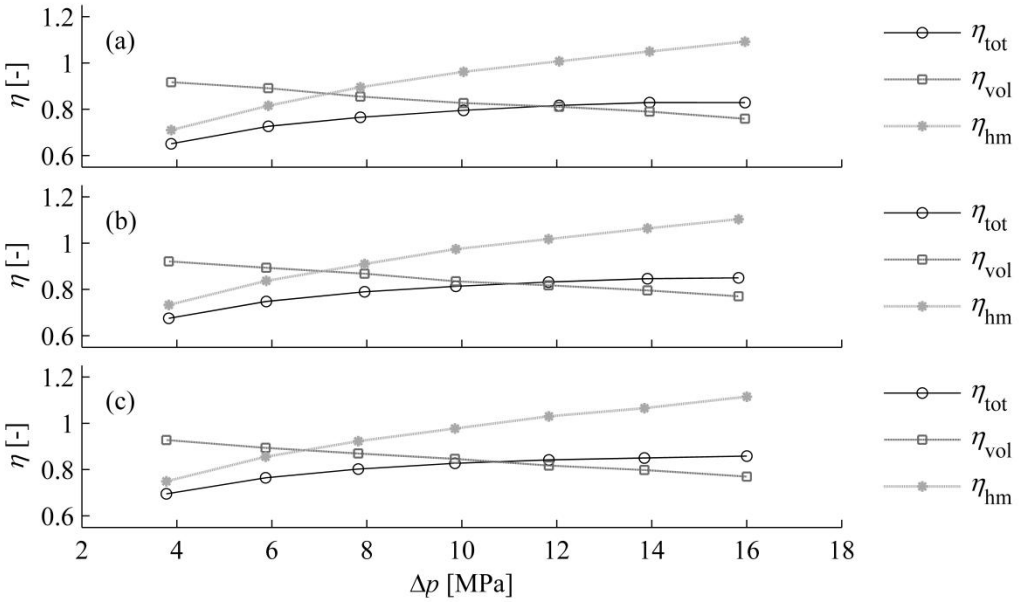

Figure 8. Total, volumetric and hydro-mechanical pumping efficiencies (full displacement with the oil temperature of 39 °C) with the rotational speeds of 1000 r/min (a), 750 r/min (b) and 500 r/min (c).

The volumetric efficiency is somewhat independent of the rotational speed as shown in graphs (b) and (c) in Figure 8. The rotational speed of 750 r/min is used in case of graph (b) and 500 r/min in case of graph (c) correspondingly. The hydro-mechanical losses decrease when lower rotational speeds are used; pressure losses in the on/off control valves are smaller at the lower rotational speeds. At the rotational speed of 750 r/min the total efficiency varies between 0.68–0.85 and at 500 r/min the total efficiency is between 0.70–0.86.

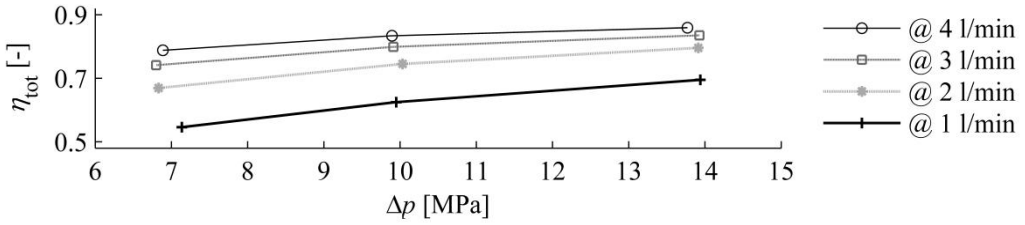

Figure 9. Total pumping efficiencies at partial displacement with the rotational speed of 500 r/min and the oil temperature of 40 °C.

For partial displacement, only the total efficiencies are measured due to challenges in determining the corresponding geometrical displacements for a piston-by-piston control. The rotational speed of 500 r/min is used while the oil temperature has been around 39 °C. In addition, the accumulator is engaged. Three pressure levels are studied resulting in the pressure differences of about 7, 10 and 14 MPa. Figure 9 shows the results: The total efficiency reduces when the volume flow decreases. With about 20% flow rate of the theoretical maximum (@ 1 l/min), the total efficiency is around 0.55–0.70. For the flow rates of 40%, 60% and 80% the numbers are 0.67–0.80, 0.74–0.84 and 0.79–0.86 respectively.

3.3. Motoring efficiency

The motoring efficiency of the DHPMS at full displacement is studied for the rotational speeds of 500, 750 and 1000 rpm. The fluid is received from the outlet A where the accumulator is engaged. The pressure differences of 6–16 MPa are studied and the oil temperature of about 37 °C is used. The volume flow loss as a relation of the motored and theoretical volume flows are shown in Figure 10. The effective volume flow is considerably smaller than the theoretical one, because the motoring valve is closed long before the BDC due to the pressure decompression (big dead volume). The volume flow loss is 6–19% depending on the working pressure and rotational speed.

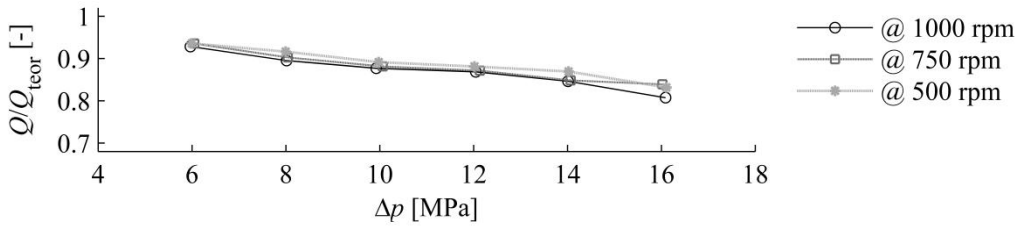

Figure 10. Relation of the motored and theoretical volume flow with the oil temperature of 37 °C.

The total, volumetric and hydro-mechanical motoring efficiencies at full displacement with the rotational speed of 1000 r/min are shown in graph (a) in Figure 11. The volumetric efficiency increases as the pressure difference rise and it varies between 1.08–1.24. The efficiencies over one are measured because the motored volume is smaller than the theoretical one due to the decompression. The hydro-mechanical efficiency varies from 0.59 to 0.68 such that it is at highest when the pressure difference is 12MPa. The total efficiency is just over 0.8 at the highest pressure, whereas the lowest number is 0.64 in case of the 6 MPa pressure difference.

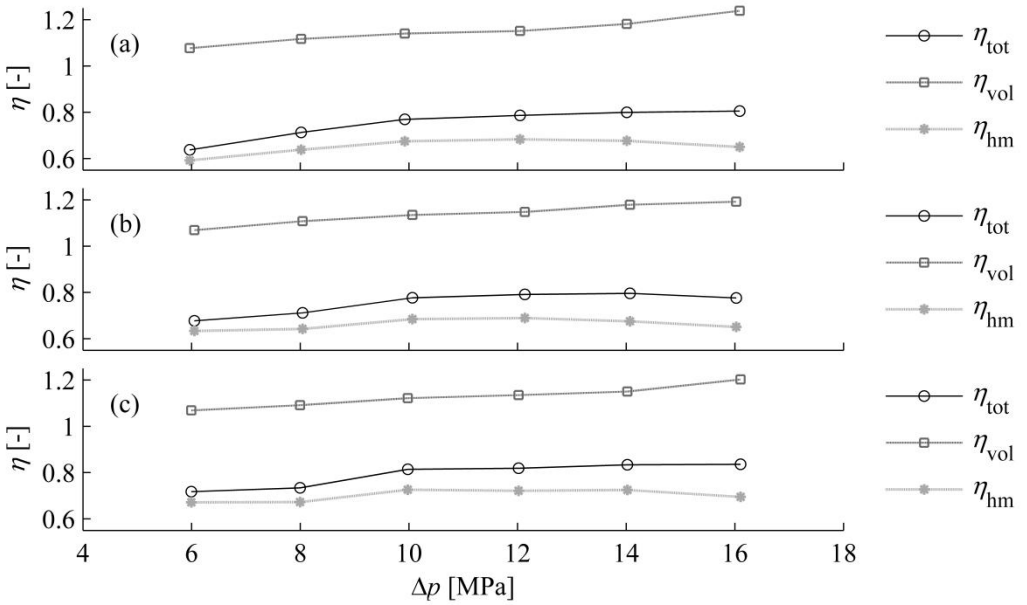

Figure 11. Total, volumetric and hydro-mechanical motoring efficiencies (full displacement with the oil temperature of 37 °C) with the rotational speeds of 1000 r/min (a), 750 r/min (b) and 500 r/min (c).

The volumetric efficiency slightly decreases at the lower rotational speeds. The hydro-mechanical efficiency is somewhat higher. The efficiencies with the rotational speed of 750 r/min are shown in graph (b) in Figure 11, whereas graph (c) in Figure 11 shows the efficiencies with the rotational speed of 500 r/min. The total efficiencies in the measurements vary between 0.68–0.80 and 0.72–0.84 respectively.

3.4. Transforming efficiency

The power transfer between the outlets is studied in a case which the fluid is received from the accumulator and pumped to another outlet (or to the tank line). The flow reference of the outlet B is set to 3 l/min and the rigid wall volume is engaged to the outlet. In addition, the loading pressure is set to about 10 MPa by using the needle valve. The accumulator has been initially charged to 13 MPa and the motoring from that outlet starts after a second the measurement has been started.

Graph (a) in Figure 12 shows that the outlet B pressure (p_B) is 9.7–10.7 MPa during the measurement. The accumulator pressure p_A starts to decrease at the moment the motoring begins ending up to 8.4 MPa. The motored volume flow Q_A increases while the accumulator pressure decreases due to the control method (graph (b) in Figure 12) whereas the pumped volume flow Q_B stays somewhat unchangeable. The hydraulic power pumped to the outlet B (P_B) is about 0.5 kW throughout the measurement as shown in graph (c) in Figure 12. At the moment when the accumulator control is enabled, the DHPMS starts to motor from the outlet A at an average power of -0.5 kW (P_A). Thus, the average power fed by the electric motor drops near the value of the constant idling loss.

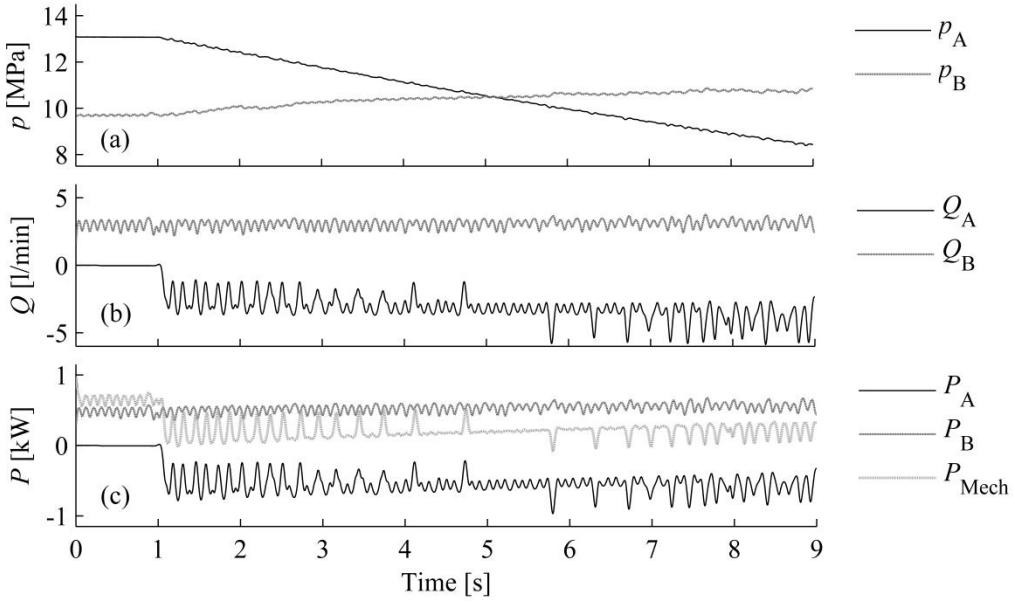

Figure 12. Power transfer between the outlets with the rotational speed of 750 r/min and the oil temperature of 43 °C: Outlet pressures (a), outlet volume flows (b) and powers (c).

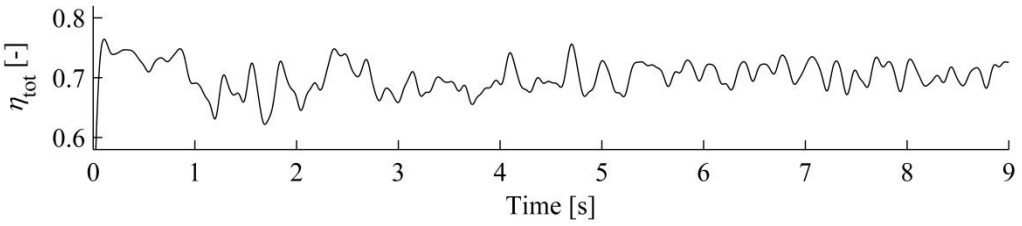

Figure 13. Total efficiency during the power transfer between the outlets.

The total efficiency of the DHPMS during the power transfer is shown in Figure 13. The efficiency is calculated by dividing the output power (P_B) by the input power (P_{Mech}–P_A) and it is about 0.7 on average. Hence, the efficiency does not drop in the transformer mode but is comparable with the pumping and motoring efficiencies.

4. DISCUSSION AND CONCLUSIONS

The results indicate that the dead volumes of the DHPMS piston chambers become large if commercial valves are used. Moreover, increasing the number of independent outlets results in even bigger dead volumes. These large compression volumes affect the produced volume flow but the compressibility does not necessarily decrease the total efficiency of the machine; the compressibility can be taken into account in the valve timing. Thus, the power required to compress the fluid can mostly be recovered when the pressure is released again. This unique feature of "digital valve plate" is also seen in the calculated efficiencies when the standardised equations are used: the hydro-mechanical efficiency can rise over one during a pumping cycle, as can the volumetric efficiency during a motoring cycle.

For pumping, the total efficiency of the studied DHPMS is mostly over 0.7. The efficiency is at its highest when the rotational speed is low or the operating pressure is high. However, the pressure losses in the control valves approximately triple when the rotational speed is doubled; therefore, the total efficiency reduces when the rotational speed increases. In addition, the pressure losses are relatively higher for the low power outputs (low operating pressures). Thus, the flow capacity of the control valves is too low for the application, in spite of the installed check valves easing the chamber filling.

For motoring, the total efficiencies are somewhat lower in comparison with the pumping efficiencies because the fluid is also returned to the tank line through the on/off control valves; the DHPMS cannot take advantage of the check valves as it does during pumping. Aside from pumping and motoring, the DHPMS can also transfer the power between the outlets. The total efficiency of the power transfer is comparable with the pumping and motoring efficiencies at similar pressure levels. Moreover, the DHPMS functions as a hydraulic transformer, as both the flow and pressure can be altered. The feature allows balancing the power of the prime mover (operation as a hydraulic hybrid).

All in all, the tested pump/motor unit fulfils most of the requirements set for the second prototype DHPMS. First of all, the control valves are leakage free, allowing effective use of the accumulator as an energy source/sink. Secondly, the decreased geometrical displacement of each pumping piston improves the fluid volume resolution at the outlets, which is beneficial if actuators are controlled directly with the DHPMS. In

addition, the DHPMS has five independent outlets, allowing the displacement control of two actuators, whereas a residual outlet can be reserved for an accumulator. A disadvantage of the studied unit is its small total displacement, leading to low power output. However, the number of the pumping pistons can be doubled by merging two pump/motor units into one. That will be the next step of the study.

REFERENCES

[1] L. Wadsley, "Optimal system solutions enabled by digital pumps," in The 52nd National Conference on Fluid Power, NCFP 2011, Las Vegas, Nevada USA, 2011.

[2] M. Ehsan, W. Rampen, and S. Salter, "Modeling of digital-displacement pump-motors and their application as hydraulic drives for nonuniform loads," Journal of Dynamic Systems Measurement and Control, vol. 122, no. 1, pp. 210–115, Jun. 1997.

[3] J. Taylor, W. Rampen, D. Abrahams, and A. Latham, "Demonstration of a digital displacement hydraulic hybrid bus," in 2015 JSAE Annual Congress (Spring), Yokohama, 2015.

[4] G. Payne, A. Kiprakis, M. Eshan, W. Rampen, J. Chick and A. Wallace, "Efficiency and dynamic performance of Digital DisplacementTM hydraulic transmission in tidal current energy converters," Institution of Mechanical Engineers, Part A: Journal of Power and Energy, March 2007, vol. 221 no. 2 pp. 207-218.

[5] M. Sasaki, A. Yuge, T. Hayashi, H. Nishino, M. Uchida and T. Noguchi, "Large capacity hydrostatic transmission with variable displacement," in The 9th International Fluid Power Conference, 9. IFK, Aachen, Germany, 2014.

[6] M. Linjama and K. Huhtala, "Digital pump-motor with independent outlets," in The 11th Scandinavian International Conference on Fluid Power, SICFP'09, Linköping, Sweden, 2009.

[7] M. Karvonen, M. Heikkilä, M. Huova, M. Linjama, and K. Huhtala, "Inspections on control performance of a digital hydraulic power management system supplying digital and proportional valve driven multi-actuator system," in The 9th International Fluid Power Conference, 9. IFK, Aachen, Germany, 2014.

[8] M. Heikkilä, M. Linjama, and K. Huhtala, "Digital hydraulic power management system with five independent outlets - simulation study of displacement controlled excavator crane," in The 9th International Fluid Power Conference, 9. IFK, Aachen, Germany, 2014.

[9] M. Heikkilä, J. Tammisto, M. Huova, K. Huhtala, and M. Linjama, "Experimental evaluation of a piston-type digital pump-motor-transformer with two independent outlets," in ASME/Bath Symposium on Fluid Power and Motion Control, FPMC 2010, Bath, UK, 2010.

DISCRETE PISTON PUMP/MOTOR USING A MECHANICAL ROTARY VALVE CONTROL MECHANISM

Michael B. Rannow, Perry Y. Li*, Thomas R. Chase
University of Minnesota
Department of Mechanical Engineering
111 Church St. SE
Minneapolis, MN 55455
Email: lixxx099@umn.edu*

ABSTRACT

Hydraulic pumps and motors are desirable for high power density and ruggedness, but they typically exhibit lower efficiency than competing technologies. In conventional devices, high pressure is maintained on each piston for its full stroke, and displacement is varied by changing the stroke length. Maintaining high pressure on all pump/motor interfaces causes leakage and friction losses to remain nearly constant as displacement is reduced, resulting in low efficiency, particularly at low displacements. A different approach is to vary the displacement by removing high pressure from unneeded pistons. This discrete piston control approach has been proposed by a number of researchers, but it is typically accomplished using two electrohydraulic valves per piston, which can increase cost, complexity, and reduce robustness. In this paper a method of discrete piston control using hydromechanical valves is described. A two degree-of-freedom valve that can rotate and translate axially controls the enabling and disabling of the individual pistons and adjusts the displacement. Several strategies for creating a discrete piston device are described, along with the structure of the control system. Preliminary experimental results from a prototype pump/motor are also presented.

KEYWORDS: Discrete piston control, bi-directional pump/motor, rotary valve, mechanical valve timing

1. INTRODUCTION

Hydraulic actuation systems provide many attractive features, such as high power density, ruggedness, robust linear actuation, and low cost, but they often suffer from lower efficiency than competing actuation technologies. The relatively low efficiency of hydraulic systems is due in part to the conventional control method of using throttling valves, and it is partially due to the efficiency of hydraulic components, such as pumps and motors. Hydraulic pumps and motors experience power losses due to friction and leakage between moving parts. Because high pressure is maintained on these moving parts regardless of the displacement of the device, these losses remain fairly constant

with displacement. This leads to devices which, while efficient at maximum displacement, can be very inefficient in other operating ranges.

Discrete piston control, or using valves to remove pressure from unneeded pistons to vary the displacement [1], has been proposed as a solution to this problem. By only maintaining high pressure on the lubricating gaps on pistons while they are needed, the leakage and friction losses can be made to scale down with displacement much more than in conventional stroke-varying devices. In comparison with conventional axial piston pumps and motors with adjustable swash plate angles, the discrete piston approach has the potential to reduce or eliminate a number of power loss mechanisms. By using valves rather than a valve plate to control the application of high and low pressure to the pistons, valve plate leakage and friction losses can be significantly reduced. A valve plate must act as a bearing and a seal, creating a trade-off between a tight fit to reduce leakage and a loose clearance to reduce friction. By separating the bearing and sealing functions using valves, the system can be better optimized. In fact, discrete piston control enables pump and motor architectures with pistons that do not rotate to have a variable displacement, eliminating the bearing losses altogether. By applying pressure to pistons only when needed, losses associated with pressurized pistons, such as leakage around the pistons, and leakage and friction at the piston slipper interface will reduce proportionally to the displacement. This is in contrast to conventional swashplate-type devices that have much more constant losses at these interfaces. The friction between the piston and bore will be affected by discrete piston control, since much of the friction is caused by the high pressure-generated side loads, which will be reduced with displacement. However, in conventional designs, the stroke length, moment arm, and relative velocity between the parts are also reduced with displacement, so benefit of the discrete piston approach with respect to the piston friction may be small, or it may be slightly detrimental. The fact that, in the discrete piston case, the stroke length is not reduced means that there will typically be more throttling losses than in the conventional case, although [2] [3] have proposed fully blocking a piston on its intake stroke to avoid this. If the control valves can be designed to have a minimal amount of throttling, the discrete piston control approach has a significant efficiency benefit as the displacement is reduced compared with conventional designs.

Discrete piston control is an active area of research, and many of the existing approaches use one or more electrically driven valve for each piston [1] [2] [3] [4] [5] [6]. While this approach gives significant flexibility, it can also increase the cost, decrease the robustness, and increase the complexity of packaging and controlling the device. In this paper, a means of achieving discrete piston control using a single mechanical control input on a bi-directional pump motor is described [7]. The approach is based on a two degree-of-freedom pilot valve that can rotate with the pump/motor shaft as well as translate axially. The pilot valve drives a simple mainstage spool valve for each piston, which connects each piston to either supply or tank. The rotary pilot valve contains a helical profile that creates a variable on/off timing signal that is sent to the mainstage valves as it rotates. By moving the valve axially, the timing of enabling/disabling the pistons is adjusted. By accomplishing the on/off switching through the rotary motion of the pilot spool which is connected to the pump/motor shaft, repeatable operation of the valve timing is ensured.

In the next section, several different strategies for the order and timing of disabling pistons are described and compared in order to decide which strategy to implement. In

section 3, the design concept of the mechanically controlled discrete piston pump/motor is described. In section 4, the results of a dynamic model and the overall predicted efficiency are presented. In section 5, some preliminary experimental results are presented that demonstrate the discrete piston concept and validate the dynamic model.

2. PISTON DISABLING STRATEGIES

With the ability to control the application of high and low pressure using valves, there is a lot of flexibility in how the individual pistons in the pump/motor are controlled. One key distinction is between the strategy of disabling a set number of pistons for their entire power stroke, or the approach of disabling all of the pistons for an adjustable fraction of their power stroke. One disabling strategy needs to be chosen before designing the mechanical input for achieving it. This section examines the advantages and disadvantages of each of these strategies.

2.1. Whole Piston Disabling

An example of the whole piston disabling approach is depicted in Fig. 1. This figure shows the flow from individual pistons in colors on the bottom, and the total output flow in black on the top. In this example, three of eight total pistons have been disabled, resulting in an effective displacement of 62.5%.

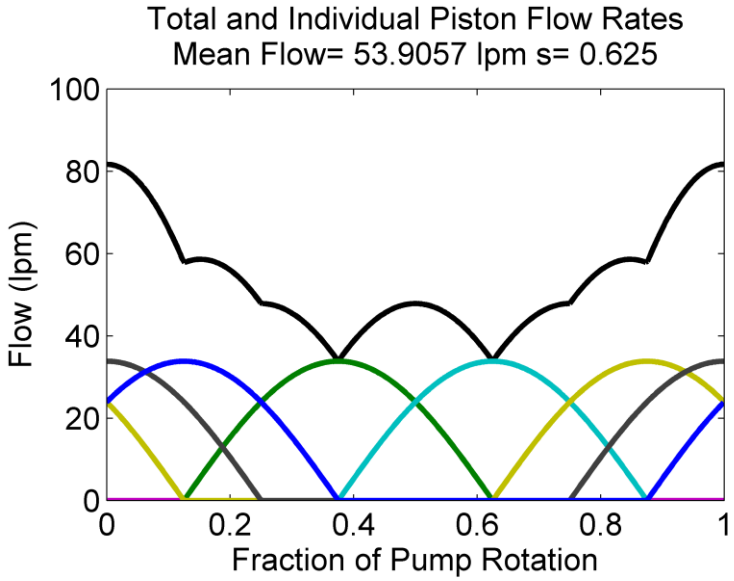

Figure 1. Individual piston and total flow rates for whole piston disabling

This example highlights a number of features of the whole piston disabling approach. First, if only whole pistons can be disabled, then, on a one-rotation basis, only discrete displacement settings are available, with the number of possible displacements set by the number of pistons. If finer adjustment of the displacement is required, it could be addressed by allowing a single piston to be disabled for a part of its stroke, while the rest of the pistons are either enabled or disabled for their entire stroke. The displacement resolution could also be increased by increasing the time window over which the displacement is averaged. For example, if five pistons are enabled for one rotation and six the next, then the two-rotation average displacement would be 68.75%.

The whole piston disabling approach can give some flexibility in that it can allow the order in which pistons are disabled to be varied. If the discrete piston valves are electronically controlled, then the disabling order can be arbitrarily varied. However, this becomes more difficult with a mechanically fixed control approach. In the example in Fig. 1, the pistons are not disabled in sequential order, but rather in an order that tries to distribute the disabled pistons around the group of pistons. The order of disabling can have a large effect on the overall flow ripple, but regardless of the order of the pistons being disabled, removing the flow of an entire piston of from the total output can result in a substantial flow ripple.

One key benefit of the whole piston disabling approach is its potential efficiency. By enabling/disabling pistons at the beginning or end of the piston stroke, when the flow in that piston is near zero, high throttling losses across the valves as they transition can be avoided. In addition, by preventing some pistons from seeing high pressure, the compressibility losses associated with the disabled pistons can be avoided.

Another factor to consider when selecting a piston disabling strategy for a mechanically controlled pump/motor is the feasibility of creating a mechanical control mechanism that can achieve it. For the whole piston disabling strategy, this can present a challenge; since all pistons are not controlled identically, there must be some way to translate a mechanical input to the sequential order of the pistons. For the approach taken in this paper, which is to use a rotating and translating valve spool, this can result in a complicated and long control mechanism.

2.2. Partial Stroke Disabling

A different piston disabling strategy is demonstrated in Fig. 2. In this example, each of the eight pistons is disabled for the same fraction of its power stroke. While the displacement and average flow in Fig. 1 and Fig. 2 are the same, the output profile of the flow is very different.

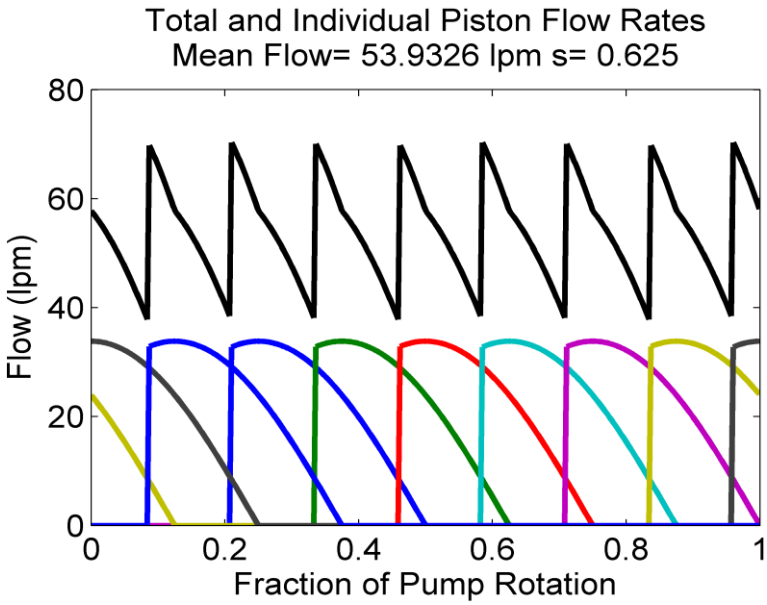

Figure 2. Individual piston and total flow rates for partial stroke disabling

The flow ripple from the partial stroke is smaller than that in the whole piston example. Figure 3 shows a comparison of the flow ripple magnitude, as measured by the 2-norm of the flow, between different discrete control techniques. This figure compares the Whole Piston (sequential order), Ordered Piston (whole piston with disabling order selected to distribute the disabled pistons), Partial Stroke disabling, Output PWM (on/off valve on pump outlet to control flow rate), or conventional Swashplate. Clearly all forms of discrete flow control have a larger flow ripple than the conventional approach, which highlights a key advantage of conventional technology. However, the discrete piston control approach has a much lower flow ripple than a digital hydraulic strategy applied to the entire output flow. This is especially true of the partial stroke disabling approach, which, other than a small region around 50% displacement, had a lower flow ripple than the ordered piston strategy.

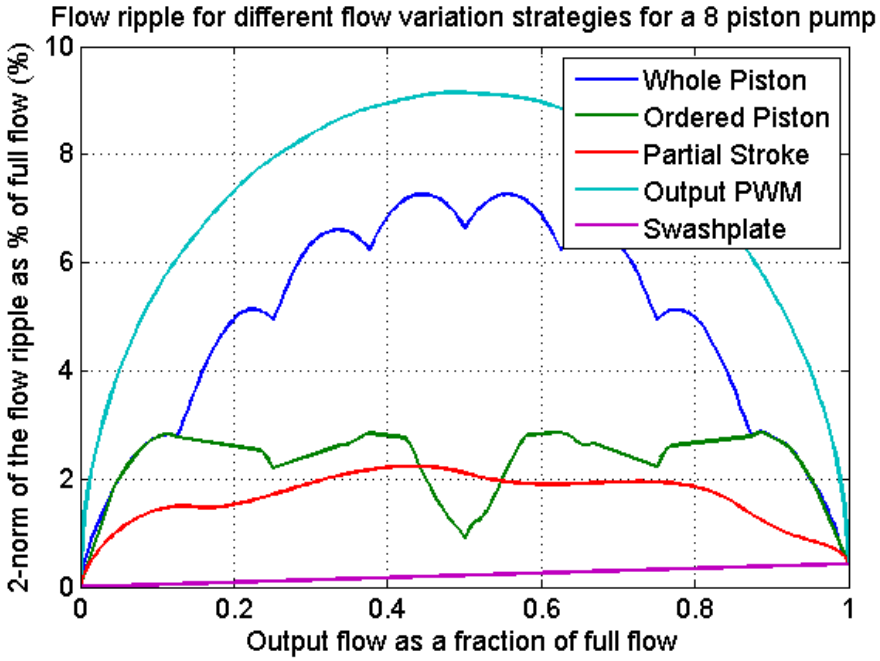

Figure 3. Comparison of flow ripple magnitude for different control strategies

The primary drawback to the partial stroke disabling approach is the additional transition and compressibility losses that result from switching. However, the transition loss can be reduced by using a fast transitioning valve, and the compressibility effect can be small, especially if pre-compression and de-compression of the oil volume are utilized.

The feasibility of creating a mechanically controlled partial stroke disabled pump/motor is significantly higher. Since all pistons are treated the same, the mechanical control system can be much more compact. In addition to creating a more compact device, a smaller control spool will have less internal leakage, which could have a larger effect on the overall efficiency than the additional transition and compressibility losses associated with partial stroke disabling. In the next section a concept for achieving partial stroke disabling with a two degree-of-freedom spool is described.

3. MECHANICAL CONTROL CONCEPT

The smaller flow ripple and the possibility of creating a simpler and more compact mechanical control mechanism favors the partial stroke disabling approach to creating a discrete piston pump/motor. The proposed design concept is to use a valve spool that rotates with the pump/motor shaft and can translate axially to adjust the timing of the piston enabling/disabling. A choice must be made between a single-stage device, in which the rotary valve is the main switching valve for each piston, or a two-stage system in which the rotary valve acts as a pilot stage for a series of mainstage valves. The advantage of the single stage approach is its simplicity; there is only one moving element, and the on/off timing is mechanically fixed to the pump/motor shaft. However, the single stage approach presents some significant design challenges. With the single rotary spool acting as the control valve for all of the pistons, the full pump/motor flow must pass through it, requiring a fairly large valve. The large valve can result in longer transition times and higher leakage. Additionally, the rotary valve will need to see full system pressure, which creates a trade off in designing the clearance on the valve; it must be tight enough to act as a seal, but loose enough to spin freely. These challenges outweighed the simplicity benefit of the single stage device.

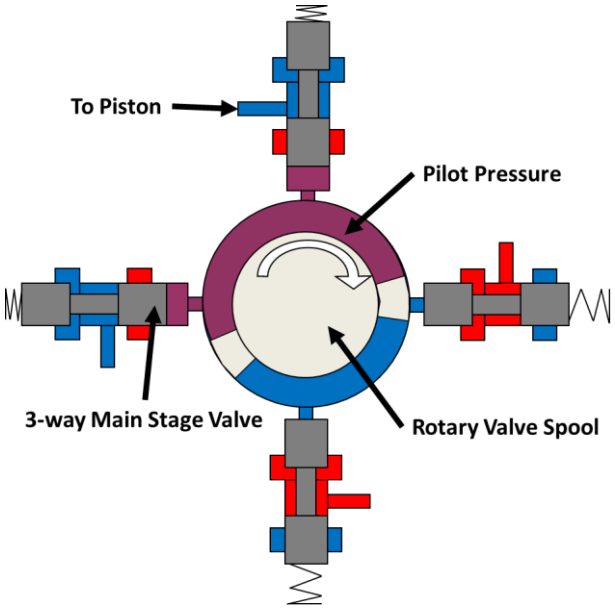

Figure 4. Sketch of three-way mainstage valves driven by a rotary pilot stage

Figure 4 presents a sketch of the two-stage valve configuration, with a single rotary valve applying either pilot or tank pressure to one end of a series of three-way mainstage spool valves. Each mainstage valve only needs to be sized to pass the flow from one piston, and the clearances on spool valve can be held tight enough to create a good seal against high pressure. The pilot spool, on the other hand, only sees pilot pressure, which allows it to rotate and translate with a looser clearance without a significant leakage loss.

3.1. Pilot spool design

A pilot spool that can accomplish variable partial stroke disabling is shown in Fig. 5. The pilot spool is separated into two sections: the control section on the left, and the pilot inlet section on the right. The pilot inlet section is connected to a pilot pressure

inlet port in the bore that allows oil to flow into the pilot spool from the pump/motor housing. The pilot pressure is then routed internally to the control section of the pilot spool. Tank pressure is also connected to the control section of the pilot spool through an internal connection to the left end of the spool. The right end of the spool connects to a shaped driveshaft that provides torque from the main pump/motor shaft to rotate the spool, and the driveshaft can translate axially with respect to the spool. To adjust the axial position of the pilot spool, a rod is pushed against the left end of the spool, while a return spring acts on the right end. On either end of the control section there are balancing grooves that connect to either the pilot or tank pressure internal passages. These notches are needed to counteract the unbalanced pressure force and moment from the pockets in the control section.

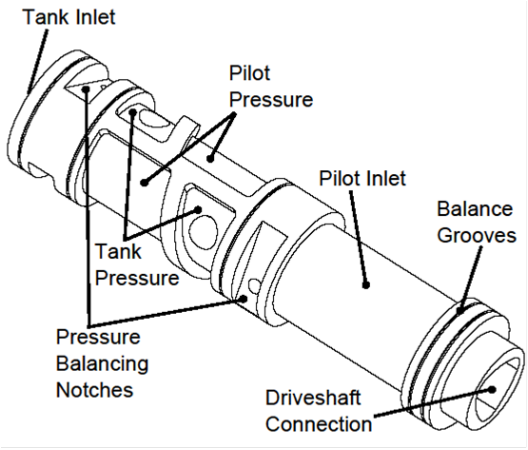

Figure 5. Rotary pilot spool

The control section of the spool connects to a series of passages in the bore that connect to the ends of the mainstage valves. There is one connection for each mainstage valve and piston. Figure 6 shows a diagram of the control section of the pilot spool if it were unwrapped from the spool. In this case, there are eight connections to the mainstage valves that are represented as circles in the figure. These connections are all at a single axial position on the pilot spool. As the valve rotates, each mainstage connection will pass over the pilot pressure (red) and tank pressure (blue) regions of the control section. When the mainstage valve is connected to tank pressure, the spring on the mainstage valve biases it to high pressure; when connected to pilot pressure, the spring is overcome and the mainstage valve moves to the low pressure position. Thus, the blue regions in Fig. 6 represent the area over which the pistons are enabled. As the pilot spool is translated with respect to the mainstage connections, the fraction of the piston stroke over which it is enabled is varied.

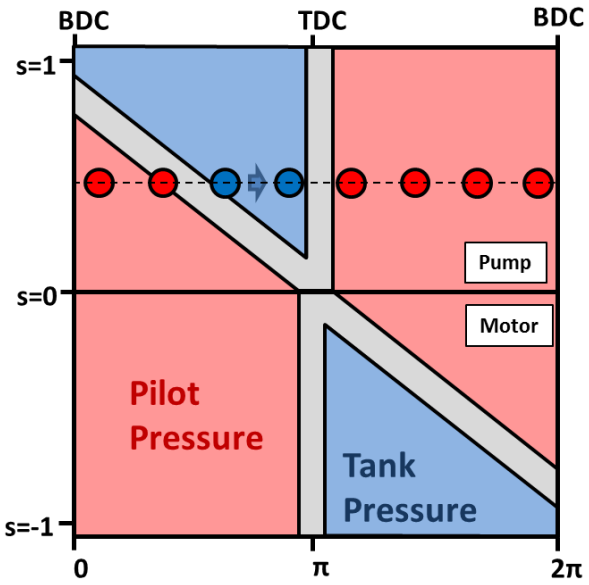

Figure 6. Diagram of the unwrapped control region of the pilot spool

For the direction shown, with the mainstage connections moving from left to right, the top half of Fig. 6 corresponds to the device acting as a pump, with the bottom half acting as a motor. The middle of the figure corresponds to each piston being at TDC. Thus, on the top half, the piston is enabled starting at some point in the stroke as it approaches TDC, causing the power stroke to start later than it would in the full displacement condition. On the bottom of the figure, the pistons will always start being enabled at TDC and then become disabled at some later point in the power stroke. The control areas are symmetric, so if the shaft rotation direction reverses, the system will still function the same, except the top of the figure will become the motor region, and the bottom will correspond to a pump. Thus, this pilot spool profile is able to achieve partial stroke disabling for the device acting as a pump or a motor in either direction. This pilot spool can be used with a piston-type pump/motor that has fixed pistons, such as a wobble plate or a radial piston device, to enable discrete piston control.

4. DYNAMIC MODEL

In order to predict the speed of the two-stage valve system, as well as the transition and compressibility losses, a dynamic model of the valves was created.

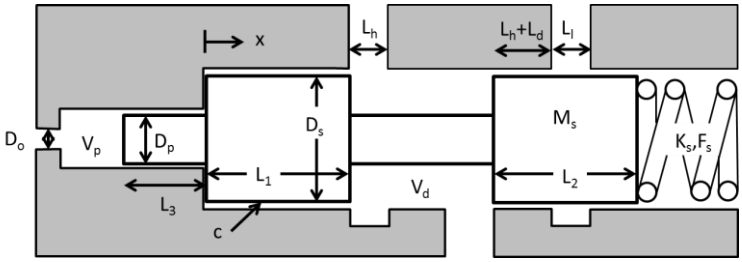

Figure 7. Sketch of the mainstage spool

Figure 7 depicts a sketch of a mainstage spool that is associated with an individual piston. The dynamic model of the control mechanism included the equation of motion for the mainstage spool, and pressure state equations for both the pressure in the piston

chamber and in the connection path between the pilot valve and the mainstage valve. The flow through the pilot and mainstage valves was assumed to follow the orifice equation. In the pressure state equations, the bulk modulus was assumed to follow the pressure-dependent model given in [8] for a mix of oil and entrained air:

$$\beta(P) = \frac{1+\left(\frac{V_{a0}}{V_{f0}}\right)\left(\frac{P_0}{P}\right)^{1/\gamma}}{1+\left(\frac{\beta_{oil}}{\gamma P}\right)\left(\frac{V_{a0}}{V_{f0}}\right)\left(\frac{P_0}{P}\right)^{1/\gamma}}\beta_{oil} \quad (1)$$

The results of the dynamic model are shown in Fig. 8. Note that, in the pump case, there is a check valve in parallel with the high pressure orifice to provide a safety mechanism in case of incorrect timing. It also helps lower the pressure drop by providing a parallel flow path.

The dynamic model predicts that the overall transition time of the mainstage valves is about 3 ms, which is more than fast enough for a pump/motor operating at 1800 RPM, which was the design speed. This speed could be increased by using a stronger spring and a higher pilot pressure (currently 20 bar).

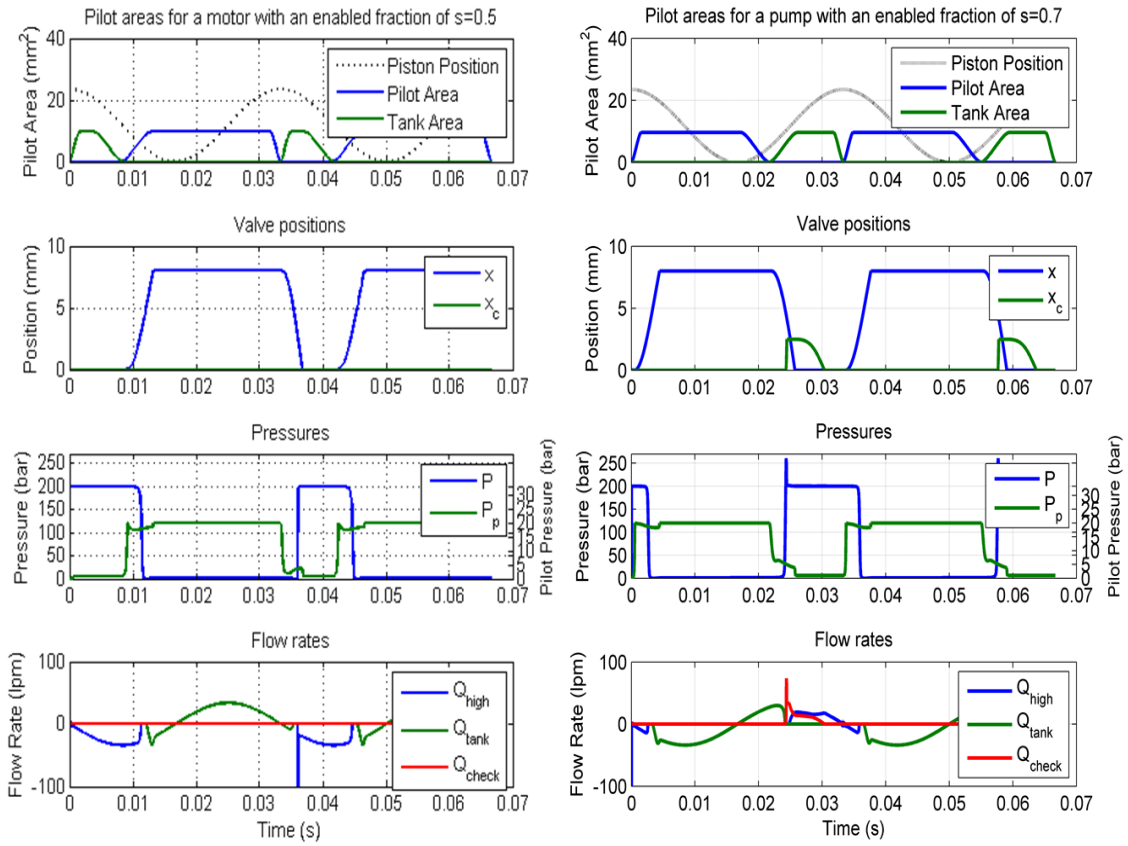

Figure 8. Simulation results for the motor (left) and pump (right) cases

By comparing the input and output power from the device, the model can be used to predict the transition, throttling, compressibility, and actuation power losses. These losses can be combined with estimates of the pilot and mainstage leakage, piston

leakage and friction, and slipper friction to generate an overall efficiency prediction for a roughly 48cc discrete piston pump motor.

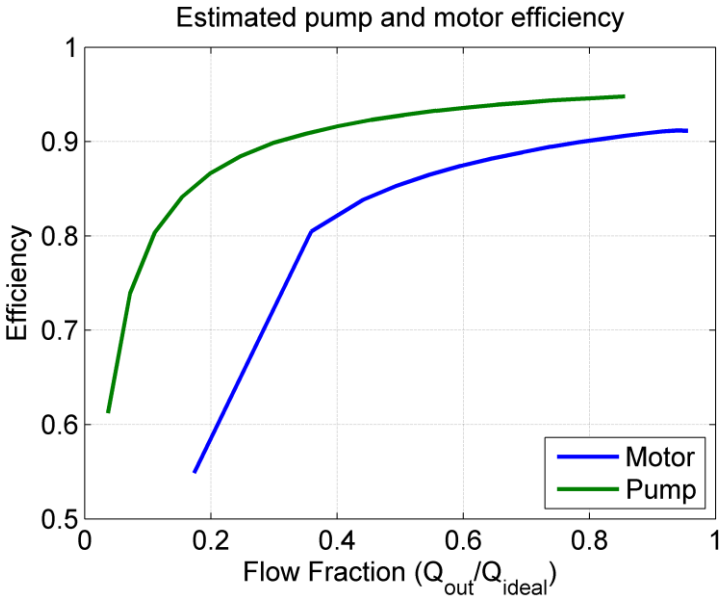

Figure 9. Overall predicted pump/motor efficiency

The predicted pump efficiency in Fig. 9 remains above 90% down to about 30% displacement, which is a wide range. The motor efficiency is significantly lower across the displacement range. This is due to the power lost when compressing the dead volume of oil at the start of the power stroke. In the pump case, this compression is accomplished by the piston travel, which is efficient. However, in the motor case, the compression is done by taking high pressure oil out of the supply line and throttling it down to the lower piston chamber so that it can be used to compress the oil. This causes a spike in power loss that does not occur in the pump case. The magnitude of this loss is heavily dependent on the dead volume of oil and the low-pressure compressibility of the oil and any entrained air. To reduce this loss, additional mechanisms can be used to shift or delay the valve timing so that the mainstage valve remains in its deadband during the compression event, allowing the piston to achieve some or all of the compression [9].

5. EXPERIMENTAL RESULTS

An experimental prototype constructed based on a wobble-plate type pump, the dynamic model described in this section, and the pilot valve in Fig. 5 was constructed. The prototype is an 8 piston, 48 cc bidirectional pump/motor. Figure 10 shows pressure traces for the device acting in motor mode with two different displacements. Depicted are the supply and tank pressures, as well as the pressure in one piston chamber and in the associated connection between the pilot and mainstages. The partial stroke disabling concept is clearly demonstrated through the varying width of the chamber pressure pulses. By measuring the time difference between the fall of the pilot pressure and the rising of the chamber pressure, the total transition time can be measured. The results across all pressures, speeds, and displacements are shown on the right side of Fig. 10. There is some variation, some likely due to the measurement technique, but the

average transition time is clearly around 3 ms, which matches closely with the dynamic model results shown in Fig. 8.

The efficiency of the pump/motor was also measured, but, unfortunately, due to unexpectedly high clearances on the mainstage valves, there was a high amount of internal leakage, which obscured any potential benefit of the discrete piston approach. There is some indication that, when the internal leakage is removed, the efficiency of the device is quite high, but this needs to be corroborated with testing done using better manufactured spools.

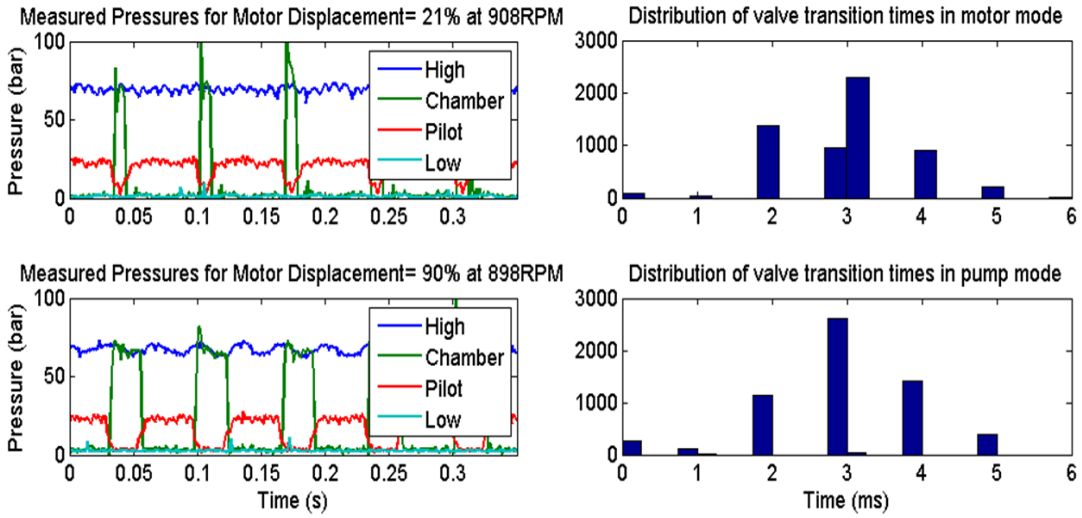

Figure 10. Experimental pressure traces for the motor case and measured valve transition times

6. CONCLUSION

A method for creating a bi-direction discrete piston pump/motor using a two degree-of-freedom valve was presented. Using mechanically and hydraulically controlled valves can reduce the cost and complexity of a discrete piston device using multiple electrically controlled valves for each piston. In this paper, several different strategies for enabling/disabling pistons were discussed, and the partial stroke variation approach was selected, due primarily to its comparatively small flow ripple and its greater feasibility for implementation using mechanical control. The structure of the control system was described, and the results of a dynamic simulation of the valve were presented. Finally, some preliminary experimental results that demonstrate the operation of the discrete piston device and validate the dynamic model were shown. This design has the potential to improve hydraulic pump/motor efficiency, particularly at low displacements, without requiring a large number of electrohydraulic valves.

REFERENCES

[1] Rampen, W., and Salter, S., 1990. "The Digital Displacement Hydraulic Piston Pump," Proceedings of the 9th International Symposium on Fluid Power, Cambridge, England.

[2] Nieling, M., Fronczak, F., and Beachley, N., 2005. “Design of a Virtually Variable Displacement Pump/Motor," Proceedings of the 50th National Conference on Fluid Power, Las Vegas, NV, pp. 323-335.

[3] Merrill, K., Holland, M., and Lumkes, J., 2011. “Analysis of Digital Pump/Motor Operation Strategies," Proceedings of the 52nd National Conference on Fluid Power, Las Vegas, NV.

[4] Merrill, K., 2012. “Modeling and Analysis of Active Valve Control of a Digital Pump/Motor," Ph.D. Thesis, Purdue University, West Lafayette, IN, 2012.

[5] Holland, M., 2012. “Design of Digital Pump/Motors and Experimental Validation of Operating Strategies," Ph.D. Thesis, Purdue University, West Lafayette, IN.

[6] Tammisto, J., Huova, M., Heikkila, M., Linjama, M., and Huhtala, K., 2010. “Measured Characteristics of an In-line Pump with Independently Controlled Pistons," 7th International Fluid Power Conference, Aachen, Germany.

[7] Rannow, M., Li, P., Chase, T., 2015. “Variable Displacement Pump Motor,” Provisional Patent.

[8] Wang, J., Gong, G., and Yang, H., 2008. “Control of Bulk Modulus of Oil Hydraulic Systems,” Proceedings of the 2008 IEEE/ASME International Conference on Advanced Intelligent Mechatronics, Xi'an, China, pp. 1390-1395.

[9] Rannow, M., 2016. “Achieving Efficient Control of Hydraulic Systems Using On/Off Valves,” Ph.D Thesis, University of Minnesota, Minneapolis, MN (In Preparation).

SIMULATION OF A VARIABLE DISPLACEMENT MECHANICALLY ACTUATED DIGITAL PUMP UNIT

Tyler Helmus
Purdue University
West Lafayette, IN, USA

Farid Breidi
Purdue University
West Lafayette, IN, USA

John Lumkes Jr.
Purdue University
West Lafayette, IN, USA

ABSTRACT

Current state of the art variable displacement pump/motors lack the ability to maintain high operating efficiency at low displacements. Digital pump/motors have been proposed to counter this shortcoming by minimizing leakages, friction losses, and compressibility losses. This is achieved by electrically controlling on/off valves at each port of each piston chamber and only pressurizing the chambers when necessary, leading to losses that scale more closely with displacement. While this raises hydraulic efficiency, the added electrical power combined with the need for advanced control hardware and algorithms to achieve the precise actuation necessary adds additional cost and complexity to the system. A mechanically actuated digital variable displacement pumping/motoring concept has been investigated with the goal to eliminate complex controls and sensors. It utilizes a variable cam, controlled by a single lever, to achieve variable displacement digital pumping and motoring using both flow diverting and flow limiting strategies. This work involves the development of a coupled-physics dynamic model of a mechanically actuated digital pumping unit. This simulation will be used to characterize and predict the efficiency and how it is affected by the implementation of a cam-driven valve system. This model can be adjusted to analyse the effects of number of pistons, valve stroke, valve area, compression angle, transition length, transition type, and cam profiles for varying pressures, speeds, and displacements. This work has shown that high efficiencies, averaging 90%, can be maintained over a wide range of displacements with the mechanical actuation of the valves and provides a viable alternative to electrical actuation to achieve variable displacement.

1. INTRODUCTION

With the increased emphasis on efficiency and more environmentally friendly systems, researchers have been working on improving the efficiency of hydraulic systems. The department of energy reported that the efficiency of mobile hydraulic systems in the United States is less than 22%, totalling more than the energy obtained by all the renewable energy sources combined [1,2]. The study concludes that a 5% increase in efficiency in hydraulic systems could save the United States alone more than $8 billion per year and reduce carbon dioxide emissions by up to 90 million tons per year. An

increase of efficiency could be obtained either through a system level improvement, such as displacement controlled actuation [3] and hydraulic hybrid systems [4, 5], or through a component level improvement, such as a more efficient pump/motor [6], hydraulic transformers [7, 8], or valves [9, 10].

At the heart of fluid power systems is the pump. Current state of the art variable displacement pump/motors have high efficiencies when operating at high displacements. However, the overall efficiency drops to as low as 40% when the pump/motor is operated at low displacements. These low efficiencies significantly reduce the overall efficiency of many hydraulic systems; especially those that utilize multiple pump/motors.

This work builds upon the success of the digital pump/motor project previously designed, simulated, built, and tested [6, 11]. It overcomes the limitations of the previous work by introducing mechanically driven valves in exchange for using high speed on/off valves per displacement chamber to achieve variable displacement. A coupled-physics dynamic model of a mechanically actuated digital pumping unit was developed; this model was used to characterize and predict the efficiency and how it is affected by the implementation of a cam-driven valve system. The model is currently being used as a design tool to help build the mechanically driven pump/motor unit. Various design parameters are being optimized, including the cam shape and curve, transition degrees, and compression angle.

2. BACKGROUND

2.1. Previous Work

Commercially available pump/motors yield high efficiency when operating at high displacements or at their targeted design conditions. However, when the pump/motor displacement is reduced, the efficiency of the unit significantly decreases. This decrease in efficiency can be attributed to the losses which do not scale down with displacement, so their effect on the efficiency is higher when the power output is lower. Those losses include friction losses between the piston and the cylinder interface, fluid compressibility losses, and leakage losses at different pump/motor interfaces.

Work has been done to improve the efficiency of pump/motor units. Some of the work included developing a digital pump/motor which relies on using electrically controlled on/off valves to actively control each displacement chamber; those units reduce the losses at low displacements by reducing the duration at which the displacement chamber is pressurized, thus yielding higher efficiencies [12].

Artemis Intelligent Power Ltd. developed a radial piston digital pump/motor utilizing an electro-hydraulic latching poppet valve configuration. Two valves were mounted onto each displacement chamber which have the ability of being latched open using a solenoid; this configuration allowed the unit to achieve variable displacement by latching the inlet valve open to divert flow back into the low pressure port; such a configuration reduces losses since the compressibility, shear and leakage losses scale more closely with displacement [13]. Artemis reported that their digital pump/motor unit achieved a high overall efficiency over a wide range of displacement [14];

however, due to the usage of latching valves, flow can't be achieved in both directions when a high differential pressure is available. This also prevents the unit from self-starting in motoring without modifying the unit's configuration.

Other research has focused on actively controlling two high speed on/off valves connected to each displacement chamber, shown in Figure 1. Such a configuration allows total freedom in controlling the digital pump/motor operation, creating several operating strategies which include partial flow diverting, partial flow limiting, sequential flow diverting, and sequential flow limiting [6]. Though such a configuration yielded high efficiencies over a wide range of displacements, the pump/motor unit was limited in speed because of the delay and transition time of the high speed on/off valves used. In addition, this unit has a complex control algorithm which actively controls the opening and closing of the valves and relies heavily on data acquisition, all of which makes it harder to commercialize.

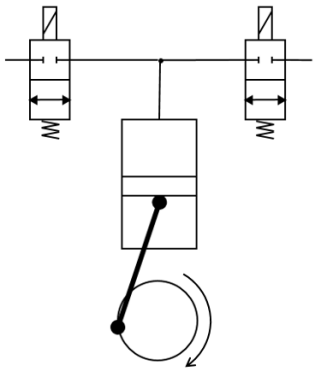

Figure 1. Individual displacement chamber [11]

This work overcomes the limitation of the digital pump/motor presented above by replacing the electrically controlled valves with mechanically driven ones. Such a configuration limits the operation of the unit, but it can achieve higher efficiency at higher shaft speeds with minimum data acquisition and control. The operating strategy used in our configuration is the partial flow diverting strategy.

2.2. Partial Flow-Diverting (FD) Variable Displacement Strategy

This work will make use of the Partial Flow-Diverting strategy to achieve variable displacement. As the name implies, with this technique excess flow is diverted back to the low pressure port rather than pumping it to the high pressure side; varying the amount of flow which is diverted back allows us to achieve variable displacement. The flow diverting strategy is pictorially illustrated in Figure 2; as the piston is moving down starting at top dead center (TDC), valve 1 opens allowing the fluid to flow and completely fill the displacement chamber. Valve 1 would still be held open as the piston moves upwards towards the top dead center (TDC); holding valve 1 open would divert the flow back to the low pressure port. The displacement of the unit is defined by the piston position at which valve 1 closes during the upward motion of the piston. When the right amount of fluid is available in the displacement chamber, valve 1 closes and the fluid is pressurized; then valve 2 opens and the high pressure fluid is pumped into the high pressure line.

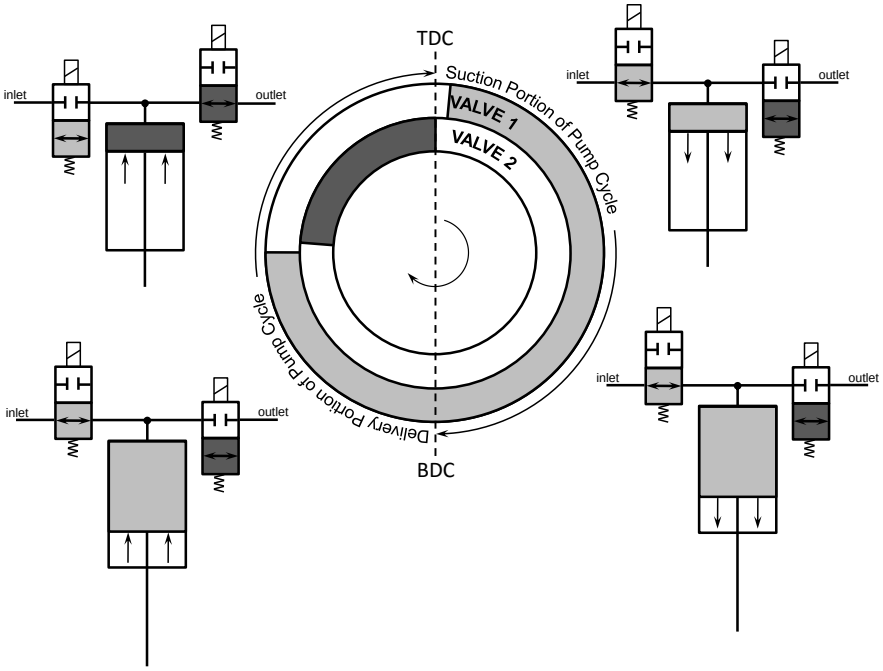

Figure 2. Partial flow-diverting pumping [6]

3. MECHANICALLY ACTUATED DIGITAL PUMP MOTOR

The mechanically actuated digital pump/motor concept builds on the digital pump/motor research using electrically controlled valves. Through simulation and testing [6], it was found that the valves played a significant role in the efficiencies achieved. In order to achieve the highest efficiencies possible, bigger, faster, and more consistent valves were needed.

To address these issues, it was determined that the repetitive nature of the valve actuation could be exploited to allow for mechanical actuation. A state analysis was performed on the valves and several configurations from a simple pump to full four-quadrant pump/motors were deemed theoretically viable. Figure 3 shows an example of the state diagrams used in this analysis. Each diagram represents the state the valve must be in, in this example open or closed, at the corresponding rotation angle.

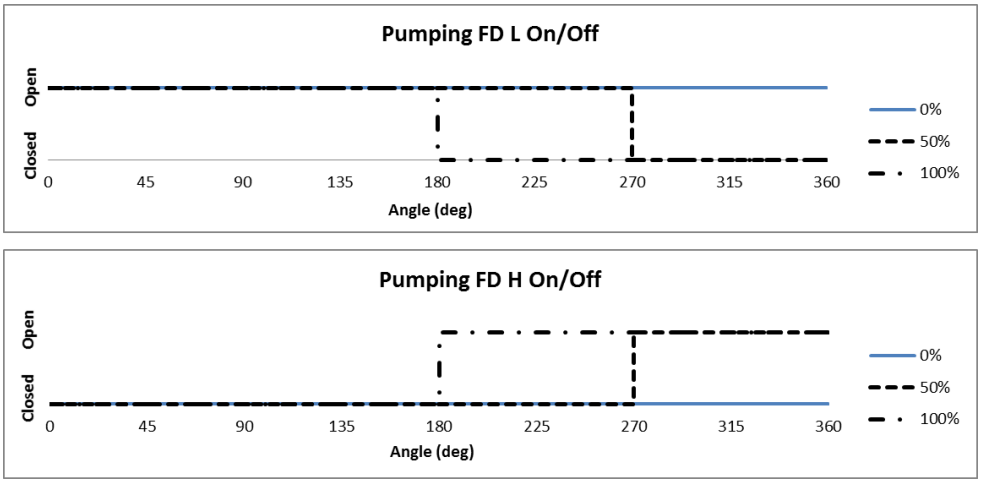

Figure 3. State analysis diagram

In order to test this new actuation system, it was decided to create a simple pump with the low pressure valve being mechanically actuated and the high pressure side using a check valve as seen in Figure 4.

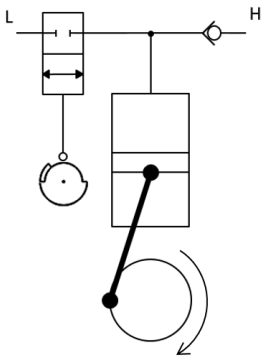

Figure 4. Cam-driven valve actuation pump

Using a cam driven by the pump input shaft to mechanically actuate the valves was the obvious choice as it is a proven mechanism which outputs relatively high actuation forces consistently. With this configuration, the speed of the valve actuation will be proportional to the speed of shaft of the pump and the high actuation forces allow for valves with larger orifice areas to be used. In order to achieve variable displacement of the pump the cam profile needs to be varied. Theoretically, by using two 50% high cam profiles, or masks, the effective cam profile can be varied from 100% to 50% high by phasing one mask relative to the other. An example of this cam phasing can be found in Figure 5. This method was chosen for its simplicity and ease of construction. A roller follower will be used to reduce the friction and size of the cams.

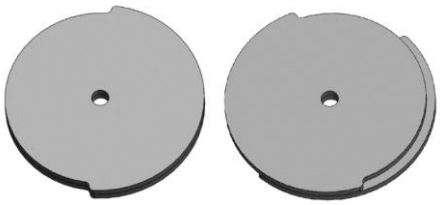

Figure 5. Variable cam half-masking

3.1. Simulation

In order to determine the most efficient configuration for the half masking cam, a simulation of the proposed pump was created in Matlab/Simscape. The kinematics and pumping chambers used in this model are based on those created for simulation of an electronically controlled digital pump motor [6]. A single piston version of the mechanically actuated Simulink model can be found Figure 6. A single piston was shown for clarity; the simulation was run with three pistons.

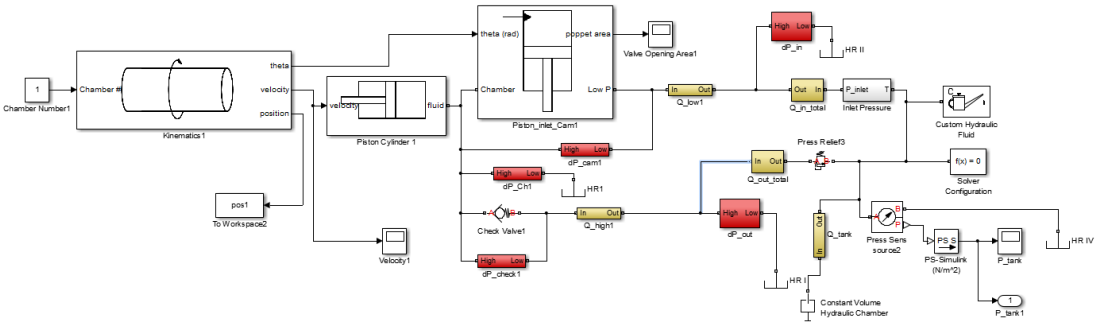

Figure 6. Simulink single piston pump model

3.1.1. Parameters

This model allows for complete manipulation of the cam profiles and allows these to be tested under any operating parameter within the scope of pump operation. The main variables to be manipulated are the transition length, compression angle, transition type, pressure difference, speed, and displacement.

Additionally, a complimentary program was written to aid in selection of the cam design. This program takes into account the parameters run in the previous simulation as well as cam base diameter, roller follower diameter, eccentricity, follower mass, and spring pre-compression. As these values have no effect on the simulation, this program can be executed separately. This file outputs the ideal compression angle, follower spring constant, and a graph of the pressure angles for each point on the cam.

Transition type is the path that is followed to increase or decrease the cam profile from the low state to the high state. While any transition type may be added easily, harmonic was chosen for this simulation as it was determined to have the lowest peak acceleration and jerk [15]. Other transition types considered included cycloidal and parabolic.

Transition length is the amount of degrees the transition type takes to transition from the low to high state. An ideal valve would have a transition length of zero resulting in no addition metering as the valve is opening; thus efficiency is inversely proportional to the amount of transition degrees. Transition length affects the acceleration of the cam follower as well as the pressure angle of the cam. A rule of thumb for industry is the pressure angle should not exceed 30^o in high speed applications to prevent seizing. The pressure angle can be calculated using (1 where e is eccentricity, x is the cam displacement profile, and r_b is the base radius of the cam.

$$\alpha_p = \tan^{-1}\left(\frac{x'(\theta) - e}{x(\theta) + \sqrt{{r_b}^2 - e^2}}\right) \tag{1}$$

Compression angle is the amount of degrees of rotation the piston cylinder needed to decompress the fluid as the piston chamber transitions from expulsion to the high pressure line to intake from the low pressure line at TDC. Figure 7 shows transition length (θ_t) and compression angle (θ_c) on the cam profile.

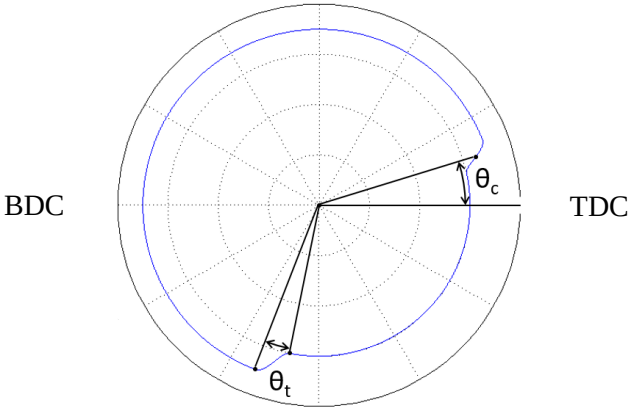

Figure 7. Cam actuation profile

The correct compression angle is necessary to reclaim the energy input into the fluid and maximize efficiency. For an ideal valve the compression angle would be calculated using the following equations. While this is still useful for estimation, the transition type and length will affect the ideal compression angle on a real machine. (2 shows the relationship between the change in volume and the change in pressure.

$$dP = K\frac{dV}{V} \tag{2}$$

Where V is the effective volume of the piston chamber which is equivalent to the dead volume and the piston area, A_p, multiplied by the piston stroke ((3). It should be noted that at TDC, x = l removing the second part of the equation. The change in volume, dV, is equivalent to the change in piston stroke multiplied by the piston area ((4).

$$V = V_{dead} + A_p(l - x) \tag{3}$$

$$dV = \Delta x\, A_p \tag{4}$$

Combining these three equations to determine the compression angle for TDC, (5 is derived.

$$\Delta x = \frac{dP\, V_{dead}}{K\, A_p} \tag{5}$$

Spring constant was calculated using (6 where m_f is the mass of the follower and x_{pc} is the spring pre-compression distance.

$$k = \max\left(-\frac{x''(\theta) * m_f}{x(\theta) + x_{pc}}\right) \tag{6}$$

Total system parameters simulated.

- Valve max opening area = 100 mm^2
- Poppet stroke = 4 mm
- Piston cylinder radial gap = 16 µm
- Piston Area = 314 mm^2

- Piston Stroke = 30 mm
- Transition Length = 6-12^{o}
- Compression Angle = 12-20^{o}
- Speed = 500, 1000, 1500, and 2000 rpm
- Pressure differential = 69 and 138 bar
- Displacement = 20%, 40%, 60%, 80%, 100%
- Number of Pistons = 3

3.2. Simulation Results

The results of the simulation showed promising results for overall efficiency. When the compression angle was optimized for the operating range of 69–138 bar, an average efficiency of 89.72% was reached at an 18^{o} compression angle. The same method used for optimization for this operating range could be used with any desired parameters.

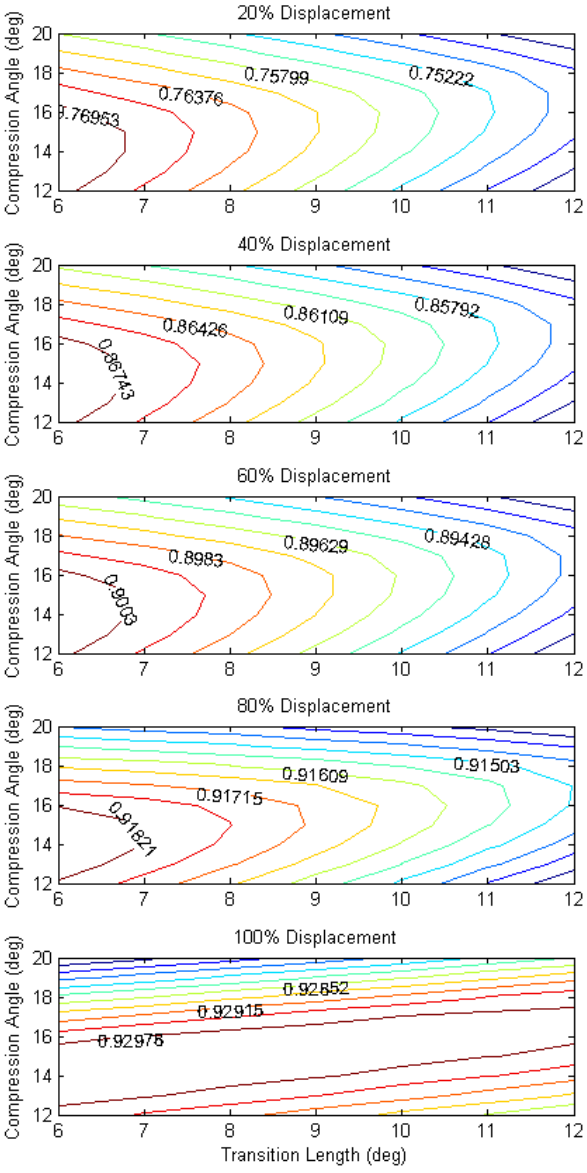

Figure 8. Efficiency at 69 bar

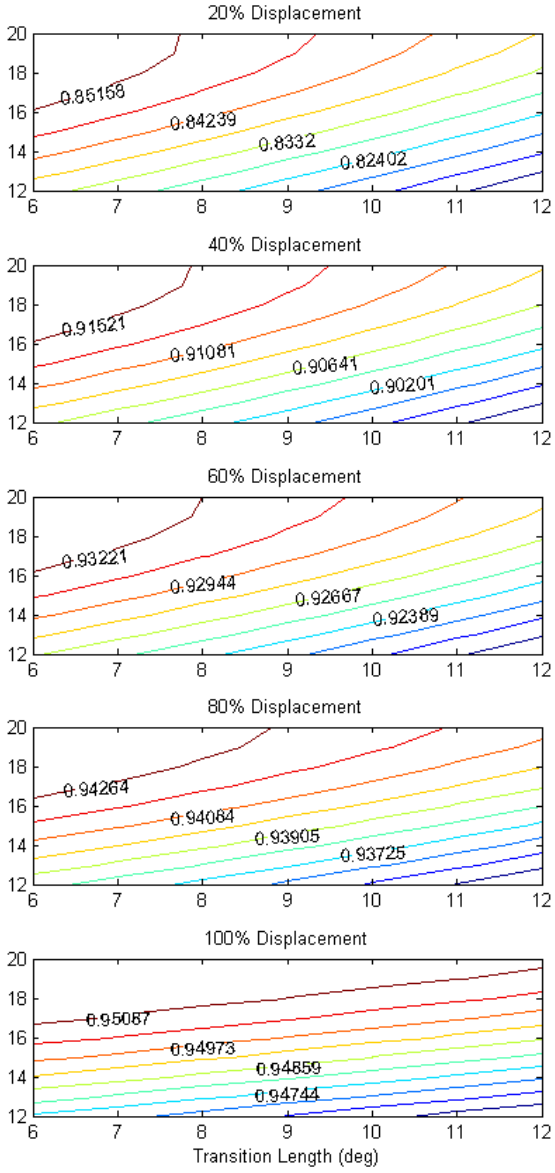

Figure 9. Efficiency at 138 bar

Figure 8 and Figure 9 show efficiency contour plots for varying displacements at a speed of 2000 rpm and differing pressures. By comparing these graphs, it is clear to see the trends of the mechanically actuated pump.

- Efficiency decreases as the transition length increases.
- Increase in pressure increases efficiency
- Increase in pressure increases the ideal compression angle.
- There is a distinct efficiency maximum at the ideal compression angle.

Ideally, the transition length would minimized to maximize efficiency, however, this is practically not feasible. In order to stay below the 30^{o} pressure angle requirement while keeping the cam size relatively small, the following values were selected.

- Cam base diameter = 140 mm
- Roller diameter = 26 mm
- Eccentricity = 20 mm
- Spring pre-compression = 2 mm
- Follower mass = 0.1 kg
- Transition length = 10 degrees

Figure 10 shows the pressure angles for the cam selected for this simulation. Notice that the maximum value is 28.47 degrees for the rising section of the cam while falling the pressure angle does reach 43.82 degrees. Eccentricity was used to shift the pressure angle in this way because during the falling section, there is less force acting upon the cam and a much lower risk of seizure.

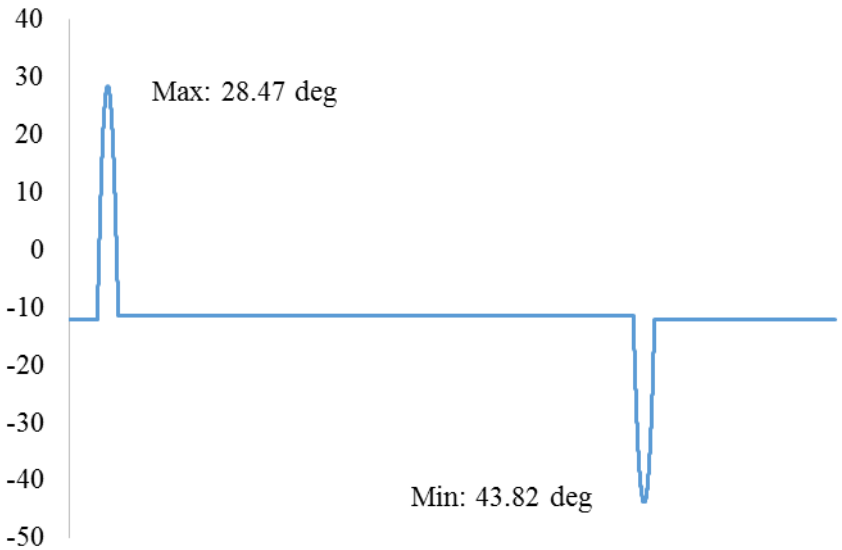

Figure 10. Pressure angles on specified cam (see parameters above)

Using the above parameters, Figure 11 shows the effect of different operating conditions on the distribution of losses when operating at 20% displacement. Notice that viscous friction losses are the losses in the piston chamber due to friction and are relatively constant for this pump regardless of operating conditions. For these operating conditions, valve losses remain lower than the frictional losses of the pump though speed is a significant factor.

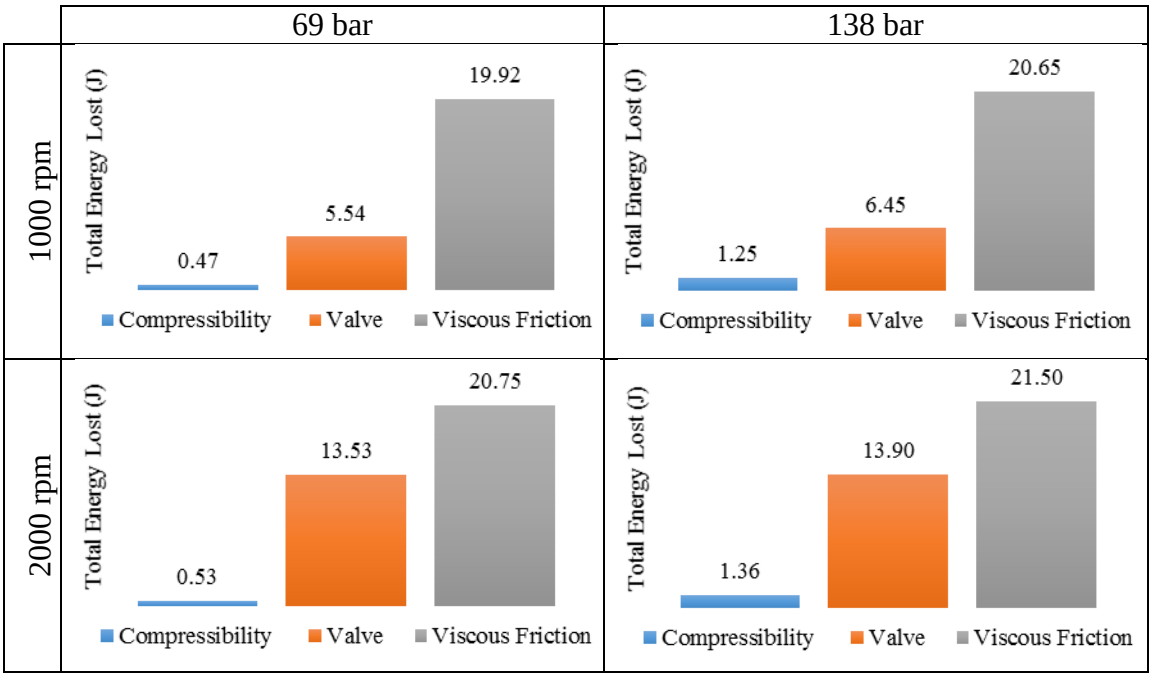

Figure 11. Loss comparison for different operating conditions (displacement = 20%, transition length = 10, compression angle = 18)

4. CONCLUSION

The mechanically actuated digital pump simulation has proven that this technique is a viable option to improve the performance of digital pumps. Results showed that high efficiency can be maintained through all displacements and operating conditions. Additionally, the cam profiles can be optimized to achieve various goals of the end user such as efficiency over specific operating condition ranges. Finally, this configuration minimizes valve losses in the pump resulting in greater operational efficiency.

REFERENCES

[1] Love, Lonnie. (August 17, 2009). Fluid power research: A fundamental concern for U.S. energy policy [PowerPoint slides]. Presented at the National Fluid Power Association Industry and Economic Outlook Conference, Wheeling, IL.

[2] Love, Lonnie. (March 5, 2014). Energy Impact of Fluid Power [PowerPoint Slides]. Presented at the 2014 IFPE Technical Conference, Las Vegas, NV.

[3] E. Busquets, M. Ivantysynova The World's First Displacement-Controlled Excavator Prototype with Pump Switching – A Study of the Architecture And Control, Proceedings Of The 9th Japan International Fluid Power Symposium, Matsue, Japan, 2014

[4] Hippalgaonkar R, Ivantysynova M. Optimal Power Management for DC Hydraulic Hybrid Multi-Actuator Machines - Part 2: Machine Implementation and Measurement. ASME. J. Dyn. Sys., Meas., Control. 2016;():. doi:10.1115/1.4032743.

[5] Sprengel, M., Bleazard, T., Haria, H., and Ivantysynova, M. Implementation of a Novel Hydraulic Hybrid Powertrain in a Sports Utility Vehicle. 4th IFAC Workshop on Engine and Powertrain Control, Simulation and Modeling E-COSM 2015 — Columbus, Ohio, USA, 23-26 August 2015. doi:10.1016/j.ifacol.2015.10.027

[6] Merrill, K. J., Breidi, F., and Lumkes, J. (2013). "Simulation Based Design and Optimization of Digital Pump/Motors". Proceedings of the ASME/BATH 2013 Symposium on Fluid Power and Motion Control. doi:10.1115/FPMC2013-4475

[7] Bishop, E. D. (2010). Digital hydraulic transformer – Efficiency of Natural Design. 7th International Fluid Power Conference, Aachen, Germany.

[8] Heikkila, M., Tammisto, J., Huova, M., Huhtala, K., &Linjama, M. (2010). Experimental evaluation of piston-type digital pump-motor-transformer with two independent outlets. Proceedings of the Bath/ASME Symposium on Fluid Power and Motion Control.

[9] Daniel Skelton, Shaoping Xiong, John Lumkes and Farid Breidi. "High Performance Actuation Systems Enabled by Energy Coupling Mechanisms", SAE 2013 Commercial Vehicle Engineering Congress, Rosemont, Illinois, United States, October 1, 2013

[10] Skelton, D., Xiog, S., Lumkes, J. (2014). Design of High Performance Actuation System for High Speed Valves. 9th International Fluid Power Conference, Aachen, Germany.

[11] Breidi, F., Helmus, T., and Lumkes, J. 2015. The Impact of Peak-And-Hold and Reverse Current Solenoid Driving Strategies on the Dynamic Performance of Commercial Cartridge Valves in a Digital Pump/Motor. International Journal of Fluid Power, http://dx.doi.org/10.1080/14399776.2015.1120138

[12] Ehsan, M., Rampen, W. H. S., & Salter, S. H. (1996). Computer simulation of the performance of digital-displacement pump-motors. Fluid Power Systems and Technology: Collected Papers, 3, 19-24. (Proceedings of the 1996 International Mechanical Engineering Congress & Exposition.)

[13] Payne, G. S., Kiprakis, A. E., Rampen, W. H. S., Chick, J. P., & Wallace, A. R. (2007). Efficiency and dynamic performance of Digital DisplacmentTM hydraulic transmission in tidal current energy converters. Proceedings of the Institution for Mechanical Engineers, Part A: Journal of Power and Energy, 221, 207-218.

[14] Rampen, W. (2006). Gearless transmissions for large wind turbines – The history and future of hydraulic drives. Retrieved from http://www.artemisip.com /sites/default/files/docs/2006-11%20Gearless%20Transmissions%20Bremen. pdf

[15] Chen, Yueh-Shao, Sung-Lyul Park, Michael Stevens, and Gary L. Kinzel. Kinematic Design and Analysis Programs. Columbus, OH: Ohio State University, 2003. Computer software.

A PILOT CONTROL METHOD FOR A VARIABLE DISPLACEMENT AXIAL PISTON PUMP USING SWITCHING TECHNOLOGY

Bin Zhang[1], Haocen Hong[1*], Qi Zhong[1], Ruifeng Guan[1], Huayong Yang[1]
1 The State Key Lab of Fluid Power Transmission and Control, Zhejiang University, Hangzhou 310027, China

ABSTRACT

Since switching valves exhibit low loss when fully opened or fully closed, the proposed system is potentially more energy efficient than metering valve control, while achieving this efficiency without any shortcomings of traditional variable displacement pumps. This paper described a pilot control method for a variable displacement axial piston pump used switching technology. Simulation and analysis showed that this kind of variable displacement pump is of good performances. Besides, by changing the control algorithm, the variable displacement pump described in this paper could achieve kinds of different variable patterns including constant pressure, constant flow, and constant power, etc. In the end, the experiment results were given and compared with simulation ones. It is indicated that this variable displacement axial piston pump pilot controlled by fast switching valve has a good prospect of application.

KEYWORDS: Pilot control, variable pump, switching technology, on-off valve

1. INTRODUCTION

The output flow of a variable displacement pump unit is directly controlled by the swash plate, which is drove by the variable control piston. To achieve different kinds of variable functions, the swash plate control system in traditional variable displacement pump always contains complex oil canals and control valves, which makes it hard to be manufactured and brings about considerable volume and weight resulting in nonlinearity and hysteresis.

Some useful research has been done worldwide. University of Minnesota contributed some useful experimental studies on software enabled variable displacement pumps [2]. Wen Ze from Zhejiang University simulated the control performance of the traditional pump and compared it to the closed loop control pump's simulation results [3]. Tung Nan Institution Technology in Taiwan adopted an electro-hydraulic proportional valve to control the swash plate angle of the variable displacement pump [4]. Gao Bo et al. had discussed a new type servo pump which be driven by a DC servo motor [5]. Zhang Bin studied the digital pump by modeling and simulation based on virtual prototype technology [6, 7].

Nowadays, digital fluid power has become a new research field in fluid power

* corresponding author, Haocen Hong, E-mail: honghaocen@163.com

technology. Generally, digital fluid power can be divided into two fundamental branches, systems based on parallel connection and systems based on switching technologies. Switching technologies utilize fast and continuous switching components, like high speed on-off valves, and the output of systems is adjusted by e.g. the pulse width ratio [1].

Roemer et al. designed a fast-switching valve using transient finite-element analysis of electromagnetic circuit. The proposed valve has a pressure drop below 0.5 bar at 600 L/min flow rate, and its switching time just about one millisecond for a travel length of 3.5 mm while submerged in oil [8]. Branson et al. did a research to investigate the use of high-speed on\off valve controlling a hydraulic actuator. This work is completed as part of efforts to improve the accuracy and smoothness of travel for a six-degree-of freedom testing machine [9]. Heitzig and Sgro composed a digital pump which contains several parallel constant pumps and a number of switching valves. The designed digital pumps tended to have better efficiencies in partial load operation than conventional pumps [10].

In this paper, different kinds of closed-loop control system based on switching technology is proposed. The mathematical model of the prototype pump is discussed at first. Then simulation models of axial piston pump, control valve are built up based on the AMESim. The numerical control system based on the LabVIEW is coded and the co-simulation interface between the AMESim and LabVIEW is established. With the simulation results, we analyze the control characteristics including the pressure control, flow control and power control of the pump. Finally we have done the experiment based on the designed structure, and the experiment results are given and compared with simulation ones.

2. MECHANISM ANALYSIS

The hydraulic schematic of the prototype pump is shown in Figure 1. The swash plate angle is controlled by two pistons (piston A and piston B) which connected to each side of the swash plate. The piston A according to Fig. 1 is the returning piston with a spring and shoved by the pump's outlet pressure. The piston B according to Fig. 1 is the control piston. It is controlled by a high speed on/off valve which driven by PWM control signal. The average output flow of control valve is determined by the duty ratio of PWM signal. An absolute angular displacement sensor is installed to detect changing of the swash plate angle and sends it back to calculate the pump's flow. A pressure sensor is installed at pump's outlet to detect output pressure.

With the feedback signals (output pressure and swash plate angle), the controller calculates the pump's flow, pressure and power, then compares them with the reference values and accomplishes the closed-loop control with PID algorithm. The high speed on/off valve serves as the only control valve and is placed in a valve seat which installed on the pump end cap.

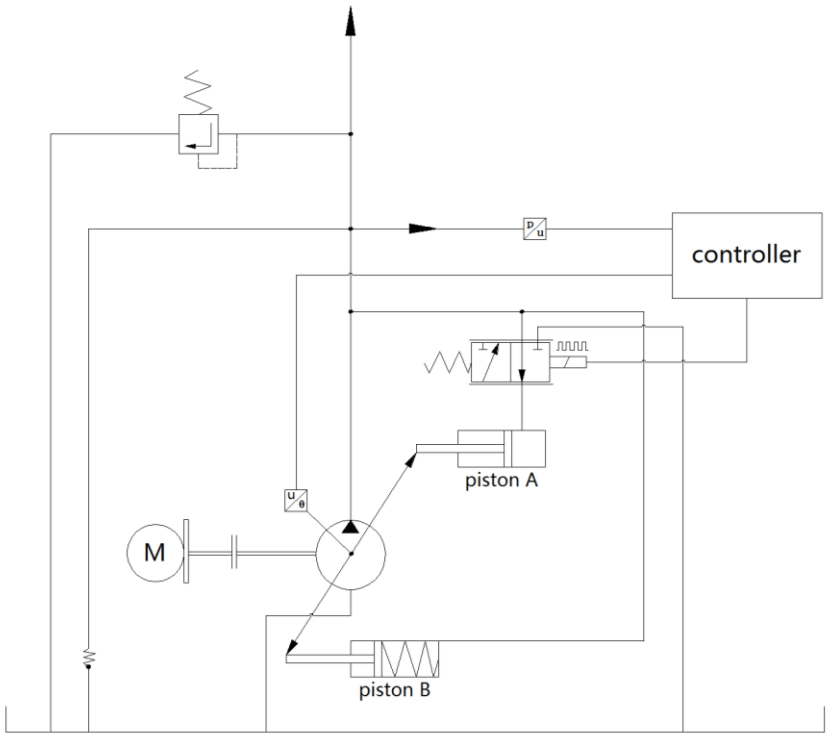

Figure 1. Hydraulic schematic diagram of the digital pump

The chosen high-speed on/off valve is a 2 position 3 way electromagnetic valve, which switching time is about 2.5ms. Three ports of the high speed on/off valve respectively are the high pressure flow port P, the control pressure flow port A and the return flow port T. Port P is connected to the pump outlet, where contains a relief valve to guarantee the pressure of port P is no less than 28 MPa. Port A is connected to the control piston whose position is determined by the flow from port A. Port T is connected to the tank. The control valve has either fully on or fully off state. At the fully on state, the high pressure fluid flows from port P to port A, and push the swash plate angle increase. At the fully off state the flow in the piston returns from port A to port T, so that the swash plate angle decreases.

3. MATHEMATICAL MODEL

The control flow into the high speed on/off valve is：

$$\bar{q}_{\tau a} = \tau c A_h \sqrt{2(p_p - p_a)/\rho} \tag{1}$$

where $q_{\tau a}$ is the average flow of the on/off valve; p_p is pump pressure; p_a is outlet pressure of valve; τ is the duty cycle of control signal; A_h is the maximum flow area ; c is discharge coefficient; ρ is the density of the oil;.

Flow return back to the tank from the control piston is:

$$\bar{q}_{\tau b} = (1-\tau) c A_h \sqrt{2 p_a / \rho} \tag{2}$$

where $q_{\tau b}$ is the average flow of the control piston;

Thus the average flow through the high speed on/off valve into the control piston is:

$$\bar{q}_\tau = \tau c A_h \sqrt{2(p_h - p_a)/\rho} - (1-\tau) c A_h \sqrt{2 p_a / \rho} \tag{3}$$

where q_τ is the average flow through the high speed on/off valve into the control piston.

As for the axial piston pump, the output flow is shown as follows without counting volumetric loss:

$$q_b = \frac{\pi}{4} d_Z^2 s_{\max} Z n_b \tag{4}$$

where q_b is the output flow of axial piston pump; d_z is the diameter of the piston; s_{max} is the maximum linear displacement of the control piston; Z is the number of the pistons; n_b is the rotation speed of the pump;

The maximum linear displacement of the control piston is calculated as follow:

$$s_{\max} = 2R_f \tan\gamma \tag{5}$$

where R_f is the pitch radius of the cylinder block; γ is the swash plate angle;

Then relationship between the output flow of axial piston pump and swash plate angle can be described as follow:

$$q_b = \frac{\pi}{4} d_z^2 D_f Z \tan\gamma \tag{6}$$

4. CONTROL PRINCIPLE

The displacement control system of the pump can be simplified as a model of cylinder position control system, which position is controlled by a high speed on/off valve. While a proper frequency of the PWM signal is set, the average output flow of the high speed on/off valve is equal to the instantaneous value qt(t,p). Linearization of the input flow into the control piston is:

$$q_{in} = K_{\tau,in}\tau - K_c p_t \tag{7}$$

where q_{in} is the input flow into the control piston; τ is the duty cycle of control signal; $K_{\tau,in}$ is the gain of the inlet; K_c is the gain of the pressure;

And the flow returning to the tank is:

$$q_{out} = K_{t,out}(1-\tau) \tag{8}$$

where q_{out} is the input flow into the control piston; $K_{\tau,out}$ is the gain of the outlet;

Then we get the instantaneous differential flow of the control piston:

$$q_\tau = q_{in} - q_{out} = K_\tau \tau - K_c p_t - K_{\tau,out} \tag{9}$$

where K_τ is the gain of duty cycle;

Considering the continuity equation of the cylinder chamber and the force equilibrium of the piston, the transfer function of the displacement of the control piston to the duty ratio of the PWM signal is:

$$G(s)=\frac{Q(s)}{\tau(s)}=\frac{K_{sp}K_\tau / A_h}{s(\frac{s^2}{\omega_n^2}+\frac{2\zeta_n}{\omega_n}s+1)} \tag{10}$$

The controller calculates the theoretical pump flow value through the swash plate angle, and adds in a compensation value according to the leakage theory.

When there is disturbance coming into the pump system, it will get back to the steady state with a tolerable jitter after a short time modulation. Different from the common variable displacement pump, the pump responses to the dynamic input signal such as a step variation of the reference pressure, flow or power.

5. MODELING OF THE DIGITAL PUMP SYSTEM

The pump simulation model is divided into several components, such as the swash plate, high speed on-off valve, the stroking and returning pistons and the digital controller. The whole system's simulation model is built up by modeling the components one by one. Simulation model of one piston in the barrel is established shown in Figure 2.

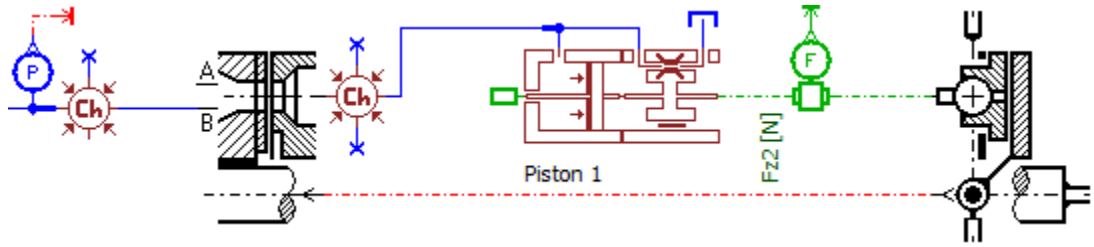

Figure 2. Simulation model of one piston in the barrel

The piston sucked and extruded fluid through the valve plate and the signal of the two freedom of motion was exchanged by the signal interface in AMESim. There are nine similar pistons distributed on the valve plate at different positions. Adding the barrel inertia and the swash plate with its control pistons in the nine-piston model we got the simulation model of the variable displacement axial piston pump shown in Figure 3.

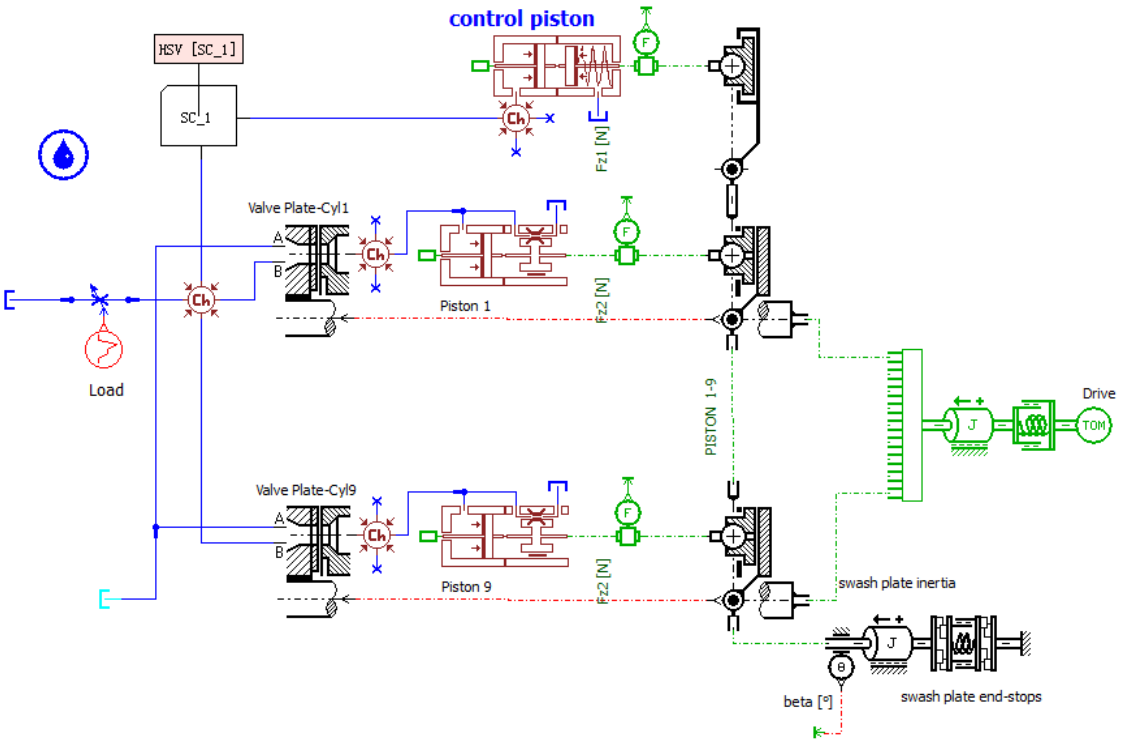

Figure 3. Simulation model of variable displacement axial piston pump

The high speed on/off valve discussed in this paper switches between two states of on and off in about 50Hz frequency. While the driving signal of the electromagnet is “1”, the spherical spool switches to the right side and links port P to port A. While the driving signal is “0”, the spherical spool switches to the left side and links port A to port T. So that port P is covered and the control fluid flows into the tank. The high speed on/off valve is driven by PWM signal whose duty ratio can be modulated by the PID controller.

The swash plate is the direct controlling object and all the control modes are realized through controlling the swash plate angle. Thus the swash plate angel control system is especially significant in the digital pump system. The returning piston has a return spring with small stiffness and always links to the outlet of the pump. The control piston is treated as a cylinder in which the flow is controlled by the high speed on/off valve. The swash plate is modeling as a rotary inertial. The swash plate angle is limited to 0-18°and detected by the angle transducer.

The co-simulation model of the pump is separated into four parts from the bottom to top. Models of high speed on/off control valve and swash plate control system have been discussed above and the PWM control signal is provided by the LabVIEW controller.

6. CONTROL PERFORMANCE OF DYNAMIC RESPONSE TO THE STEP VARIATION OF THE REFERENCE CONTROL VALUE

The pump has a distinguishing feature which is very different from the common variable displacement hydraulic pump. Its pressure, flow and power parameters can be reset by the controller without stopping the pump and it will response to the control signal immediately. The control parameters are set by the host computer though CANBus or by the embedded controller programmed in advance.

We gave the pump model a step signal which changed the reference pressure value between 5-25 MPa and the simulation result was shown in Figure 4. There are some difference between the response results in the rising and dropping edges of the step variation, because the control performance of the digital pump had little difference under different working conditions. In the pressure response of the dropping step variation the time for the digital pump changing from one stable state to another is 0.15 s with 12% over shoot and no vibration occurred. In the pressure response of the rising step variation the response time extends to 0.8 s with several vibrations before getting into steady control state. The pressure overshoot is cut and limited by the safe relief valve which opened at the pressure of 28 MPa. The corresponding response of the flow and power is shown in Figure 5.

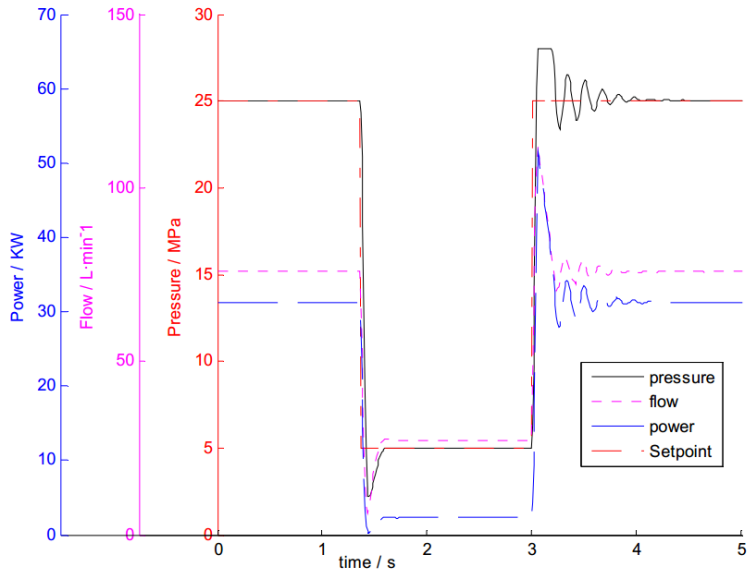

Figure 4. Simulation pressure response of the pump model

The flow response is shown in Figure 5. Step variation of the reference flow value is between 50-100 L/min. The load system is a restrictor with the orifice of 2 mm. Step response of the flow between 50-100 L/min with a 2 mm restrictor orifice causes a stage of maximum pressure output. It is because of the small restrictor orifice, while the flow reached a specific value the safe relief valve opens and the output pressure reaches the maximum value. In the rising step flow response the time for adjusting is 0.08 s without vibration and the over shoot is acceptable. In the dropping step flow response the adjusting time is 0.05 s with a very small over shoot about 1%. The dynamic flow response of the digital pump is satisfied for most working conditions of the digital pump according to the simulation results.

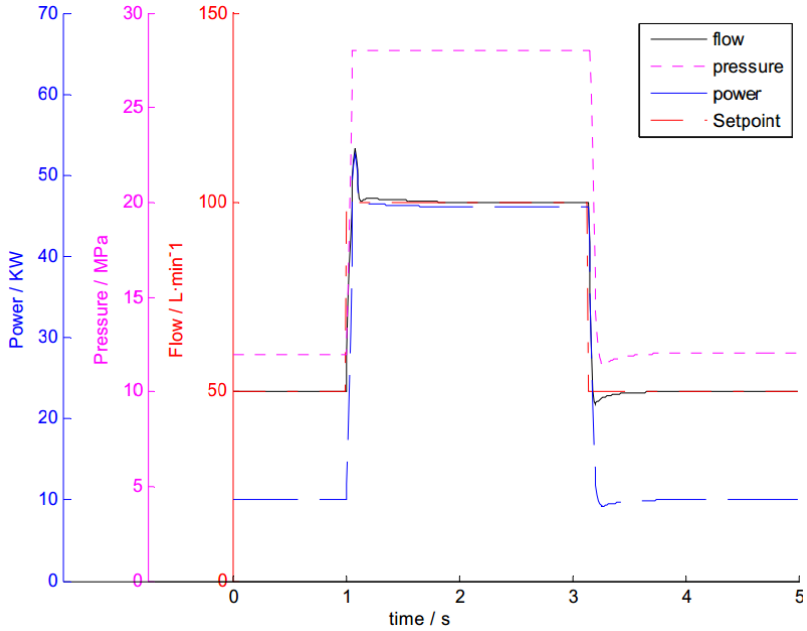

Figure 5. Simulation flow response of the pump model

The Power response is shown in Figure 6. With the same reason in the flow response the pressure reaches the maximum value during the initial stage. The reference power value steppes between 10-50 KW, and the flow adjusts between 50-120 L/min. In the power control response there is no vibration both in the rising and dropping edges. The over shoot is about 10% in both sides of the response and the adjust time of the dynamic response to the dropping and rising step variation is 0.2 s and 0.35 s.

In fact, the pressure control, flow control and power control are not isolated. The control mode and state are changed to any other working functions by the controller. The demanded signal is send into the pump by the host computer or by the program in the embedded controller.

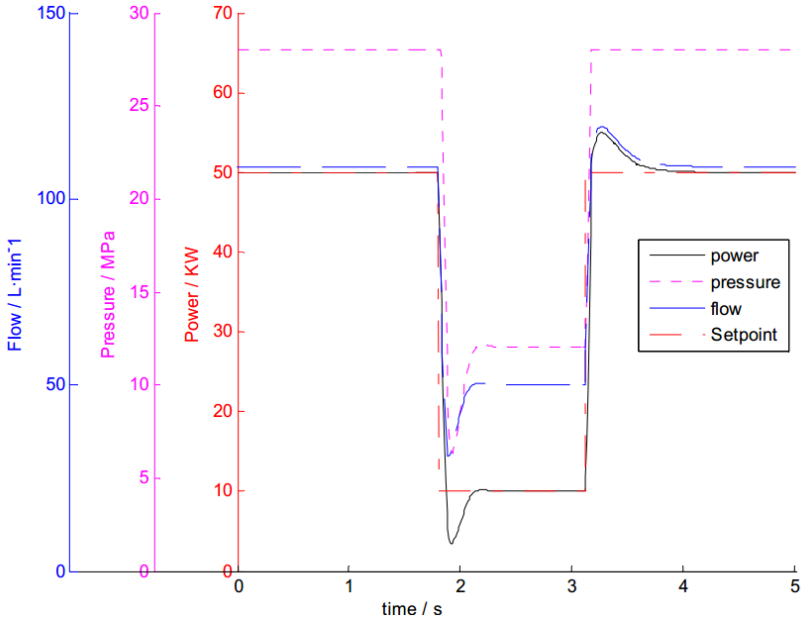

Figure 6. Power response of the digital pump to the step variation of the reference control value

7. EXPERIMENT RESULT:

For this part, we did the experiment on pump's dynamitic control characteristics. The test rig is shown as follow.

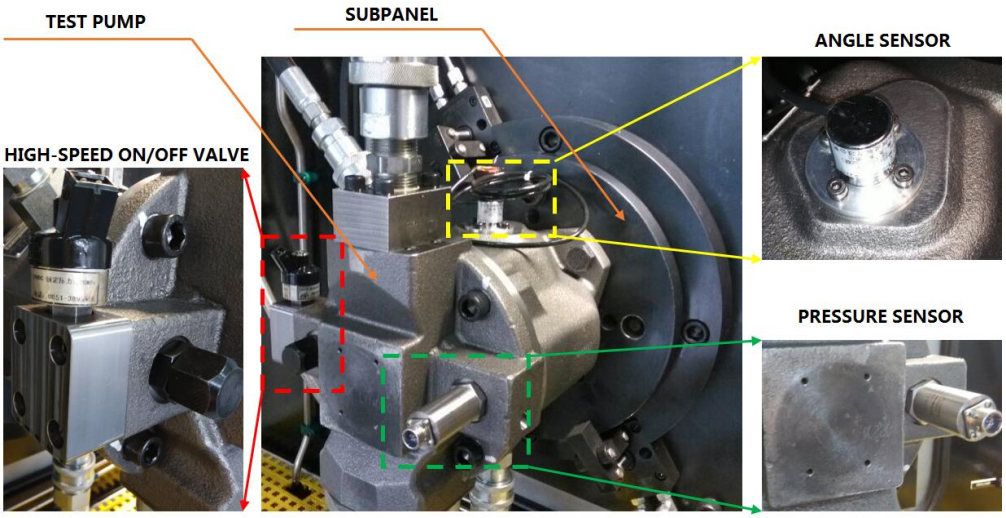

Figure 7. Structure of the test rig

Analyzing the hydraulic principle of the pump, the angle sensor is real-time monitoring and feedback the angle parameter to the controller. The swash plate angle is directly controlled by the high-speed on-off valve which switching time is about 2.5ms, and its control switching frequency is about 50Hz.

Set up the angle of inclined swash plate changing from 5 to 15° through a step signal, the swash plate angle control curve as shown in the figure below. The step response time from 5Mpa up to 15 Mpa is 1071 ms, the step response time from 15 Mpa down to 5Mpa is 360 ms. The step response time depends on the speed of high-speed on-off valve, the response speed of the model, controller performance and the PID parameters, etc. Because of the valve is turning off, the overshoot of the down step is much bigger than the up step.

Table 1. Experiment results of the swash plate angle control test

	response time	Overshoot	Steady jitter values	pressure
Up step response time	1071 ms	13.3%	1.7%	5 to15 MPa
Down step response time	360 ms	58.2%	6%	15 to 5 MPa

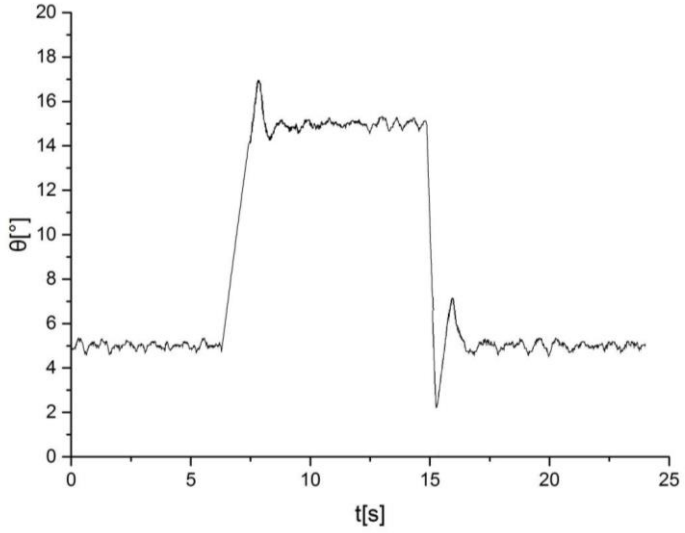

Figure 8. Angle response of the digital pump

Then set the step flow rate signal change from 5L/min to 60L/min, the output pressure is constantly 15 Mpa, and measure actual flow output of the pump. The dynamic control experimental curve as shown below:

Table 2. Experiment results of the flow response test

	response time	Overshoot	Steady jitter values	pressure
Up step response time	1036 ms	7.0%	2.5%	15 MPa
Down step response time	981 ms	100%	4.0%	15 MPa

As shown in the Figure 9, within the scope of the small flow rate, the dynamic control of the pump is fairly good.

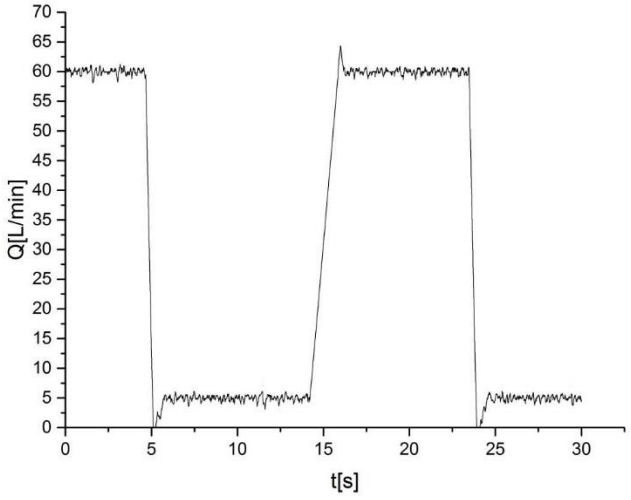

Figure 9. Flow response of the digital pump

As the experiment results shows, the dynamic control parameter is obviously optimized.

We use a step signal to control the pressure response changing from 5 MPa to 15 MPa.

The dynamic control experimental curve as shown below:

Table 3. Experiment results of the pressure response test

	response time	Overshoot	Steady jitter values
Up step response time	962 ms	15.3%	17.3%
Down step response time	715 ms	0.3%	22.2%

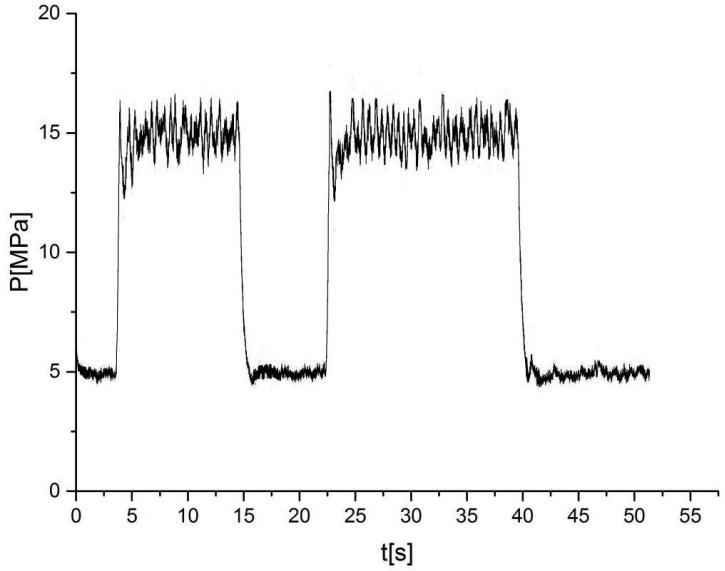

Figure 10. Pressure response of the digital pump

Because of the flow pulsation, when the pressure control at the time of high voltage, pressure of jitter is bigger.

The output power of pump is the product of the pressure and flow rate, the traditional fluid power control of variable pump is controlled by power valve. Experiments for variable power input of the control characteristics, set the power input signal for 5-15 kw step signal, detection of the actual power output of the pump to get test curve as shown in the figure below.

Table 4. Experiment results of the power response test

	response time	Overshoot	Steady jitter values
Up step response time	773 ms	9.3%	8.3%
Down step response time	543 ms	48%	14.0%

The dynamic control experimental curve as shown below:

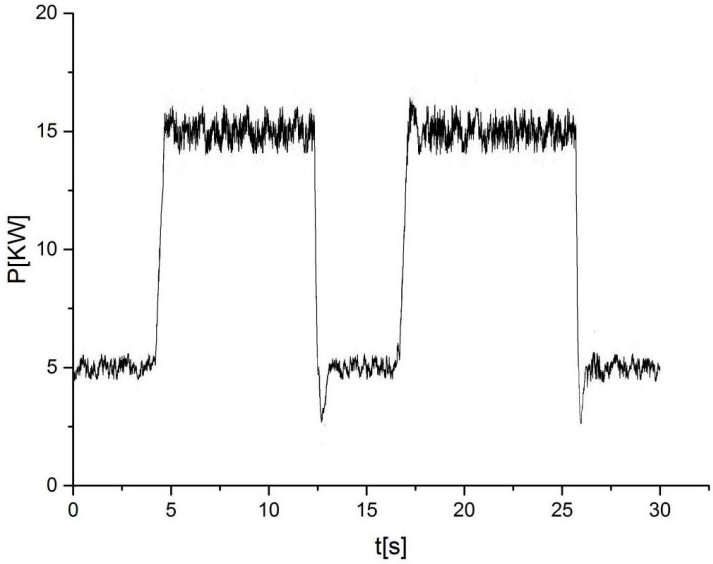

Figure 11. Power response of the digital pump

8. CONCLUSION

In this paper, the hydraulic mechanism and the control principle of a variable displacement pump are discussed. Adoption of high speed on/off valve and closed-loop control method is proved feasible by simulation. Simulation models of the pump model is established and with the co-simulation results the dynamic control characteristics are analyzed. The pressure control, flow control and power control performance of the pump are satisfied. Then the dynamic control characteristics of the pump prototype is measured by the designed test rig, and the experiment results are compared with the simulated ones. With modeling simulation and experiment results, we proved that the designed variable displacement pump controlled by switch valve can suit different kinds of working conditions. What's more this method can also improve the control performance of the hydraulic variable displacement pump and afford the pump better control accuracy and flexibility.

9. ACKNOWLEDGMENT

This work is funded by the National 04 major science and technology project (No.2012ZX04004021) and National Key Technology Support Program (No. 2014BAF02B00).

REFERENCES

[1]. Linjama M. 2011. Digital fluid power – state of the art [C]. The Twelfth Scandinavian International Conference on Fluid Power, May 18-20, Tampere, Finland.

[2]. Perry Y.Li, Cassie Y.Li and Thomas R.Chase. 2005. Software enabled variable displacement pumps [C]. International Mechanical Engineering Congress and Exposition, November 5-11, Orlando, Florida USA, pp.1-10.

[3]. Wen Z. Research on variable displacement control methods and characteristics of axial piston pump [D]. Zhejiang University China 2011.

[4]. Mint-Hwei C, Yuan K, Yi-wei C, YeonPun C. 2008. The swash plate angle control of a variable displacement pump with an electro-hydraulic proportional valve [J]. Materials Science Forum, 594, pp.389-400.

[5]. Bo G, Yong-Ling F, Zhong-cai P. 2005. Research of the servo pump's electrically driven variable displacement mechanism [C]. IEEE International Conference on Mechatronics and Automation, ICMA, pp.2130-2133.

[6]. Bin Z, Bin X, Hua-yong Y, Qiang Y, De-gang L. 2010. Study on control performance of digital piston pump based on virtual prototype technology [J]. Journal of Zhejiang University (Engineering Science), 44(1), pp.1-7.

[7]. Bin Z, Bin X, Chun-lin X, Hua-yong Y. 2009. Modeling and Simulation on Axial Piston Pump Based on Virtual Prototype Technology [J]. Chinese Journal of Mechanical Engineering, 22(1), pp.84-90.

[8]. Daniel B. Roemer, Michael M. Bech, Johansen P, and Henrik C. 2015. Pedersen. Optimum Design of a Moving Coil Actuator for Fast-Switching Valves in Digital Hydraulic Pumps and Motors [J]. IEEE/ASME TRANSACTIONS ON MECHATRONICS, VOL. 20, NO. 6, DECEMBER, p2761-2770.

[9]. David T. Branson III, John H. Lumkes Jr., Wattananithiporn K and Frank J. 2008. Fronczak. Simulated and experimental results for a hydraulic actuator controlled by two high-speed on\off solenoid valves [J].International Journal of Fluid Power 9 No. 2 pp. 47-5

[10]. Heitzig S, Sgro S. 2012. Efficiency of Hydraulic Systems with Shared Digital Pumps [J].International Journal of Fluid Power 13, No. 3 pp. 49-57

OPTIMAL DIGITAL HYDRAULIC FEED-FORWARD CONTROL APPLIED TO SIMPLE CYLINDER DRIVES

Dr. Rainer Haas, Christoph Hinterbichler, Dipl.-Ing. Evgeny Lukachev
Linz Center of Mechatronics GmbH
Drives
4040 Linz, Austria
E-mail: rainer.haas@lcm.at, christoph.hinterbichler@gmx.at, evgeny.lukachev@lcm.at

Dr. Markus Schöberl
Johannes Kepler University Linz
Institute of Automatic Control and Control Systems Technology
4040 Linz, Austria
E-mail: markus.schoeberl@jku.at

ABSTRACT

So far, optimal feed-forward hydraulic switching control has been investigated by the authors mainly to find out the performance limitations of this technology. Requiring time optimality is a trick to enforce a bang-bang type result for a basically continuous valve, in other words, to obtain an input which can be realized by switching valves. The results of these previous studies showed the feasibility of the approach for a few types of linear hydraulic drives.

The intention of this paper is to give a short and clear insight into the basics of this principle. This includes a discussion of the idea of this approach as well as a discussion of different solution techniques. Possibilities, challenges and limitations of the approach and these different solution techniques are summarized. Simple examples are stated in order to demonstrate the results.

To this end, a quite simple system composed of a differential cylinder in plunger mode with a mass and one or two digital half bridges of different size and dynamics are subject of this investigation. For this simple example, with multiple inputs, a switching feed-forward could be found.
Finally, a dual chamber cylinder is actuated using different kinds of digital valves. First, each fluid chamber is connected to a 3-3 way valve; second, each chamber is connected to a digital half bridge consisting of two 2-2- way valves; and third, the cylinder is actuated using a single 4-3 way valve connected to both fluid chambers. The optimisation problems for all these examples could be solved and the resulting feed-forward commands are realizable by switching valves.

KEYWORDS: Digital hydraulics, optimal feed-forward control, on/off valves

1. INTRODUCTION

Digital hydraulics is often used for reliable, fast and precise positioning of masses using linear actuators like hydraulic cylinders. Recurring problems of digital hydraulic drives are pressure respectively position oscillations excited by fast switching valves. Nowadays there are quite a lot of publications available dealing with pulsation respectively oscillation reduction methods designed for hydraulic circuits. The work of the following authors is just a short excerpt, e.g. [1], [2], [3]. Some of them are dealing with passive methods, like hydraulic filters, or sly actuated switching valves - operating in the ballistic mode (see [4], [5]). In the following work we will not go into the details of these papers.
In the Digital Fluid Power Workshop 2015 [6], the authors showed a new way of designing a digital feed-forward signal. This approach is based on the theory of optimal feed-forward control. It has been shown that the approach works for the chosen system under study, which contained a cylinder, a simplified model of a pipe and a 2-2 way valve. The obtained result consisted of multiple rectangular valve opening cycles which can be realized as ballistic pulses of the valve. This result was verified using a more detailed and practically relevant simulation model built in Matlab/Simulink using the hydraulic simulation toolbox hydroLib3 [7].
In order to show the practical relevance of this approach, the computed feed-forward signal was tested on a test stand in the lab. The measurements showed that it is possible to reduce ongoing oscillations after a desired position step of a hydraulic cylinder. Results of this work and the detailed description can be found in [8] – which is currently under review.

The paper of the DFP15 [6] gave just a short introduction to the theory respectively the idea why this approach can be used in digital hydraulics. This work is written in the intention to give a better insight into the approach, e.g. advantages, disadvantages as well as a discussion of some relevant effects should round-up the performed work.

1.1. Motivation

Control design methods for digitally actuated hydraulic systems are limited. That's due to the limitation of the system input to a discrete set of states, writing $u_i \in \{-1,0,1\}$. Practically this means, that hydraulic switching valves can only be fully open or closed. States in between can only be passed through, not be held for longer times as it is possible with proportional or servo valves.
A suitable approach, typically used for switched systems, is state space averaging, see [9] pp.60ff. Usually, state space averaging is used in electro techniques, e.g. the chuck converter. In the case of a pulse width modulated (PWM) electrical converter it is possible to define such an averaged dynamical system using the duty cycle κ as new continuous control input, i.e. $\kappa \in [0,1]$. Now it's possible to apply one of the well-known control design methods for continuous systems, e.g. linear-quadratic regulator (LQR) and so on.

Below we will derive an averaged system for a typical hydraulic circuit, see figure (1). The system consists of five pressure build up equations; e.g. piston- and annular-side chamber, accumulator and two pipe capacities; four inductivities; the linear equations of motion and the nonlinear flow characteristic of the pressure and tank sided valve. The valve command signals are restricted to the discrete values one and zero, i.e. $\boldsymbol{u} \in \{0,1\}$.

For further investigations it's assumed that only the system pressure sided valve V_1 is actuated.

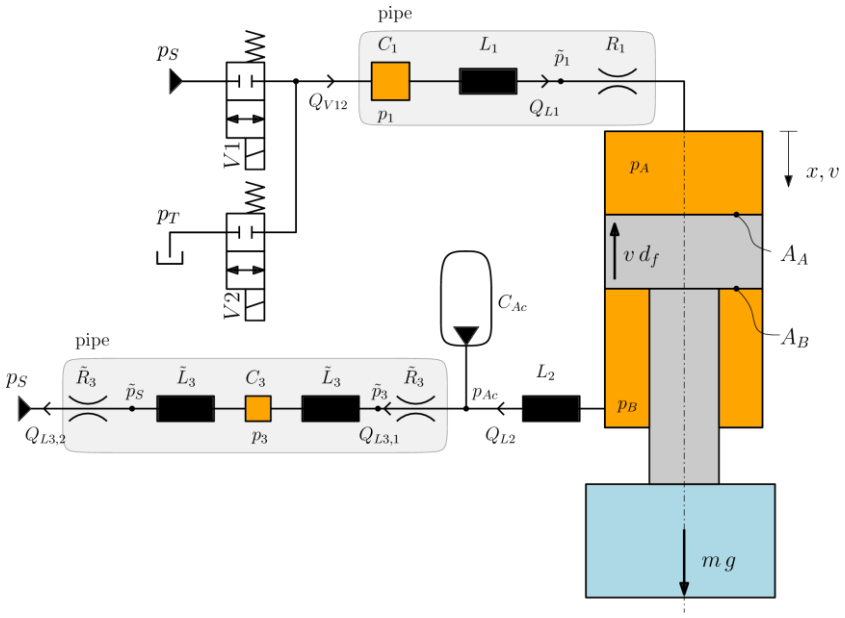

Figure 1. Sketch of the studied digital hydraulic system.

$$\dot{p}_1 = \frac{E}{V_1} \cdot \left[u\, Q_N \cdot \sqrt[\wedge]{\frac{p_S - p_1}{p_N}} - Q_{L1} \right]$$

$$\dot{Q}_{L1} = \frac{A_1}{\rho l_1} \cdot [p_1 - (Q_{L1} R_1 + p_A)]$$

$$\dot{p}_A = \frac{E}{V_{A,0} + x A_A} [Q_{L1} - v A_A]$$

$$\dot{x} = v$$

$$\dot{v} = \frac{1}{m} \cdot [p_A A_A - p_B A_B - d_f v + mg]$$

$$\dot{p}_B = \frac{E}{V_{B,0} - x A_B} \cdot [v A_B - Q_{L2}]$$

$$\dot{Q}_{L2} = \frac{A_2}{\rho l_2} \cdot [p_B - p_{Ac}]$$

$$\dot{p}_{Ac} = \frac{n \cdot p_{Ac}}{V_{Ac,0} \left(\frac{p_{Ac,0}}{p_{Ac}} \right)^{\frac{1}{n_{poly}}}} \cdot (Q_{L2} - Q_{L3,1})$$

$$\dot{Q}_{L3,1} = \frac{1}{\tilde{L}_3} \cdot [p_{Ac} - \tilde{R}_3 Q_{L3,1} - p_3]$$

$$\dot{p}_3 = \frac{E}{V_3} \cdot [Q_{L3,1} - Q_{L3,2}]$$

$$\dot{Q}_{L3,2} = \frac{1}{\tilde{L}_3} \cdot [p_3 - (\tilde{R}_3 Q_{L3,2} + p_S)]$$

Equation 1. Dynamic system equation for the system depicted in figure (1). Generally the Hagen-Poiseuille friction factor and the inductance are defined by: $R_i = \frac{128 \rho \nu l_i}{\pi d_i^4}$ and $L_i = \frac{\rho l_i}{A_i}$ where $i \in \{1,2,3\}$ and $\tilde{L}_3 = \frac{L_3}{2}$, $\tilde{R}_3 = \frac{R_3}{2}$. And $\sqrt[\wedge]{x} = \text{sign}(x) \cdot \sqrt{|x|}$.

The periodic time T_{PWM} of the PWM is divided into two sub-periods; one where the valve is fully open T_{on} and one where it is closed T_{off}. The fraction between the "on time" and the periodic time T_{PWM} is the duty cycle $\kappa = \frac{T_{on}}{T_{PWM}}$. Due to that, there exist two different vector fields, one for each. Generally, the fully opened case writes

$$\frac{dx}{dt} = \boldsymbol{f_\alpha}(\boldsymbol{x}), \quad t \in (i\, T_{PWM}, (i + \kappa) T_{PWM}] \quad \text{with } i \in \mathbb{N} \tag{2}$$

and the one for the closed valve $\boldsymbol{f_\beta}(\boldsymbol{x})$ is defined as

$$\frac{dx}{dt} = \boldsymbol{f_\beta}(\boldsymbol{x}),\ \ t \in \left((i+\kappa)T_{PWM}, (i+1)T_{PWM}\right] \ \text{ with } i \in \mathbb{N}. \tag{3}$$

The averaged state-space model can be written as follows:

$$\frac{dx_a}{dt} = \left(\kappa \cdot \boldsymbol{f_\alpha} + (1-\kappa)\cdot \boldsymbol{f_\beta}\right)(\boldsymbol{x_a}). \tag{4}$$

In the case of the system depicted in figure (1) both vector fields almost equal. They differ just in a single ordinary differential equation (ODE) – the one of the capacitance right after the valves. All but one ODE of the averaged vector field $\boldsymbol{f_a}(\boldsymbol{x_a})$ are equal to the ODEs of $\boldsymbol{f_\alpha}(\boldsymbol{x})$. The only difference arises in the pressure build up equation right after the valve, where the discrete valve command u turns into the continuous duty cycle κ. The following lines illustrate this transformation.

$$\left.\begin{aligned} \dot{p}_{1,\alpha} &= \frac{E}{V_1}\cdot\left[\, Q_N \cdot \hat{\sqrt{\frac{p_S - p_{1,\alpha}}{p_N}}} - Q_{L1}\right] \\ \dot{p}_{1,\beta} &= \frac{E}{V_1}\cdot\left[-Q_{L1}\right] \end{aligned}\right\} \quad \begin{aligned} \dot{p}_{1,a} &= \frac{E}{V_1}\left[\kappa\left(\, Q_N \cdot \hat{\sqrt{\frac{p_S - p_{1,a}}{p_N}}} - Q_{L1}\right) + (1-\kappa)(\,-Q_{L1})\right] \\ \dot{p}_{1,a} &= \frac{E}{V_1}\left[\kappa\, Q_N \cdot \hat{\sqrt{\frac{p_S - p_{1,a}}{p_N}}} - Q_{L1}\right] \end{aligned} \tag{5}$$

The hat symbol of the square root is an abbreviation for $\hat{\sqrt{x}} = \text{sign}(x)\cdot\sqrt{|x|}$. Figure (2) depicts the bode diagram for the cylinder position of the linearized continuous system, writing $G_s = \frac{x}{\kappa}$. It is evaluated at the equilibrium state: $x = 100mm,\ \ v = 0\frac{m}{s}$, $Q_{L1} = Q_{L2} = Q_{L3} = 0\ \frac{l}{min}$, , $p_B = p_2 = p_3 = p_S$ and $p_1 = p_A = \frac{p_B A_B - m\cdot g}{A_A}$.

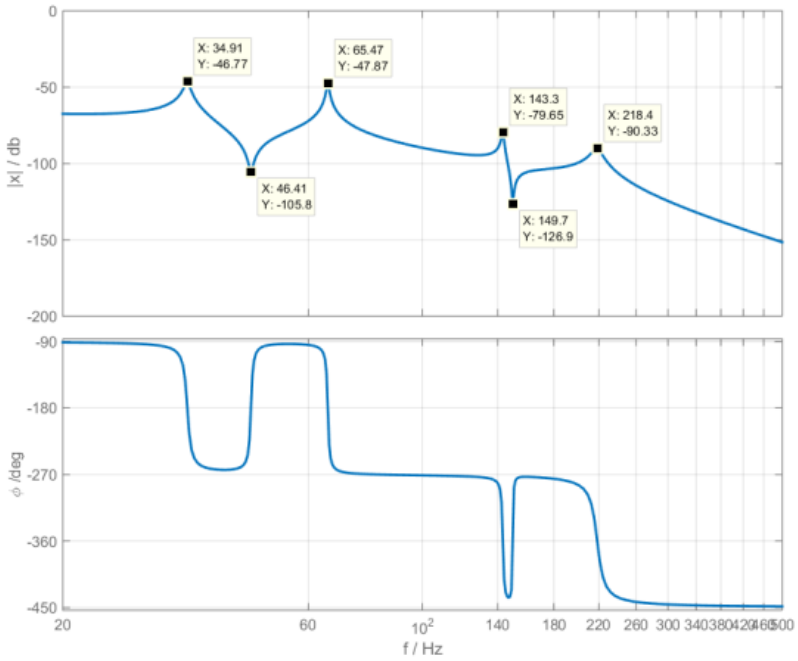

Figure 2. Bode diagram of the system under study, see figure (1).

In figure (2), it can be seen that the system resonances are at approximately: $35Hz$, $65Hz$, $143Hz$, $218Hz$.

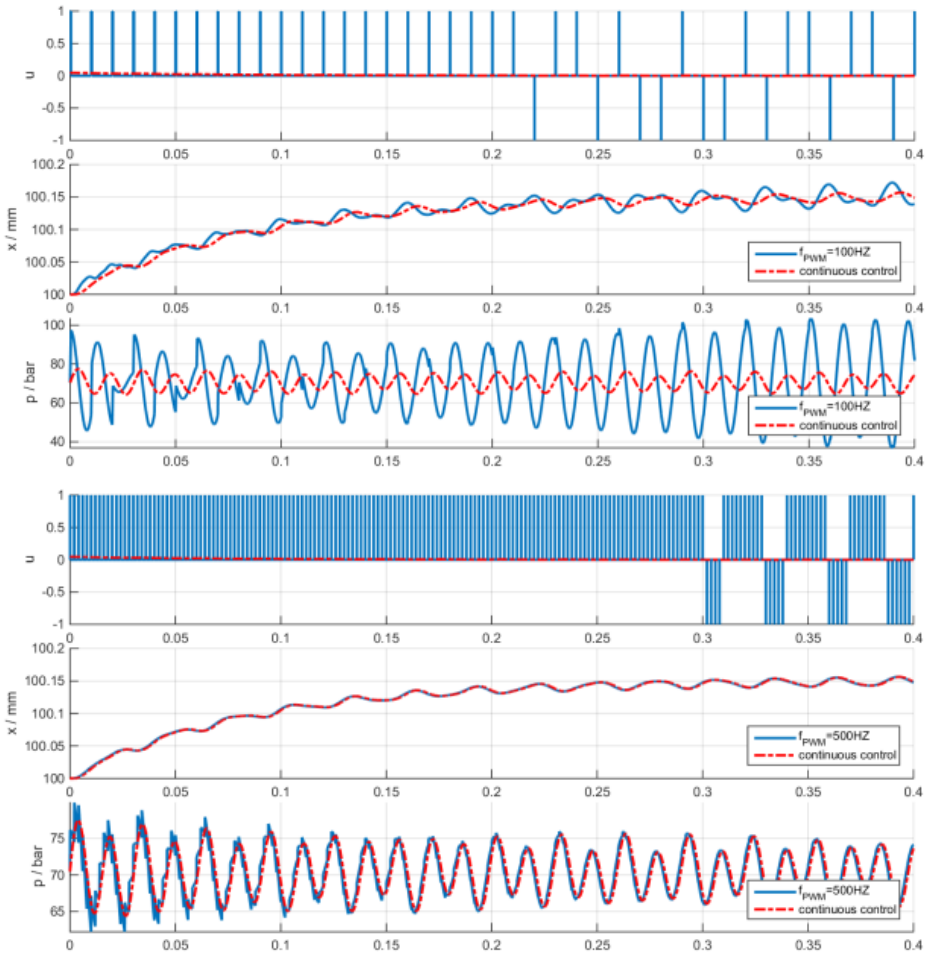

Figure 3. Results of the state-space averaging model for different PWM-frequencies. The higher the control frequency, the better are the results.

Figure (3) depicts results of the state-space averaging method of a simple proportional controlled position step for two different PWM-frequencies: once $100Hz$, second $500Hz$. In our case a PWM-frequency of about $500Hz$ would lead to a sufficiently good approximation. This behaviour corresponds to the statement from Kugi in [9] page 61, which reads "Under the assumption that the modulation frequency is much higher than the natural frequencies of the converter system … we can derive the so called average model for the PWM controlled electric circuit (3.85), see, e.g. [57], [127]."

Finally, it can be said that the switching frequency of the currently available digital hydraulic valves is limited to 100…150 Hz. Parallelisation of valves – i.e. the valves are alternating – is an easy way to increase the effective PWM frequency. However, it cannot be increased arbitrarily high, the maximum opening and closing speed being the next limiting factor.

1.2. Theoretical considerations

In the field of control theory there are much less methods for systems with switched actuators than for continuous ones. Additionally, in hydraulics we are often in the not advantageous situation that the system eigen-frequencies are quite close to the maximum possible PWM-frequency so that the usually used averaging approach is not applicable. Due to these circumstances we pan our focus to open loop control methods,

especially to the field of optimal feed-forward control.
In the following, the job of the feed-forward control is to transfer the system from one equilibrium state to another, e.g. a position step of the cylinder drive. This task can generally be formulated into the following dynamic optimisation problem:

$$\begin{aligned} \min_{\boldsymbol{u}(\cdot)} \quad & J(\boldsymbol{u}) = T \\ s.t. \quad & \dot{\boldsymbol{x}} = \boldsymbol{f}(\boldsymbol{x}, \boldsymbol{u}), \\ & \boldsymbol{x}(0) = \boldsymbol{x}_0, \quad \boldsymbol{x}(T) = \boldsymbol{x}_T \\ & |\boldsymbol{u}(t)| \leq u_{max}, \quad \forall t \in [0, T] \end{aligned} \tag{6}$$

From the optimisation theory, it is well known that an optimal feed-forward $\boldsymbol{u}^*$ – the star $*$ denotes that the control u is optimal – of a nonlinear dynamical system with bounded inputs tends to a switching shape if time optimality is chosen as a criterion and the differential equations are in the input affine form. Generally, a nonlinear system of differential equations is input affine if it can be formulated according to equation (7).

$$\dot{\boldsymbol{x}} = \boldsymbol{f}(\boldsymbol{x}, \boldsymbol{u}) = \boldsymbol{f}_0(\boldsymbol{x}) + \sum_{i=1}^{m} \boldsymbol{f}_i(\boldsymbol{x}) u_i. \tag{7}$$

For more details we refer to Graichen [10] 109ff – especially for the case of singular optimisation problems. In that case, the feed-forward can contain time intervals which are not bang-bang.

At this position just a short statement to the often used term “bang-bang”. In the case that the input resides only in the upper and lower bounds – not in between – we will call the feed-forward “bang-bang”. This designation can also be found in other literature, see [11] p. 7, [12] p. 31. If the input is bounded between minus and plus one bang-bang is mathematically formulated according to

$$|u^*(t)| = 1 \quad \text{where} \quad -1 \leq u(t) \leq 1, \quad \forall t \in [0, T]. \tag{8}$$

After this short survey of optimal feed forward control theory, we give some comments on hydraulic systems and outline the way from the definition of a dynamic optimisation problem towards the formulation of a static optimisation problem – which can be numerically solved.

1.2.1. Solving dynamical optimisation problems

Usually, numerical methods are needed to solve dynamical optimisation problems. According to the type of method, they are divided into two categories: Indirect methods and direct methods, see [10] p. 120ff. Indirect methods are known to give high precision results due to a more profound theoretical basis, see [12] p 65. But setting up the adjoint set of ODEs can be troublesome for big nonlinear sets of differential equations. Additionally, a good initial guess of the adjoint variables is important for good convergence of the numerical optimisation. Direct methods are based on the discretisation of the system, therefore less theoretical knowledge, i.e. of the minimum principle or the adjoint variables, is necessary. The use of global optimisation methods has the advantage of a larger conversion radius, this means a good convergence even in the case of a not good initial guess.

In the following we focus on direct methods. The dynamic optimisation problem (6) is transformed into a finite dimensional static one by parametrisation of the input $\boldsymbol{u}(t), t \in [0, T]$. Generally, the resulting static optimisation problem has the following shape:

$$\begin{aligned} \min_{\boldsymbol{x}\in\mathbb{R}^n} \quad & f(\boldsymbol{x}) \\ s.t. \quad & g_i(\boldsymbol{x}) = 0, \;\; i = 1, \dots, p \\ & h_i(\boldsymbol{x}) \leq 0, \;\; i = 1, \dots, q \end{aligned} \tag{9}$$

Summarizing, direct optimisation methods can be divided into two classes according to the parameterisation approach (see [10] p. 126ff):

1. Sequential method (partial discretisation): The identifying feature is the discretisation of the control signal u in the time interval $t \in [0, T]$. u can either be held constant or assumed to be linear in the subintervals obtained by the discretisation. In order to solve the nonlinear optimisation problem it is necessary to solve the set of ODEs by a subsidiary integration method, e.g. a Runge-Kutta method, see [13]. However, constraints like $x_k = x_{k-1}$ guarantee the continuity of the solution.

2. Simultaneous method (full discretisation): On the contrary to the sequential method, where only the control signal is discretized, the simultaneous method is characterized by a full discretisation of all ODEs and the control signal. It has to be noted that the discretized states are only sufficiently accurate in the case of an optimal solution. The precision of the method directly corresponds to the number of sampling points. A typical discretisation technique is the trapezoidal method.

The resulting optimisation problems can be solved by various methods designed for static problems.

1.2.2. Applied approaches

Two ways for the transformation of the dynamical optimisation problem into a static one are examined in this paper:

1. The dynamic system is differentially flat. Roughly speaking, the dynamic system of eq. (6) with m inputs is flat, if there exist m differentially independent functions $\boldsymbol{y}$ (flat outputs), such that the state $\boldsymbol{x}$ and the control $\boldsymbol{u}$ can be parameterized by $\boldsymbol{y}$ and its successive time derivatives. Hence, flat systems enjoy the characteristic feature that the (time) evolution of the state and input (control) variables can be recovered from that of the flat output without integration, see [14]. Therefore the differential equations $\dot{\boldsymbol{x}} = \boldsymbol{f}(\boldsymbol{x}, \boldsymbol{u})$ of the optimisation problem (6) are automatically fulfilled, and no more needed as optimisation constraints. By parameterisation of the flat output $\boldsymbol{y}$ through e.g. B-splines a static optimisation problem can be obtained. Just one advantage of using B-splines is that parameter changes, like rounding errors, have just local impact. This is due to the compact support of the spline. For more details see [15].
   In the following, problem (6) is not directly solved. But it is replaced by a sequence of subproblems (10) with a fixed final time T and a constrained input

$|\boldsymbol{u}| \leq \epsilon$.

$$\begin{aligned} \min_{\boldsymbol{u}(\cdot)} \quad & \epsilon \\ s.t. \quad & \dot{\boldsymbol{x}} = \boldsymbol{f}(\boldsymbol{x}, \boldsymbol{u}) \\ & \boldsymbol{x}(0) = \boldsymbol{x_0} \\ & \boldsymbol{x}(T) = \boldsymbol{x_T} \\ & |\boldsymbol{u}| \leq \epsilon \end{aligned} \tag{10}$$

The input constraint ϵ is minimized. If the resulting input constraint ϵ is greater than the desired value u_{max}, the final time T of the next iteration has to be increased. For smaller ϵ, T has to be reduced. In the case of $\epsilon = u_{max}$, the solution of this approach is equivalent to the one of the time optimal problem.

2. Another used method belongs to the class of sequential methods and is applicable to not flat systems. A detailed discussion of the discretisation as well as the numerical integration of the dynamical system can be found in [6] and [8] and is therefore no more discussed.

Table 1. Advantages and disadvantages of the different ways to transform the dynamical problem into a static one

	Variant 1	**Variant 2**
Advantages	• Smaller optimisation problem than full or partial discretisation • No subsidiary time integration needed	• Optimisation of non-flat systems possible
Disadvantages	• System has to be differentially flat	• Typically large optimisation problems ⇒ long run times

The resulting static optimisation problem including equality and inequality constraints (eq. (9)) is solved by the use of SQP-solvers (Sequentially quadratic programming). This is an iterative method solving at each iteration step a linearized sub-problem. In the following work we used an SQP-solver implementation from Matlab [16] and from the scipy-toolbox of python [17].

2. BOUNDED STATES AND BOUNDED VALVE COMMAND SPEED

First the influence of bounded system states, and second the influence of limited speed of the control command signal is discussed. Both cases are demonstrated by representative examples.
Finally, a heuristic method is described which can be used to obtain an applicable digital valve command signal. This approach works quite well in many by the authors tested cases, but nevertheless it is not guaranteed that an applicable command signal can be obtained.

2.1. Bounded system sates

A bang-bang input signal is what we need in digital hydraulics. It describes the typical operation mode of a switching valve; which can either be fully open or closed. Naturally this approach has the drawback that system states have often physical or technical bounds. One well known example is the pressure which is bounded from below, i.e.

zero absolute pressure. Other application dependent bounds like maximum piston velocity, maximum pressure at certain system locations, or even position limits are also possible. These additional restrictions to the optimisation problem can result in time optimal feed-forwards which are not bang-bang any more – there exist regions which cannot be replicated by a hydraulic switching valve. This subsection shows an example with and without bounded system states. We will also show a trick, which helped us to convert non bang-bang feed-forwards into implementable ones.

A sketch of the system under study is depicted in figure (4). It consists of a differential cylinder in plunger mode, i.e. the annular cylinder chamber is constantly at system pressure. The RLC-element between the valve and the cylinder volume represents a very simple pipe model. The optimal valve command is computed for the case of using only the pressure sided 2-2-way valve $V1$. The tank valve $V2$ is not actuated.

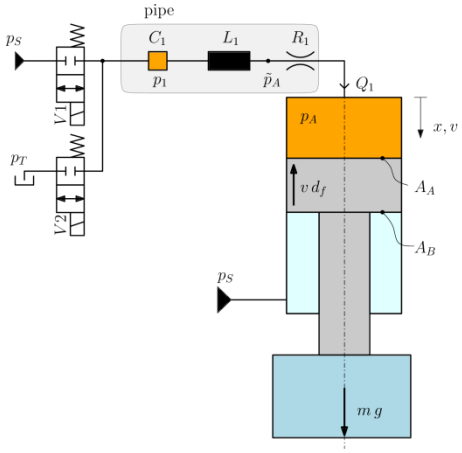

Figure 4. System sketch

$$\dot{p}_1 = \frac{1}{C_1}\left(u \cdot Q_n \hat{\sqrt{\frac{p_S - p_1}{p_n}}} - Q_1\right)$$
$$\dot{Q}_1 = \frac{1}{L_1}(p_1 - p_A - R_1 Q_1)$$
$$\dot{p}_A = \frac{E}{V_{p,0} + A_A x}(Q_1 - A_A v)$$
$$\dot{x} = v$$
$$\dot{v} = \frac{1}{m}(p_A A_A - p_S A_B + mg)$$

Equation 11. Dynamic system equation for the system depicted in figure (4)

Due to the fact that the system under study is differentially flat, the optimisation of the time optimal feed-forward takes care of this characteristic. The cylinder position x is a flat output y of the dynamic system, see equation (12). All states and the input can be expressed in terms of the cylinder position and its successive derivatives.

$$\begin{aligned}
x &= y \\
v &= \dot{y} \\
p_A &= \ddot{y}\frac{m}{A_A} + p_S\frac{A_B}{A_A} - \frac{mg}{A_A} \\
Q_1 &= \dddot{y}\frac{m}{A_A}\frac{V_{p,0}+A_A y}{E} + \dot{y}A_A \\
p_1 &= \dot{Q}_1(y,\dots,y^{IV})L_1 + p_A(y,\dots,\ddot{y}) + R_1 Q_1(y,\dots,\ddot{y}) \\
u &= \frac{\dot{p}_1(y,\dots,y^V)C_1 + Q_1(y,\dots,\ddot{y})}{Q_n \hat{\sqrt{\frac{p_S - p_1(y,\dots,y^{IV})}{p_n}}}}
\end{aligned} \tag{12}$$

In equation (12), the following abbreviations are used:

$$\begin{aligned}
\dot{Q}_1(y,\dots,y^{IV}) &= \frac{d}{dt}(Q_1(y,\dots,\ddot{y})) \\
\dot{p}_1(y,\dots,y^V)) &= \frac{d}{dt}(p_1(y,\dots,y^{IV}))
\end{aligned} \tag{13}$$

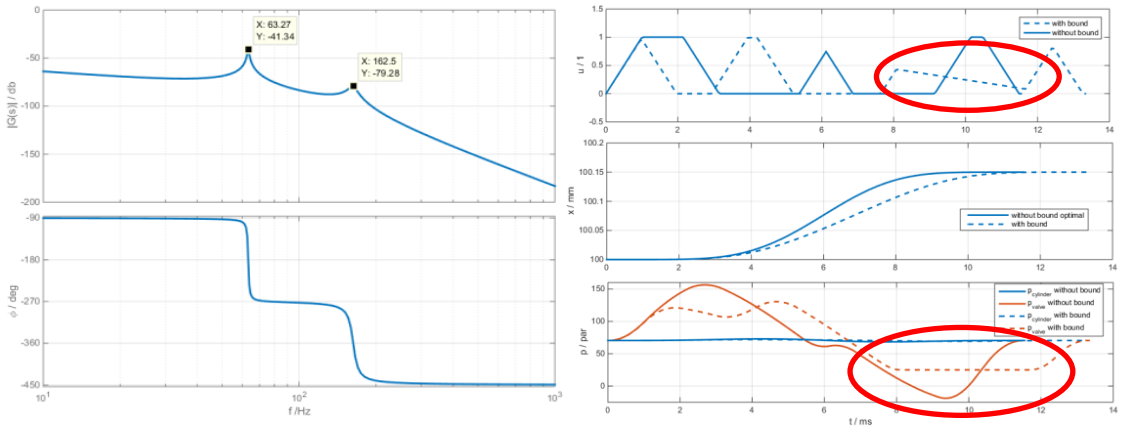

Figure 5. Left: Transfer function of the linearized system at $x = 100mm$. Right: Time optimal solutions for a system with bounded and unbounded pressure states. The minimum pressure $p_{min} = 25bar$.

The result, depicted in figure (5), shows the previously described system behaviour. Computing a time optimal position change for the case of unbounded pressure states leads to unphysical results, i.e. the pressure is negative. In real applications, cavitation occurs and limits the pressure at values greater than zero. Bounding the pressure into a range greater than zero prevents unphysical results. The outcome is that there occurs a certain part in the command signal which is not applicable for digital valves because the command signal is not in its bounds; see the dashed command signal in figure (5).

This shows that the restriction to time optimality does not always lead to usable feed-forward signals. Now there are two different approaches to solve this problem. The first is to adapt the mechanical design of the test stand, in the way that the optimal result does not lead to unphysical results. Examples could be a larger valve capacitance, an RC-filer right between the valve and the pipe, etc. A numerical approach, which pointed out to be advantageous, is described in the second following subsection.

2.2. Bounded valve command speed

The easiest way to take care of the limited opening and closing speed of the valve is to consider additional inequality constraints in the optimisation problem (9). With a consideration like this it is also possible to account for the different slopes in the case of opening and closing.
Further on, it is tested how such additional constraints affect the optimal valve command. The test case is a very simple plunger drive (annular pressure is constantly at system pressure) which is directly actuated by a digital half bridge, see figure (6).

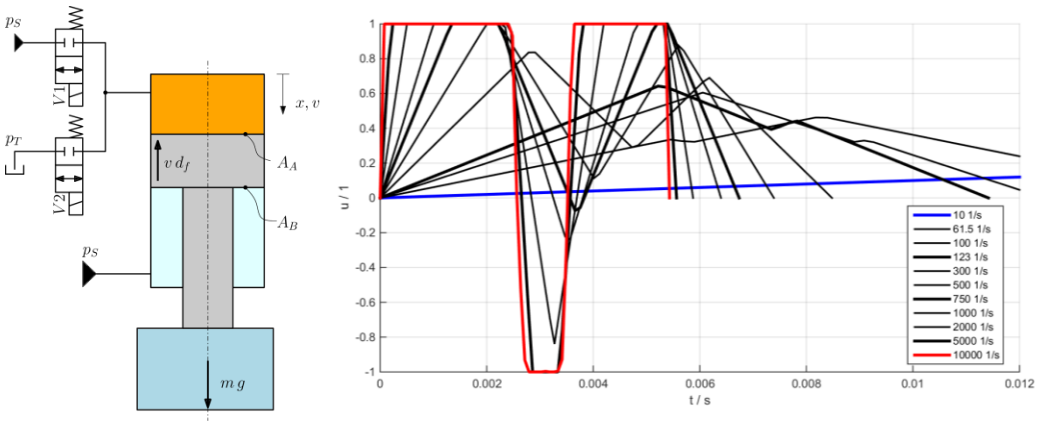

Figure 6. Effect of different maximum valve speed

In the case of an optimisation problem with unbounded $\dot{u}$ the well-known result is bang-bang. The red line of figure (6) depicts a good approximation of this behaviour.
Limiting the speed of the valve command to lower values leads to time optimal results where the "back-actuation" – this is the part where the pressure sided valve is closed and the tank valve is open – gets smaller (black lines of figure (6)). It can be seen that the limited command speed has some influence on the applicability of the result. The optimal feed-forward contains either of applicable ballistic pulses or of a shape which can hardly be used for the digital actuation of real valves, e.g. $\dot{u} = 300\frac{1}{s}$. The approach of the next subsection can be used to obtain better realisable command signals.

2.3. Heuristic approach

Next we will describe a promising approach for turning a not bang-bang input into a digitally realizable one.
The starting point is the time optimal solution of the optimisation problem. The new command signal can be obtained from a new optimisation, taking some information of the previous one into account. One difference to the initial optimization is that the criterion is changed into a here called "digital-optimal" criterion.

$$-1 \le \boldsymbol{u} \le 1 \quad \Rightarrow \quad J(\boldsymbol{u}) = \sum_i |u_i|(1 - |u_i|)$$

$$0 \le \boldsymbol{u} \le 1 \quad \Rightarrow \quad J(\boldsymbol{u}) = \sum_i u_i(1 - u_i)\,.$$

Equation 14. Digital optimisation criterion for differently bounded valve command signals

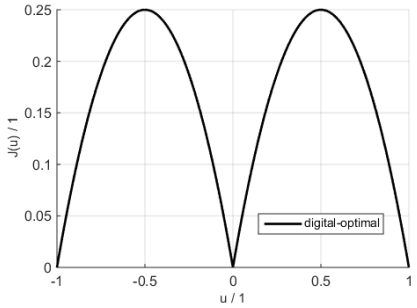

Figure 7. Digital optimisation criterion

The other important point is that the final time T of the dynamic optimisation problem is fixed to a value larger than the time-optimal time T^*, i.e. $T = \alpha \cdot T^* > T^*$. This grants that the optimizer has some freedom to change the time-optimal solution, which contains some non-digital paths, according to the new criterion. In order to get an

improvement it is important that the new final time is not too far away from the one received with the time optimal algorithm. Practical experiences of the authors are that an extension of about five to fifteen percent leads to acceptable results, writing $\alpha = 1.05 \ldots 1.15$.
Figure (8) shows the comparison between the time optimal and the digital-optimal results. It can also be seen that this approach works with or without limited valve command speed $\dot{u}$, see the right respectively the left plot. The dynamical system of this example is the same as depicted in figure (4).

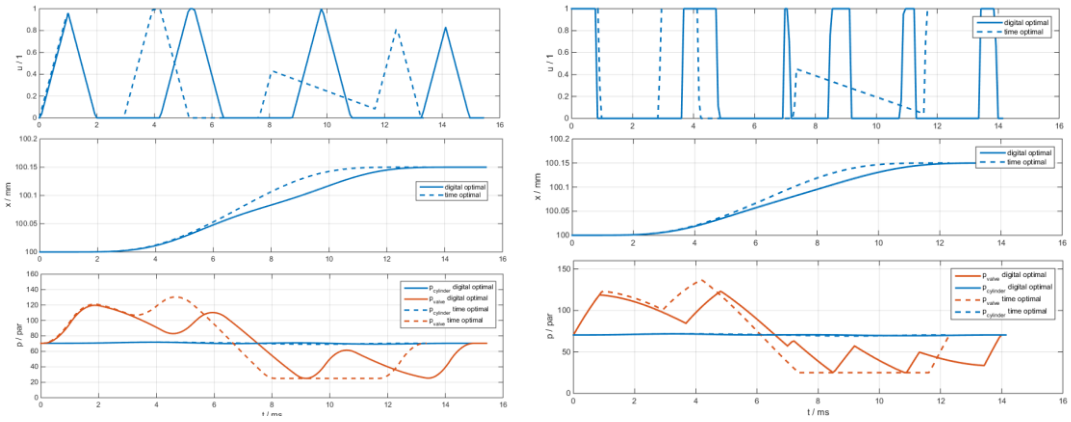

Figure 8. Optimal position changes ($\Delta x = 150 \mu m$) with and without limited valve command speed $\dot{u}$.

3. SYSTEMS UNDER STUDY

3.1. Single side actuated cylinder drive systems

This subsection shows the difference between a differential cylinder in plunger mode, actuated by one or two digital half bridges. The second half bridge is installed in parallel. The valve command speed is limited to two different values, once $\dot{u}_{max} = |800|$ and in the other case $\dot{u}_{max} = |2000|$, see the figure (9). Valves V1 and V2 are in both cases parameterized with the same limits. In the case of fast valves the result is practically realisable. There is no need of the previously described trick. In the other case, this approach helped to get an applicable result.

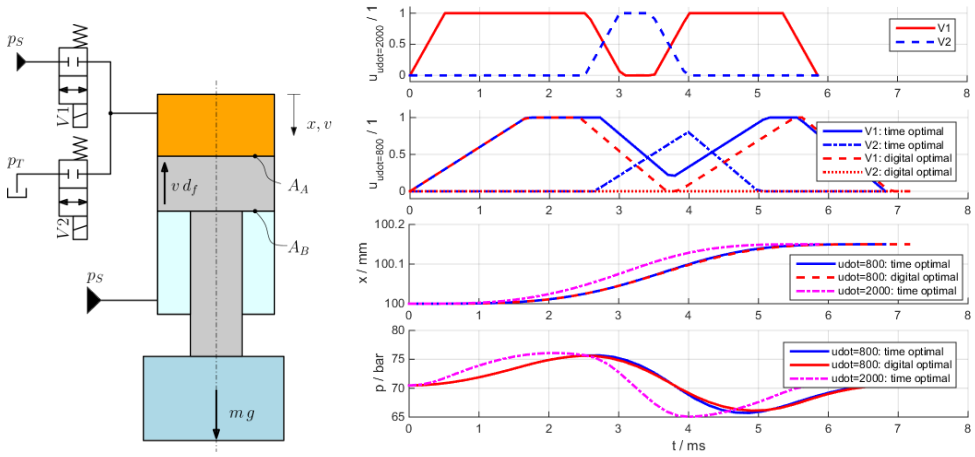

Figure 9. Single sided cylinder actuation using a single hydraulic half-bridge.

In the case of two independent command signals it is possible that the optimal solution contains of time periods where the pressure supply and the tank are partly connected. If it is of interest that these shortcuts are avoided, a half bridge can be modelled as a 3-3 way valve, see subsection 3.2.

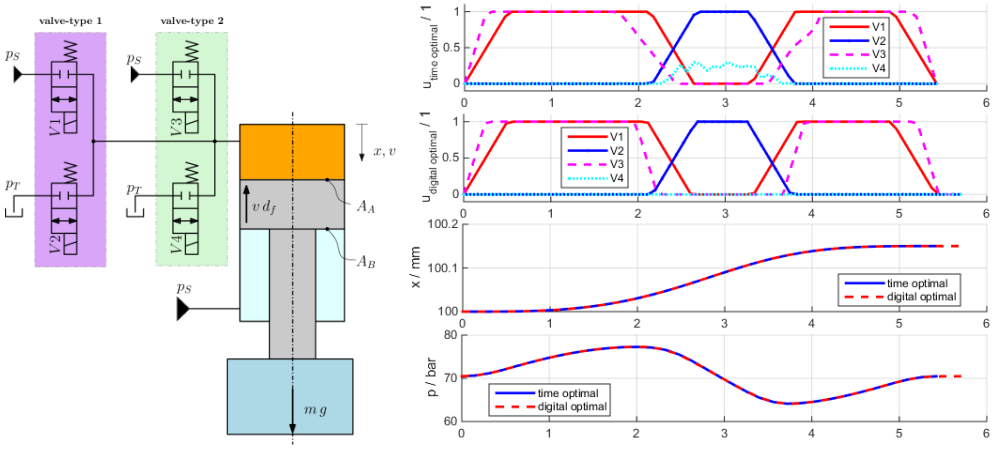

Figure 10. Single sided cylinder actuation using two hydraulic half-bridges of different size. Valve type 1: $Q_{n1}(5bar) = 45\frac{L}{min}$ and valve type 2 $Q_{n2}(5bar) = 10\frac{L}{min}$.

It is also possible to optimize the command signals for two parallel half bridges. Requiring time optimality leads in that case to an unrealizable result for the valve V4. The command signal for V3 shows also some problematic passages. Application of our approach leads again to a usable switching digital command signal. In the depicted case V4 is not used anymore and V1, V2 and V3 are adapted by the optimiser.

3.2. Non-flat system

In the case of non-flat systems it's necessary to discretize the dynamical optimisation problem using a sequential or simultaneous method. The cylinder position x of the hydraulic system shown in figure (11) is not a flat output. That's why sequential discretisation is used to formulate the static optimisation problem.

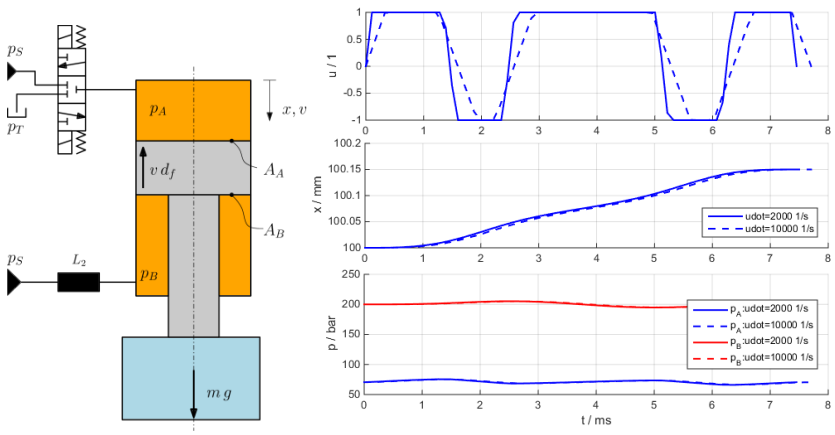

Figure 11. Time optimal optimisation result for a non-flat system. The command signal is limited according to $-1 \leq u \leq 1$ and $|\dot{u}| \leq 1$.

The result depicted in figure (11) shows that it is possible to obtain a bang-bang input signal. Results are computed using a time optimal criterion. Similar results are shown in [6] and [8].

3.3. Cylinder control using a 4-3-way valve

Another practically interesting case is the digital control of a cylinder actuated by a 4-3 way digital valve. Figure (12) depicts a sketch of such a system (left) as well as the simulation results for a time optimal and a digital optimal criterion (right).

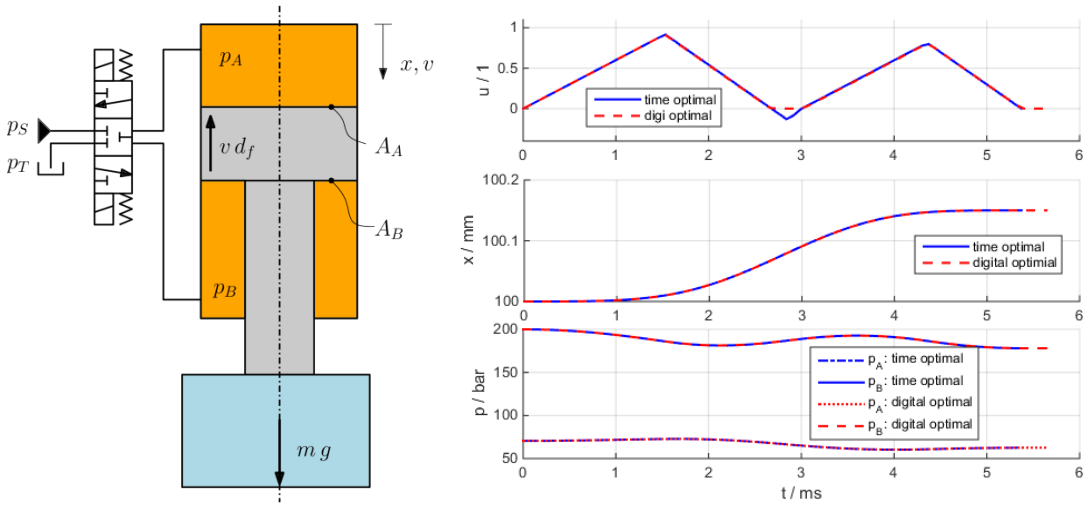

Figure 12. Double sided actuation realised using a 4-3 way valve. Left: the system sketch and right the optimisation result.

For this case it is necessary to adapt the dynamic optimisation problem slightly. From system analysis it is clear that it is not possible to define a final pressure in the cylinder chamber using one valve. Only the differential pressure between both chambers can be defined. Therefore the dynamic optimisation problem is redefined in the way that one of the final pressure values is free and the other one is fixed relative to the free one guaranteeing a certain difference in order to land at a steady state again. This pressure difference between both cylinder chambers can be computed according to: $p_A A_A - p_B A_B + m \cdot g = 0$.

3.4. Digital 3-3-way valves at the piston and at the annular sides

If it is of interest to determine the final pressure states of the system described in subsection 3.3., an additional digital valve has to be placed at the annular side of the cylinder. The system and the optimisation results are depicted in figure (13).

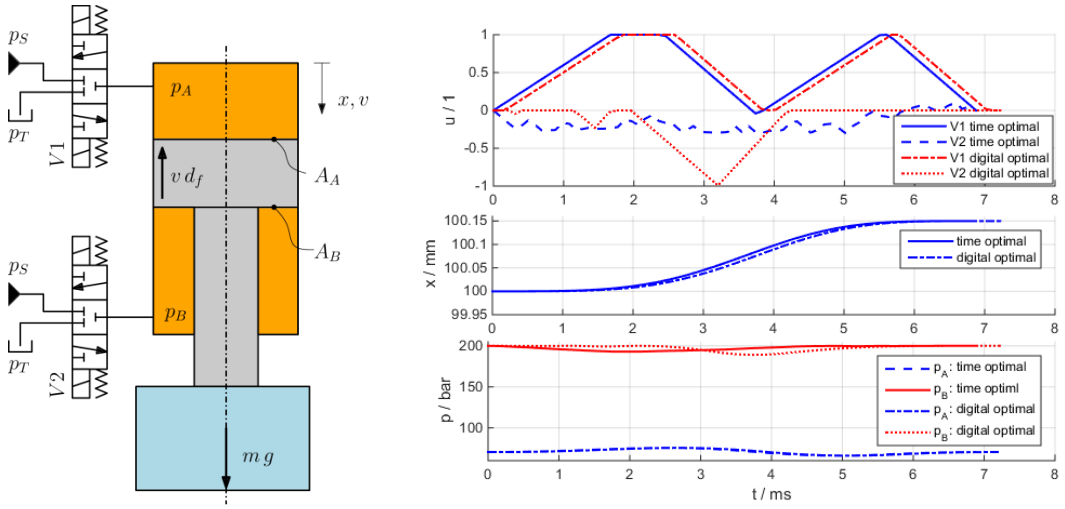

Figure 13. A sketch of the system and the optimisation results for a double sided-actuation; realised using a 3-3 way valve at the piston and at the annular chamber.

The time optimal result shows a digitally unrealizable command signal for the valve V2. Making use of the previously described trick turns the valve command signal into an applicable one.

3.5. Digital full-bridge control of a differential cylinder

This test-case shows optimisation results using two digital 2-2-way valves at the piston and at the annular cylinder chamber. The difference between this and the previous case is that here it is possible that the feed-forward contains hydraulic shortcuts at each cylinder side. Using such a system, one has again the feasibility of pretending the final pressure in the cylinder chambers.

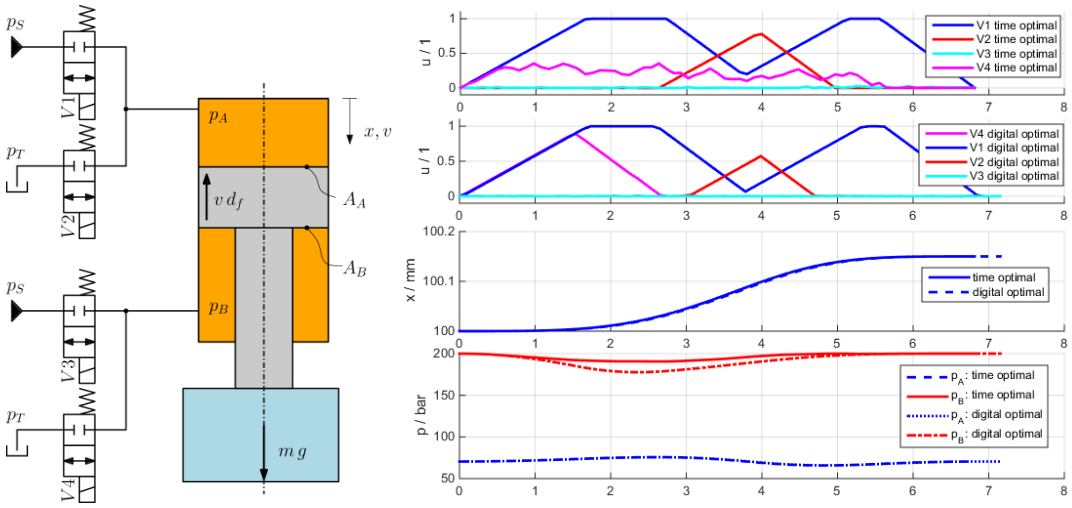

Figure 14. Double sided actuation realised using four independently commanded 2-2 way valves (left). Right: Optimisation results for a time and digital-optimal criterion.

Figure (14) shows the sketch of the drive system and a plot of the optimisation results. Again time optimality alone does not lead to digital control at all. But switching the criterion to the digital one leads to an applicable feed-forward valve control.

4. CONCLUSIONS

A short description of the state-space averaging method and it's applicability to digital hydraulic drives builds the motivation for using a control approach based on optimisation. Testing the averaging method on a typical digital hydraulic drive pointed out that it is hardly applicable. The reason is that the system eigenfrequencies are too close to the PWM-frequency of the valves. Faster valves would be a solution, but they are not available nowadays.

The theoretical part of the paper is intended to give a brief survey on optimal feed-forward control methods. The used approach of requiring time optimality leads often to bang-bang type control signals which can be realized using switching valves. Furthermore different discretisation methods are discussed, advantages and disadvantages are stated and optimisation results are depicted. One of the discussed discretisation methods is applicable on differentially flat systems and the other one is also applicable to non-flat systems.

Selected examples of dynamical systems were studied in order to show potential pitfalls and possible solutions. The influence of bounded system states and a bounded valve command speed was discussed. A good working approach was presented in order to turn non digital optimisation results into applicable ones. This approach was tested on several examples in this paper.

Finally a discussion of various cylinder drives showed a broad applicability of optimisation methods in the field of digital hydraulics.

5. AKNOWLEDGEMENT

This work has been supported by the Austrian COMET-K2 programme of the Linz Center of Mechatronics (LCM), and was funded by the Austrian federal government and the federal state of Upper Austria.

6. TABLE OF SYSTEM PARAMETERS

Table 2. System parameters

Description	Variable	Value	Unit
Cylinder			
Moved mass	m	1500	kg
Piston diameter	d_P	350	mm
Rod diameter	d_R	280	mm
Friction factor	d_f	200000	$\frac{kg}{s}$
Max. cylinder stroke	x_{max}	150	mm
Fluid			
Bulk modulus	E	14000	bar
Kinematic viscosity	ν	46	cSt
Density	ρ	860	$\frac{kg}{m^3}$
Valve 1			
Nominal flow rate	Q_n	45	$\frac{L}{min}$
Nominal pressure drop	p_n	5	bar
Valve 2			
Nominal flow rate	Q_n	10	$\frac{L}{min}$
Nominal pressure drop	p_n	5	bar
Pipe 1			
Inner diameter	d_1	18.9	mm
Length	l_1	3.4	m
Pipe 2			
Inner diameter	d_2	24	mm
Length	l_2	250	mm
Pipe 3			
Inner diameter	d_3	18.9	mm
Length	l_3	3.4	m
Accumulator			
Prefill pressure	$p_{Ac,0}$	170	bar
Initial volume	$V_{Ac,0}$	0.75	L
Ploytropic exponent	n_{poly}	1.4	1
Hydraulic supply			
Supply pressure	p_S	200	bar
Tank pressure	p_T	20	bar

REFERENCES

[1] Lukachev E., Haas R., Scheidl R., A Hydraulic Switching Control Concept Exploiting a Hydraulic Low Pass Filter. In L. J. De Vin and J. Solis (Eds.): Proceedings of the 14th Mechatronics Forum International Conference, Mechatronics 2014, Karlstad, Sweden, pp. 151-157, 2014.

[2] Haas R., Lukachev E., Scheidl R., An RC Filter for Hydraulic Switching Control with a Transmission Line Between Valves and Actuator. , International Journal of Fluid Power, Vol. 15, N. 3, pp. 139-151.

[3] Gradl C., Scheidl R., A basic study on the response dynamics of pulse-frequency controlled digital hydraulics drives. In: Proceedings of Bath/ASME Symposium on Fluid Power & Motion Control; FPMC2013; October 6-9, 2013, Sarasota, Florida, USA

[4] Flor M., Scheller S., Heidenfelder R.; „Digital hydraulics at Bosch Rexroth – A trend evolves to real applications“; Proceedings of the Fifth Workshop on Digital Fluid Power, October 24-25, 2012, Tampere, Finland; ISBN 978-952-15-2941-2, URL: http://URN.fi/URN:ISBN:978-952-15-3271-9

[5] Schepers I., Weber J.; „Comparison and evaluation of digital control methods for on/off valves“; Proceedings of the Fifth Workshop on Digital Fluid Power, October 24-25, 2012, Tampere, Finland; ISBN 978-952-15-2941-2, URL: http://URN.fi/URN:ISBN:978-952-15-3271-9

[6] Haas R., Lukachev E.; “Optimal Hydraulic Control of a Digital Hydraulic Drive”. In the Seventh Workshop on Digital Fluid Power, February 26-27, 2015, Linz, Austria, pp. 129-142, ISBN: 978-3-200-04014-4, Editors: Scheidl R., Winkler B., Kogler H.

[7] hydroLib3 Toolbox; Institute of machine design and hydraulic drives; URL: http://www.jku.at/imh/content/e139944; version hydroLib V 3.1.1 beta2.

[8] Haas R., Lukachev E.; “Optimal feedforward control of a digital hydraulic drive”; Journal of Systems and Control Engineering; Comment: Paper is reviewed and in production but not published until now!

[9] Kugi A. ”Non-linear Control Based on Physical Models”; Springer-Verlag London Berlin Heidelberg, 2001

[10] Graichen K.; ” METHODEN DER OPTIMIERUNG UND OPTIMALEN STEUERUNG”; WS 2014/2015; Institut für Mess-, Regel- und Mikrotechnik, Fakultät für Ingenieurwissenschaften und Informatik Universität Ulm

[11] Macki J., Strauss A., Introduction to optimal Control Theory; Springer Verlag New York, 1982.

[12] Griesse R. ; „Skript zur Vorlesung Kontrolltheorie“; WS2005/06 Johannes Kepler Universität Linz

[13] Hairer E., Norset S. P., Wanner G., Solving Ordinary differential Equations I: Nonstiff Problems”; 2nd revised edition; Springer Verlag, Berlin New York, 2009.

[14] Fliess, M., Lévine, J., Martin, P.,Rouchon, P. Flatness and defect of nonlinear systems: introductory theory and examples. International Journal of Control, 61, 1327–1361. 1995.

[15] De Boor, C. ”A practical guide to splines”. New York, NY [u.a.]: Springer; 2001; ISBN 978-0-387-95366-3.

[16] Matlab incl. optimization toolbox, URL: http://de.mathworks.com/products/optimization/features.html?s_tid=srchtitle

[17] Programming language python (URL: https://www.python.org/)incl. scipy (URL: https://docs.scipy.org/doc/scipy-0.14.0/reference/generated/scipy.optimize.fmin_slsqp.html)

ON THE NUMERICAL SOLUTION OF STEADY-STATE EQUATIONS OF DIGITAL HYDRAULIC VALVE-ACTUATOR SYSTEM

Adj. Prof. Matti Linjama
Department of Intelligent Hydraulics and Automation
Tampere University of Technology
P.O.BOX 589, FI-33101 Tampere
matti.linjama@tut.fi

ABSTRACT

Digital valve system uses plurality of simple on/off valves instead of proportional or servo valves in the implementation of high performance and energy efficient valve controlled hydraulic actuators. Typical digital valve system consists of 20 valves each having two states, which yields the over one million possible control combinations. A potential way to control this kind of system is the model based control utilizing the steady-state model of the system. The solution of the steady-state system equations must be made numerically because no analytical solution exists. This paper analyses the steady-state system equations, develops the condition for existence and uniqueness of the solution, and studies different iteration algorithms. The new results of the paper are: 1) system equations can be transformed into scalar form, 2) the solution exist and is unique if a simple necessary and sufficient condition holds, and 3) Ridders' method is fast and robust method for this problem.

KEYWORDS: Digital hydraulics, Ridders' method

1. INTRODUCTION

Digital valve system is a method to control hydraulic actuators with plurality of simple on/off valves [6]. Figure 1a shows a traditional four-way valve and Fig. 1b corresponding digital valve system with cylinder actuator. Mechanically coupled control edges of traditional spool valves are replaced with independent digital flow control units (DFCU). Each DFCU consists of several parallel connected on/off valves, which gives discrete controllability. Flow capacities of on/off valves are normally set according to powers of two (1:2:4:8:…), which is analogous to DA converter and gives

2^N equally spaced flow areas. Discrete controllability curves for different number of parallel connected valves are depicted in Figure 2. Five valves give good enough controllability for most applications and thus the total number of valves is typically 20.

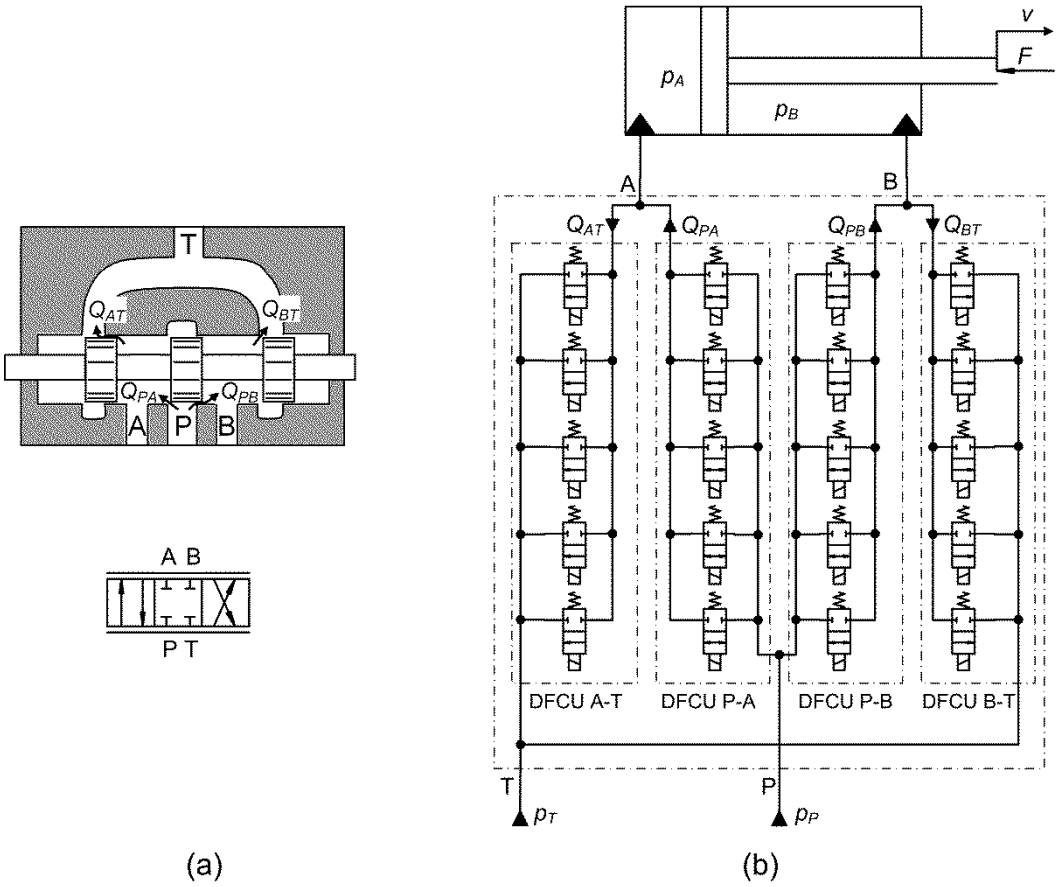

Figure 1. Traditional four-way spool valve (a) and corresponding digital valve system (b).

The control of digital valve systems differs from the control of traditional valves. The state of any valve system can be defined uniquely as flow areas of the individual control edges. Flow areas are determined by the spool position in traditional valves. The mechanical design of the spool determines both the control mode (i.e. which control edges are open) and flow areas of the control edges. The control of traditional valves is simple because the control signal and spool position are closely related. The drawback is that only predefined control modes are possible and that pressure level cannot be adjusted because of the fixed ratio between flow areas. Flow areas of the control edges are completely independent in the digital valve system and the valve system can implement different control modes together with simultaneous velocity and pressure control [5]. Controllability at low velocities can be improved significantly if non-conventional control modes having three or four control edges simultaneously open are utilized [7]. These features are not unique for digital valve system but can be achieved also with four independent analogous valves [9]. The side effect of flexibility is that control design is more complicated.

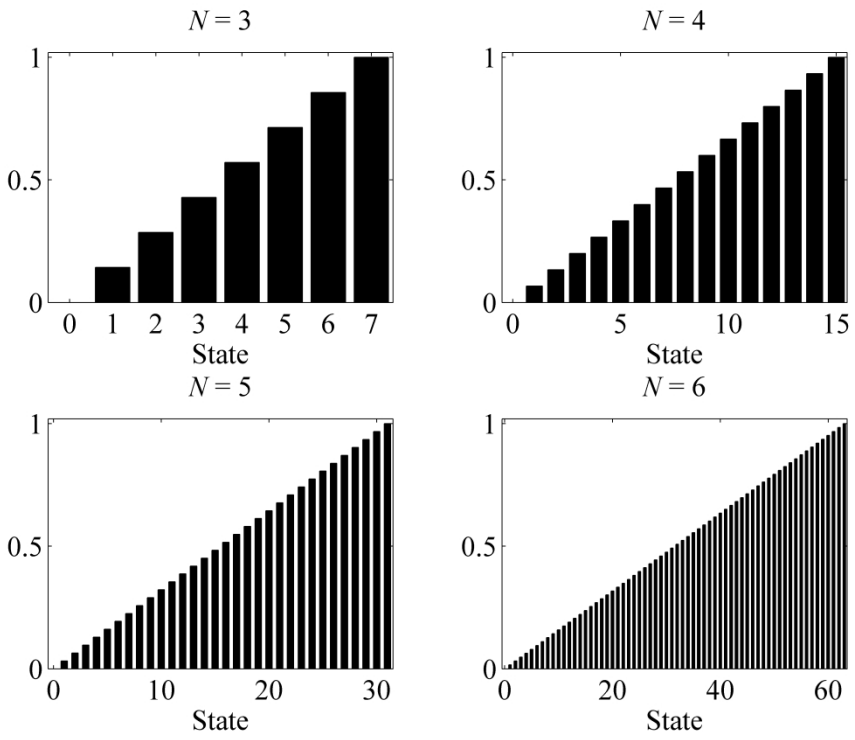

Figure 2. Theoretical controllability of binary coded DFCU with different number of parallel-connected valves.

The control problem of the digital valve system is: "Select the best possible control combination of the valves at each sampling instant". Two basic problems are how to define goodness of a control combination and how to find the best one. The system typically consists of 20 on/off valves each having two states, and the size of search space is 2^{20}. The model based control principle has been used successfully and the general flow chart is shown in Figure 3. The search space reduction is essential step in order to achieve the real time implementation. This step includes the utilization of the control mode information and e.g. flow balance analysis. The next step is to solve the steady-state system equations for the each element of the reduced search space. Finally, the best control combination is selected by minimizing a penalty function. Typical penalty terms are errors between target and calculated steady state velocity and pressures, the magnitude of power losses and the activity of valves. The solution of the steady-state system equations is computationally the most intensive task because numerical iteration must be used. Earlier research has used Newton-Raphson iterations with some heuristics to improve robustness. Problems are that relatively big number of iterations is needed and that solution is not always found. [3, 5, 7]

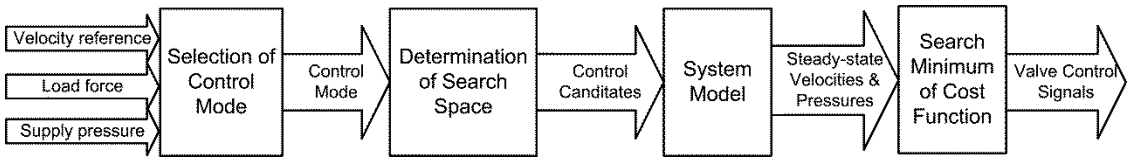

Figure 3. Simplified flow chart of the model based controller.

This paper studies the steady-state system equations in more detail, develops condition for the existence and uniqueness of the solution, and studies different iteration algorithms. The problem is unique and is not studied earlier expect slightly in [3, 5, 7]. The new results of the paper are: 1) the system equations can be transformed into the scalar form, 2) the solution exist and is unique if a simple necessary and sufficient condition holds, and 3) Ridders' method is faster and more robust than Newton's method for this problem.

2. STEADY-STATE SYSTEM EQUATIONS

The steady-state system equations of the hydraulic circuit of Fig. 1b are

$$\sum_{i=1}^{N} \left[Q_{PAi}(u_{PAi}, p_P, p_A) - Q_{ATi}(u_{ATi}, p_A, p_T) \right] - A_A v = 0 \tag{1a}$$

$$\sum_{i=1}^{N} \left[Q_{PBi}(u_{PBi}, p_P, p_B) - Q_{BTi}(u_{BTi}, p_B, p_T) \right] + A_B v = 0 \tag{1b}$$

$$A_A p_A - A_B p_B - (A_A - A_B) p_{at} - F = 0 \tag{1c}$$

where subscripts *PA*, *AT*, *PB* and *BT* refers to DFCUs P-A, A-T, P-B and B-T, see Fig. 1. Equations 1a and 1b are the flow balance equations and assume incompressible flow while Eq.1c is the force balance equation. If the control signals of the valves, supply and return pressures, and load force are known, Eq. 1 can be solved for piston velocity v and chamber pressures p_A and p_B. There is no analytical way to model turbulent flow of valves but it depends on pressures, state of valve (open or closed), valve geometry and fluid characteristics. For simplicity, constant fluid characteristics are assumed. It is generally accepted that the flow rate is closely proportional to the square root of the pressure differential at very high Reynolds numbers and proportional to the pressure differential at very low Reynolds numbers [8]. Relatively good agreement is achieved in most cases, if flow rate is assumed to be proportional to Δp^x where the exponent x is tuned according to the measured flow curve [4]. In addition, cavitation choking effect with low back pressure must be considered [2]. Therefore, the following flow model is used

$$Q(u,p_1,p_2)=\begin{cases} uK_v(p_1-p_2)^x, & bp_1<p_2\le p_1 \\ uK_v\left((1-b)p_1\right)^x, & p_2\le bp_1 \\ -uK_v(p_2-p_1)^x, & bp_2<p_1<p_2 \\ -uK_v\left((1-b)p_2\right)^x, & p_1\le bp_2 \end{cases} \quad (2)$$

The names “upstream” and “downstream” side are used to denote higher and lower pressure, respectively. Cavitation choking is modelled by limiting the smallest downstream side pressure to *b* times upstream side pressure where *b* is critical pressure ratio. The effect is that flow rate saturates even if downstream side pressure is further decreased. The shape of Eq. 2 is depicted in Figure 4. The parameters of the flow model may be slightly different for the different flow directions but the same parameters are assumed without any loss of generality.

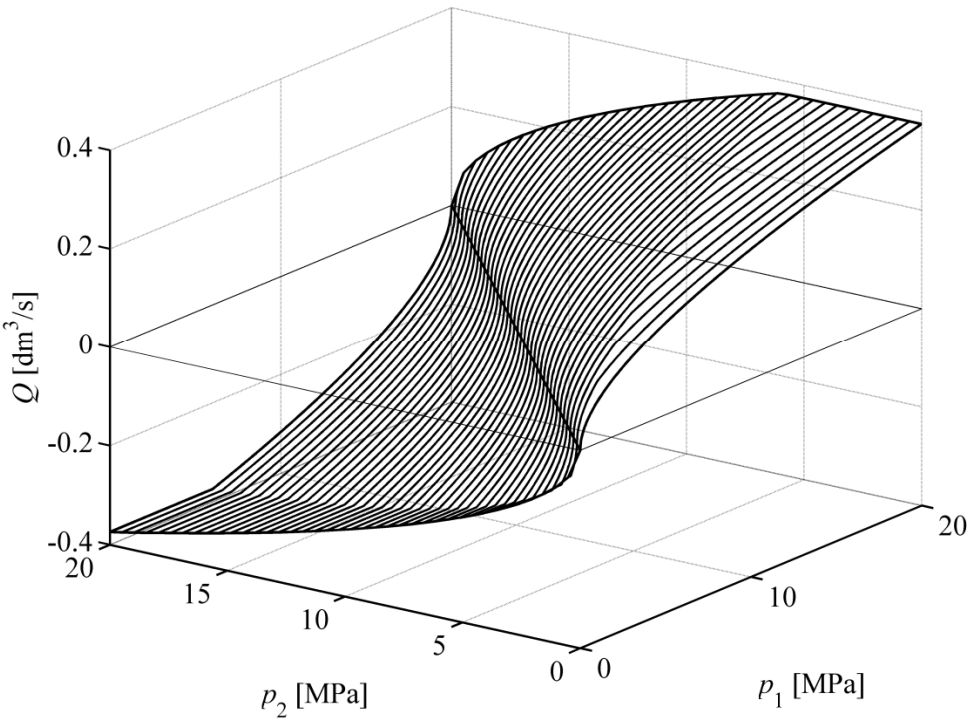

Figure 4. The value of the flow function of Eq. 2 with following parameters: Kv = 10-7 ($m^3s^{-1}Pa^{-x}$), x = 0.5, b = 0.3, u = 1.

The model of eq. 2 is not realistic at small pressure differentials i.e. small Reynolds numbers. The reason is that flow becomes laminar and proportional to the pressure differential. The flow rate at small pressure differential could be modelled as suggested by Ellman and Piché [1], but this would complicate the equations significantly. Figure 5 presents some comparisons between the valve model and measured flow curves.

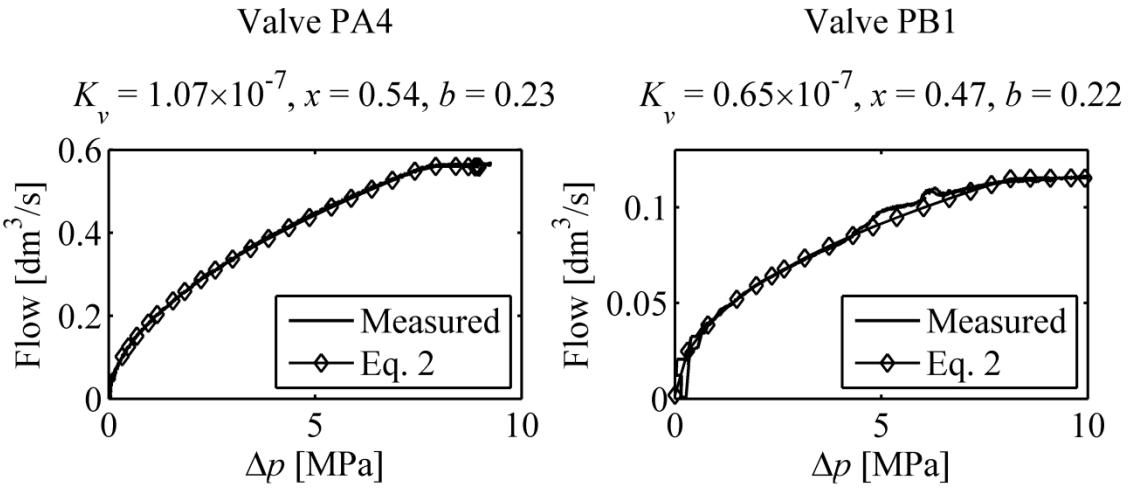

Figure 5. Two examples about the agreement between measured flow rate and the flow rate given by Equation 2.

The valid values for inputs and parameters are

$$
\begin{aligned}
&u \in \{0,1\} \\
&K_v, A_B > 0 \\
&A_A > A_B \\
&x \in (0,1] \\
&b \in [0,1) \\
&p_A, p_B, p_P, p_T \geq 0 \\
&p_P \geq p_T
\end{aligned}
\tag{3}
$$

The maximum value of the exponent x is limited to 1 corresponding to ideal laminar flow. Value 0.5 gives standard turbulent orifice model. The last assumption can be made because of the symmetry of the valve system.

3. NUMERICAL SOLUTION OF STEADY-STATE SYSTEM EQUATIONS

3.1. Scalar Form of Steady-State System Equations

Equation 1 can be transformed into scalar form by solving p_B from Eq. 1c, substituting it into Eq. 1b, solving velocity from Eq. 1a and 1b, and equating velocities. This gives:

$$
\begin{aligned}
&\left(\sum_{i=1}^{N} \left[Q_{PAi}(u_{PAi}, p_P, p_A) - Q_{ATi}(u_{ATi}, p_A, p_T) \right] \right) / A_A + \\
&\left(\sum_{i=1}^{N} \left[Q_{PBi}\left(u_{PBi}, p_P, \frac{p_A A_A - F^*}{A_B}\right) - Q_{BTi}\left(u_{BTi}, \frac{p_A A_A - F^*}{A_B}, p_T\right) \right] \right) / A_B = 0
\end{aligned}
\tag{4}
$$

where F^* is

$$F^* = F + \left(A_A - A_B \right) p_{at} \tag{5}$$

In order to simplify derivations, the left hand side of Eq. 4 is denoted by $f(p_A)$. Benefits of the scalar form are that broader set of methods are available and that there is no need for matrix calculations.

3.2. Control Modes Studied

Active DFCU means DFCU having at least one valve open. It is assumed that both A- and B-side has at least one active DFCU. This includes inflow-outflow and differential control modes as well as control modes having three or four active DFCUs. The excluded control modes are not normally used because they cause no piston movement. For each control mode, the steady-state piston velocity can be positive or negative depending on load force and supply and tank pressures. The pressure conditions for each case can be derived from the fact that flow is always from high to low pressure and that flow balance equations 1a and 1b must hold. Figure 6 presents the control modes having two active DFCUs and Figure 7 the control modes having three or four active DFCUs. Flow directions and pressure conditions are also shown for the both directions of movement.

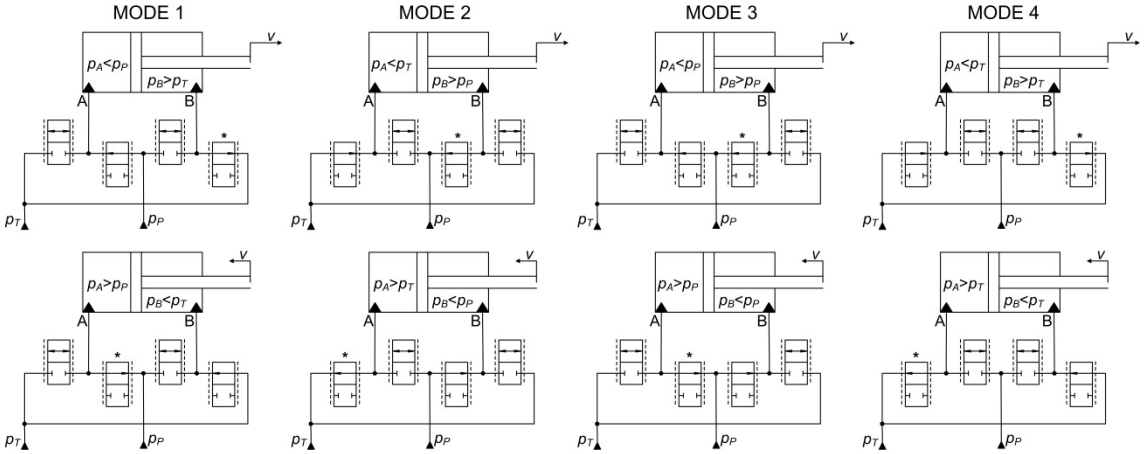

Figure 6. Control modes having two active DFCUs. Flow directions are shown in valve arrows. The star denotes a DFCU with p_A or p_B in the upstream side.

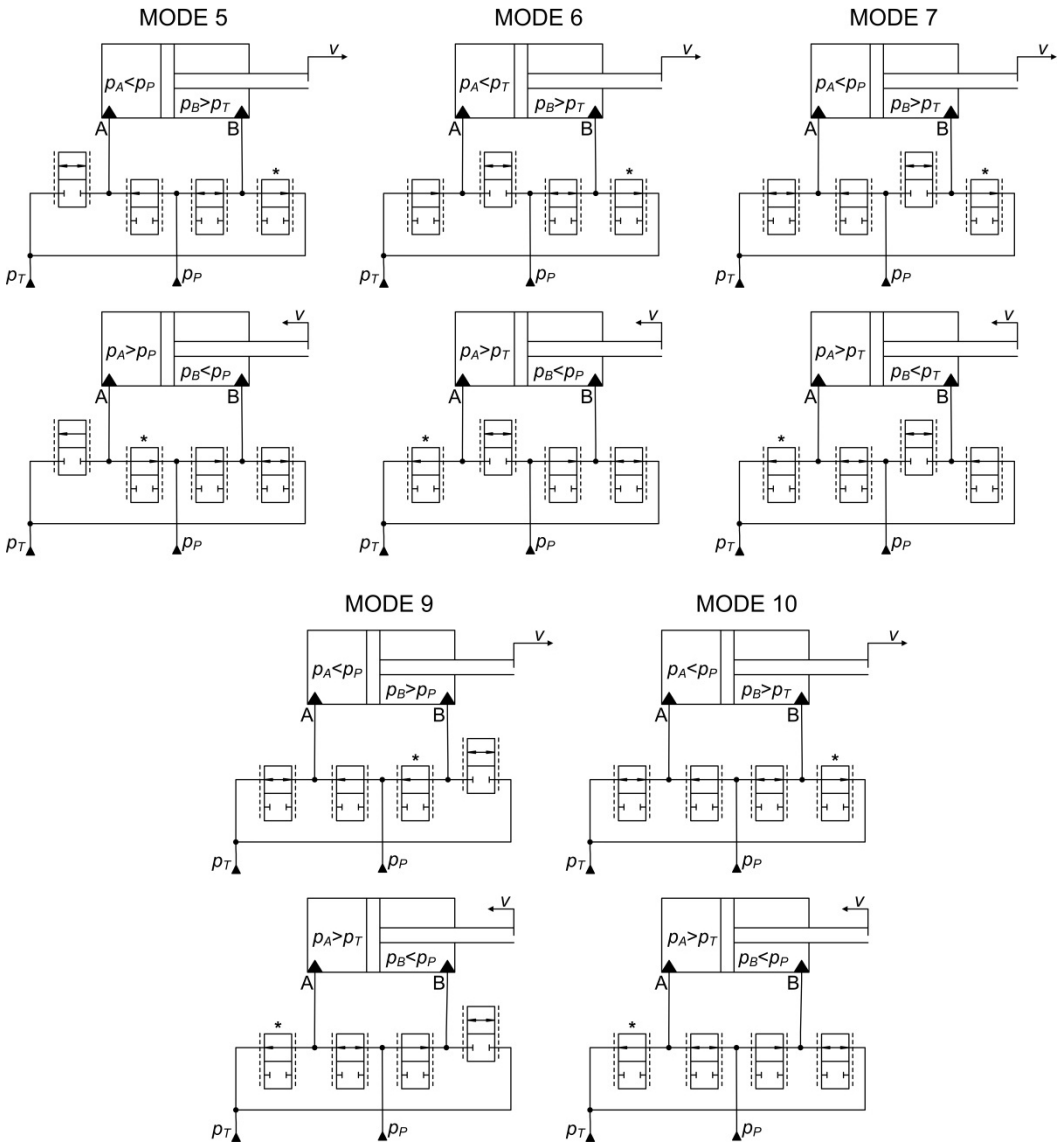

Figure 7. Control modes having three or four active DFCUs. Flow directions are shown in valve arrows and double arrow means that flow direction is not known. The star denotes a DFCU with p_A or p_B in the upstream side.

3.3. Existence of Solution

Sufficient conditions for the existence of the solution is that f is continuous and that $\text{sign}(f(p_{A1})) \neq \text{sign}(f(p_{A2}))$ for some valid p_{A1} and p_{A2}. Clearly, f is continuous because the flow function of Eq. 2 is continuous. Partial derivatives of the flow function are

$$\frac{\partial Q(1,p_1,p_2)}{\partial p_1}=\begin{cases}\dfrac{xK_v(p_1-p_2)^x}{p_1-p_2}, & bp_1<p_2\le p_1\\ \dfrac{xK_v\left((1-b)p_1\right)^x}{p_1}, & p_2\le bp_1\\ \dfrac{xK_v(p_2-p_1)^x}{p_2-p_1}, & bp_2<p_1<p_2\\ 0, & p_1\le bp_2\end{cases} \tag{6a}$$

$$\frac{\partial Q(1,p_1,p_2)}{\partial p_2}=\begin{cases}-\dfrac{xK_v(p_1-p_2)^x}{p_1-p_2}, & bp_1<p_2\le p_1\\ 0, & p_2\le bp_1\\ -\dfrac{xK_v(p_2-p_1)^x}{p_2-p_1}, & bp_2<p_1<p_2\\ -\dfrac{xK_v\left((1-b)p_2\right)^x}{p_2}, & p_1\le bp_2\end{cases} \tag{6b}$$

All derivatives are zero if the valve is closed. The sign of partial derivatives is needed in further analysis. It is seen that $\partial Q/\partial p_1$ zero only at one situation: if p_1 is smaller than bp_2 i.e. p_1 is at downstream side and cavitation choking occurs. In all other situations, $\partial Q/\partial p_1$ is strictly positive. Similarly, and $\partial Q/\partial p_2$ is zero only if p_2 is at downstream side and cavitation choking occurs. Otherwise $\partial Q/\partial p_2$ is strictly negative. Derivatives are well defined except at $p_{in} = 0$, $p_{out} = 0$, $p_{in} = p_{out}$ where they are unbounded if $x<1$.

Lemma. Equation 4 has solution for all control modes of Figs. 6 and 7, and for all valid parameter and input values of Eq. 3 if and only if

$$f\left(\max\left(0,F^*/A_A\right)\right)\hat{=}f\left(p_{A,\min}\right)\ge 0 \tag{7}$$

Proof. It follows from Eq. 1c that $p_B<0$ if $F^*<p_AA_A$. Therefore, $\max(0, F^*/A_A)$ is the smallest valid value for p_A and is denoted by $p_{A,min}$. The case $f(p_{A,min})=0$ is trivial and one solution is $p_A= p_{A,min}$. If $f(p_{A,min})>0$, Eq. 4 has solution if $f(p_A)<0$ for some $p_A> p_{A,min}$. When p_A is large enough, both p_A and p_B are bigger than p_P and p_T, and flow directions are A® P, A® T, B® P and B® T. It follows from Eq. 2 that

$$
\begin{aligned}
&\lim_{p_A \to \infty} \sum_{i=1}^{N} Q_{PAi}\left(u_{PAi}, p_P, p_A\right) = -\infty \text{ , if DFCU}_{\text{PA}} \text{ is active} \\
&\lim_{p_A \to \infty} \sum_{i=1}^{N} Q_{ATi}\left(u_{ATi}, p_A, p_T\right) = \infty \text{ , if DFCU}_{\text{AT}} \text{ is active} \\
&\lim_{p_A \to \infty} \sum_{i=1}^{N} Q_{PBi}\left(u_{PBi}, p_P, \frac{p_A A_A - F^*}{A_B}\right) = -\infty \text{ , if DFCU}_{\text{PB}} \text{ is active} \\
&\lim_{p_A \to \infty} \sum_{i=1}^{N} Q_{BTi}\left(u_{BTi}, \frac{p_A A_A - F^*}{A_B}, p_T\right) = \infty \text{ , if DFCU}_{\text{BT}} \text{ is active}
\end{aligned}
\tag{8}
$$

Substituting Eq. 8 into Eq. 4. results in

$$
\lim_{p_A \to \infty} f\left(p_A\right) = -\infty \tag{9}
$$

for all control modes of Figs. 6 and 7, which guarantees that solution exists. The slope of f is

$$
\frac{\partial f}{\partial p_A} = \frac{1}{A_A}\left(\frac{\partial Q_{PA}}{\partial p_A} - \frac{\partial Q_{AT}}{\partial p_A}\right) + \frac{1}{A_B}\left(\frac{\partial Q_{PB}}{\partial p_B}\frac{\partial p_B}{\partial p_A} - \frac{\partial Q_{BT}}{\partial p_B}\frac{\partial p_B}{\partial p_A}\right) \tag{10}
$$

Now $\partial p_B/\partial p_A = A_A/A_B > 0$ and from Eq. 6 it follows that the signs of the other derivatives are

$$
\begin{aligned}
&\frac{\partial Q_{PA}}{\partial p_A} \le 0 \text{ , if DFCU}_{\text{PA}} \text{ is active and } p_A \ge 0 \\
&\frac{\partial Q_{AT}}{\partial p_A} \ge 0 \text{ , if DFCU}_{\text{AT}} \text{ is active and } p_A \ge 0 \\
&\frac{\partial Q_{PB}}{\partial p_B} \le 0 \text{ , if DFCU}_{\text{PB}} \text{ is active and } p_B \ge 0 \\
&\frac{\partial Q_{BT}}{\partial p_B} \ge 0 \text{ , if DFCU}_{\text{BT}} \text{ is active and } p_B \ge 0
\end{aligned}
\tag{11}
$$

Thus, $\partial f/\partial p_A \le 0$ " $p_A \ge p_{A,min}$ and Eq. 7 is necessary condition for the existence of the solution.

3.4. Uniqueness of Solution

The solution is unique if $\partial f/\partial p_A$ is strictly negative in the neighborhood of $f = 0$. Figures 6 and 7 show all possible solution forms with non-zero velocity. At least one DFCU is in all cases such that p_A or $p_B=(p_A A_A - F^*)/A_B$ is at upstream side. These DFCUs are denoted by star (*) in Figs. 6 and 7. The partial derivative of flow function (Eq. 6) is non-zero for these DFCUs and it follows from Eqs. 10 and 11 that $\partial f(p_A)/\partial p_A$ is strictly negative in the neighbourhood of $f = 0$. In the case of zero velocity, the pressure differential over one or several DFCUs is zero and corresponding partial derivatives are

unlimited, which implies that solution is unique but convergence of numerical methods may be poor.

4. SOLVING STEADY STATE SYSTEM EQUATIONS

4.1. Solution Strategies

There exist several good methods for solving scalar non-linear equation, such as Eq. 4. All methods require at least one calculation of the function value at each step. The major decision is if analytical derivatives are utilized or not. Numerically the most intensive task of Eq. 4 is the calculation of power functions of the flow model. Equation 6 shows that calculation of first derivatives requires only one multiplication and one division, because power functions required are already calculated during the calculation of the function value. The same applies to higher order derivatives also. This motivates the use methods requiring analytical derivatives. On the other hand, the derivatives are unbounded at zero pressure differential, which is a counter argument for using them. Thus, two algorithms are studied. The first one is classical Newton's method:

$$x_{n+1} = x_n - \frac{f(x_n)}{f'(x_n)} \tag{12}$$

The second one is Ridders' method [10]. The algorithm starts by evaluating function at two points x_1 and x_2 such that sign($f(x_1)$) ¹ sign($f(x_2)$), and at the midpoint x_3. The new point x_4 between x_1 and x_2 is then determined by formula:

$$x_4 = x_3 + (x_3 - x_1)\frac{\text{sign}(f(x_1) - f(x_2))\, f(x_3)}{\sqrt{f(x_3)^2 - f(x_1) f(x_2)}} \tag{13}$$

The new bracketing values are then determined by using following rules:

```
if sign(f(x1)) == sign(f(x4))
   x1 = x4
   if sign(f(x2)) == sign(f(x3))
      x2 = x3
   end
else
   x2 = x4
   if sign(f(x1)) == sign(f(x3))
      x1 = x3
   end
end
```

Good property of the method is that the bracketing interval at least halves at each iteration and convergence is thus guaranteed. Drawback of the method is that the value of f must be calculated twice per iteration.

4.2. Test System and Testing Procedure

The test system of [3] is used in the evaluation of the performance of the iteration algorithms of Eqs. 12 and 13. The parameters of the valve model are given in Table 1 and Fig. 5 shows some verification results of the valve model and its parameters. The biggest valve is removed in order to reduce the number of control combinations, and each DFCU has four valves and 16 states. The piston areas are A_A = 6234.5 mm^2 and A_B = 4198.7 mm^2.

Table 1. Parameter values of valve models.

	$K_v' \, 10^7$				x				b			
P-A	0.65	0.345	0.78	1.05	0.47	0.55	0.52	0.54	0.22	0.34	0.30	0.23
A-T	0.61	0.835	1.345	0.895	0.48	0.485	0.485	0.555	0.1	0.1	0.1	0.1
P-B	0.48	0.30	1.06	1.07	0.49	0.56	0.50	0.54	0.20	0.36	0.30	0.23
B-T	0.515	0.945	1.40	1.72	0.485	0.48	0.485	0.515	0.1	0.1	0.1	0.13

The control modes of Fig. 6 are studied first. Each control mode has 15´ 15 = 225 different control combinations because two DFCUs are active. The pump and tank pressures are selected to be p_P = 20 MPa and p_T = 2 MPa. The suitable range of the load force can be estimated from the control modes 1 and 2. The zero velocity is achieved in Mode 1, if F^* = 124.1 kN and in Mode 2, if F^* = –83.6 kN. Both directions of movement are included for all control modes, if the force range is selected to exceed these limits. The determination of test situations is difficult because the existence of the solution depends on load force, control mode, and relative opening of DFCUs. Initial value has also a strong effect on the convergence of the solution in the Newton's method. A pragmatic approach is adopted here and "sufficiently large" set of situations are tested. The range of parameter values is selected wide and the cases for which the solution does not exist are simply rejected. The test situations are generated as a follows:

- All 15´ 15 control combinations are considered for each control mode
- Load force is varied between -140 and 180 kN with 10 kN increments
- In Newton's method, initial pressure for pA is mean of supply and tank pressures, i.e. 11 MPa. If the value is smaller than pA,min + 2 MPa, the value pA,min + 2 MPa is used as initial pressure.
- In Ridders' method, the initial bracketing interval is [pA,min, 60 MPa].

The mean of supply and tank pressures is reasonable guess for initial value if no a priori information is utilized. In addition, the initial experiments showed that the convergence is poor, if the initial condition is too close to $p_{A,min}$. The assumptions above give 7425

combinations. The solution does not exist for all combinations and these combinations are excluded. The following rules are used during iterations:

- The value of p_A is limited to be at least $p_{A,min}$
- The solution is considered as converged if the value of f is less than 10^{-6} m/s
- The maximum number of iterations is limited to 15. If the error is above 10^{-6} m/s after the fifteenth iteration, the solution is considered as non-converged.

Figure 8 shows the convergence results. The percentage of converged solutions is shown for each number of iterations and the sixteenth bar shows the percentage of non-converged solutions. The number of converged solutions and the number of cases for which the solution exists are shown in the titles. Clearly, the Ridders' method is more robust method for this problem.

The second test utilizes random values as follows:

- Control signal vector of each DFCU is either [0 0 0 0], [1 0 0 0], [1 1 0 0], [1 1 1 0] or [1 1 1 1] each having probability of 0.2
- Load force is uniformly distributed random number between -140 and 180 kN
- Pressure p_P is uniformly distributed random number between 10 and 20 MPa
- Pressure p_T is uniformly distributed random number between 0 and 10 MPa

The random tests include all the control modes if sufficiently big number tests are made. Figure 9 shows the results for 100000 random tests.

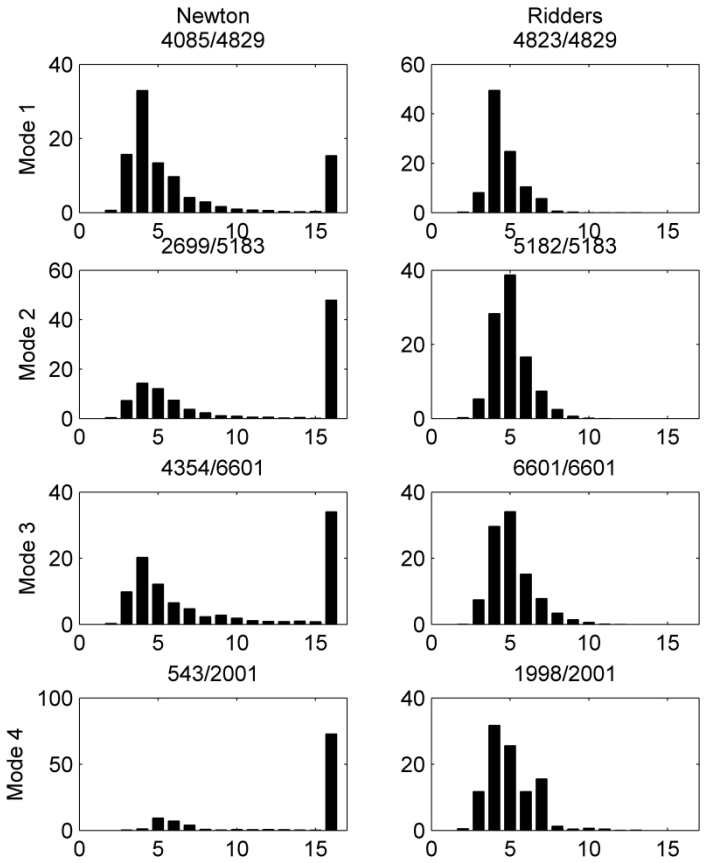

Figure 8. The convergence of the solution with different iteration methods and control modes of Fig. 6.

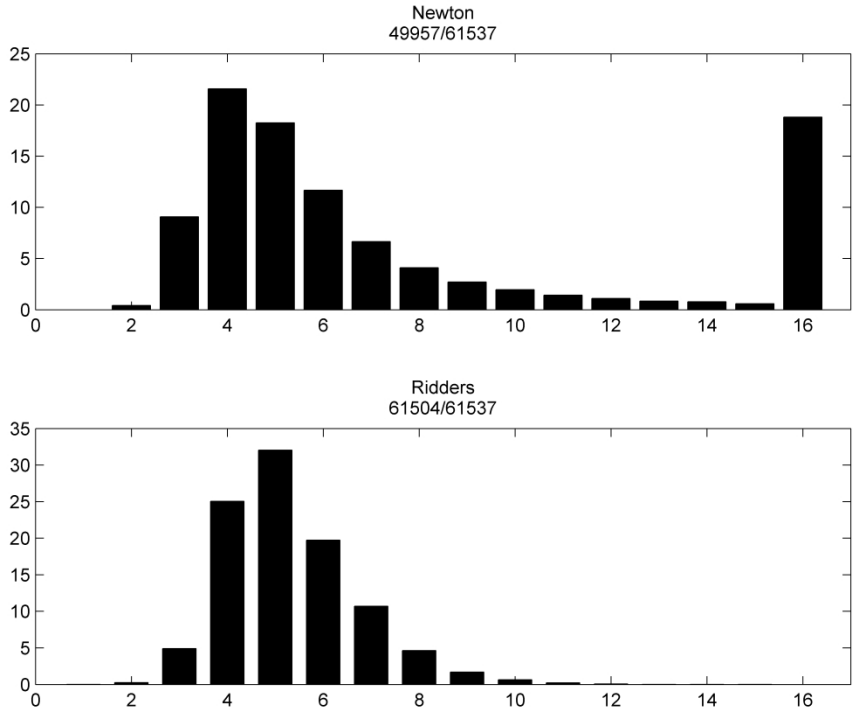

Figure 9. The convergence results of 100000 random tests including all control modes of Figs. 6 and 7.

5. CONCLUSIONS

The steady-state solution of the digital hydraulic valve system with four independent control edges has been studied. The main results are: 1) the system equations can be transformed into scalar form, 2) the solution exist and is unique if a simple necessary and sufficient condition holds, and 3) the Ridders' method is more robust solver for this for this problem than Newton's method. The results can be utilized in the development of more efficient and reliable steady-state solvers for the model based controller of digital hydraulic systems.

REFERENCES

[1] Ellman, A. and Piché, R. 1996. A Modified Orifice Flow Formula for Numerical Simulation of Fluid Power Systems. Fluid Power Systems and Technology, Collected papers of 1996 ASME IMECE, November 17–22, Atlanta, pp. 59–63.

[2] Koivula, T. 2002. Cavitation in Hydraulic Valves – Aspects on the Effect of Oil Type, Erosion and Detection Methods. Dissertation, Tampere University of Technology.

[3] Linjama, M., Huova, M., Bostöm, P., Laamanen, A., Siivonen, L., Morel, L., Walden, M. and Vilenius, M. 2007. Design and Implementation of Energy Saving Digital Hydraulic Control System, The Tenth Scandinavian International Conference on Fluid Power, May 21–23, Tampere, Finland, pp. 341-359 (Vol. 2).

[4] Linjama, M., Huova, M. & Karvonen, M. 2012. Modelling of Flow Characteristics of On/Off Valves. Proceedings of the Fifth Workshop on Digital Fluid Power, October 24–25, Tampere, Finland, pp. 209–222.

[5] Linjama, M., Huova, M. and Vilenius, M. 2008. Online minimization of power losses in distributed digital hydraulic valve system. Proceedings of the 6th International Fluid Power Conference, April 1–2, Dresden, Germany, pp. 157–171 (Vol. 1).

[6] Linjama, M., Laamanen, A. and Vilenius, M. 2003. Is it time for digital hydraulics? The Eight Scandinavian International Conference on Fluid Power, May 7–9, Tampere, Finland, pp. 347–366.

[7] Linjama, M. and Vilenius, M. 2005. Improved digital hydraulic tracking control of water hydraulic cylinder drive, International Journal of Fluid Power, 6 (1), pp. 29–39.

[8] Merritt, H. E. 1967. Hydraulic Control Systems. John Wiley & Sons, New York.

[9] Pfaff, J. 2005. Distributed Electro-Hydraulic Systems for Telehandlers, The 50th National Conference on Fluid Power, March 16–18, Las Vegas, pp. 779–784.

[10] Ridders. C. 1979. A New Algorithm for Computing a Single Root of a Real Continuous Function, IEEE Transactions on Circuits and Systems, CAS-26 (11), pp. 979–980.

THEORETICAL AND EXPERIMENTAL ANALYSIS OF A HYDRAULIC STEP-DOWN SWITCHING CONVERTER FOR POSITION AND SPEED CONTROL

Marcos P. Nostrani[1], Alessio Galloni[2], Henrique Raduenz[1], Victor J. De Negri[1]
[1]Federal University of Santa Catarina
Florianópolis, 88040-900, SC, Brazil
E-mail: marcos.nostrani@gmail.com, henrique@laship.ufsc.br, victor.de.negri@ufsc.br
[2]Università degli studi di Modena e Reggio Emilia
Modena, Italy
alessio.galloni@vishydraulics.com

ABSTRACT

The technological advance in the hydraulic field has been associated to the integration of electronic devices and improvement of manufacturing processes. However, hydraulic systems are still typically controlled by restricting the fluid passages making them extremely dissipative and, therefore, less efficient. In this context, digital hydraulics emerges as a thriving alternative solution to conventional hydraulic systems. In this paper, a positioning and speed control system using fast switching hydraulic is studied and compared with the conventional proportional system. A hydraulic step-down converter was chosen and applied to a pitch control test bench, which is able to emulate the wind forces conditions, simulating different loads in the digital hydraulic system. Efficiencies of digital and proportional system were evaluated using the model and the results show that both systems have similar efficiency for position control. On the other hand, when the system act as speed control, the digital system has a higher efficiency than the conventional system.

KEYWORDS: Hydraulic Positioning and Speed Control Systems, Digital Hydraulics, Fast Switching Hydraulics

1. INTRODUTION

Hydraulic systems are known by their low efficiency, usually below 50% [1]. This characteristic is caused by the large use of resistive valves that throttle the flow to control pressure and flow rate. However, hydraulic systems are extremely used in many fields of mechanical engineer due the low weight power ratio [2].

As a way to improve the efficiency of hydraulic systems, digital hydraulics emerges as a new technique to control pressure and flow rate avoiding resistive control. Researches in digital hydraulic systems have been increasing considerably in the last decades ([2]; [3]; [4]; [5]; [6]; [7]).

There are two technological approaches in digital hydraulics. One denominated *Parallel Connection Technology* where hydraulic components are connected in a parallel arrangement leading to discrete output values [8]. The second named *Fast Switching Hydraulics* where a *PWM* signal sets the output by varying the pulse width of the working cycle.

A configuration for switched systems under development is the one that uses switched valves with an inductive element called *Inertance Tube*. For this system, pressure and flow rate are controlled by the acceleration and deceleration of the fluid mass inside the tube. The characteristic behaviour of this system is set by the valve-tube configuration, since is possible to install the tube before or after the valve. On one case, when the tube is placed before the valve, the system is called *pressure booster* or *step-up converter* [3], [9] and [10]. On the opposite case, the system is called *flow booster* or *step-down converter* [6], [7], [10] and [11].

This paper presents the study of a digital hydraulic system that use a fast switching valve with an inertance tube in a step-down configuration to control either position or speed of an actuator. The system is assembled and experimentally evaluated on a wind turbine pitch control test bench. A mathematical model of the entire system is developed and the system efficiency is assessed.

1.1. Hydraulic Step-Down Converter

The Step-Down configuration works as a pressure regulator where the load pressure can be set between low (reservoir) and high supply pressure. An *on/off* valve with a low response time working with a high frequency is used. Figure 1 presents a Hydraulic Step-Down Converter, both hydraulic circuit and electrical analogy are presented.

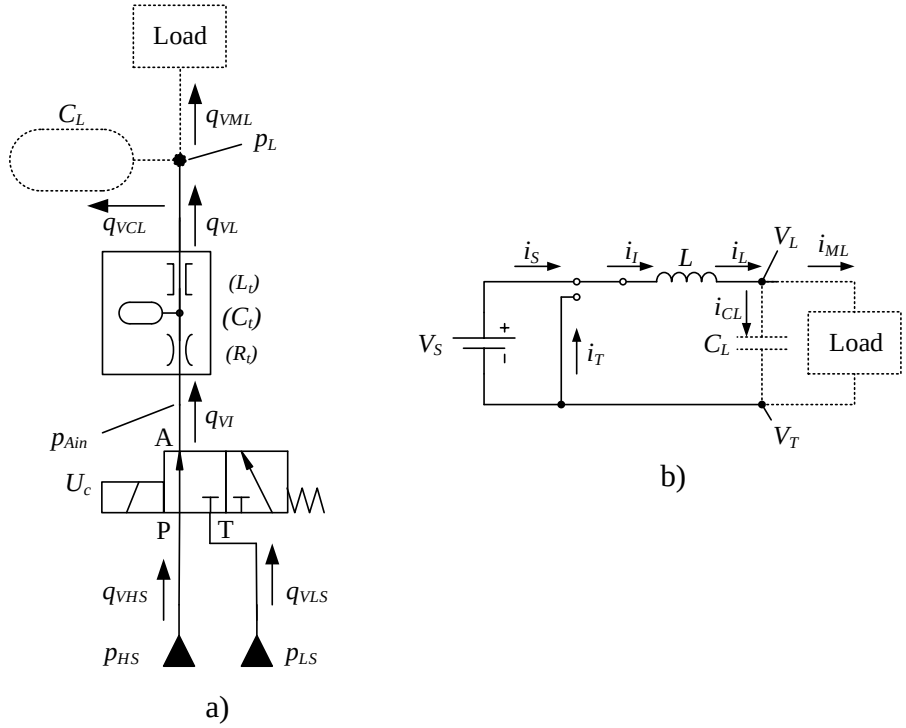

Figure 1 - Step-Down Converter: a) Hydraulic; b) Electric analogy [6].

As stated before and presented in the diagram of Figure 1, the configuration is composed by an *on/off* valve followed by an inertance tube and an accumulator. The inertance tube has a high length and a small diameter, so it works as an inductive element where fluid acceleration and deceleration is fundamental for the system functioning. An accumulator is placed after the tube to dump pressure ripple that emerge from the valve switching between high and low pressure lines.

In Figure 1 when port P is linked to port A with T closed, the internal pressure (p_{Ain}) tends to rise up to the high supply pressure (p_{HS}), causing the acceleration of the fluid inside the inertance tube. When the valve is switched to the other position, linking T to A and P closed, the fluid momentum inside the tube makes the internal pressure to fall below the low supply pressure (p_{LS}), inducing fluid suction from the low pressure supply line [6]. Because of this suction effect, it is necessary to supply a low pressure that is higher than zero aiming to avoid cavitation.

The load pressure (p_L) is controlled through the time the valve is opened or closed for a determined switching period. This time is set by the duty cycle (κ). The valve switching period (T_{sw}) is calculated with the switching frequency (f_{sw}). By the time the duty cycle is 100%, the valve remains connected to the high pressure port during the whole switching period. On the other hand, when the duty cycle is 0% the valve is permanently connected to the low pressure port. As a consequence, in case of no load applied to the system, the internal and load pressures are equal to the high supply pressure and low supply pressure respectively in the two cases indicated above. Figure 2 shows a duty cycle representation.

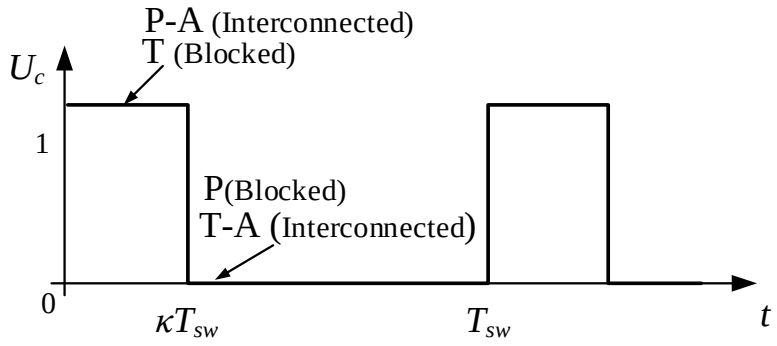

Figure 2 - Duty cycle representation [6].

2. HYDRAULIC STEP-DOWN CONVERTER MODEL

In order to predict the real system behaviour using digital or proportional position control, mathematical models representing each solution are proposed. The model was built according to the components shown in the Figure 3.

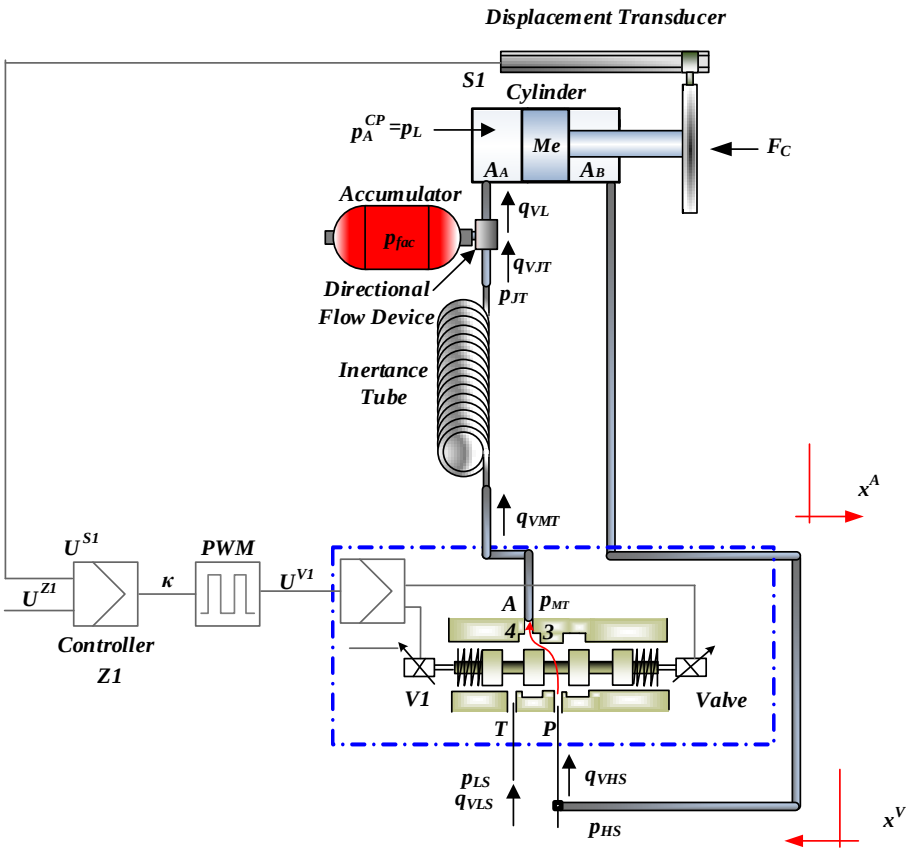

Figure 3 - Fast switching hydraulic system (Adapted from [12]).

2.1. Valve model

For both systems, valve internal leakage is considered. On the proportional system, inertance tube and accumulator were unplug from the system and port A of the valve is directly connected to cylinder chamber A. Equations (2.1) and (2.2) describe the proportional valve flow rate:

For $x^V \geq 0$ ($U^{V1} \geq 0\ V$):

$$q_{VL} = \left(K_{v_A}.\frac{U^{V1}}{U_n} + K_{vin}\right).\sqrt{p_{HS} - p_A^{CP}} - K_{vin}.\sqrt{p_A^{CP} - p_{LS}}. \quad (2.1)$$

For $x^V < 0$ ($U^{V1} < 0\ V$):

$$q_{VL} = -\left(K_{v_A}.\frac{|U^{V1}|}{U_n} + K_{vin}\right).\sqrt{p_A^{CP} - p_{LS}} + K_{vin}.\sqrt{p_{HS} - p_A^{CP}}. \quad (2.2)$$

Equations (2.3) and (2.4) represent the valve flow rate model for the fast switching system:

For $x^V \geq 0$ ($U^{V1} = 10\ V$):

$$q_{VMT} = \left(K_{v_A} . \frac{U^{V1}}{U_n} + K_{vin} \right) . \sqrt{p_{HS} - p_{MT}} + K_{vin} . \sqrt{p_{LS} - p_{MT}} . \quad (2.3)$$

For $x^V < 0$ ($U^{V1} = -10\ V$):

$$q_{VMT} = \left(K_{v_A} . \frac{|U^{V1}|}{U_n} + K_{vin} \right) . \sqrt{p_{LS} - p_{MT}} - K_{vin} . \sqrt{p_{HS} - p_{MT}} . \quad (2.4)$$

where q_{VL} is the load flow rate for the proportional system, q_{VMT} is the digital system inertance tube flow rate, $K_{v_A}$the valve flow coefficient, K_{vin} the valve leakage coefficient, p_A^{CP} the cylinder chamber A pressure, p_{MT} the inertance tube inlet pressure, U_n the nominal valve control signal, U^{V1} the valve control signal and x^V the valve spool position

2.2. Inertance tube model

The inertance tube was modelled according to the Transmission Line Method (TLM). This method proposes a mathematical model to evaluate pressure wave propagation in transmission lines. According to [13] the TLM model estimates pressure effects only in the pipe ends. All equations of TLM model were studied by [13] and improved by [14] and [15]. In this paper a TLM model that is available in the Bath University Website was used in order to use an already validated model.

2.3. Accumulator model

As it is known, the valve fast switching introduces pressure ripples that are undesirable, making the system noisy. In this paper an accumulator was used together with a directional flow device. This device forces the flow into the accumulator. This action promotes a better attenuation of pressure pikes. Figure 4 presents a schematic model of a accumulator with the directional flow device.

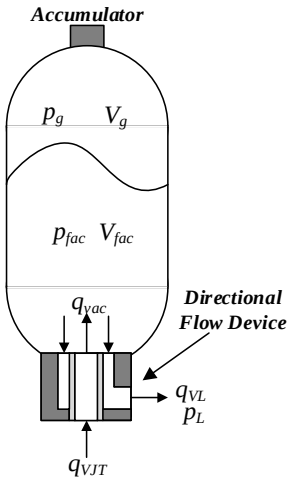

Figure 4 - Accumulator with directional flow device.

Fluid pressure variation ($\frac{dp_{fac}}{dt}$) in the accumulator interior is evaluated as:

$$\frac{dp_{fac}}{dt} = \frac{q_{VJT} - cdA_{DC}\sqrt{\frac{2}{\rho}(p_{fac} - p_L)}}{\frac{1}{\gamma}\frac{(V_0 - V_{fac})^{\gamma+1}}{V_o{}^{\gamma}}\frac{1}{p_o} + \frac{V_{fac}}{\beta_e}}. \quad (2.5)$$

where q_{VJT} is the inlet flow rate, V_0 the initial volume, V_{fac} the fluid volume, p_o the initial accumulator pressure, p_L the load pressure, cd the discharge coefficient, A_{DC} the flow passage area, β_e the bulk modulus and γ the specific heat ratio of the gas. The accumulator used has the following parameters: initial volume 0.320 L, 50 bar and flow passage area 3.4510^{-5} m^2.

2.4. Cylinder model

The position control actuator is an asymmetrical cylinder characterized by 2:1 area ratio. The cylinder parameters used in both the simulations and tests are: piston diameter 80 mm, rod diameter 56 mm and maximum displacement 500 mm. The system is assembled using a 3 way valve configuration, thus, B chamber is connect directly to the high supply pressure and its variation was considered not significant. The cylinder scheme is presented in Figure 5.

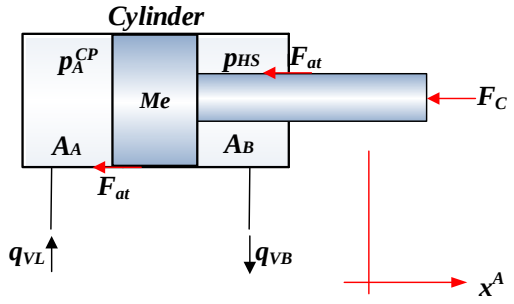

Figure 5 - Cylinder model (Adapted from [12]).

To model the cylinder, continuity equation, Equation (2.6), was applied in the A chamber and the movement equation, Equation (2.7), to piston and rod:

$$q_{VL} = A_A\frac{dx^A}{dt} + \frac{V_A}{\beta_e}\frac{dp_A^{CP}}{dt}, \quad (2.6)$$

where:

$$V_A = V_{Ao} + x^A A_A,$$

$$(p_A^{CP}.A_A) - (p_{HS}.A_B) = M_e.\frac{d^2x^A}{dt^2} + F_{at} + F_c, \quad (2.7)$$

where A_A is the A chamber area, A_B the B chamber area, p_A^{CP} the A chamber pressure, F_{at} the friction force, V_{Ao} the A chamber initial volume and the V_A the A chamber volume.

Friction force F_{at} was modelled using the variable viscous friction coefficient model, according to [16].

3. EFFICIENCY MODEL

Energy losses on valve, inertance tube and accumulator where calculated separately in order to compare digital and conventional system. These systems where evaluated when performing position or velocity control.

Equations (3.1) and (3.2) where used to calculate valve energy losses for the digital system,

$$E_V(t) = \int_0^t (p_{HS}(t) - p_{MT}(t)) q_{VHS}(t) dt, \qquad \text{for } U^{V1} = 10\,V, \qquad (3.1)$$

$$E_V(t) = \int_0^t (p_{LS}(t) - p_{MT}(t)) q_{VLS}(t) dt, \qquad \text{for } U^{V1} = -10\,V, \qquad (3.2)$$

where, U^{V1} is valve control signal (PWM) in volts.

Equations (3.3) and (3.4) where used to calculate valve energy losses for the conventional system.

$$E_V(t) = \int_0^t (p_{HS}(t) - p_A^C(t)) q_{VL}(t) dt, \qquad \text{for } U^{V1} \geq 0, \qquad (3.3)$$

$$E_V(t) = \int_0^t (p_A^C(t) - p_{LS}(t)) q_{VL}(t) dt, \qquad \text{for } U^{V1} < 0. \qquad (3.4)$$

Equations (3.5) and (3.6) describe energy losses at the inertance tube and accumulator respectively,

$$E_T(t) = \int_0^t (p_{MT}(t) - p_{JT}(t)) q_{VMT}(t) dt, \qquad (3.5)$$

$$E_{AC}(t) = \int_0^t (p_{JT}(t) - p_A^C(t) q_{VL}(t)) dt. \qquad (3.6)$$

Hydraulic and global efficiencies where also used to evaluate both systems. Hydraulic efficiency (η_H) is the ratio of hydraulic energy consumed at cylinder port A (E_A) and the supplied hydraulic energy ($E_{HP} + E_{LP}$),

$$\eta_H = \frac{E_A(t)}{E_{HP}(t) + E_{LP}(t)}, \qquad (3.7)$$

the energy delivered to cylinder B chamber is not considered.

Global efficiency (η_G) is the ratio of mechanical energy (E_{Fc}), provided by the cylinder, and the supplied hydraulic energy,

$$\eta_G = \frac{E_{Fc}(t)}{E_{HP}(t) + E_{LP}(t)}. \quad (3.8)$$

The energies involved in the equations of these efficiencies are presented in the following equations,

$$E_A(t) = \int_0^t ({p_A}^C(t) q_{VL}(t) dt, \quad (3.9)$$

$$E_{Fc}(t) = \int_0^t (F_c(t) v_c(t) dt, \quad (3.10)$$

$$E_{HP}(t) = \int_0^t (p_{HS}(t) q_{VHS}(t) dt, \quad (3.11)$$

$$E_{LP}(t) = \int_0^t (p_{LS}(t) q_{VLS}(t) dt, \quad (3.12)$$

where F_C is the controlled force and v_c is the cylinder piston velocity.

4. EXPERIMENTAL APARATUS

4.1. Pitch Control Test Bench

With the objective of evaluating the model, a test bench was built at the Laboratory of Hydraulics and Pneumatics Systems (LASHIP) of the Federal University of Santa Catarina. The test bench was previously used in the works of [16] in order to study the effect of the wind forces in the pitch control system of wind turbines.

It has a force control system that is able to generate and emulate wind forces up to 30000 N. The force control system uses an asymmetrical cylinder that has in each chamber a pressure reducer valve and a pressure transducer.

The positioning control system is composed by an asymmetrical cylinder, switching valve and, in the digital system only, an inertance tube along with an accumulator. Both cylinders are connected by a lever in order to transfer the load of the force cylinder to the positioning cylinder. The switching valve is a Parker D1FPE50MA9NB01. The bench hydraulic circuit with the digital system is shown in the Figure 6.

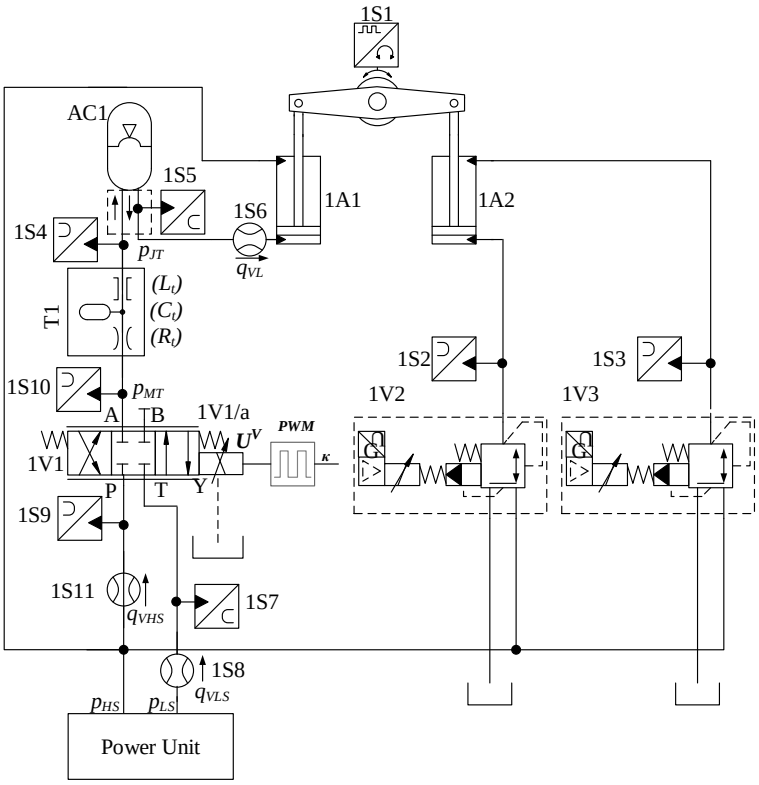

Figure 6 - Hydraulic digital bench circuit.

Sensor 1S1 is an incremental encoder responsible to evaluate the angular position of the lever and sensors 1S2 e 1S3 are pressure transducers whose feedback is the pressure signal which controls the force system. Sensors 1S6, 1S8 and 1S11 evaluate high supply flow rate q_{VHS}, low supply flow rate q_{VLS} and load flow rate q_{VL}, respectively. Sensors 1S4, 1S5, 1S7, 1S9 and 1S10 are pressure transducers that measure accumulator inlet, load, low supply, high supply and inertance tube inlet pressures respectively. Figure 7 shows the test bench.

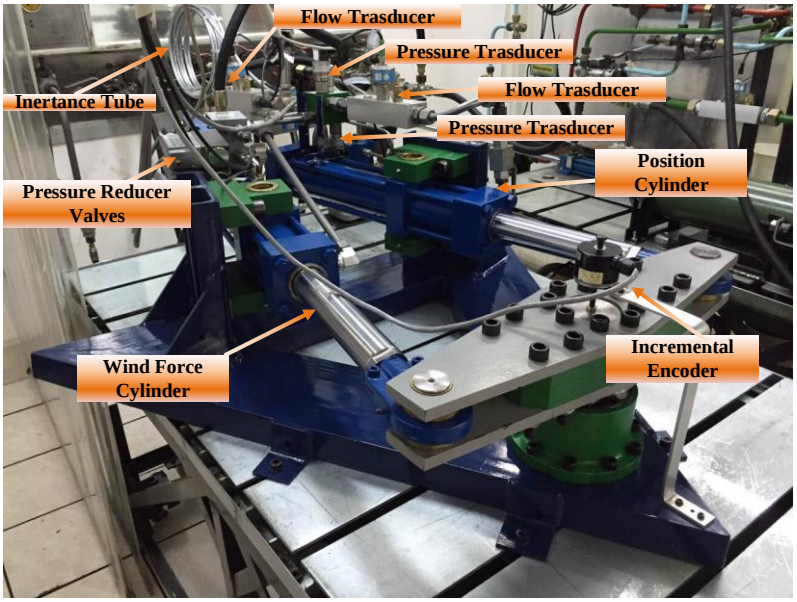

Figure 7 - Test bench.

5. RESULTS

Section 5.1 presents a comparison between simulation and experimental results for each system when performing position control. Sections 5.2 and 5.3 present obtained results for energy losses on components and the respective efficiencies for each system.

Parameters used on experimental and simulation analyses are presented in Table 1.

Table 1 - Parameters used on simulation and experimental analyses

Parameter	**Value**	**Unit**
Fluid density	870	[kg/m³]
Bulk modulus	1.4×10^{9}	[Pa]
Fluid viscosity	33.15	[cst]
Switching Frequency	32	[Hz]
Low supply pressure	10×10^{5}	[Pa]
High supply pressure	120×10^{5}	[Pa]
Tube length	6	[m]
Tube diameter	7	[mm]
Accumulator volume	0.32×10^{-3}	[m³]
Accumulator precharge pressure	50×10^{5}	[Pa]

5.1. Position Control System

Results for the proportional position system using 10000 N constant load force are shown in Figure 8. Proportional and integrative gains used are 1 and 0.1 respectively. Results were obtained for a pitch step of 0 to 8 degrees. The angle is measured considering reference 0° as the lever position at which the two cylinders have equal stroke and clockwise as the positive direction.

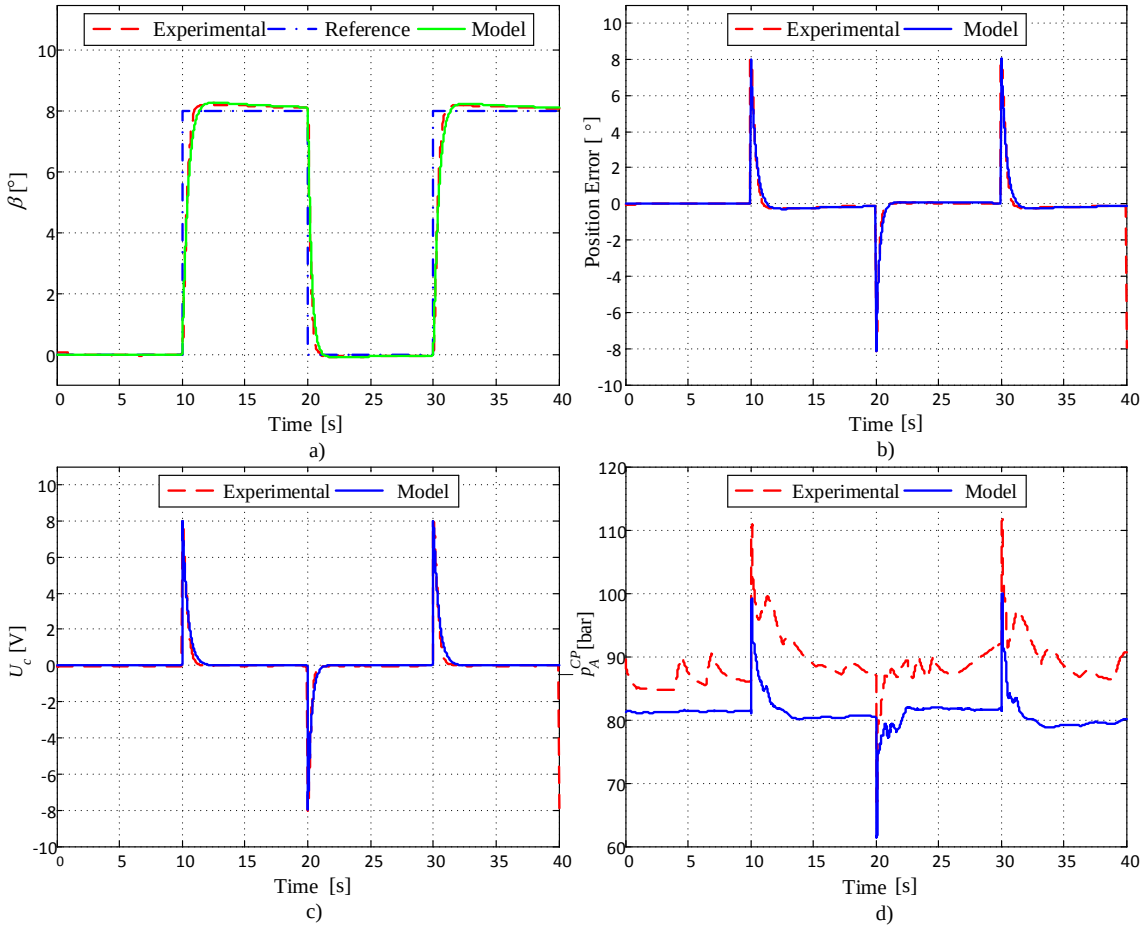

Figure 8 - Proportional position test with 10000 N: a) Position; b) Position Error; c) Control Signal; d) Hydraulic Pressure at the A Chamber.

The results presented in Figure 8 show that the model achieve values very close to those obtained by experiments, confirming that it is reliable as representation of the system. The obtained position error for both experiments and model is small, which indicates that this system shows satisfactory results in position control. For the gains used in this test, the valve control signal does not saturated, suggesting that proportional system valve size is suitable for the cylinder used. Pressure in both cases shows a similar behavior. However, it is found that there is a pressure oscillation in the experimental results when the cylinder is not moving or moving very slow. This phenomenon occurs because the valve is a zero lap spool type which causes a not complete overlap of the orifices during the transition at null point. As a result, since the valve controls the spool position constantly, any small disturbance introduces an increasing or decreasing pressure value.

Results for the digital position system using 10000 N constant load force are shown in the Figure 9. The proportional and integrative gains used are 0.7 and 0.1 respectively. The results were obtained in the same way as for the proportional system.

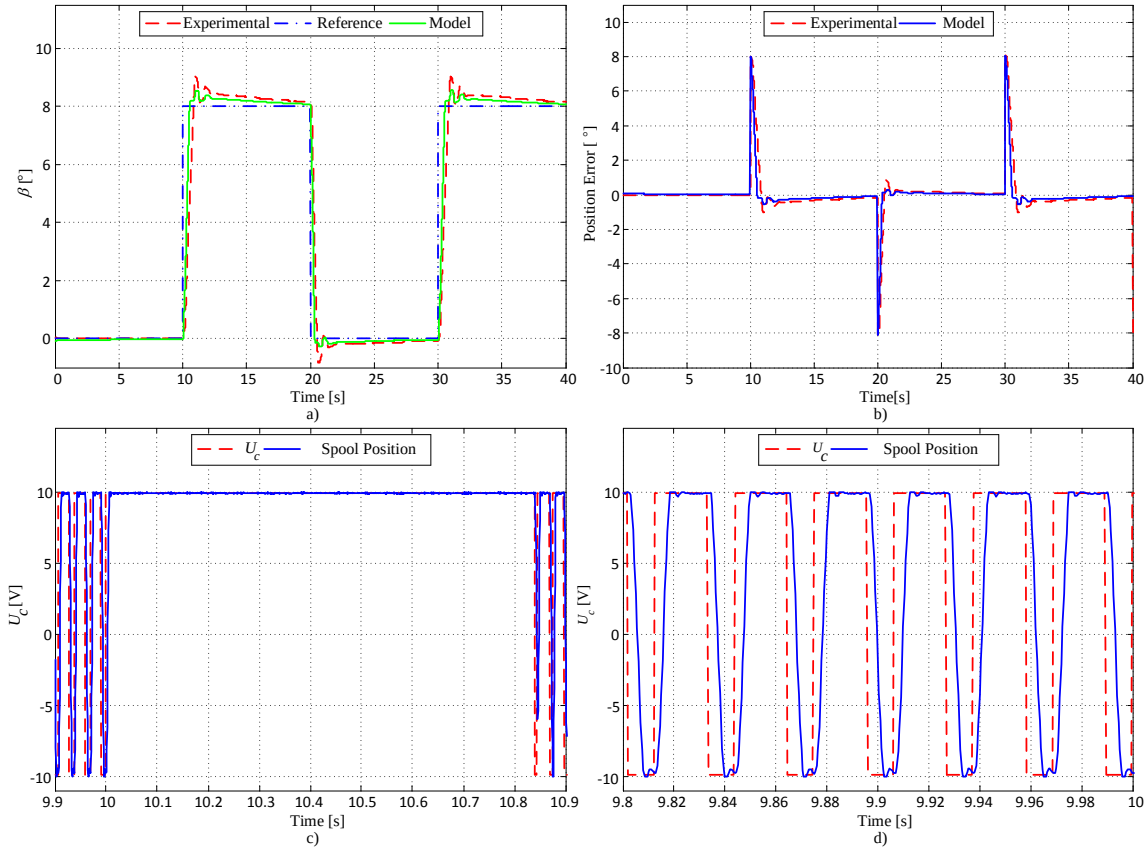

Figure 9 - Digital position test with 10000 N: a) Position; b) Position Error; c) Control Signal; d) Control Signal Zoom.

Results show that the digital system can control the pitch angle position with small error. The model shows results similar to those obtained experimentally, however, there is a overshoot in the position when it reaches the reference value. This fact is due to the controller dynamics, which is not able to regulate the duty cycle sufficiently fast in order to prevent the overshoot. Moreover, as the duty cycle varies quickly, the pressure constantly varies and does not stabilize, which create not constant forces. Figure 9c shows that the valve does not switch throughout the test duration due to saturation of the control signal that opens or closes totally, depending on the movement direction. This indicates that the valve is inadequate for the operation with the digital system. Figure 9d shows the control signal which is sent to the valve with the actual position of the spool thereof. The results show that the valve can respond to the control signal. Figure 10 shows the load, downstream and upstream pressures and duty cycle.

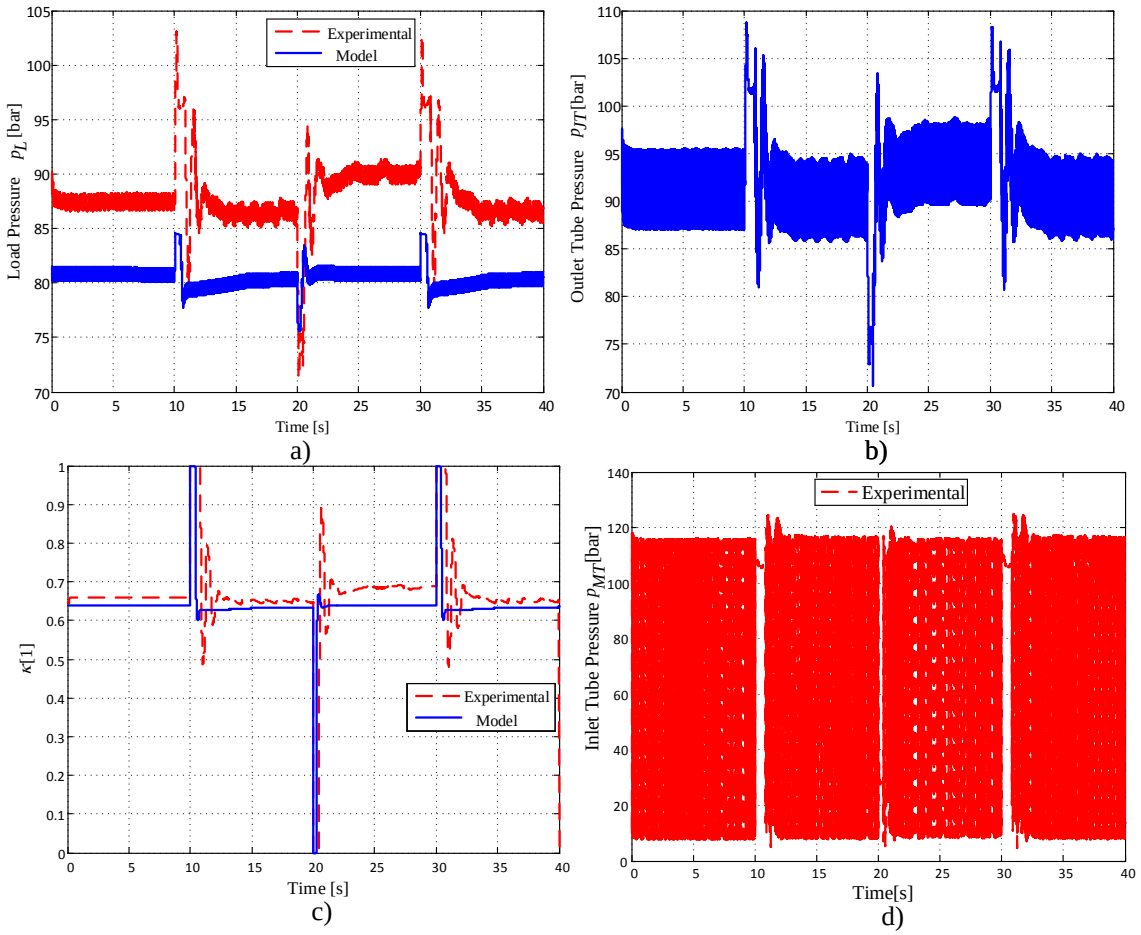

Figure 10 - Digital position test with 10000 N. a) Load Pressure; b) Downstream Pressure; c) Duty Cycle; d) Upstream Pressure.

The results from Figure 10 show that the load pressure has similar behavior compared to those obtained experimentally. Figure 10a shows the effect of addition the accumulator in the load pressure, where it becomes more stable compared to the pressure downstream (Figure 10b), softening in this way the effects of the fast switching valve. The duty cycle remains at the same value when the system stays at rest to maintain a constant loading pressure. When the angle step is applied, the control signal saturates, resulting in a duty cycle value of 0 or 1, depending on the step, for several switching periods, which correspond to the valve fully opened or closed.

5.2. System efficiency for position control

Position control efficiency is calculated while the system performs the control action for a step in the pitch angle reference signal from 0 to 8 degrees. It is performed for three different load forces. Table 2 and Table 3 present a resume with the obtained results for the digital and conventional systems respectively. Results for supplied energy (E_S) and consumed energy (E_C) are presented as well.

Table 2 - Efficiencies for the position control, digital system.

Step [°]	F_C [N]	η_H [%]	η_G [%]
0-8.86	0	58.07	0
0-8.60	5000	65.15	14.4
0-8.55	10000	72.2	21.3

Table 3 - Efficiencies for the position control, conventional system.

Step [°]	F_C [N]	η_H [%]	η_G [%]
0-8.23	0	56.9	0
0-8.24	5000	64.3	12.7
0-8.27	10000	71.5	20.3

Figure 11 presents the results from tables 2 and 3.

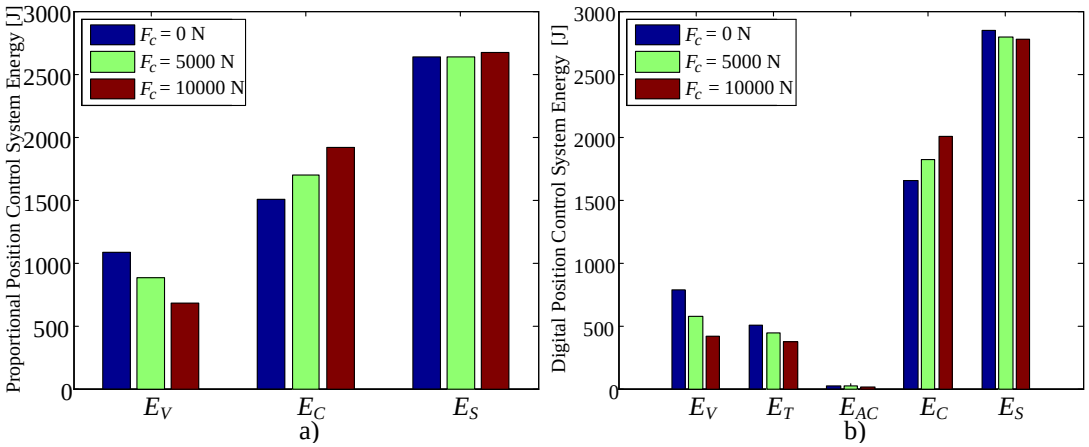

Figure 11 - Energy losses on hydraulic components for a) conventional and b) digital system, position control.

Results for position control show that the efficiencies of both systems are equivalent. That is a result of the saturation of the controller that makes the valve to stay fully opened, interrupting its switching, which makes it behave as the conventional system. In this situation energy losses on the valve and tube increase leading to a smaller system efficiency.

5.3. System efficiency for velocity control

Table 4 and Table 5 presents the results of energy losses and efficiencies for the velocity control for the digital and conventional system respectively.

Table 4 - Efficiencies for the velocity control, digital system k=0.7.

F_C [N]	v_C [m/s]	κ [1]	η_H [%]	η_G [%]
0	0.062	0.7	70.1	0.0
5000	0.041	0.7	77.1	10.3
10000	0.013	0.7	67.7	16.0

Table 5 - Efficiencies for velocity control, conventional system.

F_C [N]	v_C [m/s]	U_c [V]	η_H [%]	η_G [%]
0	0.062	3.72	53.0	0.0
5000	0.041	2.74	60.7	8.1
10000	0.013	0.995	66.3	15.6

Figure 12 presents the results from the tables.

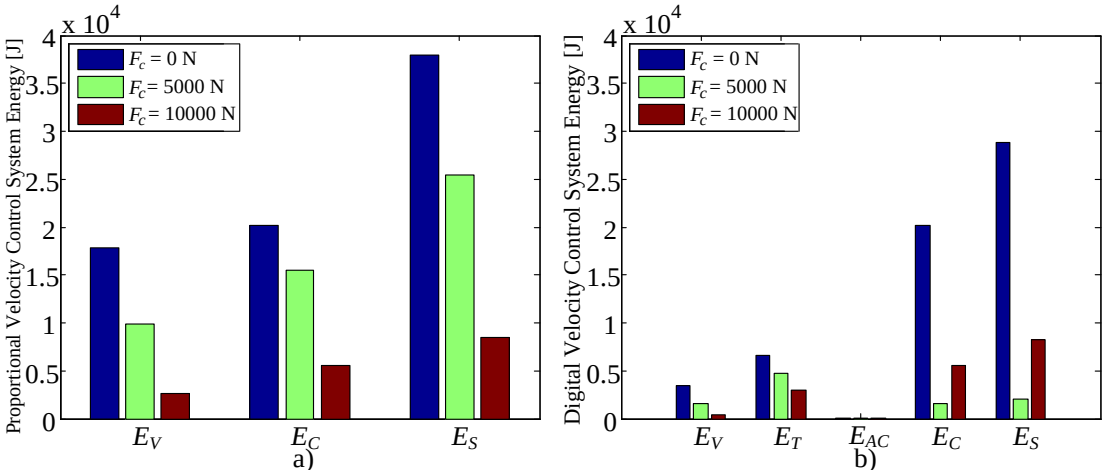

Figure 12 - Energy losses on hydraulic components for a) conventional and b) digital system, velocity control.

Results for velocity control shows an approximately 17% higher hydraulic efficiency for forces between 0 and 5000 N for the digital system in comparison to the conventional system. When comparing valve energy losses it can be seen that losses on the fast switching valve are smaller than the proportional valve. The accumulator and inertance tube presence increase system losses, however the sum of losses on the digital system remain smaller than the proportional valve. For 10000 N the efficiencies still are higher for the digital system but closer to the conventional system.

6. CONCLUSIONS

Two models that describe the conventional and digital system were developed in order to describe their behaviour through simulations. Both models were compared to

experimental results obtained from a pitch control test bench. Results showed that the models are suitable to describe both systems.

Results showed that the valve resistance has great influence on system efficiency. The use of a fast switching valve with an inertance tube was proved to be an effective alternative to conventional valves when performing velocity control. For the positioning control the systems tend to have similar efficiencies.

REFERENCES

[1] DE NEGRI, V. J., WANG, P., JOHNSTON, D. N., & PLUMMER, A.. Behavioural prediction of hydraulic step-up switching converters. International Journal of Fluid Power. Vol 15, No. 1, 1-9. 2014.

[2] LINJAMA, M. & VILENIUS, M.. Energy-Efficient Motion Control of a Digital Hydraulic Joint Actuator. Proceeding oh the 6ht JFPS International Symposium on Fluid Power, TSUKUBA, November 7-10, 2005.

[3] LINJAMA, M., LAAMANEN, A. & VILENIUS, M. 2003. Is it time for digital hydraulics? The Eighth Scandinavian International Conference on Fluid Power, May 7–9, Tampere, Finland, pp. 347–366.

[4] BELAN, H, B., LOCATELI, C. C., ENDLER, L., PIERI, E. R. D. & DE NEGRI, V.J. Aumento da eficiência energética em sistemas hidráulicos utilizando hidráulica digital. Anais do XX Congresso Brasileiro de Automática, Belo Hozironte, MG, 20 a 24 de Setembro de 2014.

[5] BELAN, H, B., LOCATELI, C. C., LANTTO, B., KRUS. P. & DE NEGRI, V. J.. Digital Secondary Control Architecture for Aircraft Application. The Seventh Workshop on Digital Fluid Power, February 26-27, Linz, Austria, 2015.

[6] DE NEGRI, V.J., NOSTRANI, M.P., WANG P., JOHNSTON D.N., & PLUMMER, A.. Modelling and analysis of hydraulic step-down switching converters, International Journal of Fluid Power, 2015.

[7] SELL,N.P., JOHNSTON,D. N., A. R. PLUMMER. & KUDZMA,S.. Control of a fast switching valve for digital hydraulics. The 13th Scandinavian International Conference on Fluid Power, SICFP2013, June 3-5, Linköping, Sweden. 2013.

[8] LINJAMA, M. & VILENIUS, M.. DIGITAL HYDRAULICS – Towards Perfect Valve Technology. Technology. Digitalna Hidravlika, Ventil 14 / / 2. pp. 138-148. 2008.

[9] PAN, M., JOHNSTON, D. N., PLUMMER, A. R., KUDZMA, S. & HILLIS, A. J. Theoretical and experimental studies of a switched inertance hydraulic system including switching transition dynamics, non-linearity and leakage. Proceedings of the Institution of Mechanical Engineers, Part I: Journal of Systems and Control Engineering, 228 (1). pp. 12-25. ISSN 0959-6518. 2014.

[10] SCHEIDL, R.; KOGLER, H.; WINKLER, B.. Hydraulic Switching Control - objectives, concepts, challenges and potential applications. *Magazine of*

Hydraulics, Pneumatics, Tribology, Ecology, Sensorics, Mechatronics, n. 1, ISSN: 1453 - 7303. 2013.

[11] JOHNSTON,N,. PAN, M,. PLUMMER, A., HILLIS, A., YANG, H. Theoretical studies of a switched inertance hydraulic system in a four-port valve configuration. The Seventh Workshop on Digital Fluid Power, February 26–27, ,Linz, Austria, 2015.

[12] SZPAK, Rodrigo. Análise Teórico-Experimental das Pressões em Posicionadores Hidráulicos. 2008. 143 f. Dissertação (Mestrado em Engenharia Mecânica) – Programa de Pós-graduação em Engenharia Mecânica, Universidade Federal de Santa Catarina, Florianópolis, 2008.

[13] KRUS, P., WEDDFELT, K., PALMBERG, J.-O. Fast pipeline models for simulation of hydraulic systems. Journal of Dynamic Systems, Measurement, and Control. Vol.116. pp. 132-136. March 1994.

[14] JOHNSTON, D.N. Efficient Methods for Numerical Modeling of Laminar Friction in Fluid Lines. Journal of Dynamic Systems, Measurement, and Control December, Vol. 128. pp. 829-834. DOI: 10.1115/ 1.2361320, 2006.

[15] JOHNSTON, D.N. The transmission line method for modelling laminar flow of liquid in pipelines. Proc. IMechE Part I: Journal of Systems and Control engineering, Vol. 226. pp. 586-597. DOI: 10.1177/0959651811430035. May, 2012.

[16] GONZALEZ, F. E.; Estudo das Forças Atuantes em Mecanismos de Regulação de Ângulo de Passo e Desenvolvimento de um Sistema Emulador de Cargas. 2012. Dissertação (Mestrado em Engenharia Mecânica)-Universidade Federal de Santa Catarina, Florianópolis, 2012.

NOMENCLATURE

β	Pitch angle	[°]
β_e	Bulk modulus	[Pa]
γ	Specific heat ratio	[1]
κ	Duty cycle	[1]
ν	Kinematic viscosity	$[m^2/s]$
η_H	Hydraulic efficiency	[1]
η_G	Global efficiency	[1]
ρ	Specific mass	$[kg/m^3]$
A_A	A chamber area	$[m^2]$
A_{DC}	Directional flow rate area	$[m^2]$

c_d	Discharge coefficient	[1]
d_t	Tube diameter	[m]
E_{AC}	Energy loss in the accumulator	[J]
E_T	Energy loss in the inertance tube	[J]
E_V	Energy loss at the valve	[J]
E_C	Consumed energy	[J]
E_S	Supplied energy	[J]
E_A	Energy in the A chamber	[J]
E_B	Energy in the B chamber	[J]
E_{MT}	Upstream tube energy	[J]
E_{JT}	Downstream tube energy	[J]
E_{HP}	Energy of the high supply pressure	[J]
E_{LP}	Energy of the low supply pressure	[J]
E_{Fc}	Load force energy	[J]
F_{at}	Friction force	[N]
F_c	Control force	[N]
K_{vA}	Flow rate coefficient	$[\mathrm{m}^3/\mathrm{s}.\mathrm{Pa}^{1/2}]$
K_{vin}	Leakage coefficient	$[\mathrm{m}^3/\mathrm{s}.\mathrm{Pa}^{1/2}]$
l_t	Tube length	[m]
M_e	Equivalent mass	[kg]
p_A^{CP}	A chamber pressure	[Pa]
p_o	Initial accumulator gas pressure	[Pa]
p_g	Accumulator gas pressure	[Pa]
p_{fac}	Accumulator fluid pressure	[Pa]
p_{Ain}	Internal pressure	[Pa]
p_{JT}	Upstream pressure	[Pa]
p_{MT}	Downstream pressure	[Pa]
p_L	Load pressure	[Pa]
p_{HS}	High supply pressure	[Pa]
p_{LS}	Low supply pressure	[Pa]
q_{VL}	Load flow rate	$[\mathrm{m}^3/\mathrm{s}]$
q_{VLS}	Low supply flow rate	$[\mathrm{m}^3/\mathrm{s}]$
q_{VHS}	High supply flow rate	$[\mathrm{m}^3/\mathrm{s}]$
q_{VMT}	Digital inertance flow rate	$[\mathrm{m}^3/\mathrm{s}]$
U_c	Control signal	[V]
U^{V1}	Valve control signal	[V]

U_n	Nominal valve control signal	[V]
V_A	A chamber cylinder volume	[m^3]
V_{Ao}	Initial A chamber cylinder volume	[m^3]
V_0	Initial accumulator gas volume	[m^3]
V_{fac}	Accumulator fluid volume	[m^3]
V_g	Accumulator gas volume	[m^3]

HIGH ACCURACY SENSORLESS HYDRAULIC STEPPING ACTUATOR

Andreas Plöckinger[1], Christoph Gradl[2], Rudolf Scheidl[2]
[1]Linz Center of Mechatronics GmbH
Linz, Austria
Altenberger Straße 69, 4040 Linz, Austria
[2]Johannes Kepler University
Institute of Machine Design and Hydraulic Drives
Linz, Austria
E-mail: andreas.ploeckinger@lcm.at

ABSTRACT

This paper presents a linear hydraulic stepper drive concept for accurate sensorless positioning control in industry. The stepping actuator consists of a cylinder piston unit which displaces defined fluid quanta by a limited forward strokes of a piston. Each fluid quantum leads to a precise motion step. In a prior, more general concept the step size was influenced by the chamber pressure (load pressure) of the hydraulic cylinder. A mathematical model in combination with a pressure sensor was needed to compensate for these influences in order to achieve a high accuracy.

The present alternative concept uses a passive pressure regulator valve to achieve a nearly constant chamber pressure in order to avoid a pressure transducer and a computational model for position estimation. For concept evaluation, a test rig was built and experiments were performed to study the positioning accuracy, repeatability, linearity, and scattering range of the proposed stepper drive concept. Two different step sizes (5 µm and 15 µm) were tested and verified by measurements. In this paper just the results for 15 µm are depicted. The results show the high accuracy of the hydraulic stepping actuator.

The practical relevance of the drive concept is proven by an application example, comprising a sensor-less control against a spring load. The experimental testing was done by hardware in the loop simulation, where the computed spring force is imposed to the physical stepper drive via a controlled hydraulic force.

KEYWORDS: hydraulic sensorless control, hydraulic stepper drive, sensorless position control

1. INTRODUCTION

Precise position control is an important actuation function in numerous industrial systems. The classical standard solution uses a cylinder with a precise position sensor and a close loop control via a proportional or servo valve. Costs and reliability are the major criteria in the development of many mechatronic systems. In this context, the avoidance of sensors in position control is advantageous. Not only the sensor contributes to cost and risk of failure but also the cabling, connectors, and controller input modules. In a complex machine system with numerous position drives the avoidance of such sensors plus accessories is an important cost reduction measure and is often a prerequisite for realizing new functionalities by additional position control.

Sensor-less control of electric drives and actuators is state of the art [1]. Different sensorless fluid power position control concepts were proposed, e.g. a pneumatic stepper motor for magnetic resonance medical imaging equipment [2], a hydraulic actuator controlled by a speed variable motor which drives a constant displacement pump [3], and a linear stepping actuators for choke valves [4]. These concepts are either quite complicated or have a low accuracy.

The authors presented an alternative solution for a hydraulic stepping actuator [5]. The first setup and measurement results described in [6] showed that for high accuracy position control an additional pressure sensor and also a computational model for position estimation are needed to compensate for oil compressibility and thermal expansion. To avoid the pressure sensor and the computational effort a modified hydraulic circuit which is presented in this paper was developed.

2. HYDRAULIC STEPPER DRIVE

2.1. Idealized working principle

The basic working principle is quite simple. It makes use of the precise and exactly known displacement of an incompressible fluid by an end to end motion of a piston in its cylinder – the so called slave cylinder.

Figure 1 shows a hydraulic cylinder acting against a load force F with a Hydraulic Stepper Unit and the main components. For a fully operable hydraulic drive two slave cylinders are necessary, one for extension (’Step Up’) and one for retraction (’Step Down’). Each slave cylinder consists of a slave piston with a sealing to avoid leakage and a return spring. The two 2/2-way switching valves (V_1 and V_2) connect the cylinder chambers alternately to the supply pressure or tank line or to the opposite chambers. With the 3/2-way switching valve V_3 the operation mode (’Step Up’ and ’Step Down’) can be chosen. For a proper function of the Stepper Unit the switching valves V_1 and V_2 have to be leak-proof.

’Step-Up’: The piston of the slave cylinder I starts at the bottom position. After switching the valve V_1 on, the piston is accelerated by the difference of system and actuator pressure. During this upward movement of the piston, oil is shifted via the consumer line to the master cylinder (see Figure 1). This amount of fluid leads to a single, precise position step of the hydraulic cylinder with a size Δs (assuming the hydraulic fluid is incompressible). After the slave cylinder piston has reached the end

position the valve V_1 is switched off and the valve V_2 in the bypass is switched on. The spring pushes the piston back to its initial position. During the downward movement the master cylinder ideally performs no position step, since the fluid displaced on the bottom side of the slave cylinder is consumed at the top side. In all phases of a 'Step Up' cycle the piston of slave cylinder II remains in the same position.

'Step-Down': For a stepwise retraction of the cylinder, the valve V_3 has to be switched to tank pressure. The operation principle is quite the same as of the extension mode. When V_1 is switched on, the piston of slave cylinder II moves from the topmost to the lowermost position driven by the difference of load and tank pressure. During that movement it extracts a fixed fluid quantum from the cylinder, hence the hydraulic cylinder performs a single, precise negative position step - Δs. After the piston has reached the lowest position, the valve V_1 is switched off and the valve in the bypass V_2 is switched on. The return spring moves the piston back to the initial position without any movement of the cylinder. The piston of the slave cylinder I is inactive during the 'Step Down' cycle. The corresponding timing diagrams are shown in Figure 1.

The characteristics and advantages of the proposed concept can be summarized as follows:

- well defined flow control, independent of pressure difference, valve dynamics and size
- stepwise position control in two directions (up and down)
- high speed bypass (up and down) by opening V_1 and V_2 to realize fast reset or full working stroke, if needed, e.g. in emergency case
- open loop control
- fix fluid quanta are generated and shifted into or out of the master cylinder
- realize precise, incremental motions without position sensors
- low cost system with high robustness against oil contamination
- step size can be easy adapted by area and stroke of the slave cylinder with respect to the master cylinder area

The step Δs has to be divided into a 'main step' Δs_m and the 'post step' Δs_p. The 'main step' is equal for all conditions concerning load pressure and temperature conditions. It equals the motion step under ideal conditions with a zero 'post step', i.e. for a fluid with constant density (incompressible and no thermal expansion) and stiff fluid conduits, cylinder walls, and seals. Under real conditions a 'post-step' occurs. Its quantity depends mainly on the load pressure p_L due to the non-zero node dead volume $V_{0,s}$ which is inevitable due to connection bores in the block. This node dead volume is defined by the connection pipework between the valve V_1 and V_2 and the two slave cylinders.

Also other effects like fluid compressibility, thermal expansion, thermo-elasticity, throttling losses and heat transfer influence the precision of the stepper actuator. In [6] a calculation model is presented to compensate these errors. The disadvantage of this system is, that the correct values of fluid compressibility in the dead volume and a additional pressure sensor is need.

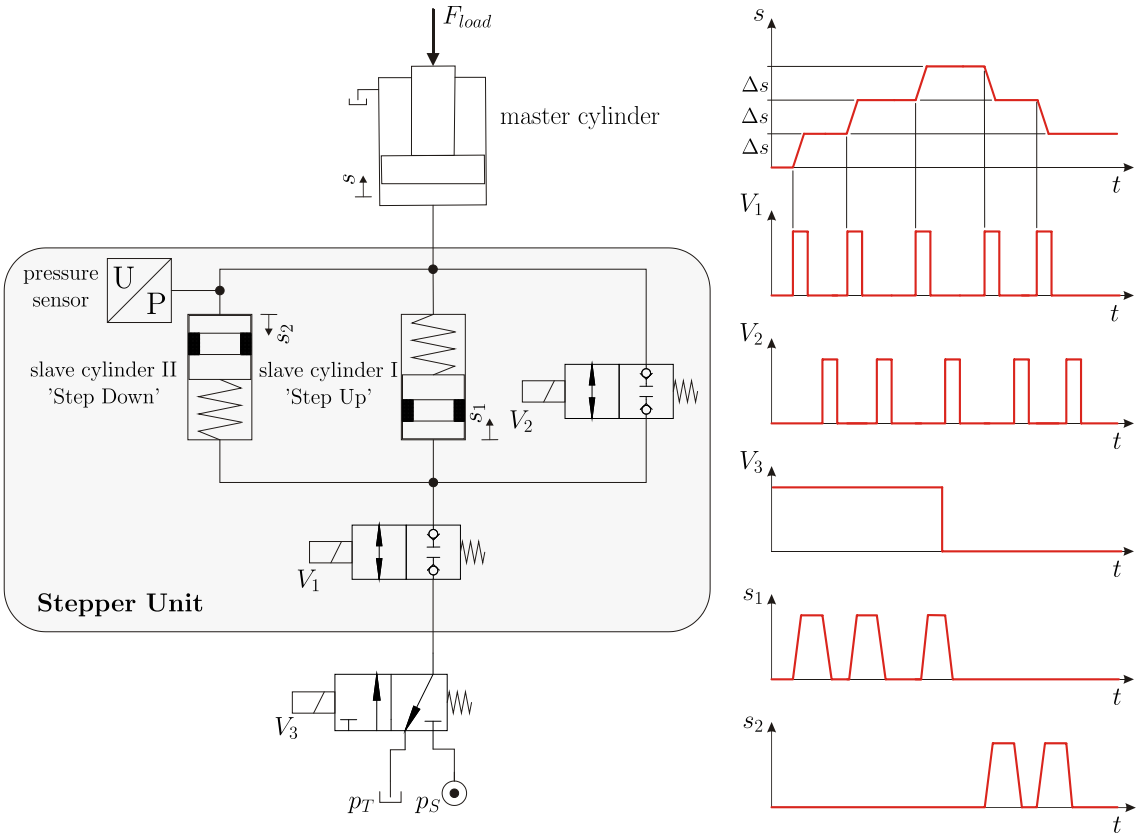

Figure 1. Schematic of the Hydraulic Stepper Unit and timing diagram.

2.2. Proposed concept

The basic idea is to keep the pressure in the cylinder chamber A_C of the master cylinder constant. This can be done by sensing the pressure in this chamber and using a simple pressure control valve to adjust the pressure in the rod chamber A_R. Starting at zero force of the load cylinder the resulting pressure forces of the master cylinder have to be zero. Assuming an area ratio $A_C = 2A_R$ the rod pressure is half the cylinder pressure. For positive load force F_{Load} the rod pressure is automatically reduced and for negative vice versa (see Figure 2).

The sensing of the pressure in the cylinder chamber and controlling the rod pressure can be done actively with a pressure transducer and a closed loop control employing a fast proportional valve. This system was used for system verification only (pressure control variant I).

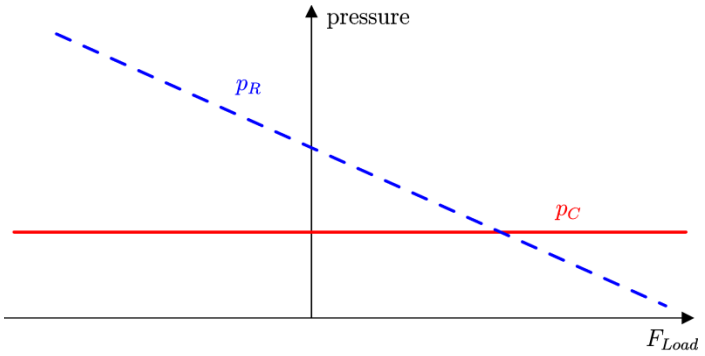

Figure 2. Pressure characteristic depending on load force F_{Load}

Pressure control variant II: The basic idea is to use a passive pressure control valve. The main benefit for this system is that no pressure sensor is necessary as the load force is automatically fed back via the valve. Thus the system would be a real “sensorless” hydraulic stepping actuator.

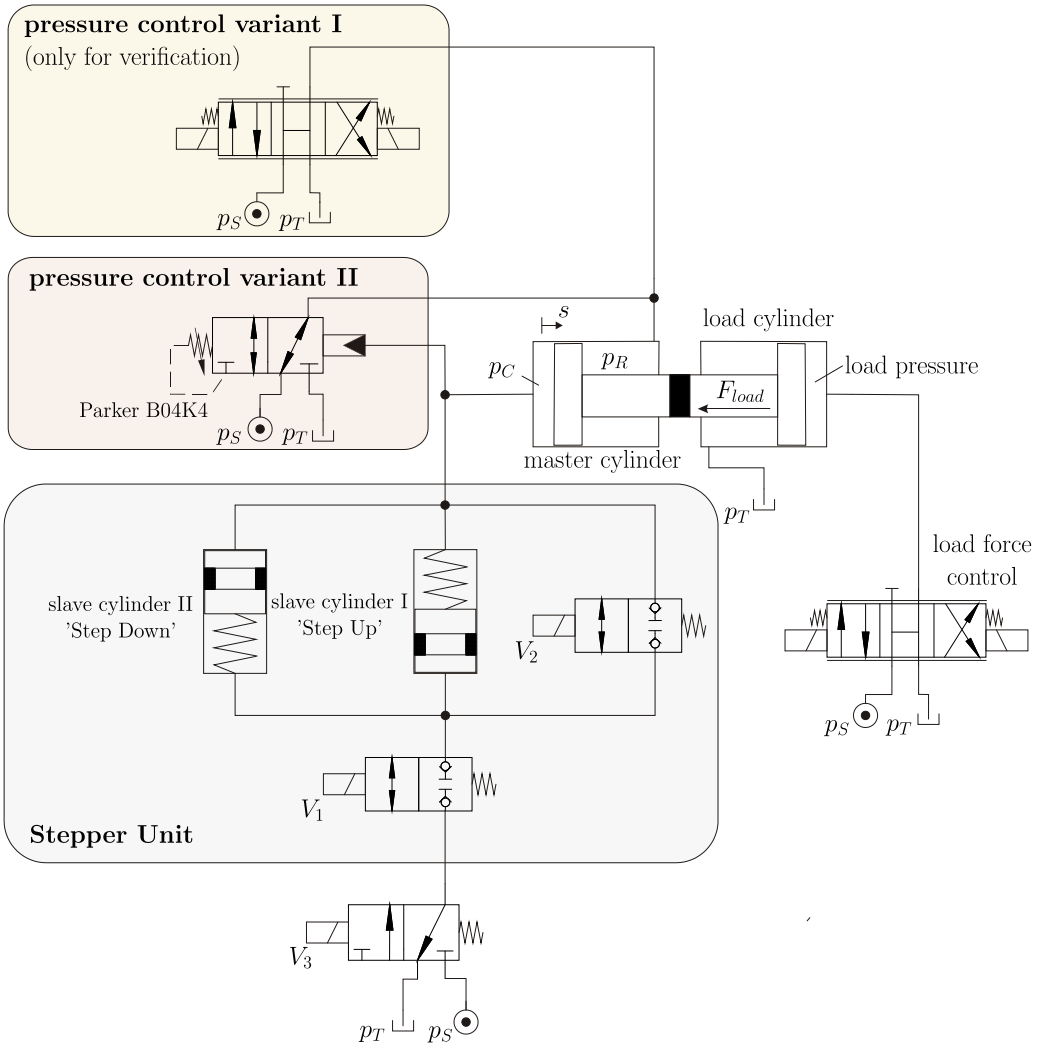

Figure 3. Schematic of the hydraulic circuit for two variants of the proposed pressure compensation concept. Variant I with an active proportional valve. Variant II with a passive pressure regulator valve.

In Figure 4 the differences of the calculated step size variation can be seen. Operation without pressure compensation is strongly dominated by the load force while in operation with pressure compensation the post step is constant and depending on the chosen ratio of supply pressure to the constant cylinder pressure. Running the hydraulic stepping actuator always at constant temperature and with fixed valve timings holds also the thermal effects constant.

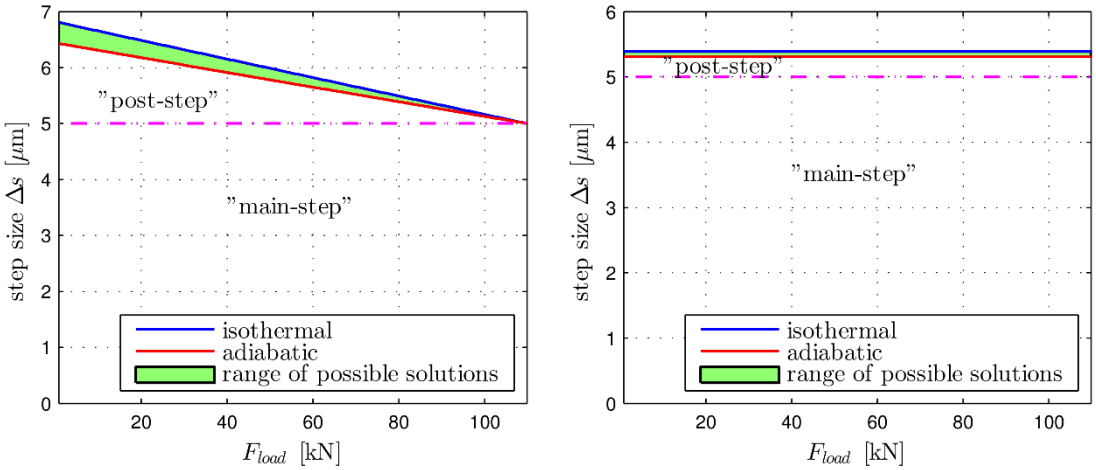

Figure 4. Calculated step size variation due to temperature and compressibility effects for different loads, limited by isothermal and adiabatic change of states; operation without pressure compensation (left) and with pressure compensation (right).

3. TEST RIG

In Figure 5 the 3D-CAD-model of the test setup is depicted. The setup consists of two directly connected cylinders. The load cylinder can be used to simulate different load forces or load cycles. The hydraulic stepper unit is directly mounted on the master cylinder. A detail view of the stepper drive with the two slave cylinders for 'step up' and 'step down' can be seen in Figure 6. In this configuration the pressure on the rod side is closed loop controlled via a pressure control valve. The position sensor is only used to verify the accuracy of the system.

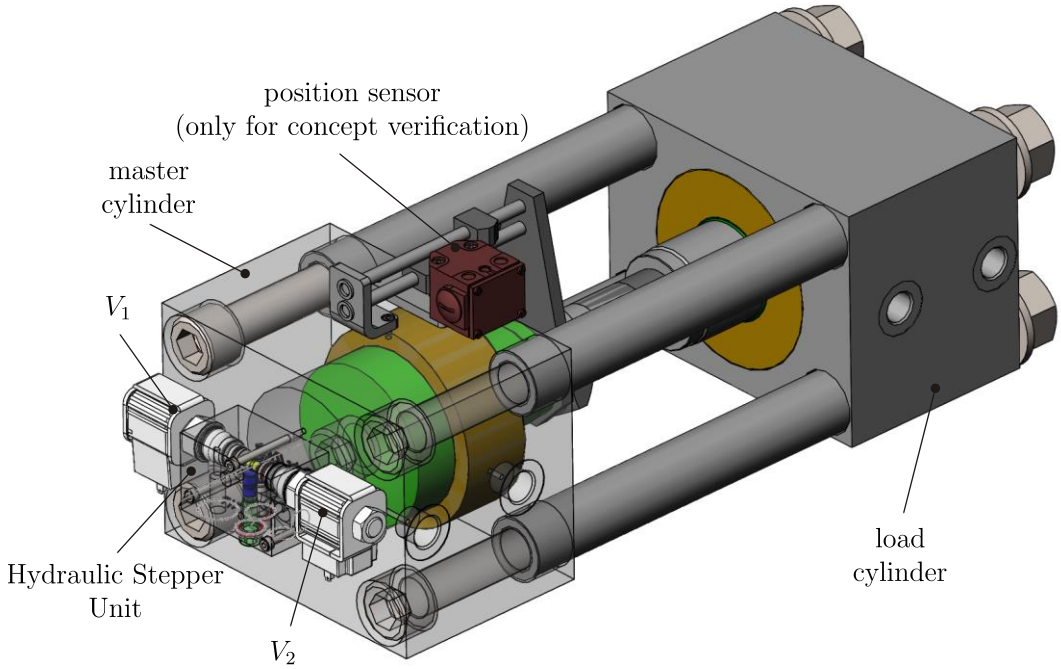

Figure 5. Mechanical design of the test rig.

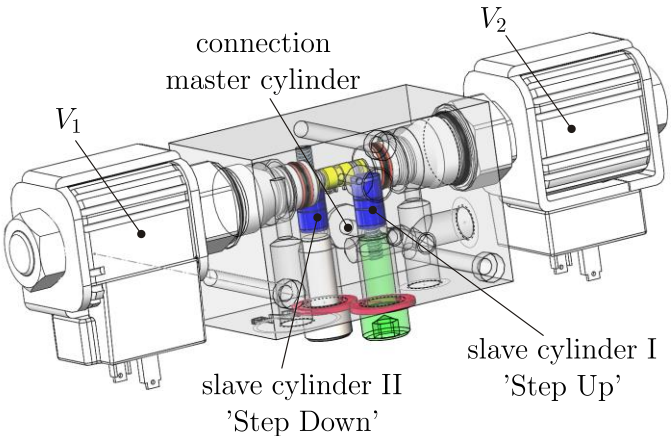

Figure 6. Detail view of the Hydraulic Stepper Unit.

Table 1. Parameter values.

Parameter	Value
Piston diameter master and load cylinder d_p	100 mm
Rod diameter master and load cylinder d_r	60 mm
Step sizes Δs	5 / 15 µm
Diameter slave cylinder d_S	8 mm
Stroke slave cylinder (5µm / 15µm) s_S	0.8 / 2,4 mm
Nominal flow rate valves (Parker GS02-73) Q_N	1 l/min @ 5 bar
Switching time of the valves T_S	5ms
Position sensor Sony Magnescale SR 721SP	0,1 µm resulution ± 5 µm accuracy (full stroke)
Node dead volume $V_{0,S}$	950 mm³
Master cylinder dead volume $V_{0,M}$	55 cm³
Prestressed spring force F_1	46 kN
Spring rate R	20 kN/mm

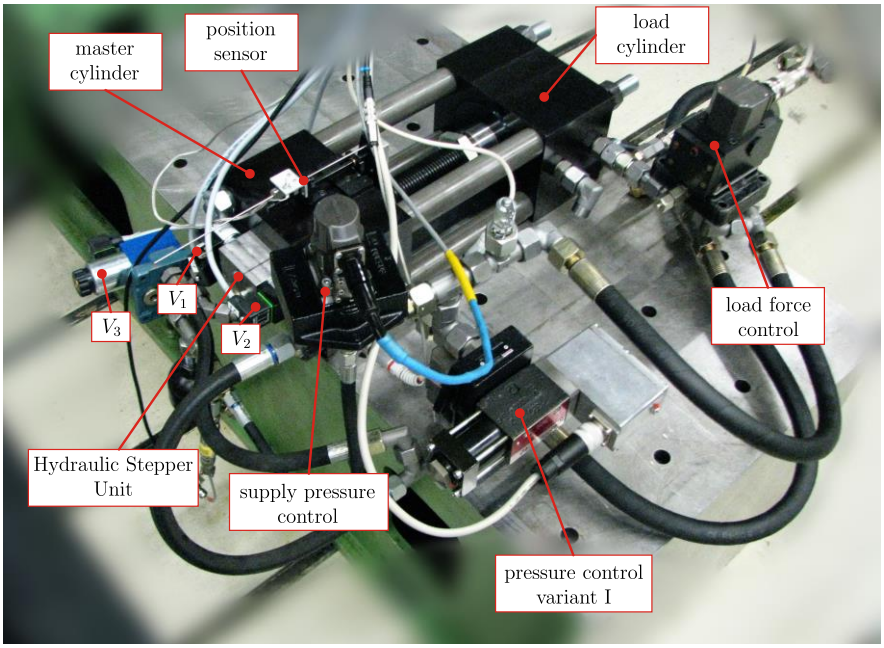

Figure 7. Test rig for variant I with additional control valves in the laboratory.

4. EXPERIMENTAL RESULTS

The test rig for the measurements for pressure control variant I can be seen in Figure 7. Due to the fact, that a closed loop pressure control with a proportional valve is easy to install and that the passive pressure control valve had some delay time, the authors started with variant I. For the test setup two different step sizes (5 µm and 15 µm) were tested and verified by measurements. As these results are quite similar just the values for the 15 µm steps are shown in this paper.

4.1. Step repeatability

As shown in Section 2.1 the step size is dominated by the volume given by the slave cylinder during the main step but there are other effects which influenced the total step size. For the design of the stepping actuator the lift of the slave cylinder was calculated just by taking the main step into account. Due to this fact and manufacturing errors the step size is bigger than the desired value of 15 µm. This was not re-adjusted. The "real" step size of the stepper drive was evaluated by taking the mean value over 50 steps. As a result of the friction of the cylinder there is a step size variation. The variation of around ±15 % of the mean value for two different load cases can be seen in the first two plots of Figure 8. On the right hand side the constant mean step size (50 cycles) during load variation can be seen.

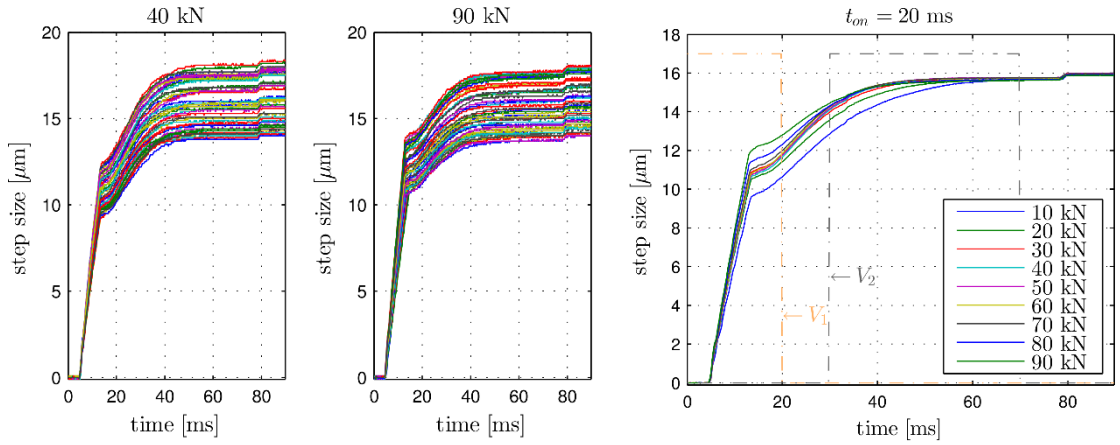

Figure 8. Scattering range two different load forces (left, middle); variation of the step size due to the load pressure (mean value over 50 steps) and the valve timing (right)

4.2. Position repeatability and accuracy of sensor-less control at constant load

The experimentally found position repeatability is shown in Figure 9. Four different test series with different step numbers and different constant load forces 50 cycles were recorded and the repeatability error was calculated. The position error is with ±0.8 µm and the relative error is less than 0.17 %.

Next is the accuracy of the sensor-less control. For that the error after 50, 100, 200, 300, 400, 600 steps and at different forces from 10 kN to 90 kN were measured and calculated. The maximum absolute error is less than 16 µm and the relative error less than 0.55 %.

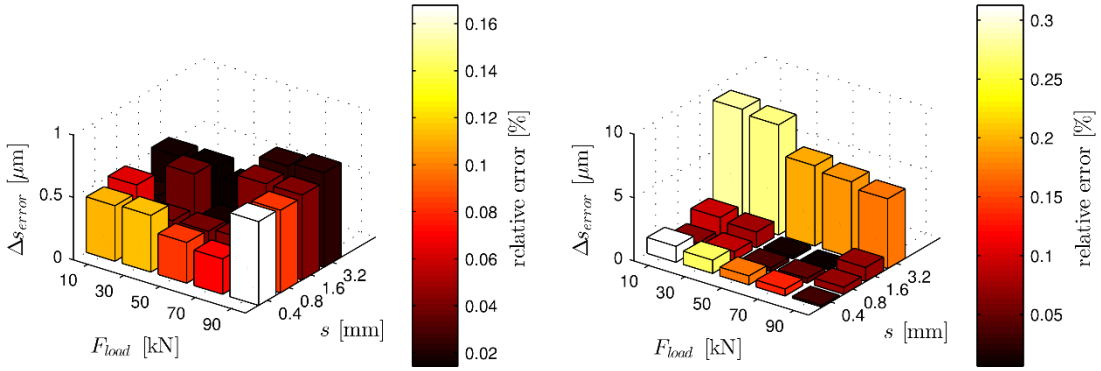

Figure 9. Position repeatability for various strokes and load forces (left); position accuracy of the sensorless control (right).

4.3. Sensorless positioning with non-constant load forces

In real applications the load forces are not constant. To test the hydraulic stepping actuator a motion against a spring which creates a linearly varying load force was studied. The details can be seen in Figure 10. The absolute error is less than 5 µm and the relative error less than 0.5 %.

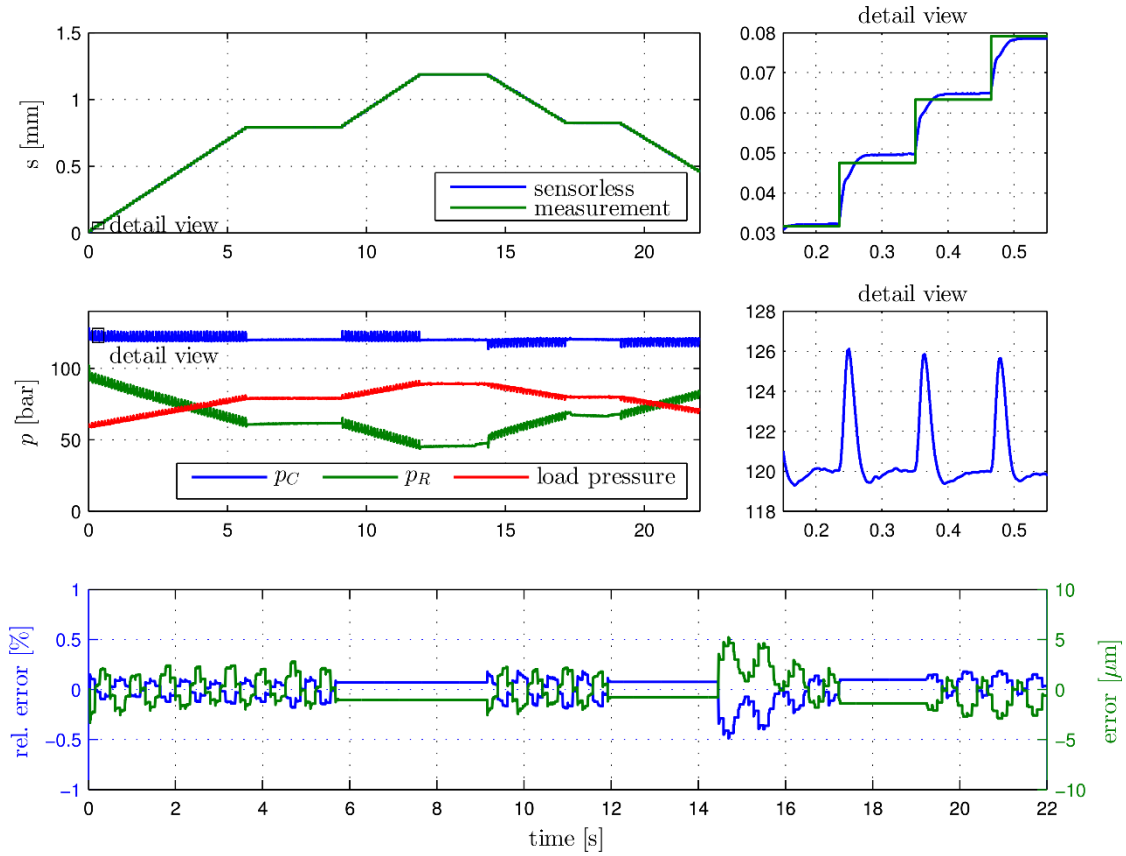

Figure 10. Position accuracy of the sensorless control for non-constant load forces - step size 15 µm.

5. CONCLUSION

The new pressure compensated sensor-less stepping actuator meets in a wide range the design goals given by the customer. To get rid of the pressure transducer a hydraulically actuated pressure control valve has to be used. If this concept is working also for high end applications no extra calculation model is needed to compensate the compressibility and thermal expansion effects. Corresponding tests are planned in future.

For low end applications the system can be already used. There are many applications where sensorless position control is the key for better performance, lower costs, or higher flexibility. These systems are cheap and easy to control. A further advantage is that instead of proportional valves just leak tight seat valves are needed and permanent leakage losses are avoided which opens the door for the application of compact hydraulic power supply units. The size of the valves is not crucial, only the slave cylinders have to be adapted to the size of the master cylinder and the required step size. The authors see numerous applications like synchronization of cylinders, mobile application for construction machines and agricultural machines.

ACKNOWLEDGMENT

This work has been carried out at LCM GmbH as part of a K2 project. K2 projects are financed using funding from the Austrian COMET-K2 programme. The COMET K2 projects at LCM are supported by the Austrian federal government, the federal state of Upper Austria, the Johannes Kepler University and all of the scientific partners which form part of the K2-COMET Consortium.

REFERENCES

[1] M. Montanari, S. Peresada, C. Rossi und A. Tilli, „Current sensorless position-flux tracking controller for induction motor drives," *Mechatronics,* Bd. 17, Nr. 1, pp. 15-30, 2007.

[2] D. Stoianovici, A. Patriciu, D. Petrisor, D. Mazilu und L. Kavoussi, „A New Type of Motor: Pneumatic Step Motor," *IEEE-ASME Transactions on Mechatronics,* Bd. 12, pp. 98-106, 2007.

[3] T. Minav, L. Laurila und J. Pyrhönen, „Relative position control in an electrohydraulic forklift," *International Review of Automatic Control (1974-6059),* Bd. 6, Nr. 1, pp. 54-61, 2010.

[4] H. Cove, *Linear hydraulic stepping actuator with fast close capabilities,* Google Patents, 2006.

[5] R. Scheidl, A. Plöckinger und C. Gradl, *Hydraulischer Antrieb und Verfahren zum diskreten verändern dessen Positionsausgangs, WO Patent App. PCT/EP2014/071,479,* 2015.

[6] C. Gradl, A. Plöckinger und R. Scheidl, „Sensorless position control with a hydraulic stepper drive—Concept, compression modeling and experimental investigation," *Mechatronics, DOI: 10.1016/j.mechatronics.2016.01.004,* 2016.

THE CONCEPT OF A ZERO-FLOWRATE-SWITCHING CONTROLLER

Dr Shuang Peng
Wuhan University of Technology, China
E-mail: rosa8416@gmail.com

ABSTRACT

Digital hydraulic technology aims to achieve simple, robust and energy efficient performance by switching on/off valves within a few milliseconds. However, flowing fluid with high flowrate has great kinetic energy. The kinetic energy is transformed into very high pressure when the valve switches off within a short time; in the same time, switching loss is created due to the pressure drop through the digital valve. In most cases, digital valve is actuated by PWM signals, thus the switching losses can be a big portion of the input power. To greatly reduce switching pulses and improve the system efficiency, this paper is to propose a zero-flowrate-switching control method which makes the valves always switch at zero-flowrate points of the waves. To obtain periodic zero-flowrate points, this method takes advantage of the output pressure pulses of a piston pump and transforms it into harmonic flowrate waves by a hydraulic resonator. This paper derivates the pressure/flowrate response for a hydraulic resonator, and builds a hydraulic circuit for the zero-flowrate switching control method. Simulation results indicate that the switching power loss for the actuating system with zero-flowrate-switching controller peaks at 1.499 watts compared to 158 watts for the actuation system without the new method. It is concluded that zero-flowrate-switching controller is a potential method to remove switching pulses and reduce switching loss for digital hydraulic systems.

KEYWORDS: Digital hydraulics, zero-flowrate-switching, pressure ripples

1. INTRODUCTION

Modern digital hydraulic technology applies several high-speed digital valves allocated in certain configurations to make the system work as a servo/proportional hydraulic system but with some new advantageous characteristics[1-3]. To match the flowrate to the load, many control methods are employed, like Pulse Width Modulation control (PWM), Pulse Code Modulation (PCM) control, or stateflow control method [1], to name just a few. One of the challenges to develop digital hydraulics is that fast response and smooth response are both required for digital hydraulics while fast response of the valves inevitably leads to pressure ripples. When the valve is on, the fluid moves through the valve orifice at a certain velocity; when the valve switches off

simultaneously, the kinetic energy of the fluid is transformed into high pressure which can be several times of the maximum supply pressure. In the past decades researchers have tried different solutions for these problems. For example, Fibonacci coding method is proposed to ease the pressure peaks by decreasing the number of digital valves switching in the same time compared to binary coding in a PCM method [4]. A flatness based controller is designed for the a Hydraulic Buck Converter (HBC) aiming to attenuate pressure ripples and oscillatory response [5]. All these methods tries to attenuates pressure ripples instead of remove pressure ripples during valve switching.

In this work a new control method is proposed to switch on/off the valve when the flowrate through the valve falls to zero. In chapter 2 the idea of zero-flowrate-switching control method is presented; then a hydraulic resonator is illustrated and the input and output of the required resonator are discussed in chapter 3; chapter 4 presents the model of a zero-flowrate control system and its operation principles; simulation results of such a system is presented and discussed.

2. ZERO-FLOWRATE SWITCHING CONTROL METHOD

The key issue to realize zero-flowrate control method is to obtain periodic zero-flowrate points. As shown in Fig. 1, a hydraulic resonator is used to transform sinusoidal pressure into sinusoidal flowrate whose average value is zero. Sinusoidal pressure is easily obtained from a normal piston pump. The amplitude and frequency of such waves are 1~2bar and about 100Hz, respectively. These waves are very stable and will not be changed by an accumulator or a piece of long hose. With proper allocation of hydraulic capacitance and inductance, such waves will be transformed into sinusoidal flowrate. Periodic zero-flowrate points are obtained in this way. By feedback controlling any valve in actuation system is possible to switch on/off always at zero-flowrate points(as shown in Fig.2).

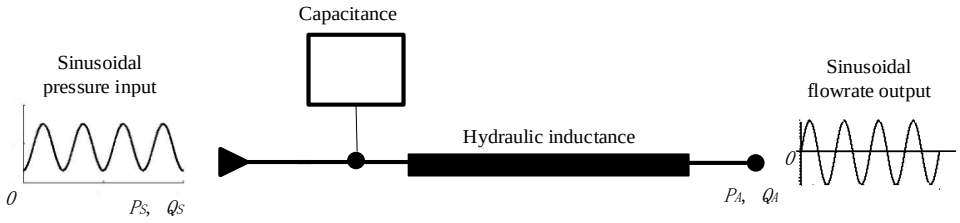

Figure 1. A hydraulic resonator

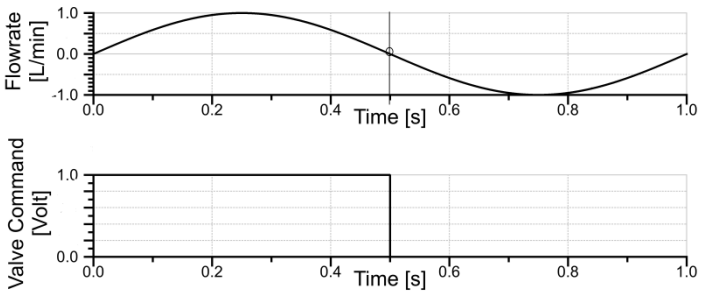

Figure 2. Power loss of hard/soft switching control methods

3. HYDRAULIC RESONATOR

In this research a hydraulic resonator is used to transform sinusoidal pressure into sinusoidal flowrate. A hydraulic resonator consists of a hydraulic inductance and a hydraulic capacitance. In this model a piece of hydraulic pipe is selected as a hydraulic inductance and a hydraulic chamber is selected as hydraulic capacitance. Mathematical model is built to obtain sinusoidal flowrate output.

3.1. A hydraulic resonator

3.1.1. A hydraulic inductance

A piece of hydraulic pipe is able to prevent sudden changes of the fluid flow due to its inertia. In this model a hydraulic pipe is chosen as inertia element due to its simple structure and low cost. A hydraulic pipe with diameter *d* and length *l* is shown in Fig. 3.

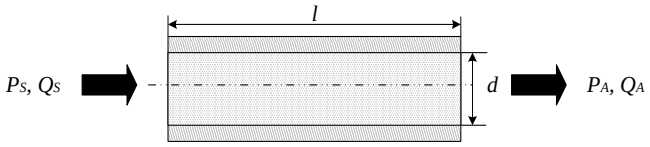

Figure 3. The hydraulic inductance

The inductance of the pipe is

$$L = \frac{4\rho l}{d^2\pi} \tag{1}$$

Where ρ is the density of hydraulic fluid.

3.1.2. Hydraulic capacitance

Cavities inside the physical system - like bores inside the valves and the manifolds - can store and relieve pressures. The capacitance of such a cavity is modelled as

$$C = \frac{V}{E} \tag{2}$$

where *E* is bulk modulus of hydraulic fluid, *V* is the volume of the capacitance.

To create resonance oscillation, the inductive impedance is equal to capacitive impedance

$$\omega_0 L = \frac{1}{\omega_0 C} \tag{3}$$

$$\omega_s = \omega_0 = \sqrt{\frac{1}{LC}} \tag{4}$$

Where ω_s is the frequency of the power source. If the existing capacitance between the valve and the inductance pipe is C_1, the compensation cavity C_2 is

$$C_2 = C - C_1 = \frac{1}{\omega_0{}^2 L} - C_1 = \frac{d^2\pi}{4\omega_0{}^2 l\rho} - C_1 \tag{5}$$

In this work the compensated capacity (cavity in Fig. 4) is realized by a cavity with a volume *V* according to Equ. (6).

$$V = C_2 E = (\frac{d^2\pi}{4\omega_0{}^2 l\rho} - C_1)E \tag{6}$$

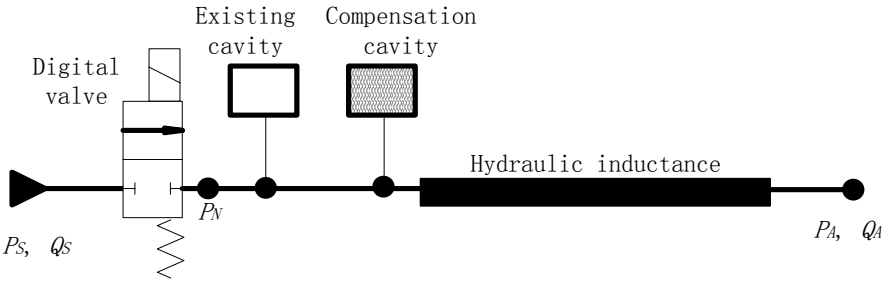

Figure 4. A resonator with compensation cavity

To further simplify the model, it is assumed that there is no existing capacitance between the node point and the output point, then the volume of the cavity is

$$V = C_2 E = \frac{d^2\pi E}{4\omega_0{}^2 l\rho} \tag{7}$$

3.1.3. Hydraulic resonator

To build a model for zero-flowrate control method, we assume that P_A and Q_A are constant outputs for the load; P_S are sinusoidal inputs

$$P_S = P_{S0} - P_{Sa}\cos(\omega t - \frac{\pi}{2}) \tag{8}$$

Where P_{Sa} and P_{S0} are the amplitude and mean value of the supply pressure. The pressure distributed along the line is

$$RQ(t) + L\frac{dQ}{dt} + \frac{1}{C}\int_0^t Q(t)dt = P_S - P_A \tag{9}$$

Where ω_0 is the natural frequency of the resonator; ω is the frequency of input pressure; P_s is the average value of the input pressure. The valve opening is assumed to be linear and the relationship between the pressure drop $\Delta\, p$ and flowrate q fulfils

$$p = Rq \tag{10}$$

The sinusoidal input pressure differentiating and dividing by L leads to the second order differential equation

$$\frac{d^2Q(t)}{dt^2} + \frac{R}{L}\frac{dQ(t)}{dt} + \frac{1}{LC}Q(t) = \frac{\omega P_s}{L}\sin(\omega t - \frac{\pi}{2}) \tag{11}$$

Hence we have

$$Q(t) = \frac{P_S}{LZ_m}\sin(\omega t - \pi/2 + \varphi) \tag{12}$$

where

$$Z_m = \sqrt{(\omega_0 R\sqrt{\frac{C}{L}})^2 + \frac{1}{\omega^2}(\omega_0{}^2 - \omega^2)^2} \tag{13}$$

$$\varphi = \arctan\left(\frac{\omega\omega_0 R}{\omega^2 - \omega_0^2}\sqrt{\frac{C}{L}}\right) \tag{14}$$

To create a resonance in the system, the frequency of the pressure source fulfils

$$\omega = \omega_0 \tag{15}$$

To get

$$Q(t) = \frac{P_{sa}}{R}\sin\omega_0 t \tag{16}$$

4. A ZERO-FLOWRATE-SWITCHING BASED ACTUATOR

4.1. a typical digital hydraulic circuit

A typical hydraulic circuit as shown in Fig. 5 is studied here. The digital valve in the circuit keeps switching to supply required flowrate to the load. Q_{req} and P_A is constant for the load; the opening/closing time for the digital valve is 2ms.

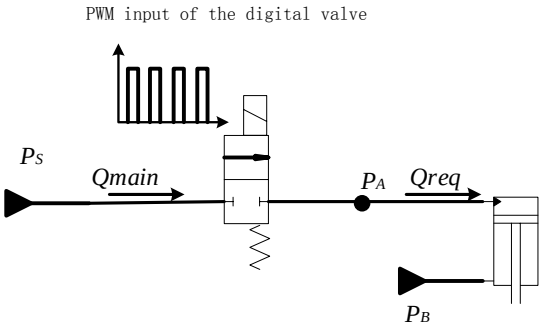

Figure 5. A typical digital hydraulic circuit (Model 1)

To remove pressure ripples created during valve switching, a zero-flowrate switching controller is applied to the basic hydraulic circuit. Fig. 6 presents such a basic control system with a by-pass line. Valve 1 functions as the digital valve in Fig. 5; a check valve is located inside valve 1 to allow back flow; valve 2 with opening/closing time of 2ms works for the resonator; the required flowrate is supplied by two branches, Q_1 from valve 1 and Q_2 from the resonator; check valve 1 prevents Q_1 from flowing back to the source; check valve 2 works by absorbing flowrate from the tank when the total value of Q_1 and Q_2 is less than required flowrate Q_{req}.

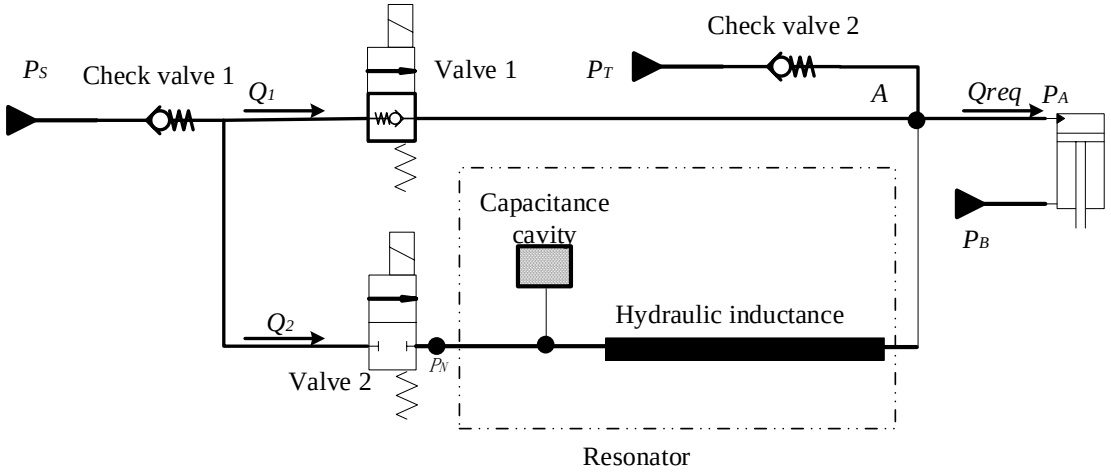

Figure 6. A hydraulic circuit with a zero-flowrate switching controller (Model 2)

The input of the circuit is sinusoidal pressure (discribed in 9) whose frequency equals that of the resonator. This is the condition to create resonate waves. When both valve 1 and valve 2 are open, the line with a resonator starts to resonate, and output sinusoidal Q_2

$$Q_2(t) = \frac{P_{sa}}{R} \sin \omega_0 t \tag{17}$$

Since Q_{req} is defined by the load, then Q_1 is

$$Q_1(t) = Q_{req} - Q_2(t) = Q_{req} - \frac{P_{sa}}{R} \sin \omega_0 t \tag{18}$$

Thus the pressure at position A is

$$P_A = P_S - \Delta \mathrm{P} = P_S - \Delta P Q_1(t) \tag{19}$$

Where ΔP is the pressure drop through valve 1. Substitute 8 and 18 for P_S and ΔP, we obtain

$$P_A = P_{S0} - P_{Sa} \cos \omega_0 t - R_1 Q_{req} + \frac{R_1}{R_2} P_{Sa} \sin(\omega_0 t + \frac{\pi}{2}) \tag{20}$$

Where R_1 and R_2 are resistance coefficients for valve 1 and valve 2 (here the opening/closing characteristics for both valves are regarded linear). If we make both R_1 and R_2 equal to R, then 20 can be simplified to

$$P_A = P_{S0} - R Q_{req} \tag{21}$$

20 and 21 tell that the modelled actuator is able to output constant pressure to the cylinder when the resistance efficiencies of valve 1 and valve 2 are equal to each other.

4.2. Operations of the zero-flowrate switching control method

To build a zero-flowrate switching controller, a system as shown in Fig. 6 is modelled. Key parameters are presented in Table 1.

Table 1. Parameters of the models

Parameters	Values
ρ	860kg/m^3
E	14000bar
V	0.4L
d	0.008m
l	2m
f_0	50Hz
P_{Sa}	1bar
P_{S0}	20bar
P_A	19.375bar
Q_{norm}	40l/min@5bar
Q_{req}	5L/min

Five modes are designed to apply zero-flowrate switching controller (Table 2). The states of the valves for five modes are presented in Table 3.

Table 2. Time periods for five modes

Modes	Time periods
1	0 ~ t1
2	t1 ~ t2
3	t2 ~ t3
4	t3 ~ t4
5	t4 ~ t5

Table 3. Valve states for zero-flowrate switching controller

Mode	Valve 1	Valve 2	Check valve 2
1	ON	OFF	OFF
2	ON	ON	OFF
3	OFF (Back flow)	ON	OFF
4	OFF	ON	ON
5	OFF	OFF	OFF

In mode 1(Fig. 7), pressure P_{S0} is supplied to the load through valve 1; valve 2 is off. The resonator is not working in this mode. the constant input pressure is obtained by filtering the waves from the output pressure of the pump.

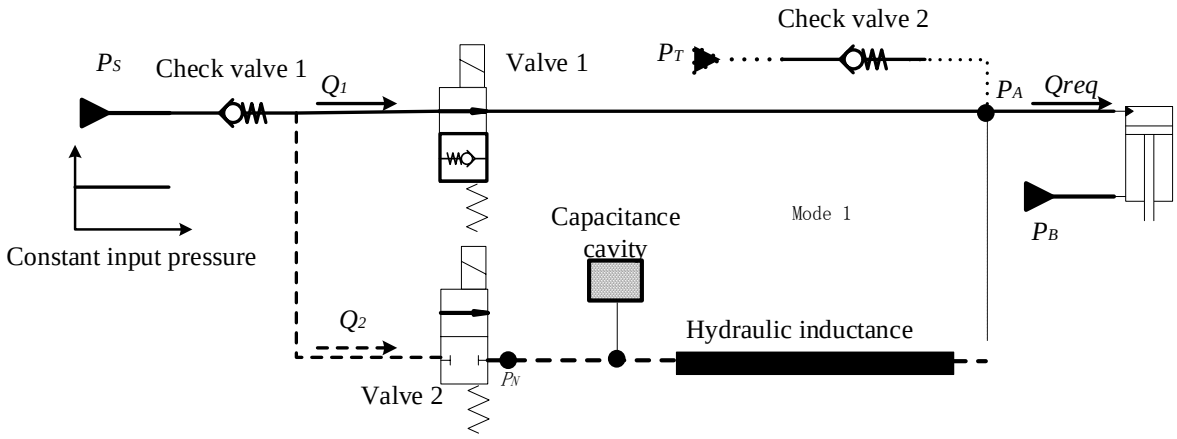

Figure 7. Mode 1 for zero-flowrate-switching controller

In mode 2 (Fig. 8), a sinusoidal pressure is supplied to the resonator branch. At the moment t1, valve 2 switches on and the resonator starts to work; the required flow rate Q_{req} is supplied to the load through both valve 1 and valve 2; Q_2 increases from zero to Q_{req} while Q_1 decreases from Q_{req} to zero. At the end of this mode, valve 1 switches off at zero-flowrate point.

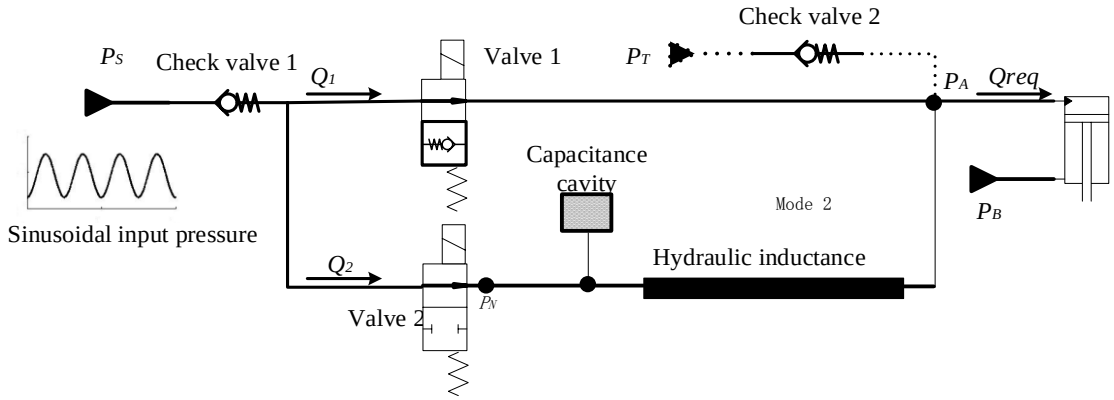

Figure 8. Mode 2 for zero-flowrate-switching controller

In mode 3(Fig. 9), Q_2 sustains increasing thus the flowrate Q_1 through valve 1 transitions to the opposite direction. To prevent the flow from going back to the source, check valve 1 is located here to separate pressures between power source and the actuation line.

In mode 4 (Fig. 10), Q_2 is reduced below Q_{req}; the flow through valve 1 stops and Q_1 becomes zero. Extra flowrate is compensated to the load through check valve 2. At the end of this mode, valve 2 switches off at zero-flowrate point and the resonator stops working.

In mode 5 (Fig. 11), both Q_1 and Q_2 are zero.

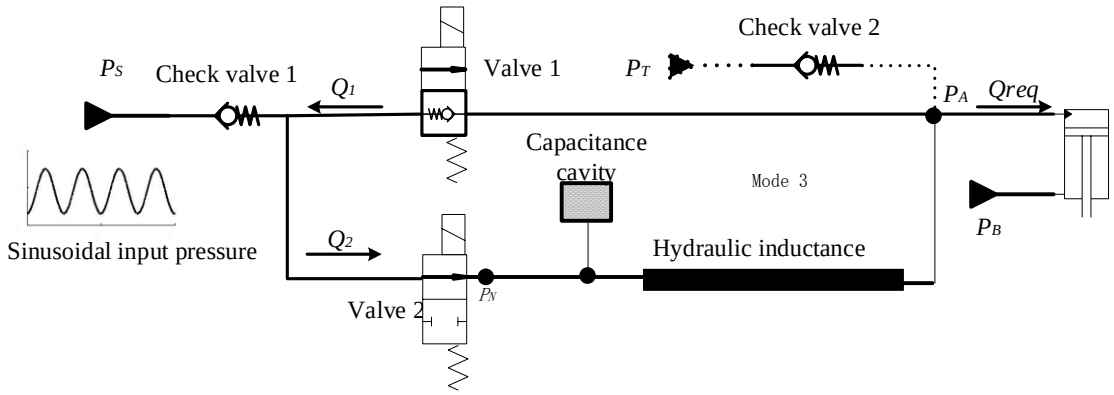

Figure 9. Mode 3 for zero-flowrate-switching controller

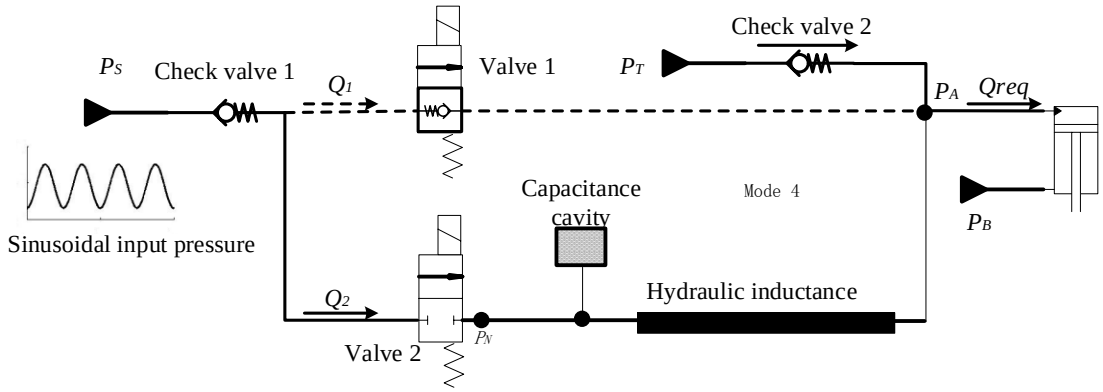

Figure 10. Mode 4 for zero-flowrate-switching controller

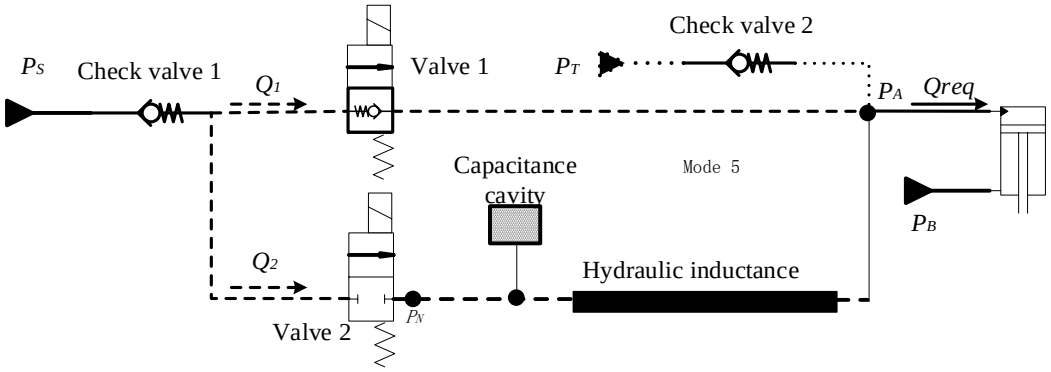

Figure 11. Mode 5 for zero-flowrate-switching controller

At the moment of t5, the system goes back to mode 1. Valve 1 switches on again at zero-flowrate point. Table 4 shows the pressure/flowrate response for the five modes.

Table 4. Pressure/flowrate response for zero-flowrate-switching controller

Mode	Input pressure	Q_1	Q_2	Output pressure
1	P_{S0}	Q_{req}	0L/min	$P_{S0} - RQ_{req}$
2	$\mathrm{P_{S0}} - \mathrm{P_{Sa}}\cos(\omega\,\mathrm{t} - \frac{\pi}{2})$	$Q_{req} - \frac{P_{sa}}{R}\sin\omega_0 t$		
3	$\mathrm{P_{S0}} - \mathrm{P_{Sa}}\cos(\omega\,\mathrm{t} - \frac{\pi}{2})$	$Q_{req} - \frac{P_{sa}}{R}\sin\omega_0 t$		
4	$P_{S0} - P_{Sa}\cos(\omega t - \frac{\pi}{2})$	0	$\frac{P_{sa}}{R}\sin\omega_0 t$	
5	NULL	0	0	P_B

5. RESULT AND ANALYSIS

Model 1 (Fig. 5) and model 2 (Fig. 6) are simulated and compared with each other. Starting/ending points for the five modes for model 2 are computed(shown in Table 5).

Table 5. Time periods for five modes

Time	Values
t1	0.02s
t2	0.0221s
t3	0.0279s
t4	0.0299s
t5	0.04s

In Fig. 12 the pressure and flowrate drops from the required value to zero right after valve 1 switches off. The power of the switching loss peaks at 158w.

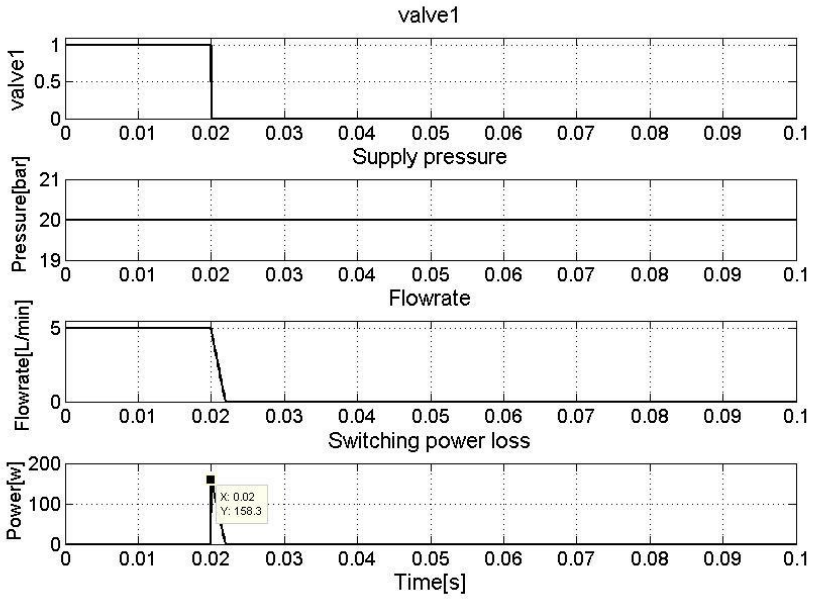

Figure 12. Pressure/flowrate in model 1

In Fig. 13, the line of resonator makes the flowrate Q_2 decreases to zero and then valve 1 switches off. The switching power loss of the valve is reduced to 1.499w. During all the modes the output pressure keeps 19.375bar and the flowrate is 5L/min.

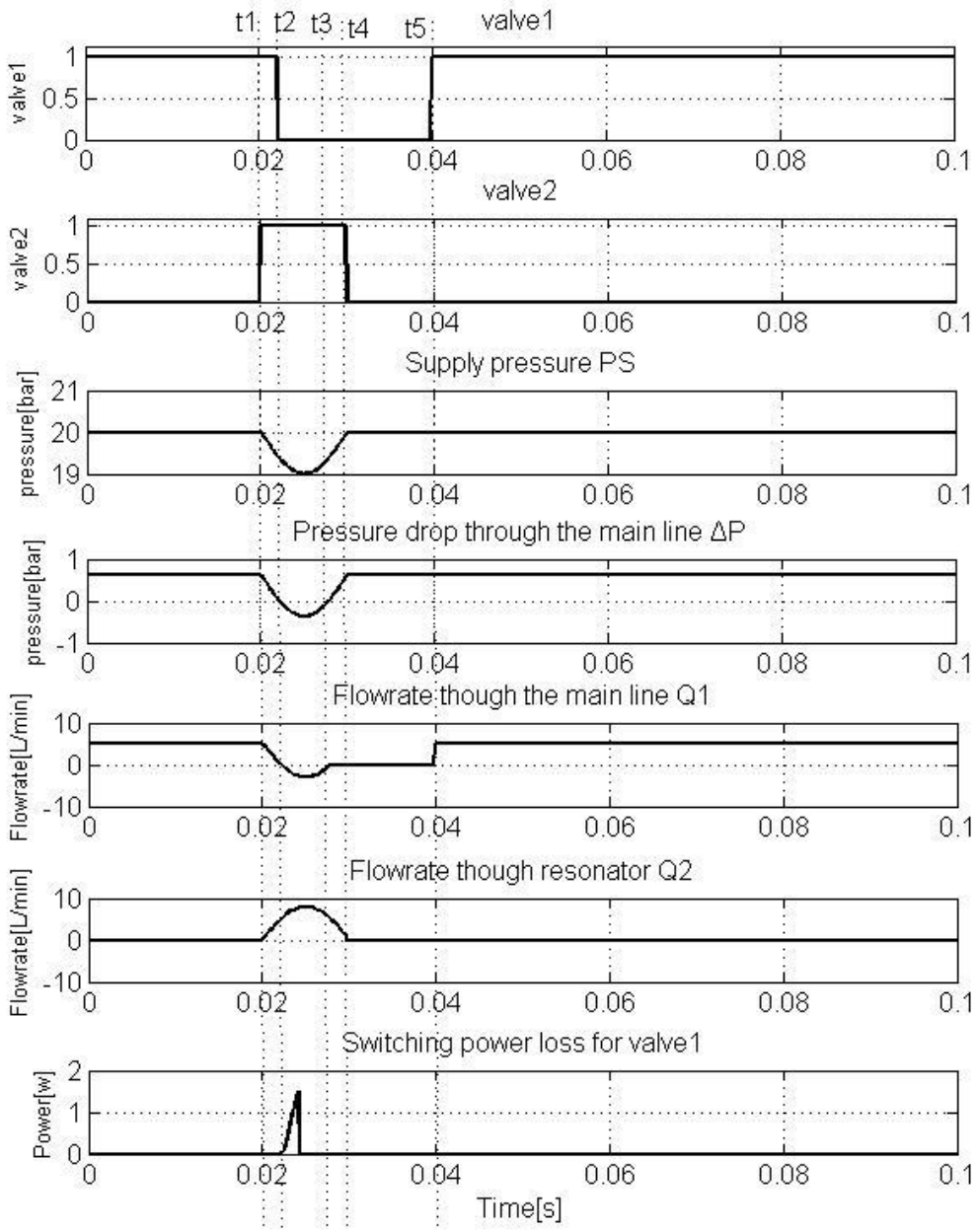

Figure 13. Pressure/flowrate response in model 2

6. SUMMARY AND OUTLOOK

This paper proposes a zero-flowrate-switching control method which aims to reduce the switching power loss of the digital valve. It employs a resonator to share part of the required flowrate and make the flowrate through the main line to fall to zero, and then switches off the valve at zero-flowrate point. By employing the zero-flowrate switching method, the output pressure and flow rate are kept constant which avoids ripples and cavitation in the system. The result shows that the new control method greatly reduces

the switching power loss. It can be a potential solution for pressure ripples and switching power loss in digital hydraulic systems.

Digital hydraulics is to replace traditional hydraulics with fast digital valves. Valves are required to be as fast as possible to achieve ideal performance while fast switching brings in pressure ripples and switching power loss. Traditional solutions like accumulator or long pipe would reduce the system efficiency. The new method is a potential solution to remove pressure ripples and greatly reduce switching power loss for PWM controlled valves.

Theoretically the piston pump output pressure waves which are very difficult to remove. This paper gives an insight that such waves can be used to remove pressure ripples and power loss during the switching of the valve. Actually the output pressure waves of the pump include several components of waves. In future solutions for hydraulic filters will be discussed.

This paper presents a zero-flowrate switching controller for a one-valve/one-direction system. In real applications the actuation system will be more complicated. The system can be a four-port digital hydraulic system, or a hydraulic buck converter. In future zero-flowrate control method will be applied to specific systems. The challenge of such applications is that potential lines should be discussed. When the value of flowrate/pressure is out of normal range, potential lines are designed to meet the requirements of the load. For example in this paper check valve 1 is to prevent the oil going back to the pump, check valve 2 is to supply extra flowrate when the total value of Q_1 and Q_2 is less then Q_{req}. The check valve inside digital valve 1 is to allow the flow going from the load to the pump direction when the value of Q_2 is higher than Q_{req}.

ACKNOWLEDGEMENT

I would like to acknowledge the contribution of Prof. Rudolf Scheidl by giving important suggestions for this new method. This work is funded by State Key Laboratory of Fluid Power and Mechatronic System, the funding number is GZKF-201520.

REFERENCES

[1] Peng. S, Branson, D., Guglielmino, E. & Caldwell, D. G. 2012. Simulated performance assessment of different digital hydraulic configurations for use on the HyQ Leg. Robotics and Biomimetics (ROBIO), Dec 11-14, Guangzhou, China, pp36-41.

[2] Yao. B. 2009. Integrated mechatronic design of precision and energy saving electro-hydraulic systems, Proceedings of the Seventh International Conference on Fluid Power Transmission and Control, April, Hangzhou, China, pp360-372.

[3] Kogler, H., Scheil, R. 2008. Two basic concepts of hydraulic switching converters, The first workshop on Digital Fluid Power, Oct 3nd, Tampere, Finland.

[4] Laamanen, A., Linjama, M. & Vilenlius, M. 2005. Pressure peak phenomenon in digital hydraulic systems – a theoretical study, Power transmission and Motion Control, Aug, Bath, UK.

[5] Kogler, H., Winkler, B. & Scheidl R. 2006. Flatness based control of a fast switching hydraulic drive, International Conference on Computational Methods in Fluid Power, Aalborg, Denmark.

[6] Linjama, M. & Vilenius, M. 2007. Digital hydraulics, toward perfect valve, The Tenth Scandinavian Conference on Fluid Power, May 21-23, Tampere, Finland.

[7] Gradl, C. & Scheidl, R. 2013. A basic study on the response dynamics of pulse-frequency controlled digital hydraulic drives, Proceedings of the ASME/BATH 2013 Symposium on Fluid Power & Motion Control, Oct. 6-9, Sarasota, Florida, USA.

[8] Kogler, H., Scheidl, R. & Schmidt B. H. 2015, Analysis of wave propagation effects in transmission lines due to digital valve switching, Proceedings of Bath/ASME Symposium on Fluid Power & Motion Control, Oct. 12-14, Chicago, Illinois, USA.

[9] Haas, R., Lukachev, E. & Scheidl, R. 2015, An RC filter for hydraulic switching control with a transmission line between valves actuator, Internationa Fluid Power, Vol. 15, No. 3, pp139-151.

[10] Scheidl, R., Schindler, D., Rila, G. & Leitner, W. 1995, Basics for the energy-efficient control of hydraulic drive by switching techniques, Third Conference on Mechatronics and Robotics, Oct. 4-6, Paderborn, Germany, pp 118-131.

DURABILITY STUDY ON HIGH SPEED WATER HYDRAULIC MINIATURE ON/OFF-VALVE

Miika Paloniitty, Matti Linjama and Kalevi Huhtala

ABSTRACT

Digital hydraulic approach that uses an array of equal valves to realize digital control edges is a promising technology that has been proposed to realize a high performance water hydraulic servo control. Recently developed water compliant miniature on/off valve, which is a key component in the technology, has faced a durability problem. In this paper, two different plunger design, diamond-like-carbon coating and three different heat treatment processes have been studied in order to improve the durability of the prototype valve. The main hardening method is the laser hardening. The supporting treatment stages are temper hardening and cold treatment. Different combinations of those are studied. The modified plunger design has narrow regions in order to absorb the shock forces. A million opening cycles have been conducted with each studied valve. Results show that the durability of any studied valve did not satisfied the target. However, the study gave the direction for the future development work.

KEYWORDS: Water hydraulics, digital hydraulics, durability, fast on/off valve

1. INTRODUCTION

Water as a pressure medium offers some unique benefits for hydraulic systems being clean, non-pollution and fireproof alternative for oil based mediums. However, water is quite challenging pressure medium due to its physical properties. Low viscosity, poor lubricating properties and corrosive nature of water makes the design of high performance control valves challenging. Digital hydraulic valve technology offers solutions to overcome the challenges that are raised from the water characteristics. Digital hydraulic approach is based on the on/off valves which are robust, can be leak tight and cheap to manufacture.

There are two main approaches to implement digital hydraulic valve control; switching method and parallel connection method. In switching method, the output is controlled by the duty cycle. In the parallel connection method, the output is controlled by the sum flow of opened valves. Both have their own benefits and drawbacks. In TUT, parallel connection technology is mainly studied. Recently, the approach that uses only one size on/off valves (equal coding) has been in the focus [1] [2] [3]. That approach has unique benefits compared with other solutions. Due to the similarity of all valves, the control is

simple, the duty of valves can be equalized and the fault tolerance can be excellent. The opening state is determined by the number of opened valves. The equal coded approach can be regarded as a technology between the switching approach and parallel connection approach since this coding method enables parallel connected switching control.

A recently developed high speed on/off valve for equal coded digital water hydraulics (Figure 1) has faced a durability problem. The following chapters explain the durability problem, the methods to enhance the durability as well as the experimental study with different plungers.

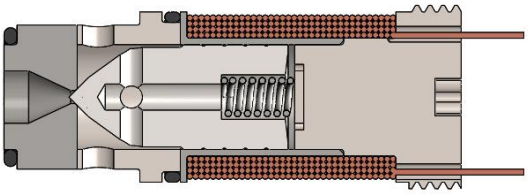

Figure 1. Structure of recently developed water hydraulic digital valve. The diameter of the solenoid is 13 mm.

2. FUNDAMENTAL DURABILITY ISSUE

With a brief inspection, it can be shown that there is a fundamental durability issue in this type of seat valves. For a fixed pressure level and orifice diameter, the pressure force that the solenoid should overcome can be calculated as:

$$F = pA_{orif}. \tag{1}$$

In the view of [4], the maximum force of the solenoid can be estimated with the simplified maxwell's equation which can be written as:

$$F_m = \frac{B^2 A_{core}}{2\mu_0}, \tag{2}$$

where B is a magnetic flux density, μ_0 is the vacuum permeability and A_{core} is the cross-sectional area of the plunger. Neglecting the spring force, F_m should equal F. Thus, substituting F for F_m and solving the relation between A_{core} and A_{orif}, we obtain:

$$R = \frac{A_{core}}{A_{orif}} = \frac{2p\mu_0}{B^2}. \tag{3}$$

It can be seen that R is determined by the design pressure and the magnetic flux density. Neither of them can be freely selected. While the valve is designed for generic use in hydraulic systems, the pressure level should achieve at least 21 MPa. The maximum magnetic flux density of a ferromagnetic material is basically the saturation flux density which is a property of a material. That can be fairly used for B when estimating the maximum force. Pure iron has quite high saturation flux density of 2.2 T but corrodes easily and cannot be used with water. All the stainless steels are not ferromagnetic at

all; however, stainless steels with a relatively high saturation flux density of about 1.7 T can be found. Thus, the minimum of R in water hydraulic valve is constantly about 18.

The relation R is an essential quantity for the durability properties of the valve. Assuming constant length plunger, A_{core} determines the weight of it. Assuming constant geometry of the seat, A_{orif} determines the contact area of the seat. Further, assuming constant contact dynamics, the relation between the weight and the contact area (now R) determines the contact pressures which are responsible for the wearing of the contact surfaces.

Now we can see that there is only one obvious way to improve the durability; to improve the durability properties of the seat and plunger materials. That can be done at least in three ways; by quenching or coating the parts in order to achieve harder surfaces or by changing the material. The change of the material is easier for the seat than for the plunger because the plunger is required to satisfy also magnetic properties. The change of the material only in the plunger tip is possible but that may lead to higher price.

Other methods to enhance the durability are to influence to the contact dynamics or to increase the contact area. By changing the plunger tip geometry to more elastic, the contact forces and pressures may decrease. Increasing the contact area also decrease the contact pressure but is somewhat questionable. There are outer and inner diameters in the contact. The inner diameter equals the diameter of the flow path (orifice). The outer diameter depends on the inner diameter and the size of the chamfer. The chamfer also determines the contact area. One open question is that which diameter should be used to calculate the pressure force. There is some pressure gradient in the contact area and the diameter of the effective sealing is something between those geometric diameters. The worst case can be calculated according to the outer diameter. In this case the chamfer should be increased inwards since the pressure force is not allowed to increase. This means that the inner diameter (orifice diameter) should be decreased and consequently the flow rate of the valve is decreased.

3. IMPROVING DURABILITY OF THE PLUNGER

3.1. Plunger geometry

The geometry of the plunger tip is changed to more elastic in order to achieve softer contact. The geometries of the original plunger and the *elastic plunger* are shown in Figure 2. Simplified analytical spring mass models are also presented in the figure.

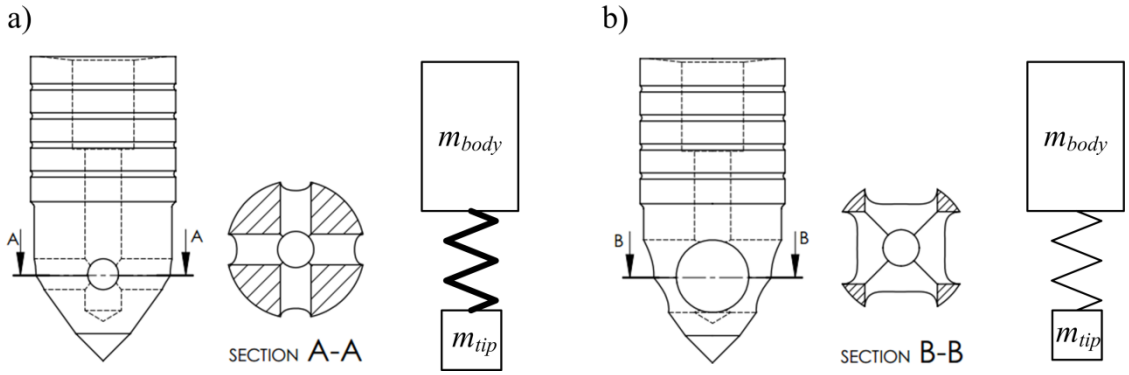

Figure 2. Geometries of the original (a) and elastic (b) plungers and corresponding spring mass models.

The only change is a diameter of the radial holes. There is significant reduction in the cross-sectional area of the plunger in the place where the radial holes are. When the diameter of the radial holes is increased, the cross-sectional area is further reduced in this region. In the analytical model, the narrow region of the cross-section is modelled as a spring and regions above and below that as mass. Thus, it is assumed that only the narrow region is elastic.

The contact forces are estimated analytically based on the kinetic energy of the plunger body and the potential energy of a spring which can be written as:

$$E_k = \frac{1}{2} m_{body} v_0^2$$
$$E_s = \frac{1}{2} k x^2, \qquad (4)$$

where m_{body} is the mass of the plunger body, v_0 is the hit velocity of the plunger, k is the spring constant of the plunger tip and x is the displacement of the spring. The plunger is assumed to hit the seat in the velocity of one meter per second. The contact force caused by the mass of the plunger tip is neglected. The spring constants and masses of the plungers are derived from CAD model, the first mentioned with FEM analysis. The maximum contact force is deduced as the spring force when all the kinetic energy is transformed to the spring potential energy. Thus, the maximum spring displacement and the maximum spring force can be calculated as:

$$x_{\max} = \sqrt{\frac{m_{body} v_0^2}{k}}$$
$$F_{\max} = k x_{\max}. \qquad (5)$$

The initial values as well as the results are gathered by table 1.

Table 1. Initial values and calculated displacements and forces

	Original plunger	Elastic plunger
v_0	1 m/s	1 m/s
m_{body}	3.9 g	3.5 g
k	420 N/µm	38 N/µm
x_{max}	3.0 µm	9.6 µm
F_{max}	1260 N	360 N

3.2. Plunger tip hardening

Since the plunger is made from modified AISI420 martensitic stainless steel (Uddeholm Stavax), it can be hardened by heat treatment processes. Unfortunately, the hardening process effects on the magnetic properties of the material [5]. Therefore, only the needle tip should be hardened. That can be conducted at least by two methods; by induction hardening or by laser hardening.

Induction hardening is a method where the needle tip is heated rapidly by eddy currents which are produced by an inductor coil. Heating is followed by a rapid cooling with a cooling liquid. In laser hardening process the surface of the needle tip is heated very rapidly by laser beam. Once the desired temperature is reached, the beam is shut off and the surface is cooled down by the surrounding material. The cooling process is called self-quenching as there is no need for cooling medium. [6]

The original needle tip was hardened by induction hardening followed by tempering twice in the temperature of 200 °C. The achieved hardness was about 650 HV. The laser hardening was expected to achieve even higher hardness and better wear resistance.

The laser hardening process was selected in this study as the hardening method for the new plungers. The reasons were high wear resistance, small requirement for after processing and its great suitability for automation.

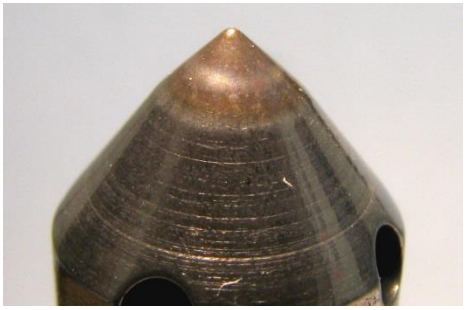

Figure 3. Plunger tip after laser hardening. The colour has changed on the heated region.

3.3. Supporting heat treatment processes

Temper hardening before laser hardening was used for some plungers. It means a hardening process where the parts are quenched and tempered. In this case, tempering was conducted at 600 °C in order to retain the magnetic properties of AISI 420. The

objective of the temper hardening is to offer better starting point for the laser hardening aiming to achieve better wearing properties.

Cold treatment in -80 °C was also used in order to improve the wear resistance. In the view of [7], the definition of the cold treatment is:

"Cold treatment of steel consists of exposing the ferrous material to subzero temperatures to either impart or enhance specific conditions or properties of the material. Increased strength, greater dimensional or microstructural stability, improved wear resistance, and relief of residual stress are among the benefits of the cold treatment of steel."

3.4. Plunger tip coating

There are various coating processes for construction parts. Using coatings in hydraulic valves is twofold. The coatings offer a method to realize very high hardness value in the thin layer on the coated surface. The drawback is that the majority of the anti-wearing properties may lie on the thin coating and if it is damaged for some reason, the valve will wear out quickly. There is also a risk for peeling.

However, one coating type was decided to be tested in this study. Diamond like carbon coating is one coating type which is previously used for water hydraulic valve parts [8]. Thus, it was chosen for this study.

4. EXPERIMENTAL DURABILITY STUDY

4.1. Studied cases

The original plan was to study the durability of ten different plungers. All the seats were similar and with similar heat treatment (vacuum hardening with cold treatment, 520 HV). In order to get clear results from the geometry change, half of the plungers were elastic design. Different hardening processes were conducted always for both the original plunger and the elastic plunger. Thus we had five plunger pairs for different hardening processes. The hardening processes of the pairs were

1. plain laser hardening,
2. laser hardening followed by cold treatment,
3. laser hardening preceded by temper hardening,
4. laser hardening preceded by temper hardening and followed by cold treatment,
5. laser hardening preceded by temper hardening and followed by diamond like carbon coating.

The plan was little changed during the study because the results did not show notable advantages from the supporting heat treatment processes. The pair 3 was expected to show similar results with the pairs 1, 2 and 4, and therefore was decided to be tested with larger chamfer in the seats. The depth of the original chamfer was 0.15 yielding the

outer diameter of 1.3 mm. The increased chamfer depth was 0.25 mm yielding the outer diameter of 1.5 mm.

4.2. Test setup and procedure

Before durability tests, the oxidation on the plunger tip and body were removed with a citric acid bath and the plungers were polished. Seven first tests were carried out with the same coil assembly. However, it was changed to the last three tests because some wearing was observed. The same spring and the sleeve were used throughout the experiment.

The durability tests were carried out with a Nessie water hydraulic power unit. The used pressure level was 14 MPa which was the maximum pressure of the unit. Water temperature was kept at about 30 °C. The durability of each plunger-seat pair was tested by conducting a million opening cycles. The switching frequency was 80 Hz with the pulse length of 6 ms for the plunger-seat pairs with the original chamfer. The frequency had to be reduced to 40 Hz for the pairs with the increased chamfer size because the power electronics required longer time to accumulate the energy for the switching against the increased pressure force.

The length of the airgaps was measured before the tests. Due to the producing inaccuracy, there was variation in that length. In the case of too high deviation, some additional machining was conducted. After corrections the airgaps were between 0.52 and 0.57 mm.

The amount of wear was estimated by measuring the length of the plunger seat pairs before and after the test and by a visual inspection with a microscope. The opening energy was estimated from the minimum capacitor voltage which could open the valve. The estimate was used to compare the original chamfer with the increased chamfer.

5. EXPERIMENTAL RESULTS

All the plungers (and seats) showed notable wearing after a million opening cycles. The measured wearing was between 0.01 mm and 0.06 mm; however, when the wearing was one-sided, the measured value diminished the amount of wearing.

The best durability was observed in the coated plunger with the original design (Figure 4). Nevertheless, the coating was slightly damaged both on the plunger and on the seat. The elastic counterpart of the coated plunger was damaged much more, even though it is not seen on the measure.

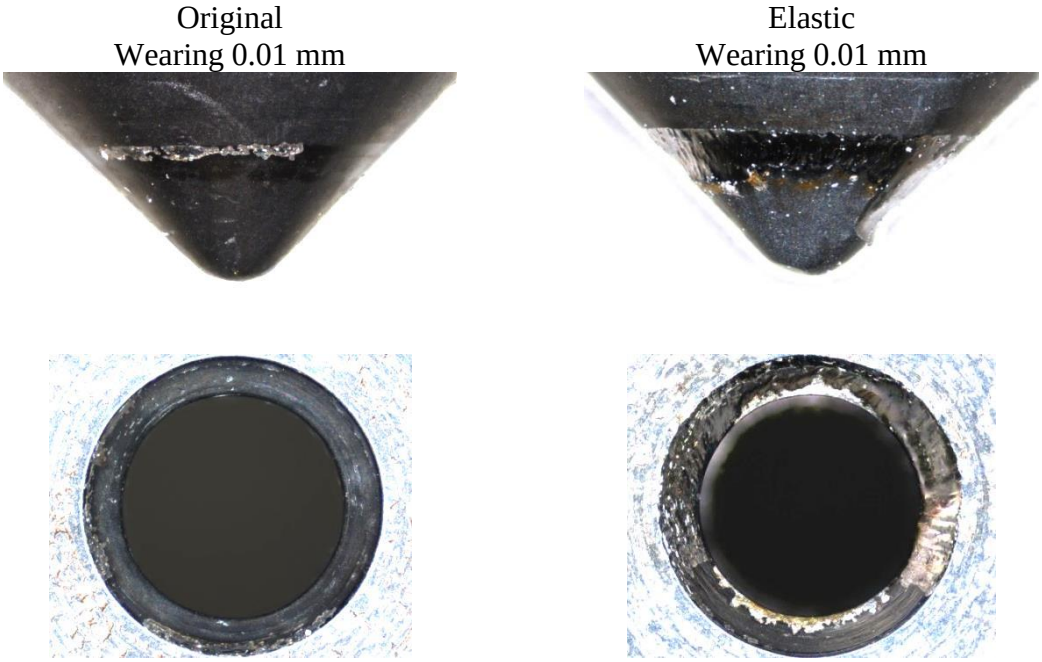

Figure 4. Plunger pair with diamond like carbon coating showing best durability with the original design.

Both plungers that were tested with larger seat chamfers showed also quite small wearing (Figure 5). However, the phenomenon called cold welding seemed to appear in these plunger-seat pairs, more clearly with the elastic plunger.

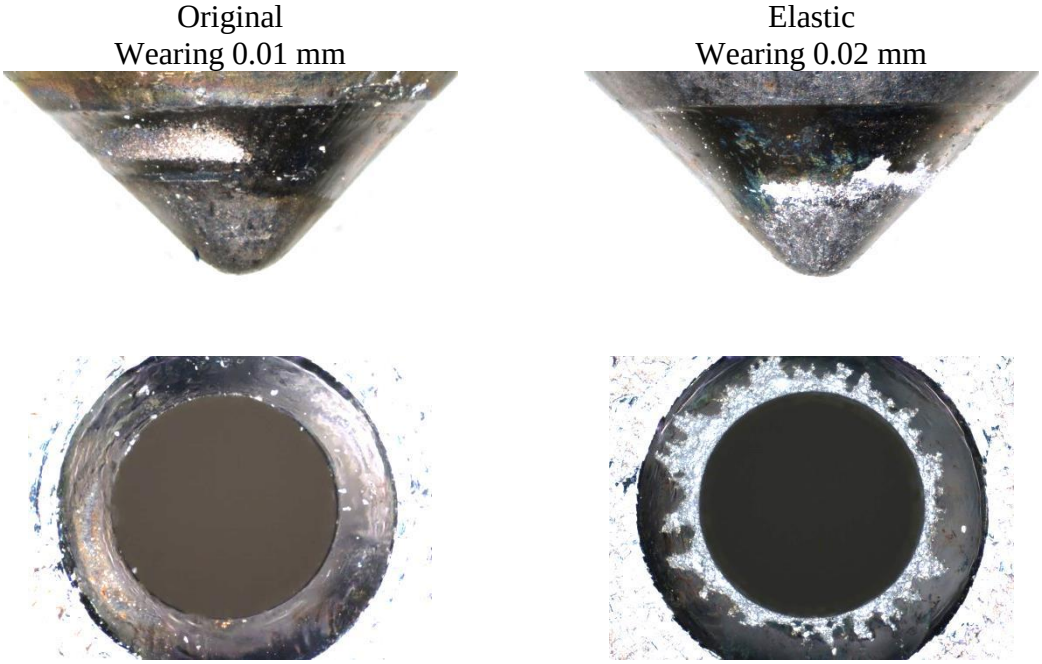

Figure 5. Plunger pair tested with the seats having larger chamfer. Rough surface of cold welded regions has drawn nice shape on the seat of the elastic plunger.

The plungers that were tested with the original seat geometry and without coating showed all significant wearing. In all cases the wearing appeared both in the plunger and in the seat. Supporting heat treatment processes showed not clear advantage to the

plunger durability. Plungers with all the heat treatment processes (Figure 6) showed similar level of wearing than the plungers with plain laser hardening (Figure 7). However, in both cases the elastic plunger has worn the seat more, staying itself less worn. Clear difference between these cases is the shape of wearing in the original design plungers: the plunger with plain laser hardening is worn uniformly and the other one-sidedly.

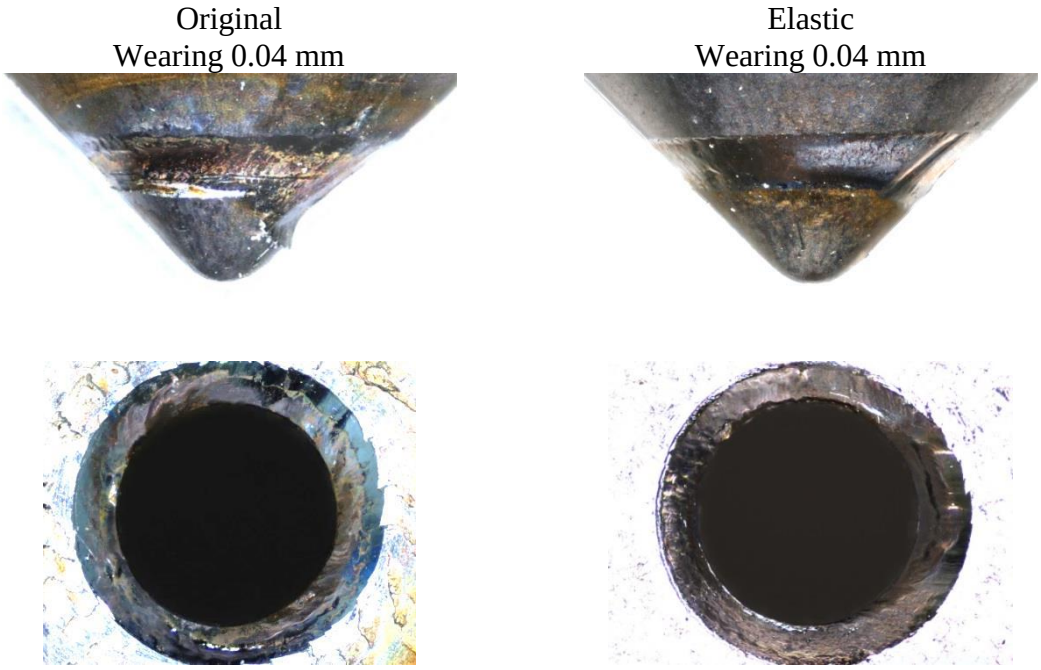

Figure 6. Plunger pair with laser hardening preceded by temper hardening and followed by cold treatment. Original design plunger showed worse wearing.

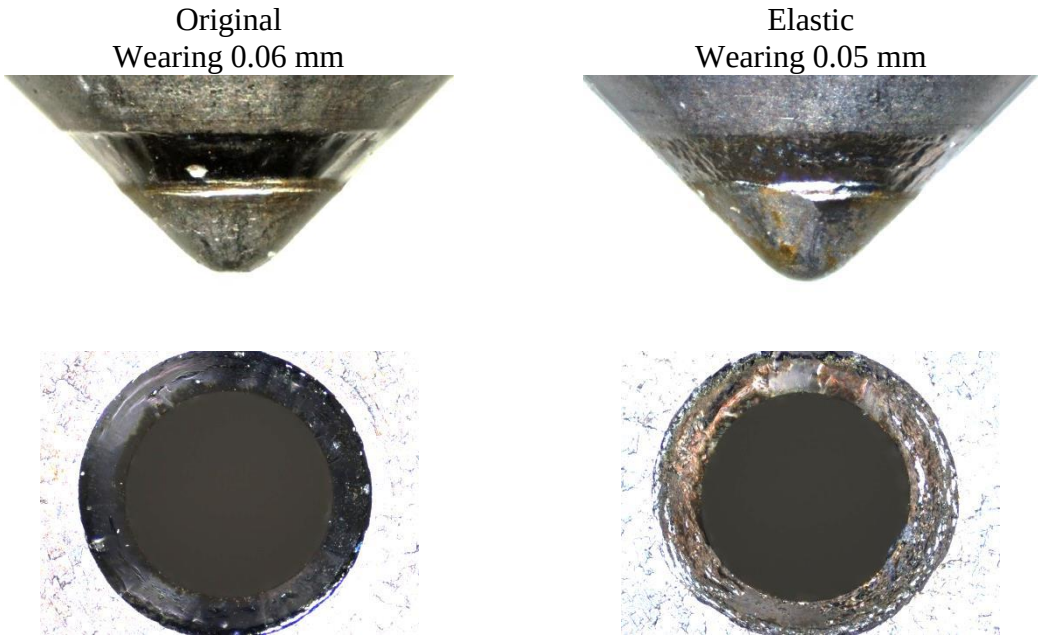

Figure 7. Plunger pair with plain laser hardening.

The elastic plunger of the pair with laser hardening and cold treatment broke before 260 000 cycles (Figure 8). The original plunger reached a million cycles. The wearing of the original plunger is strongly one-sided.

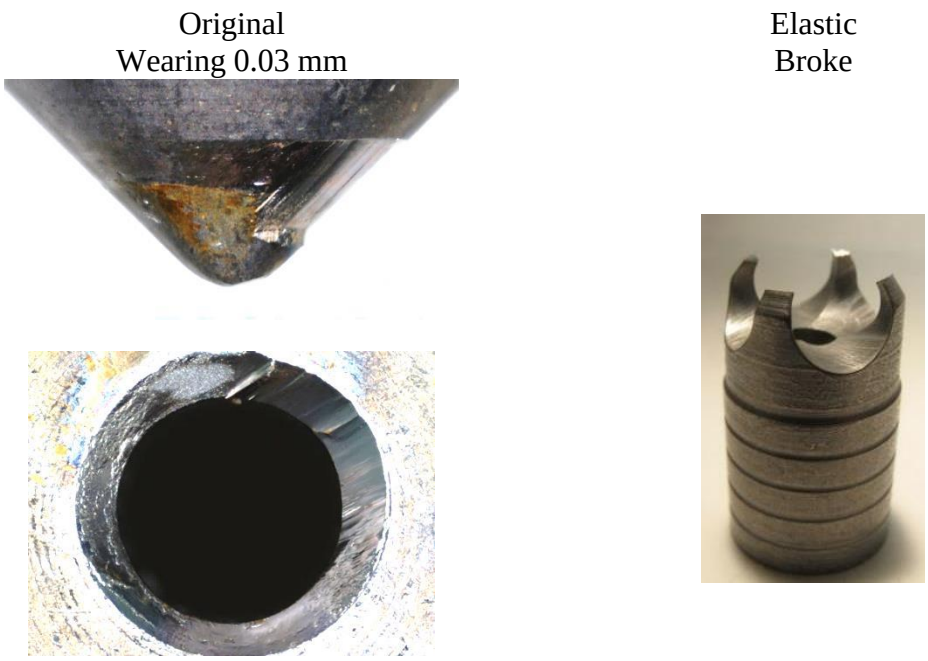

Figure 8. Pair 2: laser hardening followed by cold treatment

The measured opening energies of the valves with the original chamfer were around 76 mJ while the opening energies of the valves with larger chamfer were around 114 mJ. The increase in total area was 33 %, thus the opening energy increased more than the total area.

6. DISCUSSION

Diamond like carbon coated plunger showed best results like expected. However, unexpectedly the elastic design plunger broke the coating worse both on the plunger tip and on the seat. The coating of both the plunger and the seat broke the principle where there should be hardness difference between the contact pair in order to reduce wearing. The seats were still decided to be coated resulting in damaged coatings.

Larger chamfer in the seat proved to be effective way to reduce the wearing. The drawback is the increased pressure force and consequently increased opening energy. The measured opening energies indicated that the pressure force can be estimated using the outer diameter of the chamfer. Thus, the chamfer should be increased only inwards if the pressure level of the valve is kept constant. That can be done only by decreasing the diameter of the orifice resulting in reduced flow rate. Therefore this method is not recommended.

One-sided wearing seems to be a problem in the valve. That indicates the clearance of the plunger to be too large. The one-sided wearing did not stopped by changing the coil assembly to the new one. Thus, the clearance seems to be too large initially.

Cold welding arose in this study as a new issue in the prototype valve. It is known that stainless steels have quite high tendency to cold welding. That should be taken into account with the next design and research possibilities to avoid it.

7. CONCLUSION

The conducted durability study confirmed that there is a fundamental durability issue in the high speed water hydraulic seat valve. The study also revealed that there is no "easy" way to avoid the durability problem. Not even elastic plunger design offered clear advantage since it seemed to wear the seat more than the original plunger design. However, this study gave important information for the next design, where the durability of the plunger tip and the seat should be taken carefully into account from the beginning. One key may be a better guidance for the plunger in order to achieve better alignment of plunger and seat.

REFERENCES

[1] Paloniitty, M., Linjama M. and Huhtala K., 2014. Concept of Digital Microhydraulic Valve System Utilising Lamination Technology. Proceedings of 9th International Fluid Power Conference (9. IFK), Vol 1, pp. 302-313. Aachen.

[2] Paloniitty, M., Linjama M. and Huhtala K., 2015. Equal Coded Digital Hydraulic Valve System – Improving Tracking Control with Pulse Frequency Modulation. Procedia Engineering, Vol. 106, pp. 83-91.

[3] Linjama, M., Huova, M., Karhu, O. and Huhtala, K., 2016. High-Performance Digital Hydraulic Tracking Control of a Mobile Boom Mockup. Proceedings of 10th International Fluid Power Conference (10. IFK). Vol. 1, pp. 37-48. Dresden

[4] Meisel, Jerome. 2014. Electromagnet. AccessScience. McGraw-Hill Education.

[5] Tavares, S.S.M., Fruchart D., Miraglia S. and Laborie D., 2000. Magnetic properties of an AISI 420 martensitic stainless steel. Journal of Alloys and Compounds, Vol. 312(1-2), pp. 307-314.

[6] Ion, John C. Laser Processing of Engineering Materials. Elsevier Butterworth-Heinemann, 2005.

[7] Carlson, E.A. Heat Treating. ASM Handbook. ASM International, 1991, Vol. 4, pp. 203-206.

[8] Majdič, F., Velkavrh, I. and Kalin, M., 2013. Improving the performance of a proportional 4/3 water-hydraulic valve by using a diamond-like-carbon coating. Wear, Vol. 297(1), pp. 1016-1024.

VALVE AND MANIFOLD CONSIDERATIONS FOR EFFICIENT DIGITAL HYDRAULIC MACHINES

Daniel B. Roemer, Christian Noergaard, Michael M. Bech, Per Johansen
Department of Energy Technology
Aalborg University
Pontoppidanstraede 111, 9220 Aalborg East, Denmark
E-mail: dbr@et.aau.dk, chn@et.aau.dk, mmb@et.aau.dk, pjo@et.aau.dk

ABSTRACT

This paper seeks to shed light on the topic of design and sizing of switching valves and connecting manifolds found in large digital hydraulic motors, also known commercially as Digital Displacement Motors. These motors promise very high operation efficiencies with broad operation ranges, which set strict requirements to the switching valves and the overall manifold design. To investigate this topic, the largest known digital motor (3.5 megawatt) is studied using models and optimization. Based on the limited information available about this motor, a detailed reconstruction of the motor architecture is developed in CAD. This reconstruction is used to estimate the manifold flow losses of the complete motor with a quasi-static model, where all pressure chambers are simulated simultaneously. The pressure losses for the low and high pressure manifold are found to be small compared to the manifold pressure levels. A simplified flow model of the manifolds is established, and this result is carried on to the second study of the paper. In this second study, focus is turned towards switching valve sizing and actuator requirements. A single chamber model is developed, suitable for optimization of the switching valves when considering also the manifold flow losses.

A global optimization is conducted by use of the generalized differential evolution 3 algorithm, where the valve diameters, valve stroke lengths, actuator force capabilities and actuator timing signals are used as design variables. The results of this optimization confirm that high efficiencies in a broad operation range is possible, and gives the optimum valve sizes and actuator specifications for the reconstructed 3.5 MW motor simulated. Comments are made on these findings in relation to valve implementation.

KEYWORDS: Digital Displacement, Valves, Manifold design, optimization

1 INTRODUCTION

The so-called digital hydraulic machines, also known commercially as Digital Displacement (R) machines offers improved efficiency compared to traditional variable displacement machines used in fluid power systems. Electronic fast switching on/off valves are

used to enable and disable each individual pressure chamber, resulting in variable displacement control. Efficiencies well above 90% in a broad operation range has been reported by the leading company Artemis Intelligent Power [1]. To obtain these high efficiencies, focus must be put on minimizing all aspects of energy losses, including throttling losses of the switching valves, throttling losses in the manifolds and losses in the valve actuators.

The principle of present digital motors and their valve operation is shown in figure 1. The valves are opened by pressure forces and closed actively using electronic actuators. These actuators may be relatively small and weak, as the valves are closed during times of small pressure differential [2]. The valves may be kept open by springs, and in this case, idling is performed without actuator losses.

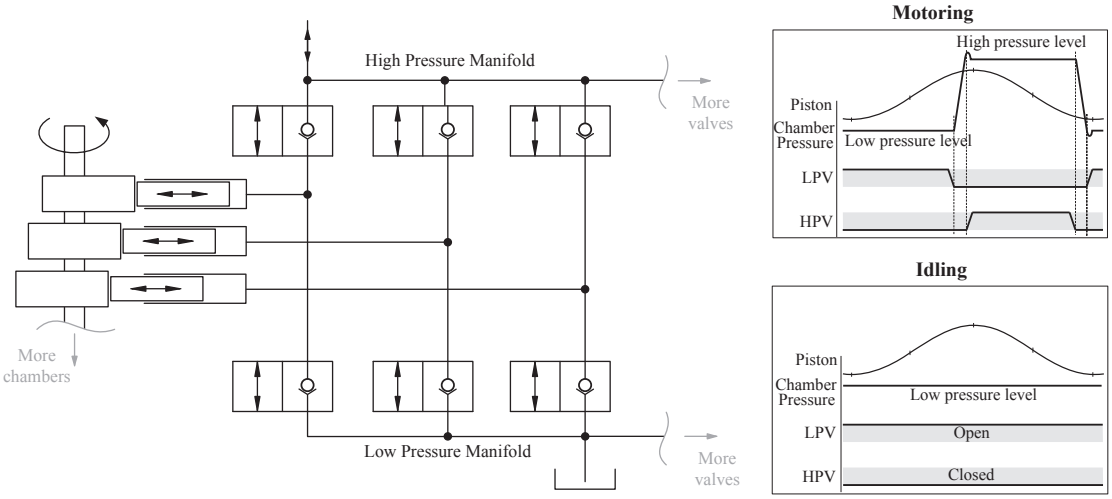

Figure 1: Working principle of digital motors. The Low Pressure Valve (LPV) and the High Pressure Valve (HPV) is controlled to obtain the motoring operation cycles illustrated.

The valves used in large capacity motors are typically annular in shape, leading to two flow edges [3, 4]. This design makes it possible to obtain large opening areas without excessive pressure shadow areas and associated pressure forces. Present designs incorporate the valves close to the pressure chamber itself to reduce the flow path and create compact machines. For optimum design, the opening area of the annular valves, and their sizes in general, must be selected when also considering the manifold throttling losses. Excessive valve sizes lead to less compact machines and increases the needed actuator power, without reducing the valve throttling losses accordingly. If only 1 % of the throttling loss is generated at the valves and 99 % at the manifold, surely a better compromise could be found by decreasing the valve sizes.

A model of the manifold flow losses would make it possible to include the manifold flow losses into a valve sizing optimization, leading to knowledge of the most suitable compromise between manifold flow losses and valve flow losses. This paper targets to develop such combined valve optimization the shed light on this aspect of efficient digital motor design.

In this paper, a state of the art digital motor is described and its architecture is reconstructed to allow analysis. The manifold design of such machine is described, and a manifold flow loss model is developed by considering the manifold to be a combination of simple flow problems where approximate solutions exist. The manifold losses are

simulated, and the manifold design is found to enable highly efficient machines. A simple approximation of the manifold model is hereafter utilized in a single chamber model, which is subject for valve sizing optimization. The optimization results are presented and the tendencies are discussed.

2 State of the art Digital Hydraulic Motor

In this section a brief description of the largest digital motor is given, where focus is put on the manifold architecture.

3.5 MW motor

The largest digital motor made, by far, is used as part of a 7 MW wind turbine drive train. The drive train consists of one large, slow rotating, digital pump and two digital motors connected to synchronous generators operating at 1000 [5]. This large scale hydraulic transmission system was constructed in 2013 by Mitsubishi Heavy Industries (owner of Artemis Intelligent Power). An overview of the drive train is shown in figure 2. The following discussion focuses on the fast rotating motors.

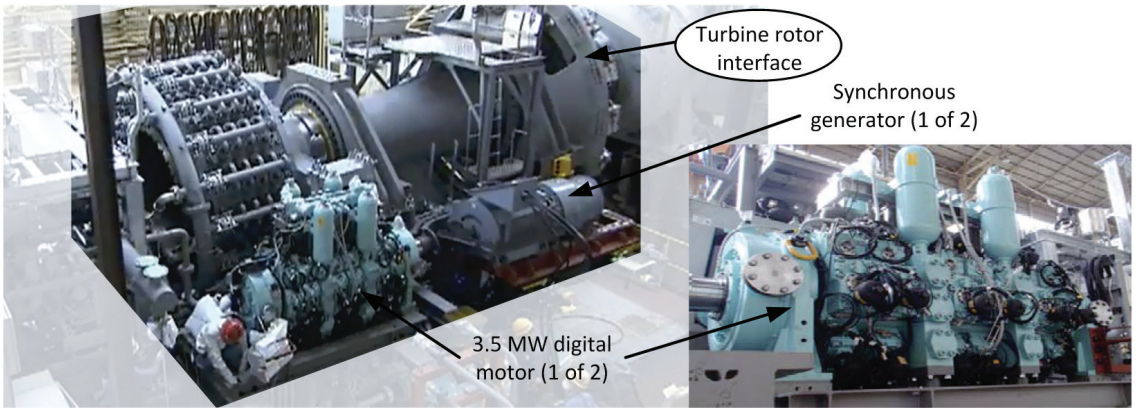

Figure 2: 7 MW wind turbine drive train using a large scale digital hydraulic pump and two digital motors [6].

The motors have a massive displacement of approximately 6800 cc and are capable of operating at 350 bar at a speed of 1000 rpm. Each motor consists of 36 pistons with two independent electronic valves connected to each pressure chamber. According to Mitsubishi, the maximum efficiency of the motors is 96 percent. Some details about the drive train have been disclosed is [5], but information about valve sizing and manifolds remain unknown. However, based on the pictures and information available, the authors have made a reconstruction of the 3.5 MW motor in order to study the manifold design, valve integration and valve sizing of such a state of the art machine.

This reconstruction is shown in figure 3. The motor is made up of six banks of radial pistons acting on a common shaft, each bank with six pistons. The low pressure manifold connects to oil return at the locations marked in blue, and the high pressure oil supply is connected at below the motor at the red locations. Relatively large accumulators are connected to the high pressure manifold, while small accumulators are connected to the low pressure manifold close to the pressure chambers.

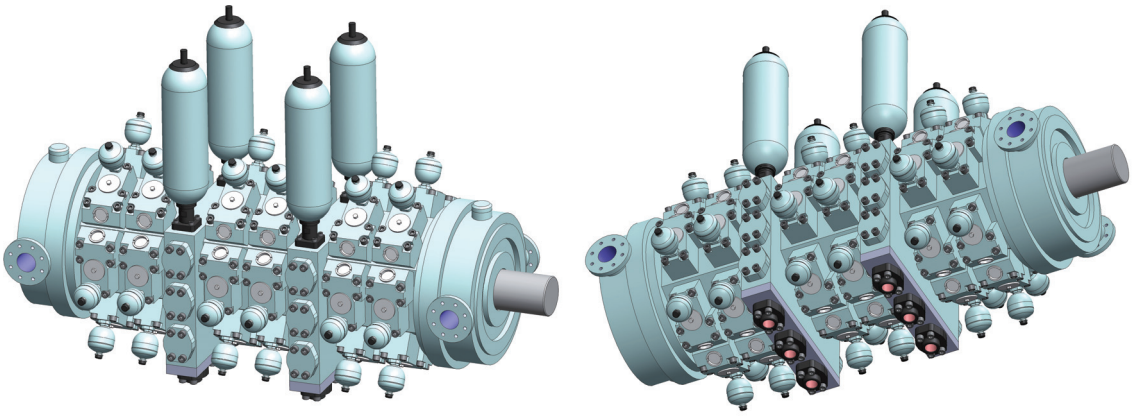

Figure 3: Reconstructed 3.5 MW motor seen from a top and a bottom view.

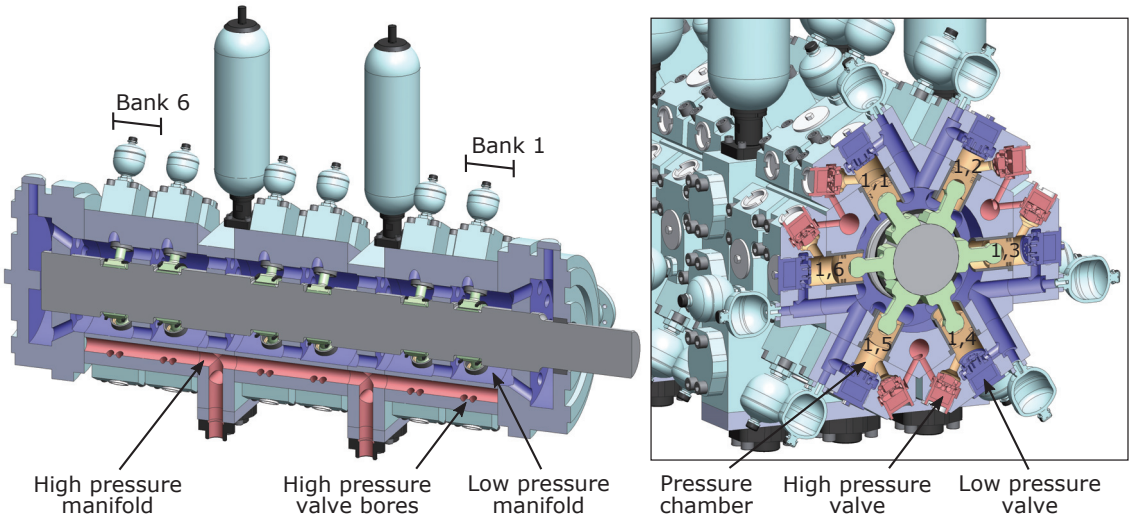

Figure 4: Internal views of the reconstructed motor. Low pressure (blue), high pressure (red) and pressure chamber regions (orange) are marked.

Internal views of the reconstructed motor are shown in figure 4. The high pressure supply is distributed through three axial bores running the entire length of the banks. The low pressure manifold surrounds the crankshaft and is thereby generously sized, and ensures a short flow path from each pressure chamber. The two electronic valves connecting each pressure chamber to the high and low pressure manifold are located close to the piston. Relatively small low pressure accumulators are located at each pressure chamber with a short flow path to the low pressure valve, which may be necessary to avoid chamber cavitation with low pressures of only 3-5 bars [5].

In generating the reconstructed geometry, the authors have performed a number of qualified guesses. The actual 3.5 machine will differ to some degree from the reconstruction, and the reconstruction should be seen as an example of how such a large scale digital machine could be designed. The remainder of the paper focuses on investigating manifold losses and valve sizing of the reconstructed 3.5 MW motor, to shed light on the these aspects of state of the art digital motors.

3 Manifold flow loss model

A simple method is used to estimate the manifold flow losses in a geometry as presented in figure 4. Ideal valves are assumed during motoring action of all chambers, such that oil flow during intake (piston movement from TDC to BDC) is conducted through the high pressure manifold and oil flow during discharge (piston movement from BDC to TDC) is conducted through the low pressure manifold. All of the 36 piston displacements are simulated, and the accumulated flows from neighbouring pistons are thus considered.

Assuming sinusoidal piston movement of each piston, $x_p = r_e(1+cos(\theta))$, the flow may be described as:

$$\mathbf{Q} = -A_p r_e \dot{\theta} \sin(\theta + \mathbf{B}) \quad \text{where} \quad \mathbf{B}_{6\times 6} = \begin{pmatrix} 0 & 60 & 120 & 180 & 240 & 300 \\ -10 & 50 & 110 & 170 & 230 & 290 \\ -20 & 40 & 100 & 160 & 220 & 280 \\ -30 & 30 & 90 & 150 & 210 & 270 \\ -40 & 20 & 80 & 140 & 200 & 260 \\ -50 & 10 & 70 & 130 & 190 & 250 \end{pmatrix} deg \tag{1}$$

where r_e is the eccentricity radius, A_p the piston area, θ the shaft angle and $\dot{\theta}$ the rotation speed. The first row of Q describes the flows of piston bank one, row two the flows of bank two and so forth. Each bank is shifted 10 deg to distribute the combined flow from all of the pistons. As such, a new piston reaches TDC for every 10 deg of shaft rotation. The high pressure and low pressure flows for each chamber is thus defines as,

$$QH_{i,j} = \begin{cases} Q_{i,j}, & \theta + B_{i,j} < \pi \\ 0, & \text{else} \end{cases} \qquad QL_{i,j} = \begin{cases} Q_{i,j}, & \theta + B_{i,j} > \pi \\ 0, & \text{else} \end{cases} \tag{2}$$

with $\theta \in [0; 2\pi[$. What remains is to describe the pressure loss of each pressure chamber as a function of the flows, that is $\Delta pH(\mathbf{QH})$ and $\Delta pL(\mathbf{QL})$. These pressure losses are calculated by considering the flow paths to be a combination of straight circular bores, bends, inflows, outflows and flows past perpendicular bores. The pressure loss of straight circular bores is calculated using [7]:

$$\Delta p = \frac{\lambda L \rho}{2DA^2} Q^2 \text{sign}(Q) \quad \text{with} \quad \lambda = \begin{cases} 64/Re, & \text{Re}<2300 \\ 0.316/Re^{0.25}, & \text{else} \end{cases} \tag{3}$$

where L is the length of the bore, ρ the oil density, D the bore diameter and A the bore cross sectional area. Reynolds number is found using $Re = \frac{|Q|D}{A\nu}$, with ν being the kinematic viscosity of the oil.

The pressure loss of the other flow situations may be estimated when knowing the geometry and the flow velocity V [7],

$$\Delta p = \xi \frac{\rho}{2} V^2 = \xi \frac{\rho}{2A^2} Q^2 \tag{4}$$

where ξ is determined by the flow type as shown in table 1.

Table 1: Flow coefficient ξ for various flow geometies.

90 degree bend	1.3
Flow past perpendicular bore	0.1
Inflow from large to small bore	0.5
Outflow from small to large bore	1.0

Table 2: Diameters and lengths used to estimate manifold pressure losses (mm).

		D_{h1}	D_{h2}	D_{h3}	D_{l1}	D_{l2}	D_{l3}	D_{l4}		
		15	60	100	35	50	50	100		
L_{h1}	L_{h2}	L_{h3}	L_{h4}	L_{h5}	L_{h6}	L_{l1}	L_{l2}	L_{l3}	L_{l4}	L_{l5}
70	200	215	700	500	2500	25	170	100	700	2500

These simple pressure loss models are combined to estimate the pressure loss associated with each displacement chamber. The method is similar for each chamber, and the model is illustrated with basis in chamber four in bank one as an example. This particular chamber is chosen as the manifolds are visible in figure 4. The motor is symmetric around bank three and four, and the flows from bank 1-3 are therefore assumed separated in the model from bank 4-6. The numbering of the each chamber in bank 1 is shown in 4. The pressure loss during flow intake from the high pressure manifold is given as:

$$\begin{aligned}\Delta pH_{1,4} = &\Delta p_{\text{straight}}(QH_{1,4}/2, D_{h1}, L_{h1}) + \Delta p_{\text{inflow}}(QH_{1,4}/2, D_{h1}) + \Delta p_{\text{bend90}}(QH_{1,4}, D_{h2}) + \\ &\Delta p_{\text{straight}}\left(\sum QH_{1,4:5}, D_{h2}, L_{h2}\right) + \Delta p_{\text{straight}}\left(\sum QH_{1:2,4:5}\right), D_{h2}, L_{h3}\right) + \Delta p_{\text{bend90}}\left(\sum QH_{1:2,4:5}\right), D_{h2}\right) + \\ &\Delta p_{\text{straight}}\left(\sum QH_{1:3,4:5}\right), D_{h2}, L_{h4}\right) + \Delta p_{\text{flowpast}}\left(\sum QH_{1:3,4:5}\right), D_{h2}\right) + \Delta p_{\text{inflow}}\left(\sum QH_{1:3,4:5}\right), D_{h2}\right) + \\ &\Delta p_{\text{straight}}\left(\sum QH_{1:3,1:6}\right), D_{h3}, L_{h5}\right) + \Delta p_{\text{bend90}}\left(\sum QH_{1:3,1:6}\right), D_{h3}\right) + \Delta p_{\text{straight}}\left(\sum QH_{1:3,1:6}\right), D_{h3}, L_{h6}\right)\end{aligned} \tag{5}$$

The diameters D_x and lengths L_x corresponds to the reconstructed motor, and their values are given in table 2. The notation $QH_{1:3,1:6}$ means all flows indicated by the indexes, in this case all 18 flows from chamber 1 to 6 in bank 1 to 3. The first two terms divides the flow in half, as two bores connects to each high pressure valve as seen in figure 4. The last three terms models a 3 m long external pipe including a 90 deg bend. Correspondingly, the pressure loss during discharge, for the same chamber, may be found:

$$\begin{aligned}\Delta pL_{1,4} = &\Delta p_{\text{straight}}(QL_{1,4}, D_{l1}, L_{l1}) + \Delta p_{\text{outflow}}(QL_{1,4}, D_{l1}) + \Delta p_{\text{bend90}}(QL_{1,4}, D_{l2}) + \\ &\Delta p_{\text{straight}}(QL_{1,4}, D_{l2}, L_{l2}) + \Delta p_{\text{outflow}}(QL_{1,4}, D_{l2}) + \Delta p_{\text{inflow}}\left(\sum QL_{1:3,1:6}/12, D_{l3}\right) + \\ &\Delta p_{\text{straight}}\left(\sum QL_{1:3,1:6}/12, D_{l3}, L_{l3}\right) + \Delta p_{\text{outflow}}\left(\sum QL_{1:3,1:6}/12, D_{l3}\right) + \Delta p_{\text{inflow}}\left(\sum QL_{1:3,1:6}, D_{l4}\right) + \\ &\Delta p_{\text{straight}}\left(\sum QL_{1:3,1:6}, D_{l4}, L_{l4}\right) + \Delta p_{\text{bend90}}\left(\sum QL_{1:3,1:6}, D_{l4}\right) + \Delta p_{\text{straight}}\left(\sum QL_{1:3,1:6}, D_{l4}, L_{l5}\right)\end{aligned} \tag{6}$$

The diameters and lengths are shown in table 2, and the division by 12 in three of the terms represents the 12 bores in the end cap of the motor. Similar expressions for the other pressure chambers have been constructed, in order to model the complete motor, but these expressions are omitted in the paper. The complete flow loss model is available on request.

4 Manifold loss results

Conducting a full displacement simulation of the reconstructed 3.5 MW motor leads to the results shown in figure 5. This figure show the difference in pressure between the pressure chamber and the outer boundary of the low and high pressure manifold respectively. The valve pressure drop is here set to zero. As expected, a larger pressure difference occur when conducting flow through the high pressure manifold compared to that when conducting through the low pressure manifold.

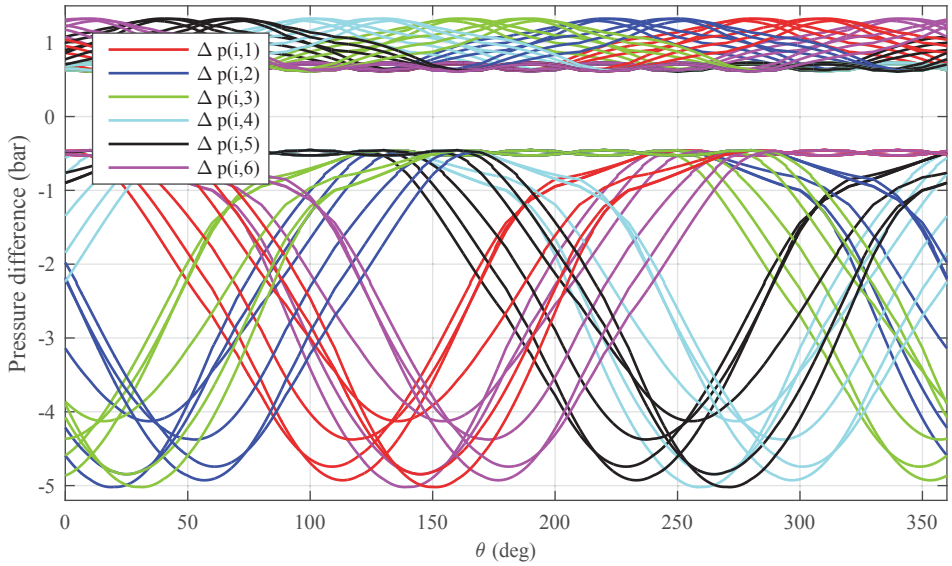

Figure 5: Manifold pressure drop of reconstructed motor. Simulated with full displacement, positive values corresponds to discharge through the low pressure manifold, negative is intake from the high pressure manifold.

The maximum pressure difference is approximately 5 bars and 1.3 bar for the high pressure manifold and the low pressure manifold respectively (at 596 l/min). The spread in maximum difference is somewhat significant for the high pressure manifold, while the low pressure manifold offers nearly equal pressure difference across the 36 pressure chambers. Noting that these pressure differences are at full displacement, the manifold design given in figure 4 does indeed provide very low pressure losses suitable for efficient digital machines.

5 Valve sizing considerations

Having established a model of the flow losses resulting from the manifold design, focus is now turned to the valve sizing and design when considering also the manifold losses. To reduce needed simulation effort, a simplification of the manifold model is imposed such that two equivalent flow coefficients are used to describe the high and low pressure manifold losses. This is done using,

$$k_{eq,H} = \frac{Q_{max}}{\sqrt{\Delta p_{max,mean,H}}} \quad \text{and} \quad k_{eq,L} = \frac{Q_{max}}{\sqrt{\Delta p_{max,mean,L}}} \tag{7}$$

where Q_{max} is the maximum flow rate for one chamber and $\Delta p_{max,mean,H}$ and $\Delta p_{max,mean,L}$ is the maximum pressure difference corresponding to the maximum flow rate taken as a mean across all of the pressure chamber. Using the approximation in (7), only a single pressure chamber needs to be studied in the following.

5.1 Single chamber model

A single chamber model including two electronic valves has been developed to conduct the valve sizing study. The target with this study is to investigate the overall trends in valve sizing and characteristics, rather than accurately capturing all dynamic effects. A model overview is given in figure 6. The parts of model are described in the following.

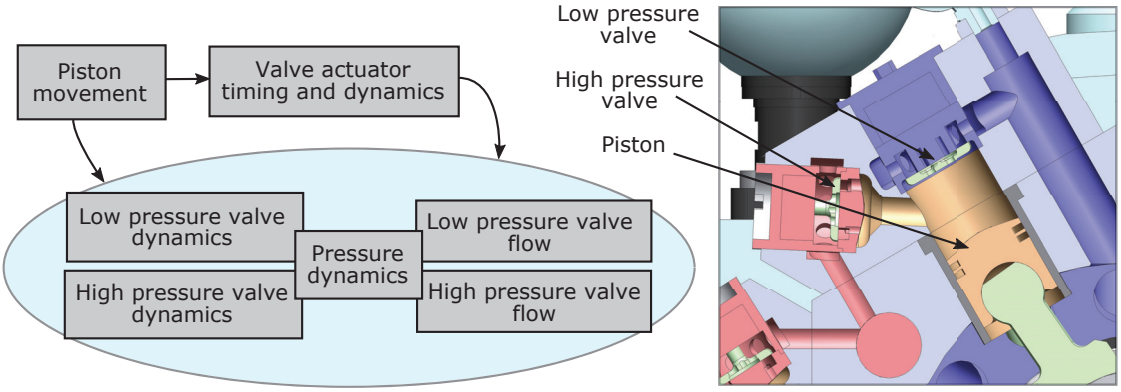

Figure 6: Single chamber model overview. The geometry shown to the right is en example, as valve sizes are considered variable in the study.

The piston movement is a forced input following $x_p = r_e(1 + cos(\theta))$, with $\dot{\theta}$ set constant corresponding to 1000 rpm. The piston position is used to control the valve actuators, that is, when to apply closing force to the low and high pressure valve. The dynamic force response of the actuator is represented by a first order system with a time constant τ = 1 ms. The piston movement and valve actuator forces is then used as inputs to the remaining parts of the system as indicated in figure 6.

5.1.1 Valve dynamics

Similar models are used to predict movement of the low and high pressure valve. The equation of motion of the low pressure valve is given as,

$$m_L \ddot{x}_L = F_{L,act} - F_{L,mov} - F_{L,fluid} \tag{8}$$

$$F_{L,mov} = \frac{8}{3} r_{L,outer}^3 \rho \ddot{x}_L + 16 \mu r_{L,outer} \dot{x}_L + \frac{128}{3\pi} r_{L,outer}^2 \rho \sqrt{\frac{\nu}{\pi}} \int_0^t \ddot{x}_L(\tau) \frac{1}{\sqrt{t-\tau}} d\tau$$

$$F_{fluid} = \begin{cases} \frac{\rho \sin\gamma}{2 C_c \pi D_L x_L} Q_L^2, & x_L > 0 \text{ 'valve open'} \\ A_{L,c}(p_{man,L} - p_c), & x_L = 0 \text{ 'valve closed'} \end{cases}$$

where m_L is the moving mass, x_L the position, $F_{L,act}$ the actuator force, $F_{L,mov}$ the fluid opposing forces resulting from movement of the moving part, $F_{L,fluid}$ the fluid forces (flow and pressure), $r_{L,outer}$ the outer radius of the moving part, μ the dynamic viscosity

of the oil, γ=30deg the assumed jet angle, C_c=0.6 the assumed contraction coefficient. D_L is the mean diameter of the two flow edges, Q_L is the valve flow rate, $A_{L,c}$ is the shadow area of the valve, $p_{man,L}$ the manifold pressure (taken locally at the valve) and p_c the chamber pressure.

The movement induced fluid force $F_{L,mov}$ follows the results in [8], and implementation of the integral term in discrete simulation models are discussed in [9]. The coefficients used for estimating $F_{L,mov}$ is those of a circular disk with the same outer radius. Only the static flow force is included for simplicity, following the study in [10]. A similar expression is used for describing x_H, with the difference that p_c acts in a positive (opening) direction and the manifold pressure $p_{man,H}$ acts negative (closing).

5.1.2 Pressure dynamics

The pressure dynamics is modeled using the continuity equation. Leakage is neglected and a pressure dependent stiffness model is applied [11]:

$$\dot{p}_c = \frac{\beta(p_c)}{V_c}\left(Q_H - Q_L + A_p\dot{x}_p + A_{L,c}\dot{x}_L - A_{H,c}\dot{x}_H\right) \tag{9}$$

$$V_c = V_0 - A_{L,c}x_L + A_{H,c}x_H \tag{10}$$

$$\beta(p) = \frac{(1-\alpha)\left(1+\frac{m(p-p_0)}{\beta_0}\right)^{-\frac{1}{m}} + \alpha\left(\frac{p_0}{p}\right)^{\frac{1}{\kappa}}}{\frac{1-\alpha}{\beta_0}\left(1+\frac{m(p-p_0)}{\beta_0}\right)^{-\frac{m+1}{m}} + \frac{\alpha}{\kappa p_0}\left(\frac{p_0}{p}\right)^{\frac{\kappa+1}{\kappa}}} \tag{11}$$

where β is the pressure dependent oil stiffness, V_c the chamber volume, V_0 the chamber initial volume, $\alpha = 0.5\%$ is the assumed air ratio at atmospheric pressure, $\beta_0 = 15500$ bar the reference stiffness, $m = 11.4$ the stiffness pressure gradient and $\kappa = 1.4$ the adiabatic constant of air. The stiffness model ensures that negative pressures occur during simulation.

5.1.3 Valve flow

As with the equation of motion, the valve flows of the low and high pressure valves are simulated with similar expressions. The low pressure valve flow is given as:

$$Q_L = \frac{1}{\sqrt{\frac{1}{k_L} + \frac{1}{k_{eq,L}}}}\sqrt{|p_c - p_{man,L}|}\,\mathrm{sign}(p_c - p_{man,L}) \tag{12}$$

$$p_{man,L} = \left(\frac{Q_L}{k_{eq,L}}\right)^2 \mathrm{sign}(Q_L) + p_L \tag{13}$$

$$k_L = C_{d,L}(Re)A_L\sqrt{\frac{2}{\rho}} \quad \text{with} \quad C_{d,L}(Re) = \begin{cases} C_{d,max}, & Re > Re_t \\ C_{d,max}\frac{\sqrt{Re}}{\sqrt{Re_t}}, & \text{else} \end{cases} \tag{14}$$

Here, p_L is the pressure at the manifold boundary, $C_{d,L}$ the discharge coefficient, A_L the combined flow area of the two flow edges, $C_{d,max} = 0.6$ the maximum discharge coefficient allowed and $Re_t = 100$ the flow transition point assumed. This flow description is treated in [10]. Reynolds number is calculated using $Re = \frac{|Q_L|d_{h,L}}{\nu A_L}$ where the hydraulic diameter is given as $d_{h,L} = \frac{4A_L}{O}$. For the annular valve, the flow area is $A_L = 2\pi x_L D_L$ and the wetted circumference is $O = 4\pi D_L$.

5.1.4 Single chamber model variables and transient response example

An overview of the single chamber model parameters, design variables and some internal states is given in table 3.

Table 3: Parameters and variables for the single chamber model.

Variable	**Value**	**Description**
D_L,D_H	[10,100] mm	Mean valve flow edge diameter
$l_{s,L}$,$l_{s,H}$	[1;10] mm	Stroke length of the valve moving member
$F_{act,max,L}$,$F_{act,max,L}$	[10;1200] N	Actuator force capability (when settled)
$\theta_{cl,L}$,$\theta_{cl,H}$	[320;350],[140;170] deg	Valve timing signals, closing
$\Delta\theta_{cl,L}$,$\Delta\theta_{cl,H}$	[1;30] deg	Valve closing signal duration
Parameter/state	**Value**	**Description**
$\dot{\theta}$	$1000 \cdot \frac{2\pi}{60}$ rad/s	Constant rotation speed
p_H	350 bar	High pressure manifold boundary
p_L	5 bar	Low pressure manifold boundary
r_e	19 mm	Eccentricity radius (half the piston stroke)
D_p	80 mm	Piston bore
V_0	150 cc	Initial chamber volume
ν	46 cSt	Kinematic oil viscosity
ρ	870 kg/m^3	Oil density
μ	$\nu\rho$	Dynamic oil viscosity
W_L,W_H	$2l_{s,L}$,$2l_{s,H}$	Width between flow edges. Set to match flow area through valve.
$A_{L,c}$,$A_{H,c}$	$\pi D_L W_L$,$\pi D_L W_L$	Valve chamber shadow area.
$k_{eq,L}$,$k_{eq,H}$	$2.74\cdot10^{-5}$,$1.46\cdot10^{-5}$ $\frac{m^3}{s\sqrt{Pa}}$	Equivalent manifold flow coefficient.
$r_{L,outer}$,$r_{H,outer}$	$\frac{1}{2}(D_L+W_L)$,$\frac{1}{2}(D_H+W_H)$	Outer radius of the valve moving member
K_{Mass}	20.4 kg/m^2	Scale from prototype valve moving member, 25g/(35mm)^2
m_L,m_H	$K_{Mass}D^2_{L,outer}$,$K_{Mass}D^2_{H,outer}$ kg	Mass found using scale from prototype
τ	1 ms	Time constant actuator response
$F_{spr,L}$	$1.1\left(\frac{Q_{max}}{k_{L,max}}\right)^2 A_{L,c}$	Spring force, 10% overhead
$F_{spr,H}$	$1.1\left(\frac{Q_{max}}{k_{H,max}}\right)^2 A_{H,c}$	Spring force, 10% overhead
$F_{act,L}$	ON/OFF-Signal$\cdot\frac{F_{act,max,L}}{\tau s+1}+F_{spr,L}$	Actuator force
$F_{act,H}$	ON/OFF-Signal$\cdot\frac{F_{act,max,H}}{\tau s+1}+F_{spr,H}$	Actuator force

The 10 design variables are used to define a given design point, which is subject for optimization in the following section. To illustrate the transient response of the single chamber model, the simulation results of an example design point is given in figure 7. This response corresponds to the design point:

$$\begin{aligned} X &= (D_L, D_H, l_{s,L}, l_{s,H}, F_{act,max,L}, F_{act,max,L}, \theta_{cl,L}, \theta_{cl,H}, \Delta\theta_{cl,L}, \Delta\theta_{cl,H}) \\ &= (50mm, 50mm, 3mm, 3mm, 1000N, 1000N, 330deg, 145deg, 30deg, 30deg) \end{aligned}$$

The closing signals controls the actuator forces, resulting in closure of the low and high pressure valve close to TDC and BDC respectively of the piston movement. Two cycles are simulated, firstly a motoring cycle (0-60 ms) followed by an idling cycle (60-120 ms). During the motoring cycle oil is conducted through the high pressure valve during intake resulting in effective torque generation. During idling, the low pressure valve is kept open throughout the entire piston cycle without pressurization.

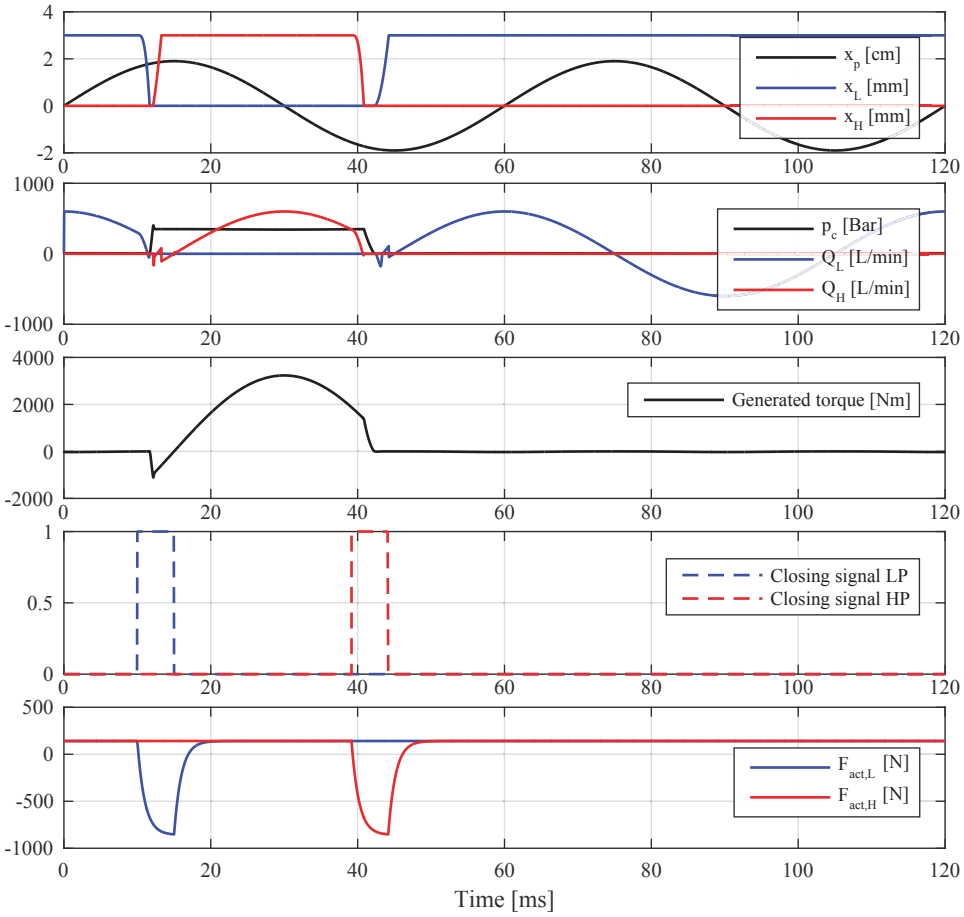

Figure 7: Transient response for example design point. Two cycles are simulated, motoring in the first cycle and idling in the second.

6 Valve sizing optimization

In this section, it is investigated which valve sizes/dimensions are most suitable for obtaining high operation efficiency of the digital motor considered. Which valve diameters and stroke lengths minimizes the flow losses (when considering the needed actuator power)? Should the low and high pressure valve be similar in size? Is it possible to obtain high efficiencies with low stroke lengths (aiding the actuator design)?

Only flow losses and the needed actuator power is considered. In order to obtain very high efficiencies in a broad operation range, both of these losses must be sufficiently small. The main objective is selected to be machine efficiency, defines as:

$$\eta = \frac{E_{out}}{E_{in}} = \frac{E_{in} - E_{loss}}{E_{in}} = 1 - \frac{E_{loss}}{E_{in}} \tag{15}$$

where E_{loss} is the energy loss in a given operation cycle and E_{in} is the input energy taken over the same cycle. To investigate the efficiency at part displacements, the following expression is utilized:

$$\eta(\alpha) = 1 - \frac{\alpha E_{\text{loss,motoring}} + (1-\alpha) E_{\text{loss,idling}}}{\alpha E_{\text{in,motoring}} + (1-\alpha) E_{\text{in,idling}}} \tag{16}$$

where α is the displacement ratio (0-1), and the energy losses and energy inputs are evaluated for a motoring cycle and an idling cycle. Using (16), the machine efficiency over

the full displacement range may be calculated based on simulations of a motoring cycle and an idling cycle as shown in figure 7. The input and output energies are found during simulation by integrating the instantaneous power associated with oil flows (pressure/flow products) and the instantaneous actuator power of the low and high pressure valve (force/velocity products).

The efficiency as a function of the displacement ratio $\eta(\alpha)$ is integrated to obtain a metric for evaluating the total operation range efficiency:

$$\Psi = \int_{0.1}^{1} \eta(\alpha) d\alpha \tag{17}$$

where α=0.1 is selected as the lower limit when evaluating the combined efficiency. The range efficiency Ψ is used as main objective in the optimization algorithm, in the form $1-\Psi$. Secondary objectives are related to the requirements for the valve actuators, specifically the needed stroke lengths, force capability and average power.

6.1 Optimization algorithm

A Generalized Differential Evolution 3 (GDE3) algorithm is used to perform the global problem optimization, an algorithm which uses Pareto optimization to return a set of solutions which are non-dominated by any other solution [12, 13]. This enables investigation of couplings between different objectives, which is used in this paper to study the influence of valve actuator parameters on the machine efficiency. A set of constraints has been formulated for the optimization problem, which is loosely defined below.

C1 Simulation success indicator. Depending on the design point, the machine cycle may only be completed partially (too weak actuators, valve did not move ect.). If the machine cycle does not complete as expected, this constraint returns a positive number indicating violation. Violation degree is set based on how far in the cycle the design point managed to be successful.

C2 Efficiency low out of range. An efficiency in the range 0.75-1.0 is expected, and this constraint is considered violated if the evaluated efficiency is outside this region.

C3 Energy utilization indicator. The output energy during motoring should be at least half of the ideal output energy, $A_p(p_H - p_L)2r_e$. Otherwise, this constraint is violated.

C4 Chamber cavitation indicator. Cavitation should be avoided during idling intake, and a minimum limit of 2.0 bar is set using this constraint.

6.2 Optimization results

The results of the optimization are given in figure 8. These design points represent the best 100 designs when considering the mean actuator power as the secondary optimization objective. The corresponding values for the valve actuator maximum forces and stroke lengths are also shown in the figure, and the optimum design point with respect to the efficiency integral is marked. A maximum efficiency integral value of $\Psi = 0.877$ is obtained. This integral is calculated with a maximum efficiency of 98.5 percent and an efficiency at α=0.1 of 92.7 percent. Note that these efficiencies includes manifold losses but exclude

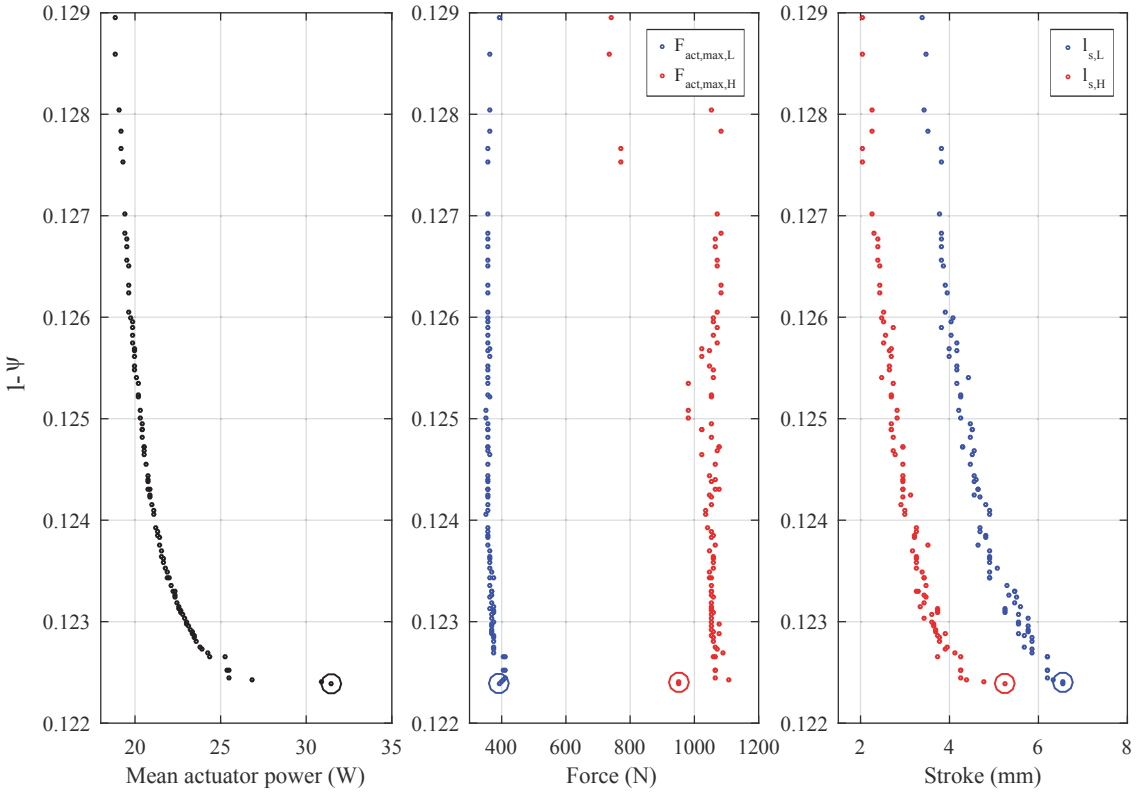

Figure 8: Optimization results. The range efficiency integral Ψ is maximized by minimizing 1-Ψ. Mean actuator power is for both the low and high pressure valve actuator.

losses other than flow loss and actuator input. This confirms the high efficiency potential of digital hydraulic machines.

The optimum point highlighted in figure 8 corresponds to the following design point:

$$X = (D_L, D_H, l_{s,L}, l_{s,H}, F_{act,max,L}, F_{act,max,L}, \theta_{cl,L}, \theta_{cl,H}, \Delta\theta_{cl,L}, \Delta\theta_{cl,H})$$
$$= (55.2\,mm, 59.9\,mm, 6.6\,mm, 5.3\,mm, 394\,N, 953\,N, 320.4\,deg, 140.7\,deg, 10.3\,deg, 4.9\,deg)$$

The valve diameters are seen to be below the piston bore of 80 mm, easing the valve implementation in the reconstructed motor. Furthermore, the low pressure valve is seen to require a longer stroke compared to the high pressure valve, even though the valve diameters are close. This optimum may reflect the need for the low pressure valve to exhibit very low losses to improve the efficiency at low displacement levels. Figure 8 shows that a combined actuator power of approximately 30 W is sufficient, verifying that the actuators may indeed be low power even for large capacity motors. The force capability requirement of the high pressure valve is somewhat larger than the low pressure valve.

Variable reluctance (solenoid) actuators are commonly used in these digital motors. In designing such actuators, the stroke length of the valve is important and has a strong coupling to the actuator design. The results in figure 8 give an indication of the change in efficiency when lowering the stroke lengths compared to the optimum point highlighted. It is seen that a stroke length above 4 mm for the low pressure valve is needed to ensure performance close to optimum, while the high pressure valve stroke length may be reduced below 3 mm while maintaining high efficiencies.

7 Conclusions

The manifold architecture of a state of the art machine has been investigated. The design ensures a low pressure manifold with fewer losses than the high pressure manifold, supporting very high part load efficiencies. A possible manifold design has been presented, which may resemble that of the state of the art machine.

A quasi-static manifold loss model has been developed and applied to the reconstructed 3.5 MW motor design. At maximum displacement rate of 596 l/min, the pressure drop is approximately 1.3 bar for the low pressure manifold and 5.0 bar for the high pressure manifold.

A single chamber model suitable for optimization of valve and actuator sizing has been developed, and optimum valve sizes and actuators have been found. The optimum valve diameters are smaller than the piston bore, which may aid to ease the valve implementation. The optimum stroke length to diameter ratios have been found to differ for the low and high pressure valve, 11.9 percent being the ratio for the low pressure valve and 8.8 percent for the high pressure valve.

In total, the results confirm that digital hydraulic machines may be designed for high efficiencies above 90 percent in a broad operation range, and the radial piston architecture allows for large valves to be implemented together with manifolds exhibiting low throttling losses.

References

[1] Grgory S. Payne, Uwe B.P. Stein, Mohammad Ehsan, Niall J. Caldwell, and W H.S. Rampen. Potential of digital displacement hydraulics for wave energy conversion. In *In proc. of the 6th European Wave and Tidal Energy Conference, Glasgow, UK*, August 29th - September 2nd 2005.

[2] Win Rampen. *The Development of Digital Displacement Technology*, chapter Keynote address, pages 12–17. Fluid Power and Motion Control (FPMC), 2010.

[3] William Rampen, Niall Caldwell, and Uwe Stein. Annular valve, 07 2002. Patent No. US 7077378.

[4] Jamie Taylor. Online video, ”Power for Change - Intelligent Power - the development of digital hydraulics”, 2009.
Available at www.youtube.com/watch?v=P1wZb_RKRQg.

[5] Masashi Sasaki, Atsushi Yuge, Toshikazu Hayashi, Hiroshi Nishino, Michiya Uchida, and Toshihide Noguchi. Large Capacity Hydrostatic Transmission with Variable Displacement. In *The 9th International Fluid Power Conference, 9. IFK*, 2014.

[6] Artemis Intelligent Power Ltd. 7 MW DD Transmission - Progress Report, November 2013. Video available at www.artemisip.com/news-media/videos.

[7] Birger Bech Jensen and Bent Halling. *Hydraulikstaabi*. Praxis - nyt teknisk forlag, 1996. Original in swedish.

[8] R. Y. S. Lai. Translatory accelerating motion of a circular disk in a viscous fluid. *Applied Science Research*, 27:440–450, 1973.

[9] Daniel B. Roemer, Per Johansen, Lasse Schmidt, and Torben O. Andersen. Modeling of dynamic fluid forces in fast switching valves. In *Proceedings of the Bath/ASME Symposium on Fluid Power and Motion Control, FPMC*, 2015.

[10] Herbert E. Merritt. *Hydraulic Control Systems*. John Wiley & Sons, Ltd., 1967.

[11] S. Kim and H. Murrenhoff. Measurement of effective bulk modulus for hydraulic oil at low pressure. *Journal of Fluids Engineering, Transactions of the ASME*, 134(2), 2012.

[12] R. Storn and K. Price. Differential evolution a simple and efficient heuristic for global optimization over continuous spaces. *Journal of Global Optimization*, 11:341–359, 1997.

[13] S. Kukkonen and J. Lampinen. GDE3: The third evolution step of generalized differential evolution. In *The 2005 IEEE Congress on Evolutionary Computation, 2005.*, volume 1, pages 443–450 Vol.1, Sept 2005.

HIGH FREQUENCY HIGH FLOW GAIN ON/OFF HYDRAULIC CONTROL VALVES

Mohamed Elgamil*, Adham Saboun** and Saad Kassem***
Assistant Professor, Postgraduate Student, and Professor Emeritus
Faculty of Engineering, Cairo University
12613, Giza, Egypt
elgamil@eng.cu.edu.eg, adhamosha@gmail.com, sdkassem@eng.cu.edu.eg

ABSTRACT

High frequency valves can be realized when the required stroking forces and displacements of the valving elements, whether poppets or spools, are minimized to cope with the capabilities of compact actuating devices. A new class of valves are proposed and analyzed in this work, in which the valving elements are subjected to the high inlet pressure at both sides that have small area difference. This would result in reducing both the required driving forces and the strength needs of the valving elements. The valving element return to its initial position in this case results from the pressure and flow forces unbalance only, or with additional assistance of a spring force. The proposed large control edge length allows obtaining appreciable large control orifice area from a small valving element displacement, and hence high flow gain. The small valving element displacement reduces the dynamic forces, the demands on the actuating devices and allows the use of piezoelectric actuators of short stroke, magnified when required, or the electromagnetic driving devices that generate high forces at narrow gaps and reasonable ampere-turn values. The configurations of the fast switching valves well fit the purpose of Pulse Width Modulation control techniques. Examples of using the proposed valves as 3/2 and 2/2 directional control valves of size NG 6 are shown and the flow gain and forces acting on the valving elements are numerically evaluated. The concept is applicable for larger sizes. The flow gain is comparable with conventional directional control valves of similar size. Four 2/2 valves can be assembled in one housing to control the connections between the two load ports and the pressure and tank ports independently for highest efficiency and minimum number of control pulses. As pilot valves, they provide a low cost technique for upgrading conventional valves to fast switching valves. If controlled by a proportional electromagnetic device or an adjustable spring, the valve can be designed to operate as a relief or a reducing valve.

KEYWORDS: Fast switching, hydraulic, valve, directional control, pressure control

1. INTRODUCTION

Fast switching valves with high flow rate gain are key components in modern digital hydraulics applications. The valving elements in this type of valves should be of small mass and have relatively small displacements to be actuated by short stroke fast response actuators, such as piezoelectric actuators or electromagnetic device of narrow gap and high force. The valve design should be developed so as to allow high flow rates in spite of the valving element limited stroke.

A piloted seat type fast switching valve utilizing the Horbiger plate concept had been presented in [1]. Another design having a 3/2 solenoid operated directional control valve as the pilot stage, which drives the main stage consisting of multiple poppet valves, has been presented in [2]. The switching times of these valves are generally less than 5 ms and the nominal flow rates attain up to 100 l/min. A piezo stack actuator had been utilized in [3] to actuate a fast switching high flow rate directional control valve. Kudzma et al. [4] presented a servo valve driven 3/2 spool valve with multi metering edges, which have a switching time less than 1 ms and a flow rate amounting to 65 l/min at 1.5 MPa pressure drop. Elgamil et al. [5] showed that a servovalve with a two land spool can be operated stably when the pilot stage is of the closed center type, and they theoretically determined the flow forces acting on the spool in this case. Elgamil et al. [6], and on the basis of the analysis and results of [5], presented and theoretically analyzed some performance aspects of a proposed two stage fast switching directional control valve in which two 3/2 piezo stack actuated poppet valves are used in the pilot stage to drive the spool of the valve main stage. Valves of this type with two or four land spools were theoretically verified to operate satisfactorily, and would have a speed of response exceeding that of a servo valve of the same size. Elgamil [7] described the details of a new type of fast switching high flow gain valves, suitable for different control functions in hydraulic systems. In this paper some design details for this valve are proposed and the valve static characteristics are theoretically analyzed.

2. VALVE DESCRIPTION

The main forces acting on the valving element of a valve, which have to be overcome by any actuator, are pressure, flow, inertia, and friction forces. Strength and rigidity in addition to these forces should be considered during the valve design stage.

2.1. Poppet valve configuration

Figure 1 shows a layout for a novel poppet valve design in a 2/2 configuration that takes these factors into account. The poppet (2) is inserted in the valve housing (1), and is acted upon by a closing pressure force equal to the pressure p times the small area (4). The ports (P) and (A) are consequently closed hermitically with a force that increases with the increase of the pressure p. A spring (3) can be added for closing the connection

hermitically if the pressure p is low, and would help in increasing the valve closing speed. For connecting the ports (P) and (A), a force f is to be applied to the poppet to displace it a distance x. The required force component to overcome the pressure force would consequently be small since the area (4) can be made as small as required by the strength considerations.

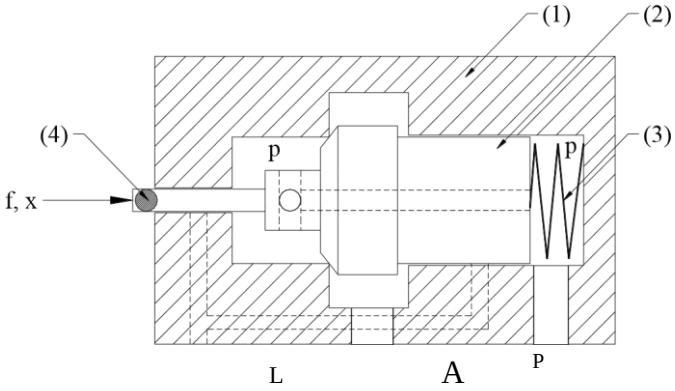

Figure 1. Layout for a 2/2 poppet valve

Figure 2 shows an example for the poppet (2) and its surroundings. In this arrangement a pusher (5) is guided inside a sleeve (6) to enable the poppet (4) to be floating so as to adjust itself when seated.

Besides, it allows for adding another port for the valve if required. The large poppet diameter allows a small poppet displacement to generate large control orifice area. This short poppet stroke well suits capabilities of powerful actuators that generate high forces at small gaps. Pressure control actions (relief or reducing) can be achieved through the proper connections of the valve ports. The control of pressure can be realized by electric actuators as in proportional pressure control valves, or through spring loading.

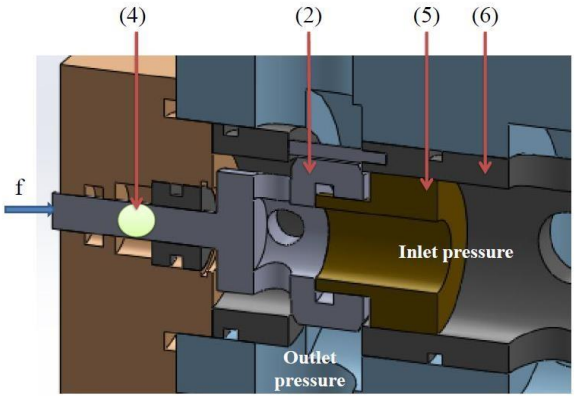

Figure 2. Main parts of a proposed 2/2 poppet valve

Figure 3 shows designs and symbols for fast switching directional control valves composed of either two 3/2 poppet valves or four 2/2 valves of this configuration, assembled in one housing. The symbols shown are for electrically operated valves. The poppet and spool are designed so as to reduce their share in carrying the reacting force resulting from diverting the flow direction and hence reduce the actuating force demand.

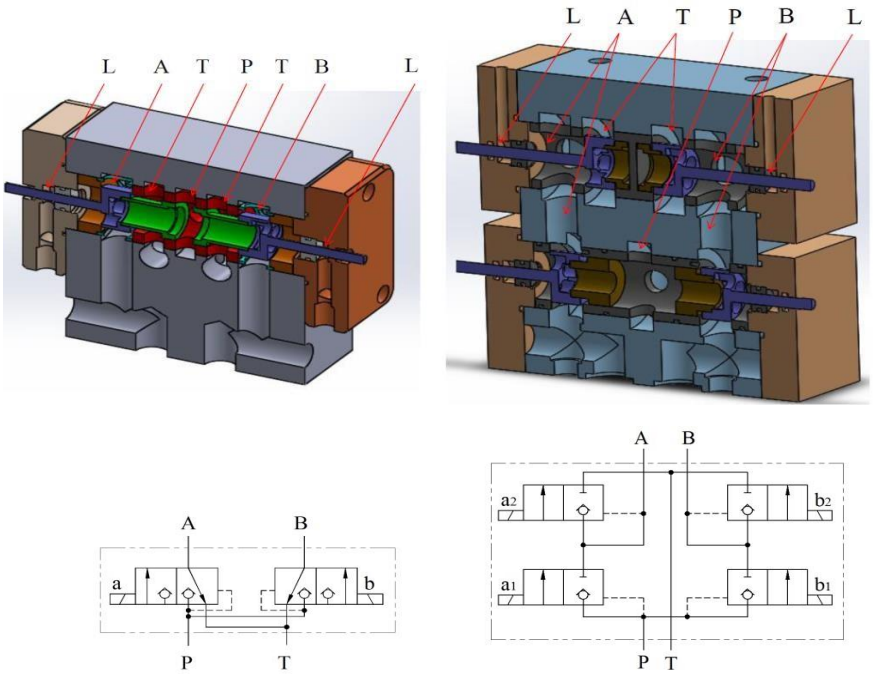

a. Two 3/2 valves *b. Four 2/2 valves Figure*

3. Examples of fast switching directional control valves

These designs allow precise control by fast switching PWM signals, and allow also decoupling of the load ports. Compared with servo and proportional valves used for precise control of actuators, PWM directional control valves would render also precise control, reduce costs, and improve efficiency. Further, decoupling the load ports control improves the controllability and reduces the number of the required control pulses and in some cases components.

2.2 Spool valve configuration

Figure 4 shows a proposed design in which the poppets are replaced by spools.

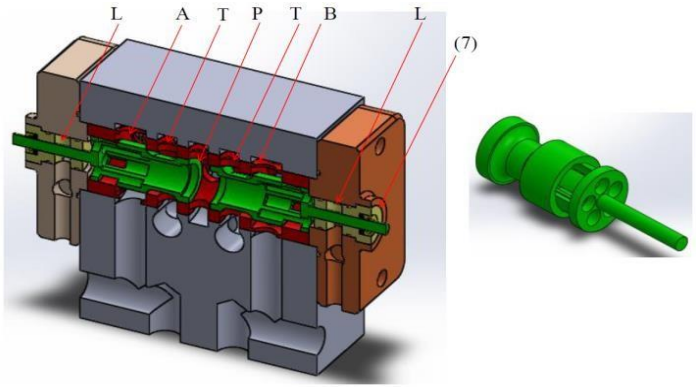

Figure 4. 3/2 Fast switching directional spool valve configuration and valve spool

This design avoids the shocks of the poppet on its seats. With these fast switching valves, production costs are considerably reduced since the accurate matchings of the

several control edges required in servo and proportional valves are avoided. The spool initial position can simply be altered using the threaded part (7) to adjust the required match of the two only control edges. Contrary to the poppet which is split into two parts; namely a pusher and a poppet, all the spool lands are integrated in one piece.

3. FLOW RATES AND VALVINEG ELEMENT FORCES

Ansys-Fluent software package has been used to determine the pressure and flow distributions inside the valve, as well as the valve flow rates and the forces acting on the valving elements, for poppet and spool valves of nominal size NG 6. The poppet and the spool diameters were taken equal to 13 mm during the analysis, and the unbalanced area diameter was 3 mm. The mass of these elements is about 0.025 kg and they have small displacements, which would result in sensible reduction in their inertia forces. A 3-D model has been adopted assuming that the oil density and viscosity are 860 kg/m^3 and 0.03 Ns/m^2 respectively. Standard wall function is selected in FLUENT for modeling the near wall boundary layer.
The mesh type is “tetrahedral cells”, and the number of mesh cells is about 175,000 for the poppet valve and 198,000 for the spool valve. It is worth mentioning that increasing the number of cells to one million rendered only about one percent change in the results. The boundary conditions are “pressure inlet ranging from 10 bar to 200 bar and pressure outlet equals 0 bar - wall conditions elsewhere”, the convergence criteria is “solution residuals < 10^{-5} ”, and the turbulence model is “realizable k-epsilon”.

3.1 Poppet valve

Figure 5 shows the domain of analysis for the flow from the high pressure port to the low pressure one for the two 3/2 poppet valve. It shows also the resulting pressure and velocity distributions within the domain at full control orifice opening of 0.5 mm, when the pressure difference between the inlet and outlet ports is 10 bar. This analysis is also applicable for the 2/2 valve since it has the same domain.

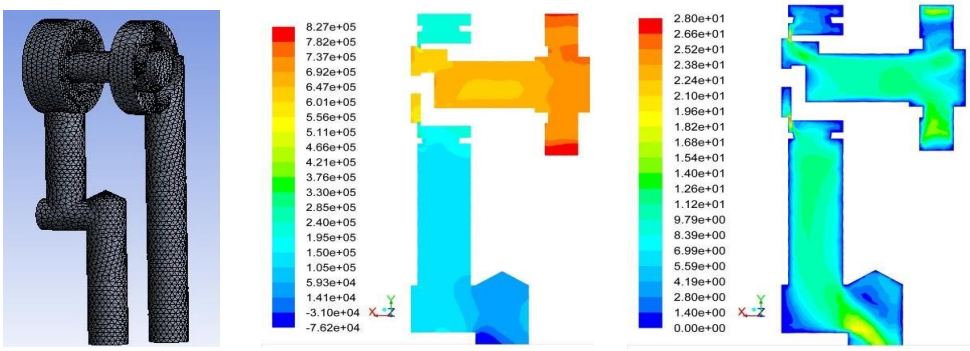

a. The domain *b. Pressure distribution* *c. Velocity distribution*

Figure 5. The CFD simulation results for the 3/2 poppet valve

The maximum flow velocity is seen to be 28 m/s and occurs locally at the control orifice, and the velocity reaches about 10 m/s when passing through the poppet. Passing through the poppet imposes about 1 bar pressure drop across it, which leads to about 11 N undesired extra closing force. This force, which increases with the flow rate increase, can be significantly reduced by bypassing the majority of the flow in a parallel path away from the poppet inside path. This solution might lead to the increase of the valve dimensions because the selected valve of size NG 6 can hardly accommodate all the required paths inside its small housing.

Figure 6 shows the variation of the valve flow rate with the variation of the pressure drop between the inlet and outlet ports (P to A or P to B) at various control orifice openings.

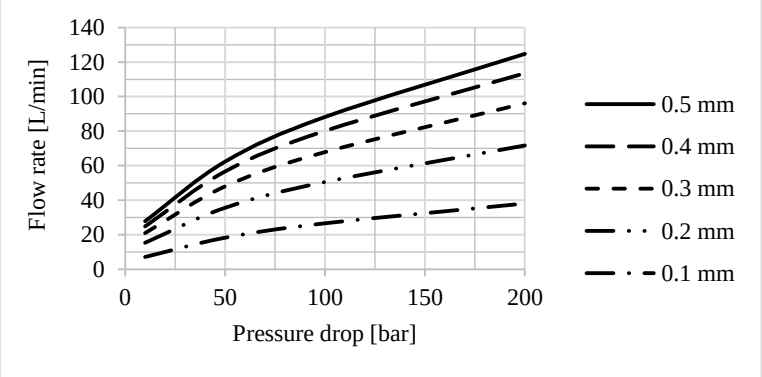

Figure 6. Flow rate vs pressure drop at various poppet displacements

Keeping in mind that this pressure drop is calculated per one control edge only, this valve would replace a servovalve of size NG 10, with higher efficiency and speed of response and lower cost. If one control edge is kept fully opened while modulating the other one, the system efficiency would furtherly and evidently increase.

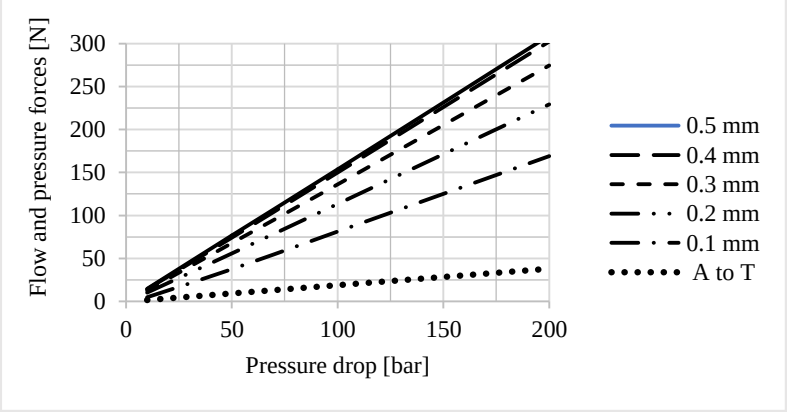

Figure 7. Flow and pressure forces vs pressure drop at various poppet displacements

Figure 7 shows the variation of the combined flow and pressure forces acting on the poppet with the variation of the pressure drop between the inlet and outlet ports at various control orifice openings. It is to be noted that these forces are of a closing nature.

At the selected maximum opening of 0.5 mm, the closing force acting on the poppet is 15 N when the pressure drop is 10 bar, and 302 N when the pressure drop is 200 bar. These forces are manageable by piezoelectric or electromagnetic actuators. A CFD study for the case of connecting the ports (A) and (T) in the upper part of Figure 3.b, where the flow passing through the poppet is avoided, has been carried out. The analysis showed in this case that the flow rates are kept the same but the forces are drastically reduced, at 0.5 mm opening, to 1.6 N at 10 bar pressure drop and 38 N at 200 bar pressure drop as shown by the dotted line in Figure 7. This arrangement for connecting a high pressure port to a low pressure one can be applied to all connections, but on the account of increasing the number of passages in valve body and the valve dimensions.

The pressure considered during this analysis is the pressure drop between the inlet and outlet ports. However, the value of inlet pressure should be taken into account when calculating the force acting on the poppet. For example, if the inlet pressure is 300 bar and the load pressure at port (A) is 100 bar, the pressure drop is 200 bar. The 100 bar pressure difference applied to the unbalanced area (4), of 3 mm diameter, adds 70 N closing force.

The flow rates from the port (A) or the port (B) to the port (T) in case of 3/2 valves are of the same order, and the pressure and flow forces are small and ensure keeping the connections opened.

3.2 Spool valve

Figure 8 shows the domain of analysis for the flow from the high pressure port to the low pressure one for the two 3/2 spool valve, and the resulting pressure and velocity distributions within the domain, when the pressure difference between the inlet and outlet ports is 10 bar, at 0.5 mm control orifice opening. This analysis is also applicable for the 2/2 valve since it has the same domain.

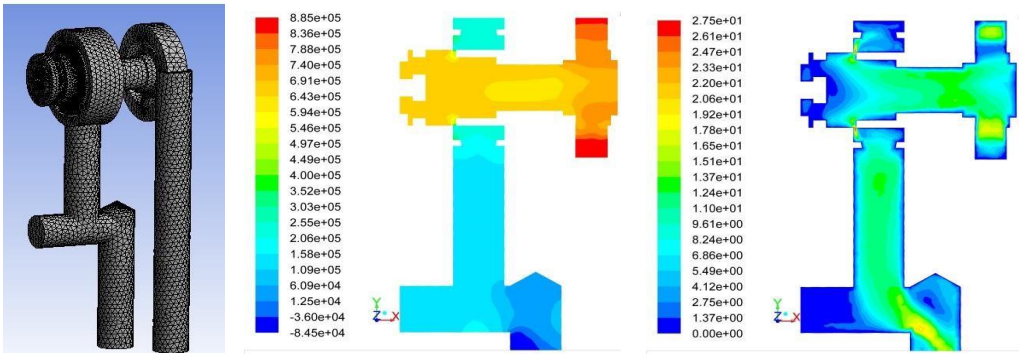

a. The domain *b. Pressure distribution* *c. Velocity distribution*

Figure 8. The CFD simulation results of the spool

Figure 9 shows the variation of the valve flow rate with the variation of the pressure drop between the inlet and outlet ports (P to A or P to B) at various control orifice openings.

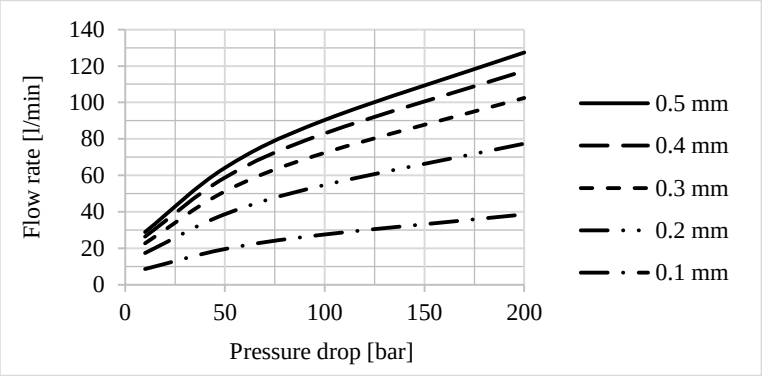

Figure 9. Flow rate vs pressure drop at various spool displacements

Figure 10 shows the variation of the combined flow and pressure forces acting on the spool with the variation of the pressure drop between the inlet and outlet ports at various control orifice openings. It is to be noted that these forces are of a closing nature.

It can be seen that the flow gain and the combined flow and pressure forces are slightly larger in this case than those of the poppet type. Except for the absence of seat shocks present in poppet valves, all the analysis mentioned in 3.1 for the poppet valves is applicable in the case of spool valves.

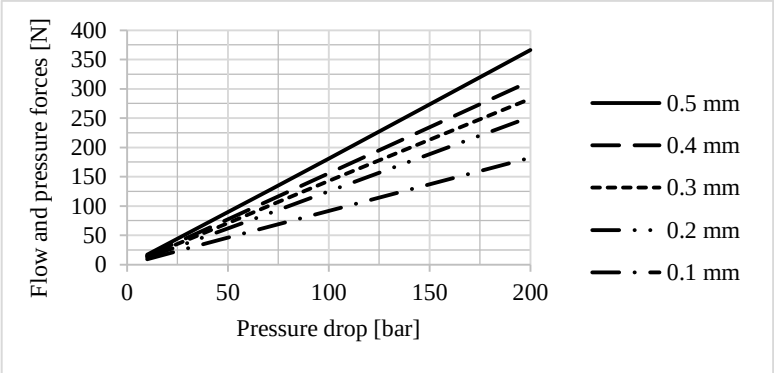

Figure 10. Flow and pressure forces vs pressure drop at various spool displacements

4. CONCLUSIONS

Configurations and some design features of new fast switching valves that can be used for directional or pressure control purposes are presented. The presented valving elements, whether poppets or spools, are close to be hydrostatically balanced in order to reduce the stroking force and strength requirements. The large diameters of the valving elements, which are of small masses, result in obtaining high flow gains at small displacements. The valving elements short displacements and small masses reduce the inertial dynamic forces and allow using actuators of small strokes and strong forces at small gaps. Flow diverting reaction forces on moving parts, and induced forces due to the flow through these parts are studied in order to minimize the flow forces. CFD simulations have been carried out to obtain the pressure and velocity distributions within

poppet and spool valves, and to calculate the flow rates and the forces acting on the moving elements. The study shows that the values of the valving elements stroking forces suit the capabilities of the piezoelectric actuators as well as the electromagnetic actuators of small gaps. The CFD analysis showed also that smaller actuators can be used when the flow passing through the valving elements is avoided. The resulting flow gains show that the studied NG 6 valve can replace a larger NG 10 servovalve, with a higher speed of response. Decoupling the ports connection control, the absence of pilot stage, and the absence of the need to match the control edges make these valves replacing servovalves of larger size not only with higher speed of response, but also with lower cost and larger efficiency.

5. ACKNOWLEDGMENTS

This research has been supported by the Egyptian Science and Technology Development Fund (STDF) through the research project "Development of a Variable Geometric Volume Positive Displacement Pump and New Hydraulic Servovalve", Grant no. 2466. The authors are indebted for STDF for the offered financial support.

REFERENCES

[1] Winkler, B. and Scheidl, R., 2007. Development of a Fast Seat Type Switching Valve for Big Flow Rates. The Tenth Scandinavian International Conference on Fluid Power, SICFP'07, Tampere, Finland.

[2] Winkler, B., Ploeckinger, A.,and Scheidl, R., 2010. A Novel Piloted Fast Switching Multi Poppet Valve. International Journal of Fluid Power, 11(3), 7–14.

[3] Branson, D., Johnston, D. N., Tilley, D., Bowen, C. and Keogh, P., 2010. Piezoelectric Actuation in a High Bandwidth Valve. Ferroelectrics, 408 (1), pp. 32-40.

[4] Kudzma, S., Johnston, D. N., Plummer, A. R., and Sell, N. P., 2012. A high flow fast switching valve for digital hydraulic systems. In The Fifth Workshop on Digital Fluid Power, Tampere.

[5] Elgamil, M., Amin, M., and Kassem, S., 2014 Development of a New Hydraulic Servovalve with Two Land Spool and New Pilot Stage. 9th JFPS International Symposium on Fluid Power, October 28-31, Matsue, Shimane Japan pp. 423 – 430.

[6] Elgamil, M., Amin, M., and Kassem, S., 2015. Development of High performance High Flow Fast switching Hydraulic Directional Control Valves. 14th Scandinavian International Conference on Fluid Power, May 20-22, 2015, Tampere, Finland.

[7] Elgamil, M., 2016. Fast switching 3/2 direct operated hydraulic directional control valve, PCT/EG2016/00010.

OPTIMAL DIGITAL VALVE CONTROL USING EMBEDDED GPU

Johan Ersfolk[1], Pontus Boström[1], Ville Timonen[1], Jan Westerholm[1],
Jonatan Wiik[1], Otso Karhu[2], Matti Linjama[2] and Marina Waldén[1]

[1]Åbo Akademi University, Finland
[2]Tampere University of Technology, Finland

ABSTRACT

Digital hydraulics is a technology where simple valve components are used together with intelligent automation to achieve efficient control of hydraulic systems. A major challenge with digital valve systems is that efficient control requires the combination of reliable real-time control and computationally expensive optimization. In this paper we present a control system which is extended with an embedded graphics processor which provides massive parallelism to perform optimizations while critical control is performed by safety critical components. The focus in this paper is on how well a complex graphics processor can function as part of a reliable real-time control system.

KEYWORDS: Digital hydraulics, graphics processors, optimization

1. INTRODUCTION

Digital hydraulics is a promising technique to achieve high performance and energy efficiency by a combination of simple on/off components and intelligent control [1]. The combination of using simpler components together with more intelligent automation can be expected to result in more easily operated machines but also in better maintainability. The major challenge for the utilization of digital hydraulics is the lack of suitable computation units to process the measurement data for optimal control. While expensive laboratory equipment has been used to obtain good results, such devices are expensive and too sensitive for practical use. The problem is especially severe in working machines, which operate in extreme environmental conditions: temperatures vary between -40 and +50 ºC, and the machines are exposed to moisture, snow, dust, vibrations and impacts.

Automotive engine control units (ECUs) are attractive alternatives to implement the control systems for digital hydraulics for working machines. Such components are designed for harsh conditions and provide the robustness and real-time properties that are needed to build a reliable control system. A modern embedded graphics processor (GPU), on the other hand, is a powerful computational device which enables implementing more advanced features of digital hydraulics than what is possible with an ordinary processor. The challenge with GPUs is that they are not well suited for safety-critical systems as the

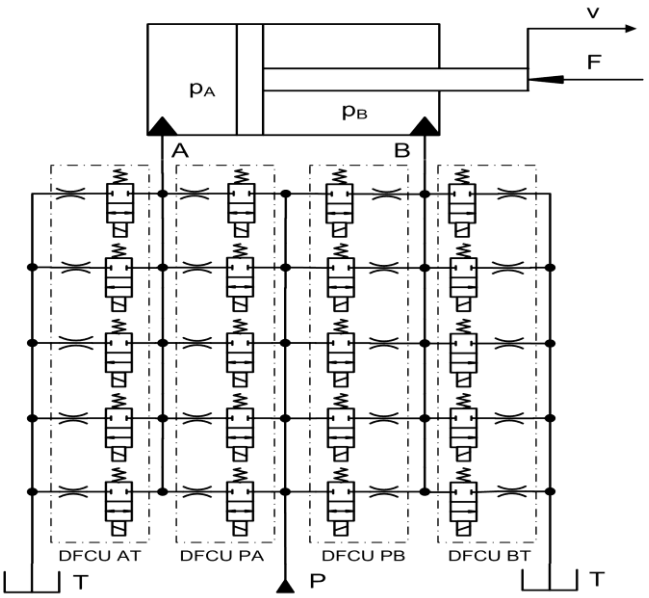

Figure 1. A cylinder with 4x5 valve setup

hardware and driver software are complex and do not provide real-time guarantees [2]. In this paper, we study the possibility to implement advanced control features of digital valve systems by using a modern embedded GPU, while real-time critical control is implemented in automotive ECUs. Our design is thus that the system must be able to work possibly suboptimally without the GPU, however, optimal control is achieved when the computational power of the GPU can be used by the control system.

To achieve fault tolerance in a real-time system we need to ensure that a component violating its timing constraints does not result in a timing failure of the system. One approach to achieve this is to implement a *primary* and an *alternate* version of a critical task [3, 4]. The *primary* version may be more complex and produce a better solution, in some sense, but may result in timing faults. The *alternate* is simpler which makes it possible to verify its functional and timing behavior, but at the expense of producing only acceptable solutions. This approach resembles our problem of having a complex GPU performing the primary computations while alternative computations are performed on the ECU which also performs an acceptance test on the control signal produced by the GPU. Compared to the work in [3, 4], the architecture used in this paper uses separate hardware for the different versions of the controller which means that both the primary and the alternate version are always computed.

The focus of this paper is on the capabilities of an embedded GPU to function as part of a control system. An embedded GPU as opposed to a high-performance workstation GPU, provides massive parallelism at a lower speed to decrease power consumption. For a large hydraulic system the power consumption of the GPU is insignificant, however, it means that an embedded GPU can manage without active cooling which is an important property in harsh conditions. In this paper, we show how an embedded GPU can be used to optimize a digital hydraulic system which have four valve units each with five parallel digital valves. The results of the paper are the following 1) in Section 3 we present strategies for how to develop highly optimized code for the controller, 2) in Section 4 we present the capabilities of embedded GPUs in this context. We will start by presenting the controller model in the next section.

2. CONTROL APPROACH

The central feature in digital hydraulics is that each flow path is controlled by a number of parallel on/off valves to achieve a stepwise flow control. A digital flow control unit (DFCU) with N parallel connected valves, where the flow capacity of the valves are set according to a binary sequence, controls the flow path with 2^N discrete states. The type of system we analyze in this paper consists of a hydraulic cylinder which is controlled by four DFCUs, each with five parallel-connected valves, according to Figure 1. Each DFCU controls one flow path, either from the hydraulic pump P to one of the cylinder chambers A, B, or from one of the cylinder's chambers to the tank T. To control the velocity of the piston, the required pressure difference between the cylinder's chambers is achieved by a combination of DFCU states.

The flow rate of the parallel valves of a DFCU is assumed to follow the equation of turbulent flow [1, 5]. The flow of the four different flow paths are given by:

$$Q_{PA} = \sum_{i=1}^{N} \left(u_{PA} \cdot K_{vPA,i} \cdot SP\left(p_S - \hat{p}_A\right)^{\alpha_{PA,i}} \right) \tag{1}$$

$$Q_{AT} = \sum_{i=1}^{N} \left(u_{AT} \cdot K_{vAT,i} \cdot SP\left(\hat{p}_A - p_T\right)^{\alpha_{AT,i}} \right) \tag{2}$$

$$Q_{PB} = \sum_{i=1}^{N} \left(u_{PB} \cdot K_{vPB,i} \cdot SP\left(p_S - \hat{p}_B\right)^{\alpha_{PB,i}} \right) \tag{3}$$

$$Q_{BT} = \sum_{i=1}^{N} \left(u_{BT} \cdot K_{vBT,i} \cdot SP\left(\hat{p}_B - p_T\right)^{\alpha_{BT,i}} \right) \tag{4}$$

where p_S is the supply pressure, $\hat{p_A}$ and $\hat{p_B}$ are the pressures in the cylinder chambers, u is a binary value representing the state of a valve, K_v is the flow unit constant for that specific valve, and $SP(x)^y$ indicates the signed power and is equivalent to $sgn(x) \cdot |x|^y$.

In practice the system is a bit more complicated as the piston moves as a result of the pressure differences and the pressure in one chamber depends on the pressure in the other chamber. What we want to know is the steady state of the system for a given combination of valve positions. As a result, we have an equation system with three unknowns, namely the velocity of the piston $\hat{v}$, the pressure in the A-chamber $\hat{p_A}$, and the pressure in the B-chamber $\hat{p_B}$:

$$\begin{aligned} Q_{PA} - Q_{AT} &= A_A \cdot \hat{v} \\ Q_{PB} - Q_{BT} &= -A_{AB} \cdot \hat{v} \\ F &= A_A \cdot \hat{p}_A - A_B \cdot \hat{p}_B \end{aligned} \tag{5}$$

In the equations, piston areas A_A and A_B and the measured properties of each of the valves are constants, while the supply pressure p_S is a measured value as well as the external force F which is calculated from measurements of the pressure in the chambers A and B. The measured pressures p_A and p_B, should not be confused with the variables $\hat{p_A}$ and $\hat{p_B}$

which are estimates of the future steady state. Furthermore, the state of each of the valves u_i is considered a constant, as we calculate the steady state for a specific valve combination; on the other hand, to find the optimal control we calculate the steady state for every possible combination of valves. The equation system is solved numerically by the Newton-Raphson method where the solution is found by iterating:

$$x_{k+1} = -J^{-1}H + x_k \tag{6}$$

where

$$x = [\hat{v} \quad \hat{p}_A \quad \hat{p}_B]^T$$

$$H = \begin{bmatrix} Q_{PA} - Q_{AT} - A_A \cdot \hat{v} \\ Q_{PB} - Q_{BT} - A_B \cdot \hat{v} \\ A_A \cdot \hat{p}_A - A_B \cdot \hat{p}_B - F \end{bmatrix} \qquad J = \begin{bmatrix} -A_A & J_{1,2} & 0 \\ A_B & 0 & J_{2,3} \\ 0 & A_A & -A_B \end{bmatrix} \tag{7}$$

$$J_{1,2} = -\frac{Q_{PA} \cdot \alpha}{|p_S - \hat{p}_A|} - \frac{Q_{AT} \cdot \alpha}{|\hat{p}_A - p_T|} \qquad J_{2,3} = -\frac{Q_{PB} \cdot \alpha}{|p_S - \hat{p}_B|} - \frac{Q_{BT} \cdot \alpha}{|\hat{p}_B - p_T|}$$

The solutions found are accepted if the solution is within given pressure limits, otherwise it is discarded. In some cases, Newton-Raphson does not converge and the solution is discarded after a maximum number of iterations, say 10. The solutions found, describe the steady state for each of the possible DFCU states, or more exactly how the hydraulic cylinder will behave if that state is chosen. To achieve optimal control, this means that we must choose a control state which gives the minimal value of a cost function.

Selection of Optimal Control Optimal control means that the performance of the system is optimal with regard to a cost function. The performance in turn can be evaluated based on properties such as deviation of velocity and pressures with respect to given reference values. To make the usage of the hydraulic system more efficient, valve activity and power losses are also considered in the cost function. To find the optimal control state, the steady-state equation systems for each of the $(2^5)^4=2^{20}$ DFCU states are calculated with Newton-Raphson as described above. Each of the solutions is then evaluated using the cost function in (8), which gives a single number describing the penalty of the solution [1].

$$\begin{aligned} Cost = {} & (v_{ref} - \hat{v})^2 + |v_{ref}| \cdot W_{pres}\left\{(p_{A,ref} - \hat{p}_A)^2 + (p_{B,ref} - \hat{p}_B)^2\right\} \\ & + |v_{ref}| \cdot W_{pow}\{K_1(p_S - \hat{p}_B)Q_{PB} + K_2(\hat{p}_A - p_T)Q_{AT} \\ & + K_3(p_S - \hat{p}_A)Q_{PA} + K_4(\hat{p}_B - p_T)Q_{BT}\} \\ & + W_{sw}\{n_{PA,sw} + n_{AT,sw} + n_{PB,sw} + n_{BT,sw}\} \end{aligned} \tag{8}$$

Finally, the lowest cost solution must be found among the large number of solutions. With the given system, with four DFCUs each having five parallel valves, we have more than one million equation systems to solve. This becomes a real challenge when we add real-time constraints and require the computations to complete within a few milliseconds. Fortunately, this type of tasks which consist of a large number of calculations that are independent until the last stage when the solutions are compared, is fairly well suited for graphics processors.

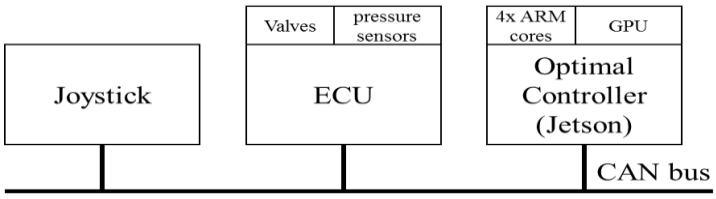

Figure 2. The main components of the control system

3. CONTROL SYSTEM ARCHITECTURE

The optimal controller is part of a larger system consisting of automotive ECUs controlling actuators and reading sensors, an input device (i.e. a joystick), and a CAN bus which connects these devices (see Figure 2). The hydraulic components are also modeled in the controller as the steady state equations with a few parameters (α, K_v, A_A, A_B) describing the properties of the hydraulic valves and cylinders.

To implement the controller we use the NVIDIA Jetson TK1 board which features a Tegra K1 system on chip, which includes a quad-core ARM Cortex A15 and a Kepler GPU with 192 CUDA cores. The board is further extended with a CAN bus interface connected to its PCI Express Mini slot. The controller runs Linux (Ubuntu) as its operating system and uses the CUDA run-time to access the GPU.

The controller software consists of two parts: a single thread that runs on one ARM core and communicates with the CAN bus and triggers the second part, which is the actual model based controller which runs on the GPU. From a real-time perspective, what we are interested in is how fast a new control signal is produced. More precisely, how long the delay is between sending the controller a request on the CAN bus until the response is received, and how much this delay varies.

3.1. Parallel Controller for GPU

A graphics processor is a massively parallel computation platform. To enable a program to utilize the full computational capacity of a GPU, the program needs to be constructed to reflect the underlying single instruction multiple data (SIMD) architecture, as some programming constructs will limit the parallelism and thereby also the utilization of the processor.

The programming model of a graphics processor is shown in Figure 3. Computations are organized into multiple levels, where the lowest unit of a single sequential computation is a thread while a block is a group of threads that virtually execute the same instruction simultaneously. The blocks are further organized into grids which provide the means for the programmer to organize the computations into independent blocks. The division into blocks and grids also dictates how threads can share memory. Each thread has its own registers, and the threads in a block are allocated fast local memory called shared memory, which, as the name implies, is used for sharing data between threads in the same block. Threads in different blocks can share data through global memory which is large but slow compared to the shared memory. The global memory is also used for inputs and outputs of the GPU.

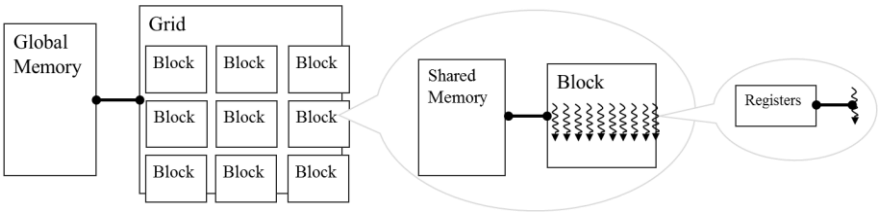

Figure 3. The GPU programming model

Work Distribution The controller algorithm is well suited for being distributed on a GPU. The computations can be split into two parts. First, a large number of independent equation systems (each valve combination) are solved and a cost function is evaluated for the solutions to the equation systems. Second, the cost function values are compared and the optimal result with respect to the cost function is chosen. The equation solver is computationally expensive while the memory accesses are few and regular. The only inputs are the measured pressures (p_S, p_A, p_B) which are common for all tasks, and the initial solution ($\hat{v}$, $\hat{p}_A$, $\hat{p}_B$) for Newton-Raphson which is individual for each valve combination. The output for each of the equations is the result of the cost function and the solution to the equation system.

The high-level structure of the computations is shown in Figure 4. The calculations are divided into tasks horizontally, with the computations of a thread shown as an arrow which starts and ends in a memory block. The wide memory blocks between the tasks represent global memory while the narrower boxes are shared memory which can be used for communication between threads within a block. The global memory is used for keeping results between different invocations of the controller and for sharing results with the general purpose processor. The global memory accesses of the Newton-Raphson and cost functions are regular in the sense that successive threads access adjacent memory locations. This is beneficial because global memory is accessed in larger chunks by the memory controller of the GPU and as the threads within a warp access adjacent locations, the number of memory transactions is minimized. In practice the data structures are structured such that a thread uses its thread index plus an offset to access its data.

In our particular case, with the 4x5 valve system, the results from the equation solver is about one million 4-tuples with the three estimated variables and the cost value: ($\hat{v}$, $\hat{p}_A$, $\hat{p}_B$, *cost*). To minimize the number of iterations required by Newton-Raphson, these values can be used as the start values of the following invocation of the controller. The physical properties that affect the solution to the equation system is the external force F (calculated from the measured pressures as in equation (5)) and the supply pressure p_S.

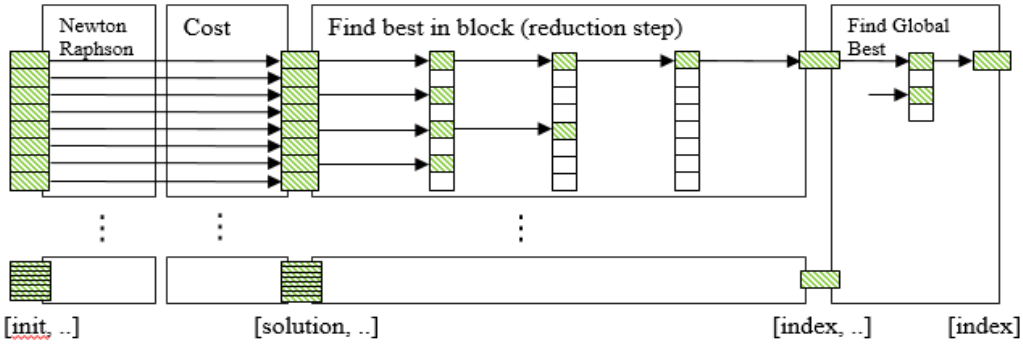

Figure 4. The structure of the computations and memory accesses

When there are only small changes in these physical values, only a few iterations are needed to find the new steady state. This way, the average runtime of the controller can be diminished, however, it does not improve the worst case. The speedup from this optimization is shown in Table 1 as *start from previous*, where the speedup is measured after the optimizations above in the table already has been applied. The two last rows in the table, which describe the impact of reusing previous solutions, is measured for the case where the external conditions do not change and a second case where the external load increases linearly. As expected, the speedup is smaller when there is a change; the impact of external conditions will be further discussed in the next section.

In order to find the optimal control state we compare the costs for each valve state and choose the state with the lowest cost. In practice, this is a straightforward reduction problem on the GPU. As shown in Figure 4, in each reduction step each thread compares two values and chooses the better one. This way, all N solutions can be compared in a $log_2 N$ steps.

Code Optimization The computationally most expensive part of the controller is the Newton-Raphson iterations. The pseudo-code for this is presented in Algorithm 1 where the calculations correspond to solving the steady state equations in (5) by using (7). The first part of the equation system, Q_{PA}, which corresponds to (1), is described more in detail and is highlighted in Algorithm 1, while the other parts are similar and have been omitted. The instructions within these few lines of code have a significant impact on the performance of the controller, as they are repeated up to 10 times for each of the 2^{20} equation systems. Optimizing this part of the controller is, on the one hand, about minimizing the time one iteration takes, and on the other hand, about minimizing the number of iterations needed. The following optimizations were needed to decrease the runtime of the controller from about 40 ms to less than 10 ms which is the given deadline.

It is obvious from Equations (1) to (4) that the number of power functions to be computed is significant. In previous work, α has been approximated by the square root as the value of α typically is close to 0.5, which makes the computations faster [5]. One of the goals with using an embedded GPU in the controller is to enable more precise control, and for this reason it is important to be able to use more precise and individual values of α for each of the 20 valves. For this reason, one iteration of the Newton-Raphson solver contains 20 power functions. The values that are remembered between computations or iterations are only the start values for the next iteration of Newton-Raphson. For this reason, we can use the *fast math* library to favor speed over precision [6]. The measured difference between computed results when the fast math functions are used are several orders of magnitude smaller than the precision of the results we are interested in, and the precision errors do not propagate and grow larger as the results are recalculated every iteration. The impact on speed, however, is significant. We measured a speedup of about three times as a result of using *fast math* (see Table 1).

Table 1. Impact of optimizations

Optimization	Time	Std. Deviation	Comment
Sequential ARM	1350 ms	16 ms	-
Original GPU	44.86 ms	0.15 ms	-
+ fast math	13.56 ms	0.02 ms	error < 10^{-6}
+ break illegal	9.92 ms	0.08 ms	-
+ signed pow	8.61 ms	0.10 ms	-
+ start from previous	5.63 ms	0.15 ms	when no change
+ start from previous	7.19 ms	-	when F changes

Algorithm 1: Newton-Raphson GPU pseudo code for equation system (5).

$idx = BlockIdx \cdot BlockDim + ThreadIdx$
$u_{PA}, u_{AT}, u_{PB}, u_{BT} = f(idx)$ ▷ Give each thread an individual valve combination
$v, p_A, p_B = solution[idx]$
repeat
  $diff = p_S - p_A$ ▷ First part of (5): $\sum_{i=1}^{n} u_{PA,i} \cdot K_{v_{PA,i}} \cdot SP\,(p_S - p_A)^{\alpha_{PA,i}}$
  for $i \in 0..4$ **do**
    $p = powf(fabsf(diff), \alpha_{PA,i})$
    $u_{PA,i} = u_{PA}$ bitwiseand $(1 << i)$
    $H.x = H.x + u_{PA,i} \cdot K_{v_{PA,i}} \cdot copysignf(p, diff)$
  end
  $J_{1,2} = -H.x \cdot \alpha / fabsf(diff)$
  $H.x, H.y, H.z, J_{1,2}, J_{2,3} = ...$ ▷ According to the other parts of (5)
  $invdetJ = 1.0/(A_A \cdot A_A \cdot J_{2,3} + A_B \cdot A_B \cdot J_{1,2})$
  $\delta_x = (A_A \cdot J_{2,3} \cdot H.x - A_B \cdot J_{1,2} \cdot H.y - J_{1,2} \cdot J_{2,3} \cdot H.z) \cdot invdetJ$
  $\delta_y = (-A_B \cdot A_B \cdot H.x - A_A \cdot A_B \cdot H.y - A_A \cdot J_{2,3} \cdot H.z) \cdot invdetJ$
  $\delta_z = (-A_A \cdot A_B \cdot H.x - A_A \cdot A_A \cdot H.y + A_B \cdot J_{1,2} \cdot H.z) \cdot invdetJ$
  $v, p_A, p_B = \delta_x, \delta_y, \delta_z$
  $residual = fabsf(\delta_x \cdot 10.0) + fabsf(\delta_y \cdot 10^{-6}) + fabsf(\delta_z \cdot 10^{-6})$
until $(iter \leq maxiter \vee residual \leq maxresidual \vee (iter \geq 4 \wedge illegalpressure))$;
$solution[idx] = v, p_A, p_B$

The best optimization is to avoid unnecessary work. Clearly, if we can deduce before the calculations that the solution will be discarded, time should not be spent on calculating these. Also, when a solution clearly converges towards an illegal state, it is unnecessary to continue searching for the exact solution. In a sequential program, it is trivial to implement conditional code that stops iterating when some condition is satisfied. On the GPU, the computational work is divided into groups of 32 threads called warps. The threads in a warp run physically in parallel. Branch divergence occurs within a warp when there is data-dependent branches. When the threads of the warp diverge as a result of a conditional statement, each path of the conditional code is executed disabling the threads that does not take that path. This has some implications on how the device should be programmed as terminating one thread when a solution either is found or discarded, does not enable the core for new calculations as the thread must wait for the other threads in the warp to terminate.

The algorithm is essentially a large repeat-until statement containing the Newton-Raphson iterations. While it is important that an iteration of the solver is as fast as possible, the number of iterations is equally important. This is also a case of branch divergence as the threads of a warp must wait until all the other threads of the warp finish their iterations. Obviously, the better the initial solutions are, the fewer number of iterations is needed. A second issue is that threads that do not converge towards a legal solution should be identified as soon as possible and the iterations terminated. Measurements show that the solver has converged close to the final solution after a few iterations, and on average, a thread is finished after 4 iterations. When the solution is outside the allowed pressure levels after 4 iterations, we assume that the final solution will not be a legal solution. To make this claim stronger, the iterations are always started from a legal state, either from the previous result or if the previous state was not legal,

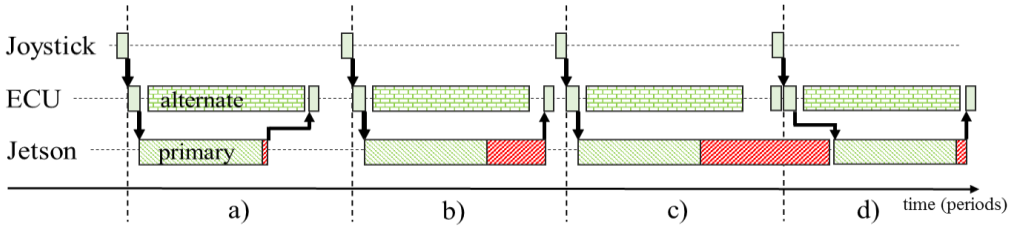

Figure 5. A timeline for four periods of the control system. The only varying property is the jitter of the optimal controller.

from the middle of the range of allowed pressure values. The check needs to be delayed until after a few iterations as the first steps of Newton-Raphson may be large and temporarily be outside the allowed range. We measured a speed-up from about 13 ms to 10 ms from this optimization, this is shown as *break illegal* in Table 1.

In the equation system, the only part that potentially needs conditional code is the signed power $SP(|x|)^{\alpha}$ where the result of the power function is multiplied with minus one if x is negative. A more efficient alternative is to use the *copysignef* function which applies the sign of one variable to another, as is seen on lines 7 and 9 in Algorithm 1. This rather small modification of the code improves the speed of the controller, roughly with 1.5 ms which is close to 15% of the runtime (see Table 1).

With these optimizations of the code, we are able to achieve a primary controller with a delay small enough to work in a system where the control signal is updated every 10 ms. It is, however, difficult to give any guaranties that the controller will not miss deadlines due to its complexity. This, in addition to that it is hard to guarantee functional correctness, is why the safe alternative controller is needed. To give some estimate of the quality of the control system, the success rate of the primary controller will be measured in the next section.

4. DELAY AND JITTER OF THE OPTIMAL CONTROLLER

In the previous sections we have shown that an embedded GPU can be well suited for calculating an optimal control signal for a digital valve system. The exact speed of the computations is not as such interesting as the control system could be designed with a slightly slower sampling period if needed, still, it shows that the GPU can perform the calculations well within a required time frame of 10 ms. The complexity of the optimal controller including the operating system and GPU drivers adds a level of uncertainty to the time it takes to produce the results, and makes it impossible to verify the real-time properties of the optimal controller. The real-time properties of the whole control system must still hold. For this reason, the ECU controlling the valves also runs a simplified alternative controller which is verified to produce a legal, but not necessarily optimal, solution within the given time frame.

To achieve fault tolerance, the alternate controller must have been verified to have certain properties and is run on a hardware platform targeted towards reliable real-time systems. Verification of digital hydraulics controllers implemented as Simulink models have been presented in [7, 8]. By using such models for the alternate controller while the primary controller is implemented on the embedded GPU, both performance and safety aspects

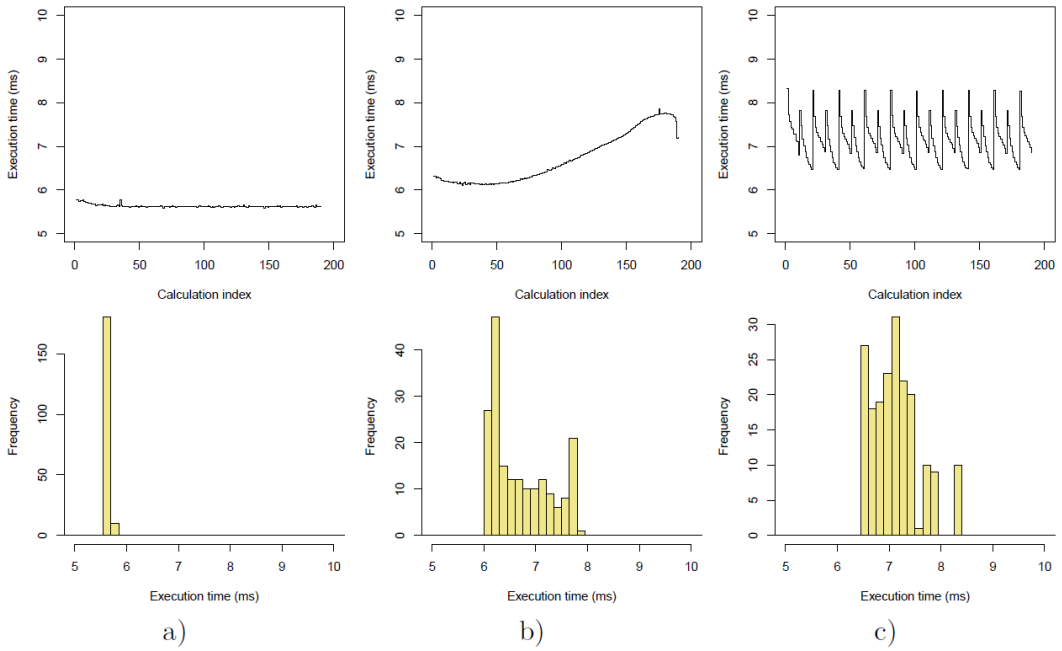

Figure 6. The response time (top) and the distribution (bottom) of the controller during 2 seconds of operation, with an external force which is a) constant, b) slowly changing, c) switching between extremes

are addressed. An alternative approach to achieve more computational performance is to generate parallel programs from such Simulink models. In [9], an approach for derivation of parallel programs from Simulink models for a many-core platform is presented. However, such an approach is not possible in our case as the GPU needs to be carefully optimized for high performance and because of the complexity of drivers, no guarantees could be given.

The operation of the control system is illustrated in Figure 5. The component named *joystick* represents the part of the system that converts the input of the machine operator to the desired value (velocity) of the hydraulic cylinder. The joystick periodically sends the desired velocity after which the ECU sends its measurement of pressures, calculates a control signal, and receives a control signal from the optimal controller. The runtime of the optimal controller is illustrated as a minimum delay plus jitter, which is a result of system properties that are out of our control. Figure 5 shows a few periods each with one scenario regarding the total delay of the optimal controller we need to consider: a) the optimal controller finishes before the ECU, b) the ECU must wait for the optimal controller, c) the optimal controller misses a deadline, and d) the previous deadline miss delays the start of the computations of the next period. For efficient control, deadline misses of the optimal controller should be extremely rare.

Distribution As presented in the previous section, the delay of the controller grows slightly when the inputs (F, p_S) change their values, and more iterations are required to find the steady state. Another property of the controller is that different combinations of input values result in variations in the delay; the reason for this is that a larger number of legal solutions implies that the controller cannot terminate as many iterations early. The variations in the controller delay was measured with three different external conditions: 1) a constant load, 2) a load that changes slowly, and 3) a load that jumps between two

extremes. The two first conditions correspond to normal operation of a work machine while the third is an extreme case where the machine drops the load ten times every second. The third case is meant as a stress test of the controller.

The measurement results from running the controller for two seconds are shown in Figure 6. As expected, the constant load performs extremely well as, after a few iterations, the solutions to the steady state equations are found and are used as starting values for the following runs. We can see from the histogram in Figure 6a that there are only small variations in the run-time. The more interesting cases, where the external force changes, the delay of the controller obviously grows and varies more. Still, for both cases, the deadlines are met. In the third case, where the external load varies between extremes, we can see peaks in the controller delay at the times when load changes. This is an expected result as the start values of Newton-Raphson then are further away from the new steady state, which leads to more iteration.

Worst Cases The previous measurements show how the controller works under normal operation. As the measurements only correspond to a few seconds of operation, no sporadic variation of the controller delay was identified. To get a more realistic view of how often a deadline miss may occur, and for how many periods the miss affects the controller, a second much larger experiment is needed. We constructed an experiment where the controller is run 10 million times, which corresponds to roughly 28 hours of operation. In order to model a realistic case, the controller input is a combination of a slowly changing load with large variations every few seconds. The recorded execution times are then used to analyze how often deadlines are missed and how many samples are affected by a deadline miss.

The first metric simply describes the number of consecutive deadline misses. What this means is that, when a deadline miss occurs, the start of the next computation may be delayed which in turn may result in several deadline misses. The controller misses its deadline when the delay of the controller exceeds 10 ms, when this occurs, the controller misses the following deadline if the sum of the delays from both periods exceeds 20 ms. This means that two consecutive deadline misses may occur also when the second computations is fast enough. During the 28 hours of operation the controller exceeded the 10 ms deadline three times, one of these resulted in a sequence of 4 consecutive deadline misses. This measurement corresponds to the *occurrences* in Table 2.

The second metric describes the worst case execution time for sequences of consecutive controller invocations of different length. In practice, this computation compares every subsequence from the measured controller delays of length *n* and chooses the maximum. This can be described as: $D_n = \max_{k>0}\left(\sum_{i=k}^{k+n} delay_i\right)$, and the results are presented as *worst case* in Table 2. As expected, the sum of consecutive delays converge towards an average run-time rather fast also for the worst cases. This is a promising result as, even though it is not possible to give guarantees regarding the timing of the GPU platform, deadline misses are rare.

Table 2. Worst case execution times and deadline misses for 10 000 000 runs

# periods	1	2	3	4	5	6
deadline	10.0 ms	20.0 ms	30.0 ms	40.0 ms	50.0 ms	60.0 ms
worst case	18.1 ms	25.7 ms	33.2 ms	40.8 ms	48.4 ms	56.0 ms
occurrences	3	1	1	1	0	0

5. CONCLUSIONS

In this paper we investigate how GPUs can be used as part of a control system for digital hydraulics. The results show that the massive parallelism of such devices will enable many features that are not possible with ordinary processors. However, the complexity of both GPU software and hardware makes it hard to give guarantees regarding timing and it is necessary to combine these with reliable components performing backup computations in case of timing failure. The experiments show that a GPU controller works well in general and deadline misses are extremely rare. This makes GPUs a promising candidate for improving controller performance.

REFERENCES

[1] Matti Linjama, Mikko Huova, Pontus Boström, Arto Laamanen, Lauri Siivonen, Lionel Morel, Marina Waldén, and Matti Vilenius. Design and implementation of energy saving digital hydraulic control system. Proceedings of 10th Scandinavian International Conference on Fluid Power (SICFP'07). Tampere University of Technology, 2007.

[2] G.A. Elliott and J.H. Anderson. Real-world constraints of gpus in real-time systems. In Embedded and Real-Time Computing Systems and Applications (RTCSA), 2011 IEEE 17th International Conference on, volume 2, pages 48–54, Aug 2011.

[3] A.L. Liestman and R.H. Campbell. A fault-tolerant scheduling problem. Software Engineering, IEEE Transactions on. 1986.

[4] Petr Alexeev, Pontus Boström, Marina Waldén, Mikko Huova, Matti Linjama, and Kaisa Sere. Fault-tolerant scheduling of stateful tasks in uniprocessor real-time systems. In Proceedings of the 3rd International Conference on Pervasive Embedded Computing and Communication Systems, pages 189–194, 2013.

[5] Matti Linjama and Matti Vilenius. Improved digital hydraulic tracking control of water hydraulic cylinder drive. International Journal of Fluid Power, 2005.

[6] NVIDIA. CUDA C Best Practices Guide Version 7.5. 2015.

[7] Pontus Boström, Matti Linjama, Lionel Morel, Lauri Siivonen, and Marina Waldén. Design and validation of digital controllers for hydraulics systems. Proceedings of 10th Scandinavian International Conference on Fluid Power (SICFP'07). Tampere University of Technology, 2007.

[8] Pontus Boström, Mikko Heikkilä, Mikko Huova, Marina Waldén, and Matti Linjama. Verification and validation of a pressure control unit for hydraulic systems. Software Engineering for Resilient Systems, Lecture Notes in Computer Science. Springer, 2014.

[9] Sergey Ostroumov, Pontus Boström, and Marina Walden. Derivation of parallel and resilient programs from simulink models. 23rd Euromicro International Conference on Parallel, Distributed, and Network-Based Processing. Conference Publishing Services, 2015.

On the Control Strategy for Pneumatic Robot Driven by High Speed Solenoid On/OFF Valves above Rough Ground

Shi Guanglin, Lee Binjie, Yang Lihua
School of Mechanical Engineering of Shanghai Jiaotong University
Shanghai, China, 200240
shiguanglin@sjtu.edu.cn

ABSTRACT

Pneumatic system has good flexibility, and has clean, safe, light and relatively low cost as its advantages, which make it is able to work in special environment. However, the control strategy has to be modified when the pneumatic robot works on a walking machine. Thus research on the control strategy for pneumatic robot driven by high speed on/off valves above rough ground has practical application. In this paper, experimental research based on the pneumatic robot worked on a walking machine has been discussed. Furthermore, a kind of position feedback fuzzy control strategy with pressure compensation to improve system response and position accuracy is introduced in this paper. Besides, the modeling and simulation of pneumatic robot driven by high speed on/off valves above rough ground has been done in AMESim. The effectiveness of the control strategy has also been proved by co-simulation between AMESim and Matlab/Simulink. On the other hand, an experimental platform is built with a 6-DOF parallel platform for simulating the rough ground and a pneumatic robot driven by high speed on/off valves with 3 DOF is designed and equipped above it. At the same time, both the high speed solenoid on/off valves and proportional directional valves are used to control the pneumatic robot and the comparative analysis is made in this paper. Both the simulation and the experimental results prove that the position feedback fuzzy control strategy with pressure compensation can improve the motion ability and the robust characteristic of the pneumatic robot driven by high speed on/off valves. On the other hand, the experimental results show that the joint's tracking characteristics are fine under this control strategy.

KEYWORDS: pneumatic robot, high speed solenoid on/off valve, proportional directional valve, 6-DOF platform, pressure compensation

1. INTRODUCTION

1.1. Background

With the development of robotics, kinds of robot turn into our factory and replace people to do routine work, especially under the environment of high temperature and high pressure. Moreover, pneumatic systems in fixed installations, such as factories, use compressed air, which usually has moisture removed, and a small quantity of oil is added at the compressor to prevent corrosion and lubricate mechanical components [1].

Besides, pneumatic robots are easily designed using standard cylinders and other components, which have long operating lives and require little maintenance. Thus, pneumatic robots are usually used as agricultural harvesting robot, painting robot and so on.

1.2. Related research

The University of California presents the state space of a single valve control cylinder form linear mathematical model and uses PD control strategy to control servo-pneumatic system with large load [2]. Technische Universität Ilmenau deduces the system zero dynamics equation and control ratio based on the feedback linearization [3]. Motion curve is solved by pressure signal and reduces the motion time. Uni DuE university studies the modeling of pneumatic rodless cylinder servo system, using multidimensional membership function, which has better approximation ability than one dimensional membership function [4]. University of Manitoba in Canada proceeds a pressure cascade control to improve the anti-jamming ability significantly without increase the complexity of external loop controller [5]. Xi 'an Jiaotong University in China studies on the mathematical model of pneumatic servo position control system and designs PID algorithm with friction feedforward and pressure feedback [6].

1.3. Main work

However, the control strategy has to be modified when the pneumatic robot works on a walking machine [7]. Thus the research on the control strategy for pneumatic robot driven by high speed on/off valves above rough ground has practical application. Therefore, an experimental platform is built with a 6-DOF parallel platform for simulating the rough ground and a pneumatic robot driven by high speed on/off valves with 3 DOF is designed and equipped above it. Furthermore, both the high speed solenoid on/off valves and proportional directional valves are used to control the pneumatic robot and a comparative analysis is made [8]. The object of this paper is to implement inexpensive on/off solenoid valves, rather than expensive proportional valves or servo valves, to develop a fast, accurate, inexpensive and intelligent pneumatic control system applied in the robot.

2. ROBOT STRUCTURE

The pneumatic robot consists of three jointed arm, which is driven by one vane-type pneumatic rotary cylinder and two linear cylinders, and a pneumatic gripper assembled as the end effector. These three joints named waist joint, shoulder joint and elbow joint. The 3D prototype is designed with UG software and 2D drawings are created with AutoCAD, as shown in Figure 1. The vane-type pneumatic rotary cylinder's rotate diameter is 40mm and rotate angle is 270 °, whose model type is FESTO DSMI-40-270-A-B. Besides, the shoulder joint is driven by DSNU-40-125-PPV-A cylinder and the elbow joint is driven by DSNU-32-125-PPV-A cylinder. The pneumatic paw is driven by three 10mm cylinder with 47.1N thrust force and 39.6N pull force under 6bar pressure.

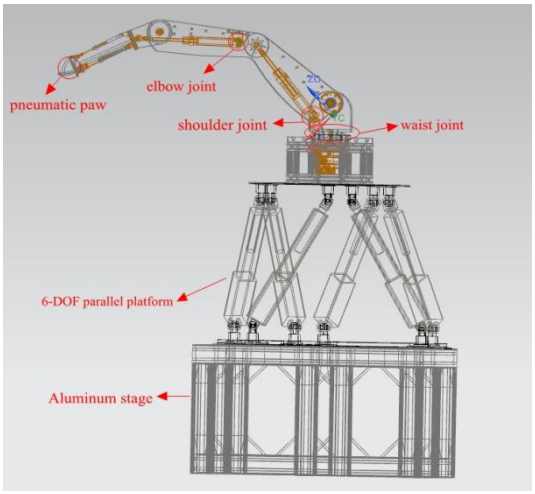

Figure 1. Experimental platform

The experimental platform consists of two parts, the pneumatic robot and a 6-DOF parallel platform. The 6-DOF parallel platform is built to heave, sway and surge, simulating the rough ground with rigid against unwanted movement [9]. Moreover, the technical index is shown in Table 1.

Table 1. Technical index for 6-DOF parallel platform

DOF	Range	Velocity	Acceleration	Size	Value
Surge	±190mm	600mm/s	0.6g	Load	100kg
Sway	±190mm	600mm/s	0.6g	Upper radius	250mm
Heave	±190mm	650mm/s	0.6g	Lower radius	300mm
Pitch	±20 °	25 °/s	200 °/s^2	Upper joint beeline	100mm
Yaw	±20 °	25 °/s	200 °/s^2	Lower joint beeline	120mm
Roll	±20 °	25 °/s	200 °/s^2	Servo cylinder length	610mm

The pneumatic robot is driven by high speed on/off valves: two high speed on/off valves are used as a pair to control one chamber of the vane-type pneumatic rotary actuator [10]. The schematic diagram is shown in Figure 2. If the control signal to the valve is ON and ON/OFF, the chamber is connected to the air source and the pressure will be raised up. If the control signals are OFF, the chamber is isolated. If the control signals are OFF and ON, the chamber is exhausting. In conclusion, the combination of two high speed on/off valves with PWM control algorithm can theoretical control the motion of the rotary actuator [11]. Besides, one high speed on/off valve is used for each chamber of linear cylinder and the chamber cannot be isolated. And the photography of experimental platform is shown in Figure 3.

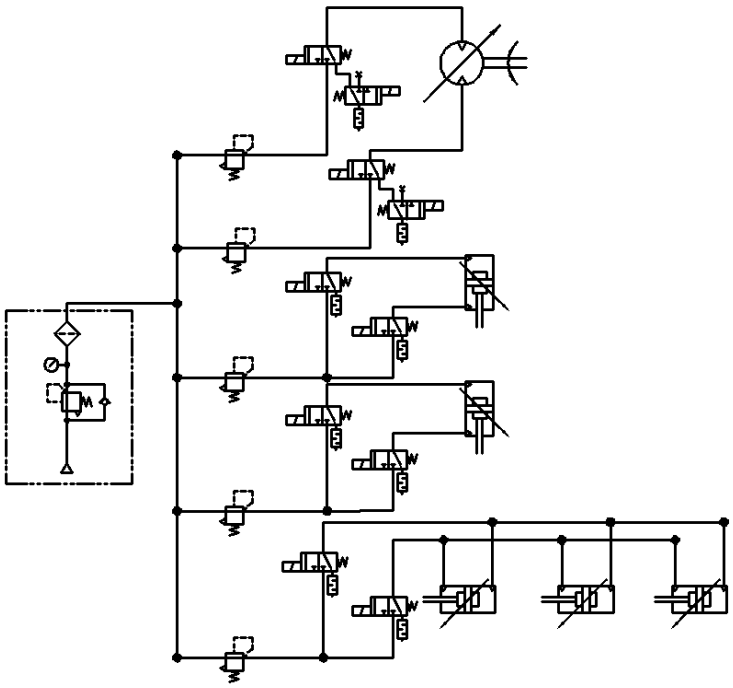

Figure 2. Schematic of system with high speed solenoid on/off valves

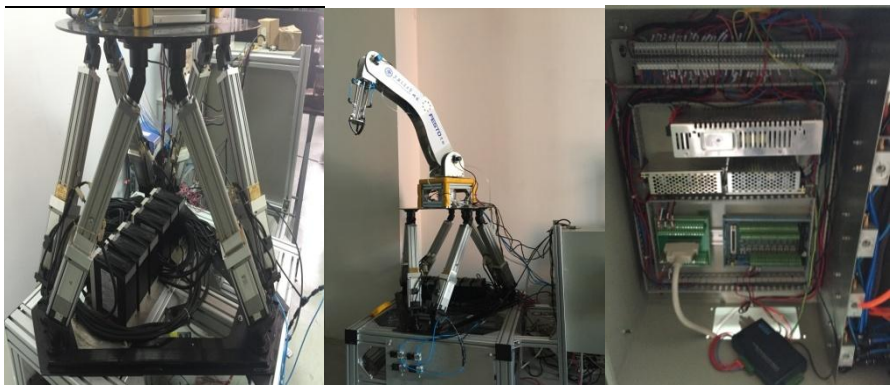

Figure 3. Photography of experimental platform

3. MODELING AND SIMULATION

For the 6-DOF parallel platform, the control strategy is that tracking a certain point in the upper platform and solves the motion curve for each electric cylinder through reverse kinematic analysis [12]. In this paper, the coordinate system for the 6-DOF parallel platform is set as Figure 4. The static coordinate system is named $(Oxyz)_0$ and the moving coordinate system is named $(Oxyz)'$. The original ground points' spatial coordinates homogeneous matrix in the static coordinate system is solved according to Table 1, which is shown in Equation (1) and Equation (2).

$$\mathbf{A}=\begin{bmatrix} 244.95 & 244.95 & -79.17 & -165.78 & -165.78 & -79.17 \\ -50 & 50 & 237.13 & 187.13 & -187.13 & -237.13 \\ 0 & 0 & 0 & 0 & 0 & 0 \\ 1 & 1 & 1 & 1 & 1 & 1 \end{bmatrix} \quad (1)$$

$$\mathbf{B}=\begin{bmatrix} 198.93 & 198.93 & 95.01 & -293.94 & -293.94 & 95.01 \\ -224.56 & 224.56 & 284.56 & 60 & -60 & -284.56 \\ 0 & 0 & 0 & 0 & 0 & 0 \\ 1 & 1 & 1 & 1 & 1 & 1 \end{bmatrix} \quad (2)$$

Once the curves for all coordinates in transfer matrix **T** (Equation (3)) are determined, all electric cylinders' routines are obtained from Equation (4).

$$\mathbf{T}=\begin{bmatrix} \cos\theta_y\cos\theta_z & -\cos\theta_x\sin\theta_z+\sin\theta_x\sin\theta_y\cos\theta_z & \sin\theta_x\sin\theta_z+\cos\theta_x\sin\theta_y\cos\theta_z & x \\ \cos\theta_y\sin\theta_z & \cos\theta_x\cos\theta_z+\sin\theta_x\sin\theta_y\sin\theta_z & -\sin\theta_x\cos\theta_z+\cos\theta_x\sin\theta_y\sin\theta_z & y \\ -\sin\theta_y & \sin\theta_x\cos\theta_y & \cos\theta_x\cos\theta_y & z+582.68 \\ 0 & 0 & 0 & 1 \end{bmatrix} \quad (3)$$

$$\Delta d_k=\left|\left(\mathbf{T}\cdot\mathbf{A}-\mathbf{B}\right)\cdot\mathbf{e}_k\right| \quad (4)$$

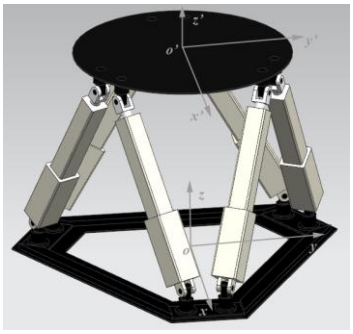

Figure 4. The coordinate systems for 6-DOF parallel platform

The LP-Research Motion Sensor CAN bus and USB version (LPMS-CU) is a miniature inertial measurement unit (IMU) / attitude and heading reference system (AHRS) and it's located at the top of the platform to measure the three angle and acceleration value. The unit is very versatile, performing accurate, high speed orientation and displacement measurements. By the use of three different MEMS sensors (3-axis gyroscope, 3-axis accelerometer and 3-axis magnetometer) drift-free, high-speed orientation data around all three axes is achieved (in Figure 5.). The LPMS-CU is connected to the host system via USB connection. Communication with high data transfer rates of up to 400Hz and internal sampling processing at 800Hz is possible. The LPMS-CU fits both machine and human motion measurements for size and cost sensitive applications.

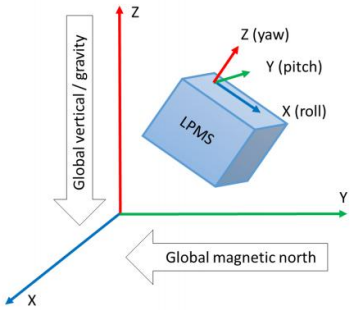

Figure 5. Relationship between local sensor coordinate system and global coordinates

Then, the motion algorithm introduced before in Equation (4) for 6-DOF parallel platform is simulated in Matlab/Simulink. The center point at the upper surface of the

platform is selected as the target point, whose motion curve is rotating along x-direction. Then the movement curve of each electric cylinder is solved in Simulink as in Figure 6. Moreover, these curves are imported into UG to simulate the motion of the platform, which is similar to the desired movement.

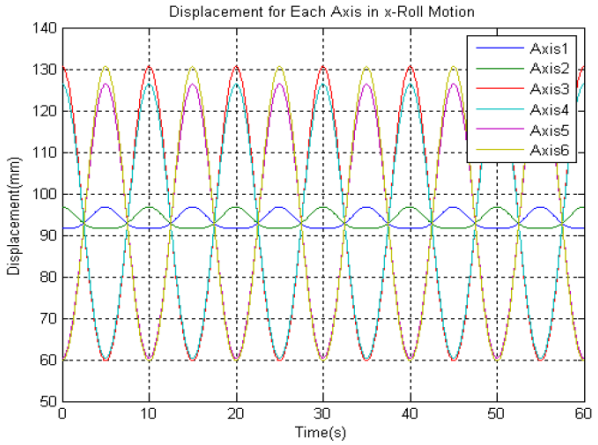

Figure 6. The displacement curve of each electro-cylinder

On the other hand, the system's transfer function can be obtained by valve flow equation, dynamic equation and pressure differential equation [13]. Besides, AMESim is skilled in modeling the pneumatic system, which can share with Matlab and other software for calculation. Thus, the schematic diagram of pneumatic system is built in AMESim and control algorithm is compiled in Matlab/Simulink(in Figure 7). Co-simulation is done to verify the strategy correctness. In the simulation, Fuzzy control algorithm with pressure feedback is used to control these high speed on/off valves. Besides, the fuzzy rule table is shown in Table 2. The mechanical arm exerts torque load on the waist angle, which is undetermined due to the 6-DOF parallel platform's attitude.

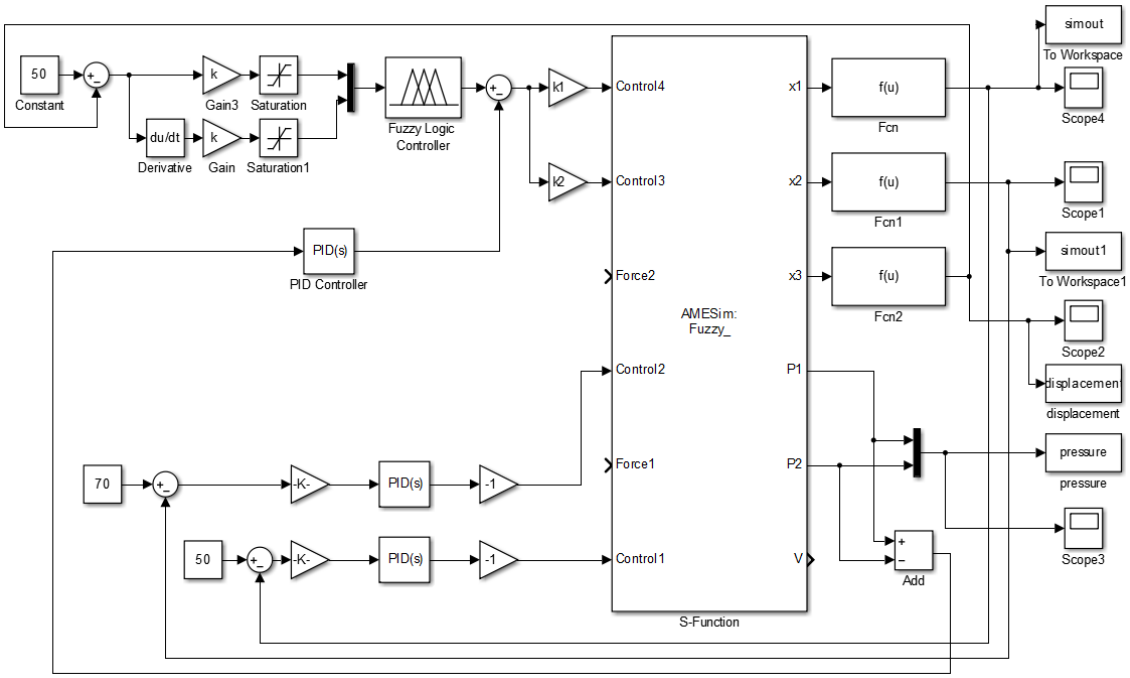

Figure 7. The control logical diagram in Simulink

Table 2. The fuzzy rule table in Simulink

MISO	NL	NS	ZO	PS	PL
NL	NL	NS	NS	NS	ZO
NS	NS	NS	NS	ZO	ZO
ZO	NS	NS	ZO	PS	PS
PS	ZO	ZO	PS	PS	PS
PL	ZO	PS	PS	PS	PL

In the co-simulation, the waist joint is considered important as the large load on it. These specifications for the pneumatic system are got in FESTO manual. With back pressure, vessel pressure is speed up effectively, and the back pressure is determined to be 3bar through simulation. In the simulation, the waist target angle is set to 50 °, and result is shown in Figure 8. It reveals that the waist angle takes 4s to reach the top with 10% overshoot and declined in 2s, with the steady error in 0.5 °.

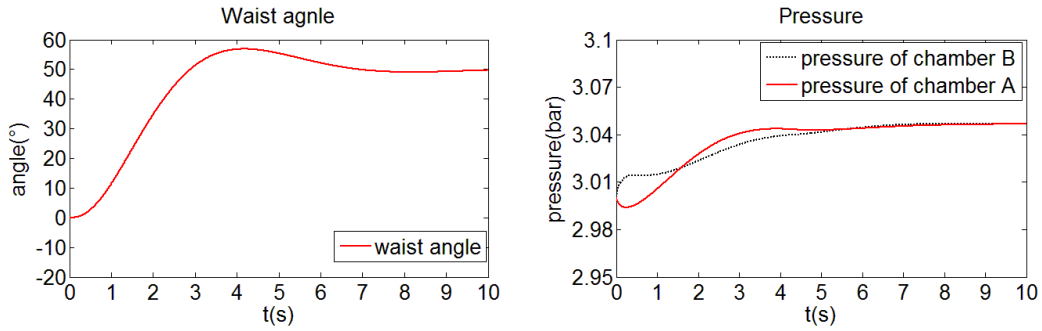

Figure 8. Waist angle and chamber pressure in simulation

3.1. Experimental purpose

In the experiment, the control strategy is compiled in LabVIEW, which is a development environment designed specifically to accelerate the productivity of engineers and scientists, with a graphical programming syntax that makes it simple to visualize, create, and code engineering systems. The control block diagram is shown in Figure 9. In the position controller, the input is position, position error and pressure of chamber A [14]. A fuzzy logical controller is used to determine the desired pressure of chamber A and depends on the position error and its derivative. Furthermore, another fuzzy logical controller along with integral element is used for pressure closed loop to achieve the desired pressure [15]. The signal flow graph for position controller is shown in Figure 10.

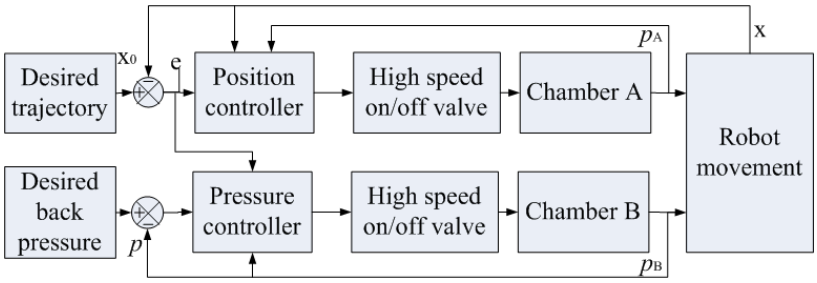

Figure 9. The control block diagram

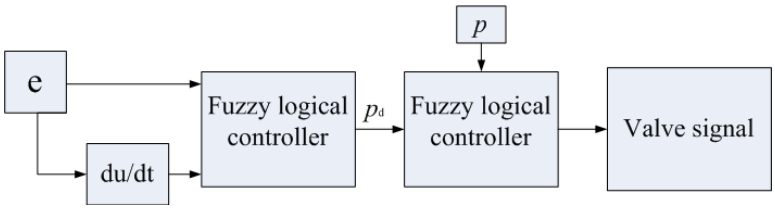

Figure 10. The signal flow graph for position controller

In the test, three kinds of condition are constructed and different experimental methods are performed.

(1) The 6-DOF parallel platform is stationary, the pneumatic robot's three joints are tested for positional accuracy.
(2) The 6-DOF parallel platform is in motion(rotating about x-y axis is used) and the pressure controller is self-adapted to keep the angle of joints still and pneumatic robot motionless.
(3) The 6-DOF parallel platform is inclined(a random attitude, pitch angle and yaw angle >5 °)and a disturbance is exerted, the robot need to be reset, especially the waist joint, which is driven by rotary cylinder with large load.

3.2. Stationary position tracking

First, a step position signal is tested for elbow joint, and the result is shown in Figure 11. The initial value is 70 ° and the target value is 100 °, the elbow joint takes 4s to arrive 100 ° and a small oscillation keeps for 3s until the angle stay at 100 °. Several step signals with different position are given, and the position error stays at about 0.5 °. The shoulder joint is driven by linear cylinder, which is similar to the elbow joint in both structural and result. The steady errors for elbow joint and shoulder joint are small, attributing to that the load is relatively low.

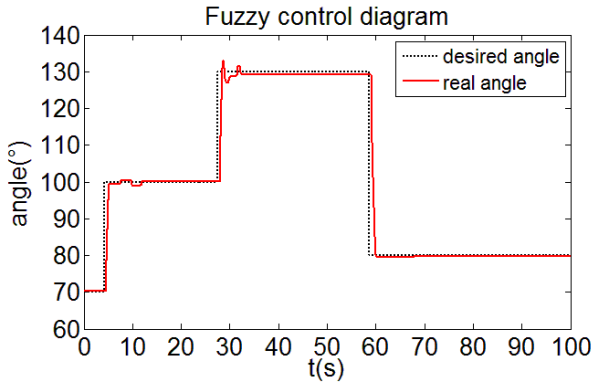

Figure 11. A step response for elbow joint

3.3. Stable position above rough ground

Then, the 6-DOF parallel is rotating about x-axis at -10 °-10 °. As pneumatic system has large compressibility and the robot is the load for rotating, the waist joint is unstable without pressure compensation. Thus, the LP-Research Motion Sensor is used to detect the *x*, *y*, *z* angle, which is the input for the pressure controller in Figure 9. Moreover, the robot can stay at any waist joint angle with pressure compensation and the experimental data is shown in Figure 12. Figure 12(a), 12(c) and 12(e) are waist angle, chamber

pressure and displacement of each cylinder for 6-DOF parallel platform without pressure controller. The waist angle is shaken largely and the pressures in both chambers are chaotic, due to the motion of 6-DOF parallel platform. However, the fuzzy pressure controller with attitude angle feedback can maintain the waist angle in ±0.15°, while the pressures in both chambers are orderly with the platform motion. These experimental results are shown in Figure 12 (b), 12(d) and 12(f). The photograph record is shown in Figure 13.

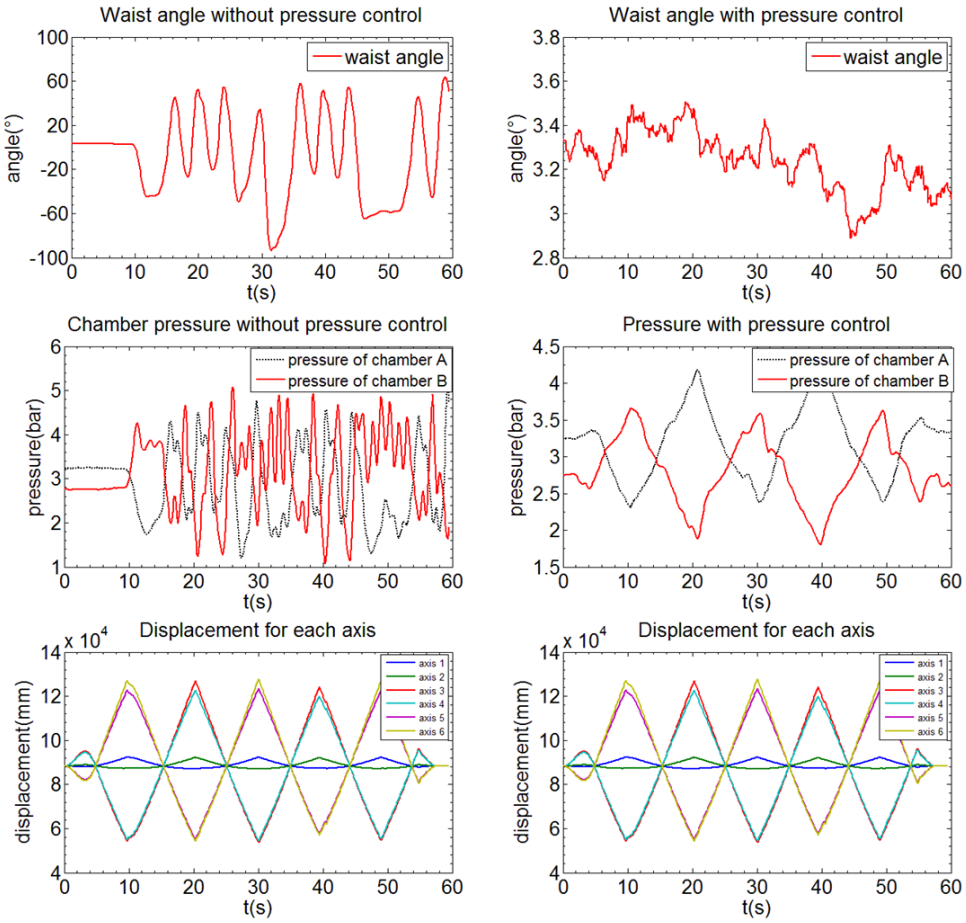

Figure 12. Stable position data with rotating 6-DOF parallel platform

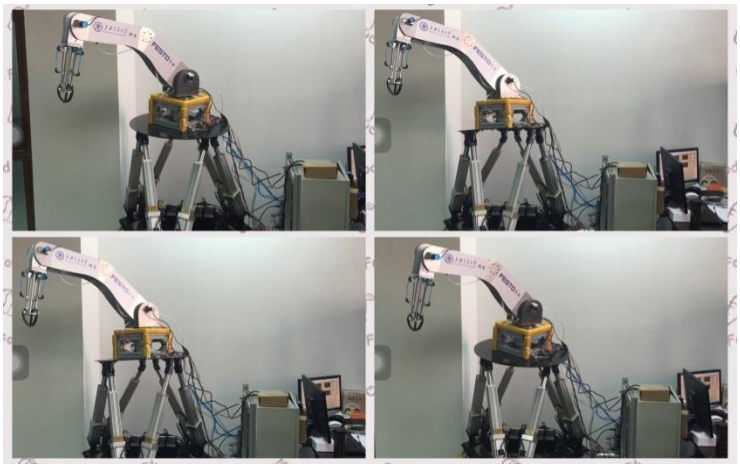

Figure 13. Photography of pressure controller with x-rotate

3.4. Position tracking above rough ground

Then, the 6-DOF parallel platform is set to inclined with surge angle at -5 ° and yaw angle at -7 °. Structurally, the waist joint is an oscillating cylinder with the mechanical arm as work load, whose weight is about 7kg. The cylinder is driven by high speed on/off valves or proportional directional valves. In the system with proportional directional valves, the pressure closed loop is designed as a combination of fuzzy control and integral element, which is able to keep the steady error at 0.01bar. In the position tracking, the overshoot is relatively large, while accommodation time is about 5s to increase the waist angle from 0 ° to 50 ° and the steady waist angle error is smaller than 1 ° (Figure 14). Besides, the system with high speed on/off valves can keep the steady angle error smaller than 1.5 ° (Figure 15). The pressures in both chambers are shown in Figure 16 and the control signals are shown in Figure 17. Because two valves are designed to control single chamber, the OFF/OFF signal combination is assumed to isolate the chamber from atmosphere. However the valve leakage disturbs the pressure balance, the PWM control signals for both valves are limited to 7ms as minimum intervals, which lead to the pressure in chamber is vibrate with the error about 0.1bar. Thus, the joint displacement is not as smooth as that with proportional directional valves.

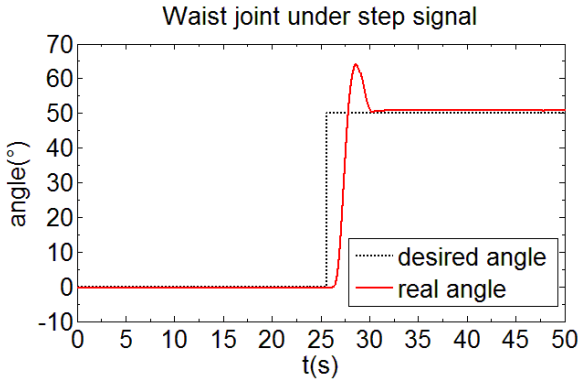

Figure 14. Waist joint angle diagram with proportional directional valves

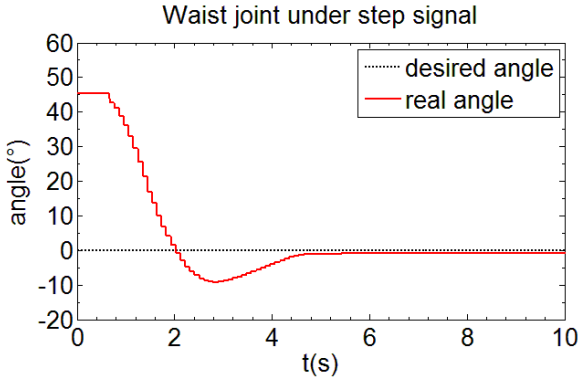

Figure 15. Waist joint angle diagram with high speed on/off valves

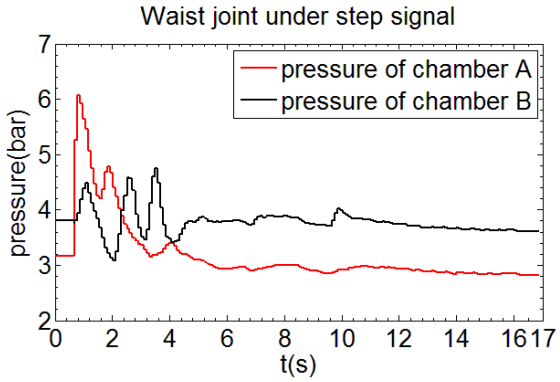

Figure 16. Waist joint pressure diagram with high speed on/off valves

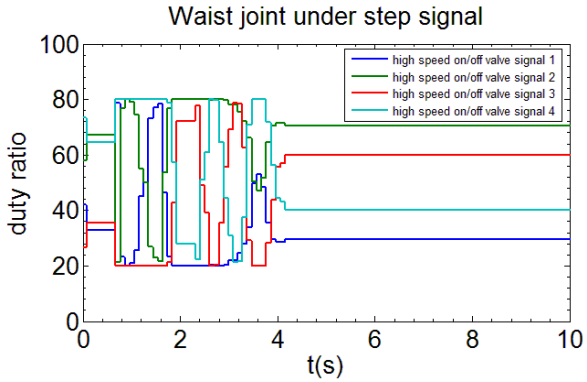

Figure 17. Waist joint control signal diagram with high speed on/off valves

In section 4.3, it is proved that the mechanical arm is able to keep stable while the 6-DOF parallel platform performs randomly. Furthermore, the pneumatic robot should overcome the disturbance which is much larger than the resistance with pressure control and forces a sway in each angle. Once the waist is forced from -5 °to -95 °, the controller eases the error in 6s, with final angle at -3.3 °, while the difference between initial angle and final angle is about 1.7 °. The results are shown in Figure 18 and Figure 19.

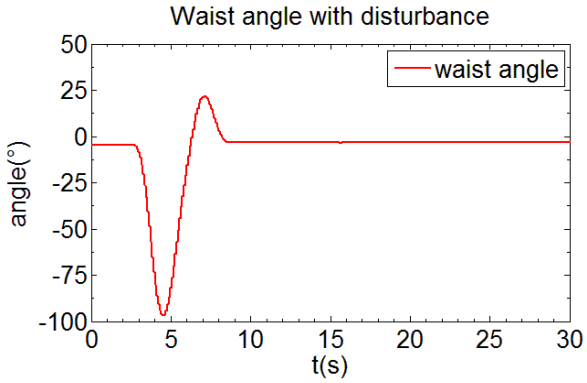

Figure 18. Waist angle after step disturbance

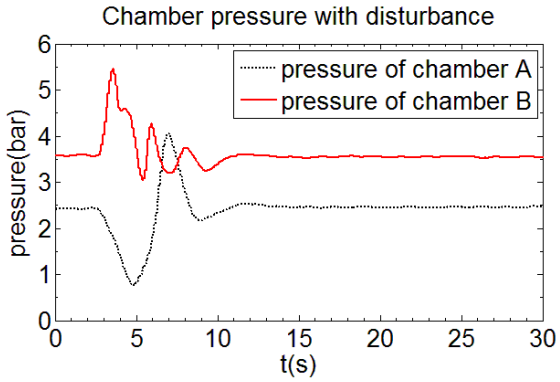

Figure 19. Pressure of each chamber after step disturbance

4. CONCLUSION

The experimental results prove that the position feedback fuzzy control strategy with pressure compensation can keep the steady error in 0.5 °while the platform is stationary with high speed on/off valves. Secondly, the pressure closed-loop control with attitude angle feedback can maintain the waist angle in ±0.15 °, while the pressures in both chambers are orderly with the platform motion. Thirdly, the pressure accuracy is 0.1bar and positional accuracy is 1.5 °with high speed on/off valves, which is based on the any attitude of the platform, though the chamber's pressure is tough than that with proportional directional valves. Finally, the robot has the ability to recover from large disturbance quickly, with the steady error less than 1.5 °.

REFERENCES

[1] Bobrow J.E, McDonell B.W. Modeling, identification, and control of a pneumatically actuated, force controllable robot. IEEE Transactions on Robotics and Automation, 1998, 14(5), pp. 732-742.

[2] Liu S, Bobrow J.E. An analysis of a pneumatic servo system and its application to a computer-controlled robot. ASME Journal of Dynamic Systems, Measurement and Control, 1988, 110(2), pp. 228-235.

[3] Sawodny O, Hildebrandt A. Aspects of the control of differential pneumatic cylinder. Proceedings of the 10th Japanese German Seminar on Nonlinear Problems in Dynamic Systems, Noto, Japan, Sep, 2002, pp. 247-256.

[4] Kroll A. Fuzzy-modeling of systems with uncertain nonlinearities and its application on pneumatic drives. Proceedings of the IEEE International Conference on Systems, Man and Cybernetics, Beijing, China, Oct, 1996, pp. 1056-1061.

[5] Karpenko M, Sepehri N. Design and experimental evaluation of a nonlinear position controller for a pneumatic actuator with friction. Proceedings of the 2004 American Control Conference, Boston, USA, Jun30-July2, 2004, pp. 5084-5089.

[6] Li XH, DU YT, et al. The control of pneumatic position servo system with compensation I-PD algorithm. Hydromechatronics Engineering, 2004, (1), pp. 58-59.

[7] Gulati N, Barth E.J. Pressure observer based servo control of pneumatic actuators. Proceedings of the 2005 IEEE/ASME International Conference on Advanced Intelligent Mechatronics, Monterey, California, USA, July 24-28, 2005, pp. 498-503.

[8] Jang J.S, Kim Y.B, Lee I.Y, et al. Design of a synchronous position controller with a pneumatic cylinder driving system. Proceedings of the SICE Annual Conference, Sapporo, Japan, Aug 4-6, 2004, pp. 2943-2947.

[9] K.D. Do, J. Pan. Nonlinear Control of An Active Heave Compensation System [J]. Ocean Engineering, 2008, (35), pp. 558-571.

[10] Zhu X, Tao G, Yao B, et al. Adaptive robust posture control of a parallel manipulator driven by pneumatic muscles. Automatica, 2008, 44(9), pp. 2248-2257.

[11] Tu H C, Rannow M B, Wang M, et al. Modeling and validation of a high speed rotary PWM on/off valve[C]. Proceedings of the ASME Dynamic Systems and Control Conference 2009. Hollywood, CA, USA, 2009, pp. 629-636.

[12] Yangjun Pi, Xuanyin Wang. Trajectory tracking control of a 6-DOF Hydraulic Parallel robot manipulator with uncertain load disturbances[J]. Control Engineering Practice, 2011, (19), pp. 185-193.

[13] Xue Yang, Peng Guangzheng, Fan Meng, Wu Qinghe. New Asymmetric Fuzzy PID Control for Pneumatic Position Control System. Journal of Beijing Institute of Technology, 2004, 13(1), pp. 28-31.

[14] Hamdan M, and Gao Z. A Novel PID Controller for Pneumatic Proportional Valves with Hysteresis, IEEE of Industry Applications Conference, 2000, Vol.2, pp. 1198-1201.

[15] Miyajima T, Fujita T, Sakaki K, et al. Digital control of high response pneumatic servo valve. Proceedings of the SICE Annual Conference, Sapporo, Japan, Aug4-6, 2004, pp. 787-792.

ENERGY EFFICIENT TRACKING CONTROL OF A MOBILE MACHINE BOOM MOCKUP

Adj. Prof. Matti Linjama, Dr. Tech. Mikko Huova,
Dr. Tech. Otso Karhu & Prof. Kalevi Huhtala
Tampere University of Technology
Department of Intelligent Hydraulics and Automation
P.O.Box 589
33101 Tampere, Finland
E-mail: matti.linjama@tut.fi

ABSTRACT

Energy efficiency of hydraulic machinery is an important trend. Another trend is more automatic machines, which sets new demands for the controllability of hydraulic actuators. High-performance distributed valve systems can satisfy these requirements. Recently, the authors have developed a new high performance digital hydraulic tracking control solution for force, velocity and position tracking. This paper further develops the solution by improving energy efficiency. A new method to control supply pressure is developed. Experimental results with a 1-DOF boom show that the new control solution can combine good controllability and energy efficiency.

KEYWORDS: Energy efficiency, tracking control, digital hydraulics

1. INTRODUCTION

Energy efficient motion control is an important challenge of hydraulic systems. One approach to reduce losses is to use independent metering valves [1–3]. Digital valve system is digital hydraulic version of independent metering valve, in which metering edges are implemented by parallel connected on/off valve series [4]. Important benefit of digital version is fast and amplitude-independent response time, which allows online switching between inflow-outflow and more energy efficient regenerative control mode [4]. However, the mode switching procedure presented in [4] is complex and it has many tuning parameters. Recently, the authors have developed high performance force controller, which has been used in the implementation of force, velocity and position tracking control [5, 6]. The solution allows also independent control of chamber pressures. This paper further develops the solution such that it is capable of energy efficient control. A new suboptimal solution is developed to control the supply pressure in energy efficient way. The solution is much simpler than solution presented in [4]. Experimental and simulated results with a 1-DOF boom show that it is possible to combine good controllability and energy efficiency.

2. CONTROLLER

2.1. Overview of the controller

The controller is presented in detail in [5] and only main points are repeated here. Figure 1 shows the overview of the control system. The inner-loop force controller is a non-linear selection scheme, which tries to find such valve openings that the estimated chamber pressures and piston force are close to the target values after one sampling period. The outer loop velocity controller is simple P-controller and PID-controller is used in the position loop.

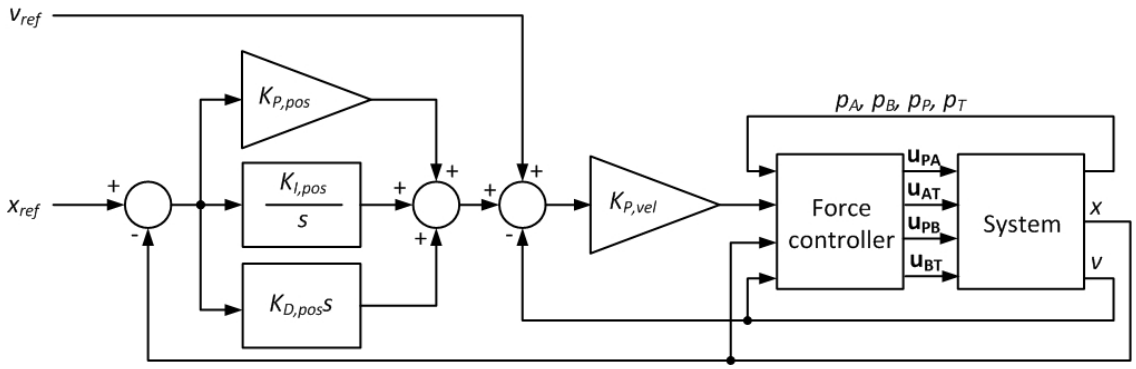

Figure 1. Block diagram of the controller.

2.2. Inner loop force controller

Consider a system in which inertia is so large that the piston velocity does not change significantly during one sampling period of the system. The pressure dynamics can be approximated as follows:

$$\begin{aligned}\dot{p}_A &= \frac{B_A}{A_A x + V_{0A}}\left(Q_{PA}(\mathbf{u_{PA}}, p_P, p_A) - Q_{AT}(\mathbf{u_{AT}}, p_A, p_T) - A_A \dot{x}\right) \triangleq \\ &\quad f_A(x, \dot{x}, p_P, p_A, p_T, \mathbf{u_{PA}}, \mathbf{u_{AT}}) \\ \dot{p}_B &= \frac{B_B}{A_B(x_{max} - x) + V_{0B}}\left(Q_{PB}(\mathbf{u_{PB}}, p_P, p_B) - Q_{BT}(\mathbf{u_{BT}}, p_B, p_T) + A_B \dot{x}\right) \triangleq \\ &\quad f_B(x, \dot{x}, p_P, p_B, p_T, \mathbf{u_{PB}}, \mathbf{u_{BT}})\end{aligned} \tag{1}$$

The flow rates Q_{PA}, Q_{AT}, Q_{PB}, and Q_{BT} are controlled by N parallel connected on/off valves and their flow rates are modelled by generalized turbulent flow model [7]:

$$Q_{XY} = \sum_{i=1}^{N} \mathbf{u_{XY}}(i)\mathbf{K_{v,XY}}(i)\,\mathrm{sgn}(p_X - p_Y)\left(|p_X - p_Y|\right)^{\mathbf{x_{XY}}(i)} \tag{2}$$

where XY is either PA, AT, PB, or BT and $\cdot(i)$ refers to the i:th element of the vector. If pressures p_P, p_T, p_A and p_B, and piston velocity and position are measured, the pressures after one sampling period for given control vectors $\{\mathbf{u_{PA}}, \mathbf{u_{AT}}, \mathbf{u_{PB}}, \mathbf{u_{BT}}\}$ can be estimated by using Heun's method:

$$\dot{p}_A(k+1) = p_A(k) + T_S f_A\left(x(k), \dot{x}(k), p_P(k), p_A(k), p_T(k), \mathbf{u_{PA}}(k), \mathbf{u_{AT}}(k)\right)$$
$$\hat{p}_A(k+1) = p_A(k) + \frac{T_S}{2}\Big(f_A\left(x(k), \dot{x}(k), p_P(k), p_A(k), p_T(k), \mathbf{u_{PA}}(k), \mathbf{u_{AT}}(k)\right) + \quad (3)$$
$$f_A\left(x(k) + T_S \dot{x}(k), \dot{x}(k), p_P(k), \dot{p}_A(k+1), p_T(k), \mathbf{u_{PA}}(k), \mathbf{u_{AT}}(k)\right)\Big)$$

The equations for the B-chamber pressure are similar. The primary objective of the force controller is to minimize the force error while the secondary objective is to keep the chamber pressures near the target values. This is solved by first selecting such control candidates for the A- and B-side that the estimated error in chamber pressures is small, and then calculating force error for each combination of the control candidates. The control candidates are selected according to the following cost functions:

$$\begin{aligned} J_A &= \left| A_A\left(p_{A,ref} - \hat{p}_A(k+1)\right)\right| + W_u \mathbf{b}^{\mathrm{T}}\left(\mathbf{u_{PA}} + \mathbf{u_{AT}}\right) + W_P\left(\left(p_P - p_A\right)Q_{PA} + \left(p_A - p_T\right)Q_{AT}\right) \\ J_B &= \left| A_B\left(p_{B,ref} - \hat{p}_B(k+1)\right)\right| + W_u \mathbf{b}^{\mathrm{T}}\left(\mathbf{u_{PB}} + \mathbf{u_{BT}}\right) + W_P\left(\left(p_P - p_B\right)Q_{PB} + \left(p_B - p_T\right)Q_{BT}\right) \end{aligned} \quad (4)$$

where **b** is vector defining relative sizes of valves and W_u and W_P are tuning parameters. The cost functions have three terms. The first term sets penalty for the pressure error, the second for the opening of the DFCUs and the third for the power losses of the DFCUs. The N_{cand} control candidates are selected for both sides for further analysis. All N_{cand}^2 combinations are analyzed by using following cost function:

$$\begin{aligned} J = &\left| F_{ref}(k) - \hat{F}(k+1)\right| + W_u \mathbf{b}^{\mathrm{T}}\left(\mathbf{u_{PA}} + \mathbf{u_{AT}} + \mathbf{u_{PB}} + \mathbf{u_{BT}}\right) + \\ &W_P\left(\left(p_P - p_A\right)Q_{PA} + \left(p_A - p_T\right)Q_{AT} + \left(p_P - p_B\right)Q_{PB} + \left(p_B - p_T\right)Q_{BT}\right) \\ \hat{F}(k+1) = &\hat{p}_A(k+1)A_A - \hat{p}_B(k+1)A_B \end{aligned} \quad (5)$$

The control input combination, which minimizes J is selected.

2.3. Outer-loop velocity and position controllers

The tuning of the outer-loop velocity and position controllers is made according to [6]. The result is robust against variations in the bulk modulus, system delay and inertia. The resulting tuning is $K_{P,vel}$ = 450 000 N s m^{-1}, K_P = 12 s^{-1}, K_I = 12 s^{-2} and K_D = 0.

2.4. Supply pressure control

The correct control of supply pressure is the key for energy efficient control. In this paper, a new and relatively simple approach is used. If force error is big positive and piston velocity is also positive, there is not enough supply pressure and it is increased. Similarly, if force error is big and negative while piston velocity is negative, the supply pressure is increased. The supply pressure is decreased if force error is small and valve control signals are not saturated. Fuzzy logic is used in order to make the supply pressure control smooth. The membership functions are shown in Figure 2. The minimum function is used as a fuzzy AND operator and the Simulink implementation is shown in Figure 3. The solution has two parameters F_{tol} and u_{lim} as shown in Figure 2.

The third parameter is the maximum increase/decrease rate Δp_P per sampling period. Finally, the supply pressure is limited between $p_{P,min}$ and $p_{P,max}$.

The main drawback of the solution is that it cannot optimize supply pressure for regenerative connection. The controller switches automatically into regenerative connection if the supply pressure allows it but the supply pressure controller does not actively increase the supply pressure such that the regenerative connection becomes possible. The solution is thus suboptimal.

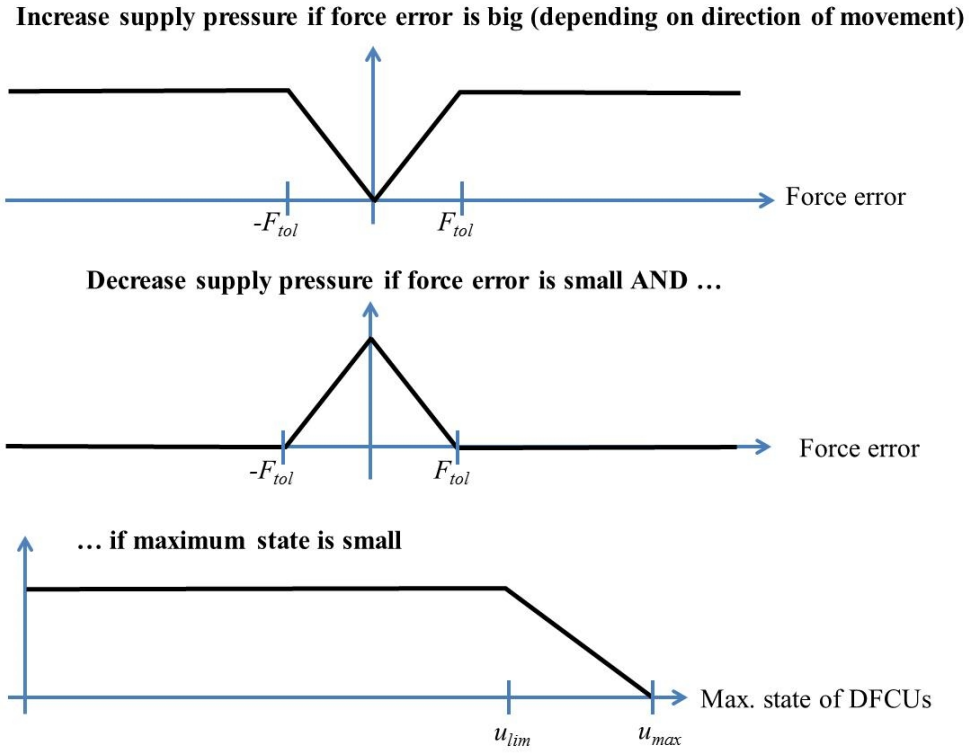

Figure 2. Fuzzy membership functions of the supply pressure controller.

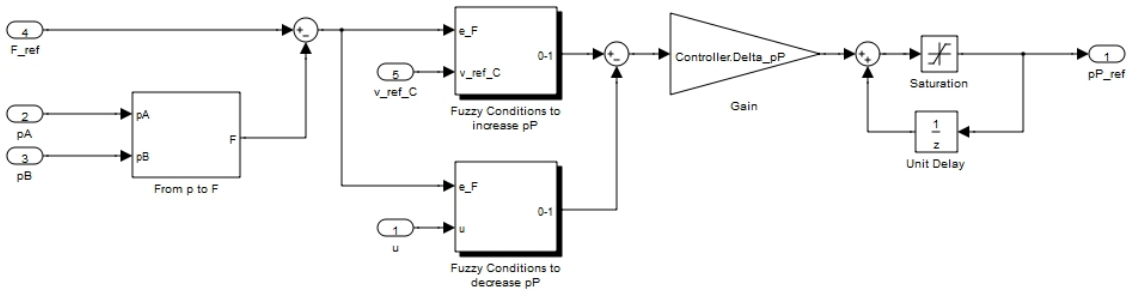

Figure 3. Simulink implementation of the supply pressure control.

2.5. Selection of target chamber pressures

The selection of correct target pressures is essential step in the successful use of the force controller. The earlier papers [5, 6] have used simple rule: The control mode is selected to be normal inflow-outflow mode and pressure differentials over both active DFCUs are the same. This is not optimal in terms of controllability and energy

efficiency and it does not take into account physical limitations of the system. In order to maximize the stiffness and to avoid cavitation, the target pressures are selected as high as possible taking into account the current supply pressure. For the extending motion, the pressure differential over DFCU PA is selected to be at the nominal value Δp_N unless it would yield too high pressure in the B-chamber. The minimum pressure is also limited to p_{min} at both chambers. These rules give:

$$p_{A,ref,ext} = \max\left(p_{min}, \frac{p_{min}A_B + F_{ref}}{A_A}, \min\left(p_P - \Delta p_N, \frac{p_{max}A_B + F_{ref}}{A_A}\right)\right) \quad (6)$$

For the retracting movement, similar rules lead to:

$$p_{B,ref,ret} = \max\left(p_{min}, \frac{p_{min}A_A - F_{ref}}{A_B}, \min\left(p_P - \Delta p_N, \frac{p_{max}A_A - F_{ref}}{A_B}\right)\right) \quad (7)$$

Now one chamber pressure is known for each direction of movement and the other one can be solved from the equation:

$$F_{ref} = p_{A,ref}A_A - p_{B,ref}A_B \quad (8)$$

2.6. Taking physical limitations into account

The final step is to consider the physical limitations of the system. The nominal pressure differential may be too small for fast movements, for example, or the system may not be capable for stepwise changes in target pressures. These limitations are considered by determining the smallest and the biggest obtainable chamber pressure by Eq. 3. The chamber pressures are limited such that the force balance equation holds if possible and that pressures stay between the smallest and biggest possible value. Figure 4 shows the Simulink implementation. The implementation is not perfect in the sense that A-side pressure may not be within limits. Another option would be that the pressure references are not consistent with the force reference.

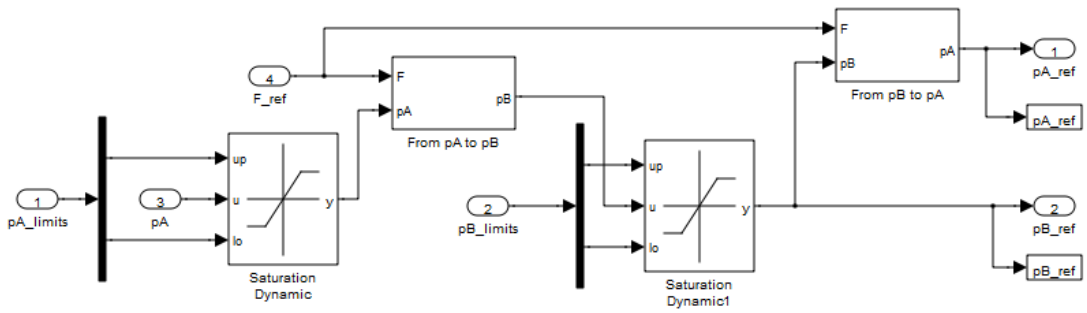

Figure 4. Simulink implementation of the physical limitations of the pressure references.

3. SIMULATION AND EXPERIMENTAL RESULTS

3.1. Experimental setup

The test system and its hydraulic circuit diagram are shown in Figure 5. The system mimics the dynamics of the joint actuator of a typical medium sized mobile machine boom and its natural frequency is about 3 Hz with 400 kg load mass. The digital valve system consists of 4x16 miniaturized fast on/off valves [8]. All valves have the same flow capacity and the response time of valves is about 3 ms. The flow rate of the pressure side and tank side valves are approximated by equations $Q = 8.0' 10^{-9} Dp^{0.53}$ and $Q = 7.5' 10^{-9} Dp^{0.53}$, respectively. The pressure signals have an anti-aliasing RC filter with a corner frequency of 720 Hz. After A/D conversion, pressures are filtered by a non-linear filter, which buffers five data points, removes maximum and minimum value and returns mean value of remaining three data points. Finally, chamber pressures and supply pressure are filtered by the discrete-time first order filter with time constants of 2 ms and 6 ms, respectively. The position signal is filtered by the discrete-time first order filter with time constant of 6 ms. Filters run with 0.25 ms sampling period. The supply pressure is controlled by a Moog RKP-D 80 cm^3 servo pump.

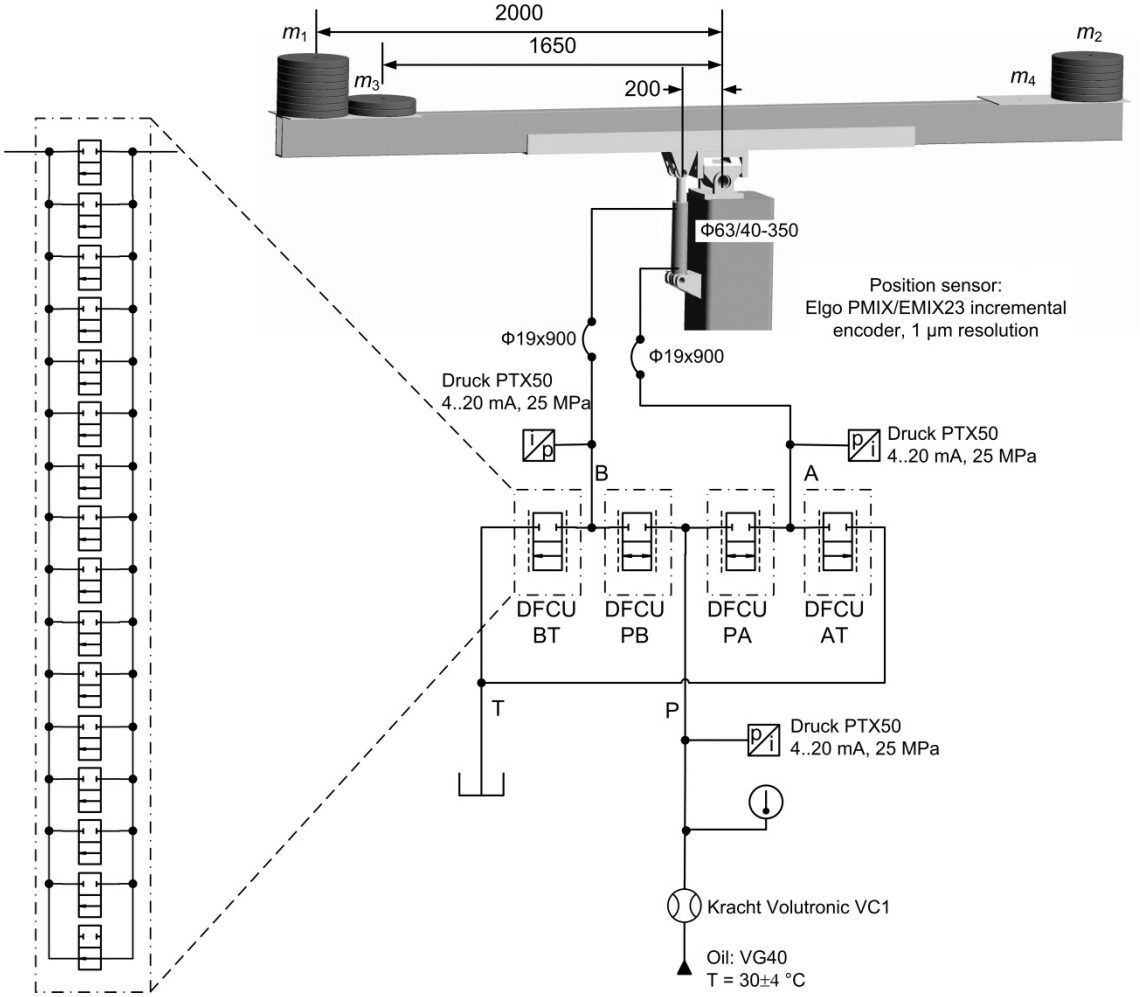

Figure 5. Hydraulic circuit diagram of the test system.

3.2. Controller parameters

The system and controller parameters are given in Table 1. Although the objective is simple controller, the number of parameters is still relatively big. Most of the parameters can be found by using simulations and linear analysis presented in [5].

Table 1. System and controller parameters.

System parameters		
A_A	3117.2 mm^2	A-side piston area
A_B	1860.6 mm^2	B-side piston area
x_{max}	350 mm	Piston stroke
V_{0A}, V_{0B}	0.4 dm^3	Dead volumes
b	$[1\ 1\ \ldots\ 1]^T$	Relative sizes of valves
Force controller		
B_A, B_B	1500 MPa	Estimate of the bulk modulus
N_{cand}	12	The number of A- and B-side control candidates.
T_S	5 ms	Sampling period
W_u	100 N	Weight for opening of DFCUs
W_P	2 N/W	Weight for power losses of DFCUs
Velocity and position controllers		
$K_{P,vel}$	450 kN s/m	Velocity controller gain, see Fig. 1
$K_{P,pos}$	12 1/s	Position controller gain, P-term, see Fig. 1
$K_{I,pos}$	12 1/s^2	Position controller gain, I-term, see Fig. 1
$K_{D,pos}$	0	Position controller gain, D-term, see Fig. 1
deadzone	0.1 mm	Integration is stopped when error is smaller than deadzone
Supply pressure control		
F_{tol}	2 kN	Tolerance for force error, see Fig. 2
u_{lim}	12	Limit for maximum state for DFCUs, see Fig. 2
Δp_P	0.3 MPa	Maximum change of supply pressure during one sampling period
$p_{P,min}$	2 MPa	Minimum supply pressure
$p_{P,max}$	10 MPa	Maximum supply pressure
Pressure references		
Δp_N	1 MPa	Nom. pressure differential over supply side DFCU
p_{min}	0.5 MPa	The smallest allowed target pressure
p_{max}	13 MPa	The biggest allowed target pressure

3.3. Simulated response

Simulations are used to tune the system parameters and to find out the system performance when all parameters are known and almost ideal supply pressure control is used. The supply pressure dynamics is modelled with a first order lag with time constant of 20 ms. Figure 6 shows an example simulation when load mass is 200 kg at both ends. The true mechanism is not modelled but a constant effective inertia of 53000 kg is used. The total system delay is assumed to be 4 ms and the effective bulk modulus is 1200 MPa. The acceleration phase runs in the inflow-outflow control mode while the system switches into energy efficient regenerative control mode automatically during braking.

This is interesting result because the supply pressure controller does not deliberately increase the supply pressure in order to make regenerative control mode possible. The transition between modes is smooth and can be seen in valve control signals only. The controller has some difficulties when the B-side target pressure is at maximum. The reason for the oscillations is unknown.

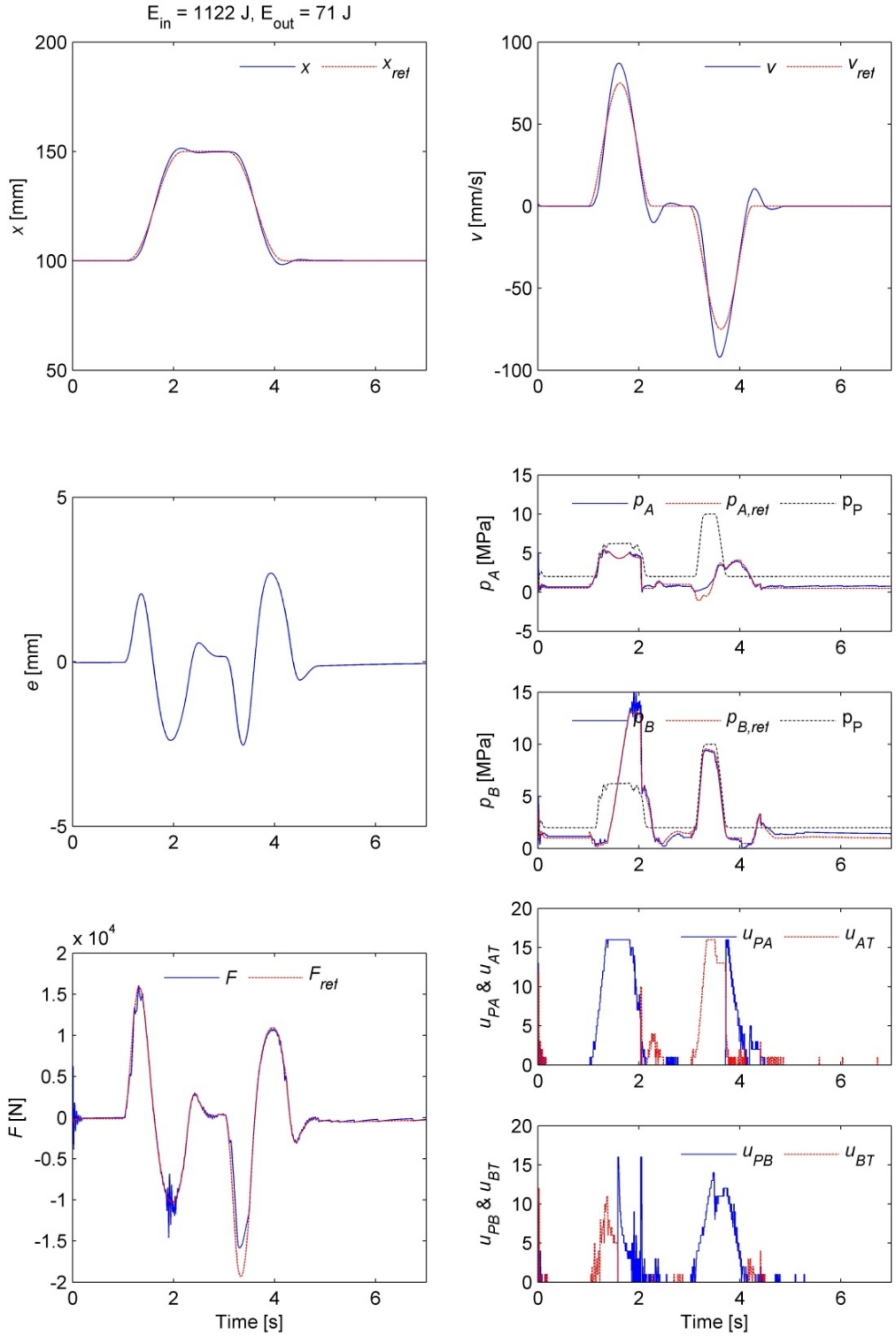

Figure 6. Simulated response

3.4. Measured response

Figure 7 shows the measured response when load mass is 200 kg at both ends. The controllability and tracking error are quite similar to the simulated response. The system also uses regenerative connection during braking, and the mode switching is smooth. The measured input power is 1.35 kJ while simulations predict 1.12 kJ only. The difference is probably caused by non-ideal supply pressure control.

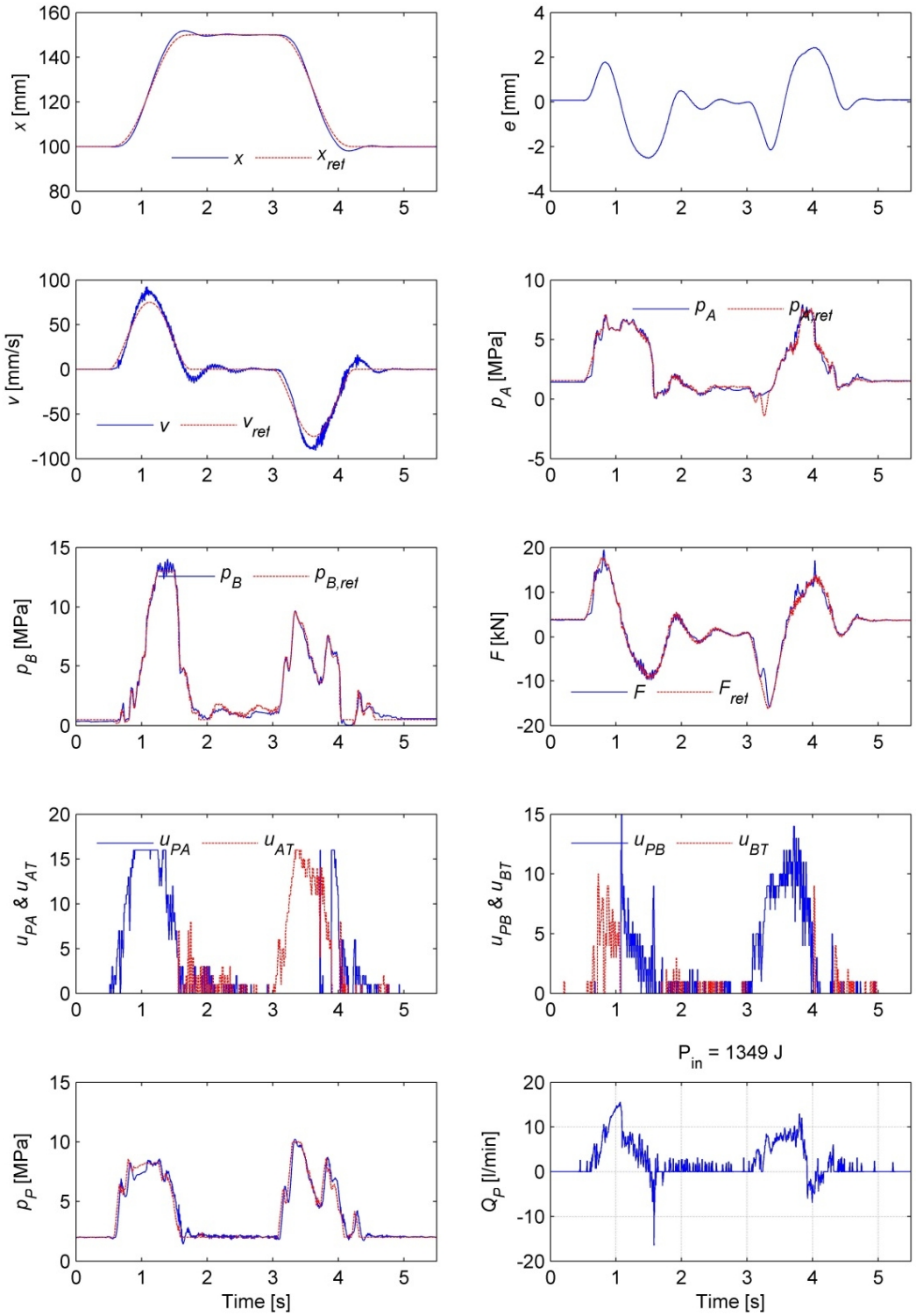

Figure 7. Measured response.

4. DISCUSSION

The measured input energy for the system is 1.35 kJ for 2x50 mm movement. The characteristic input energy is thus 13.5 J/mm. The measured results with the same system in [4] demonstrated input energy of 6.1 kJ for 2x35 plus 2x70 mm movements. The characteristic input energy is thus 29 J/mm, i.e. 115 % more. However, the results cannot be compared directly because this study uses single 63 mm cylinder while a double cylinder with 63 mm diameter was used in [4]. Taking this into account it can be concluded that the energy consumption of the new system is slightly smaller. This is significant result because the solution of this paper is much simpler. The controllability of the boom is much better than in [4]. This is also significant result because the system has smaller cylinder. The suggested method to determine the chamber pressure references is not perfect in the sense that it yields negative A-chamber pressure reference near t = 3.1 s.

5. CONCLUSIONS

The experimental results show that it is possible to combine good controllability and small power losses. This is due to high performance pressure and force controller. This paper uses a new approach to control supply pressure and chamber pressures without complicated mode switching logic. The solution works but it cannot optimize the supply pressure for regenerative connection. Nevertheless, the measured power losses are even smaller than in the previous research publication [4].

ACKNOWLEDGEMENTS

The research was supported by Academy of Finland (Grant No. 286401).

REFERENCES

[1] Liu, S. & Yao, B. 2002. Energy-Saving Control of Single-Rod Hydraulic Cylinder with Programmable Valves and Improved Working Mode Selection. Proceedings of the 49th National Conference on Fluid Power, March 19-21, 2002, Las Vegas, Nevada, USA, pp. 81-91.

[2] Mattila, J. 2000. On Energy Efficient Motion Control of Hydraulic Manipulators. Dissertation, Tampere University of Technology, Publications 312, Tampere, Finland.

[3] Eriksson, B., Larsson, J. & Palmberg, J.-O. 2006. Study on Individual Pressure Control in Energy Efficient Cylinder Drives. Proceedings of 4th FPNI-PhD Symposium, June 13–16, 2006, Sarasota, Florida, USA, pp. 77-99.

[4] Linjama, M., Huova, M., Bostöm, P., Laamanen, A., Siivonen, L., Morel, L., Walden, M. & Vilenius, M. 2007. Design and Implementation of Energy Saving Digital Hydraulic Control System. In: Vilenius, J. & Koskinen, K.T. (eds.). The Tenth Scandinavian International Conference on Fluid Power (SICFP'07), May 21–23, Tampere, Finland, pp. 341–359 (Vol. 2).

[5] Linjama, M., Huova, M. & Huhtala, K. 2015. Model-Based Force and Position Tracking Control of an Asymmetric Cylinder with a Digital Hydraulic Valve. Accepted for publication in the International Journal of Fluid Power.

[6] Linjama, M., Huova, M., Karhu, O. & Huhtala, K. 2016. High-Performance Digital Hydraulic Tracking Control of a Mobile Boom Mockup. Accepted for publication in the 10th International Conference on Fluid Power, March 8–10, 2016, Dresden, Germany.

[7] Linjama, M., Huova, M. & Karvonen, M. 2012. Modelling of Flow Characteristics of On/Off Valves. Proceedings of the Fifth Workshop on Digital Fluid Power, October 24-25, 2012, Tampere, Finland, pp. 209-222.

[8] Linjama, M., Paloniitty, Tiainen, L. & Huhtala, K. 2014. Mechatronic Design of Digital Hydraulic Micro Valve Package. Procedia Engineering, Vol. 106, pp. 97–107 (doi:10.1016/j.proeng.2015.06.013).